Enhancing Materials Properties *via* Targeted Doping

Inauguraldissertation

zur
Erlangung der Würde eines Doktors der Philosophie
vorgelegt der
Philosophisch-Naturwissenschaftlichen Fakultät
der Universität Basel

von

Miglė Graužinytė
von Litauen

2019

Originaldokument gespeichert auf dem Dokumentenserver der Universität Basel
edoc.unibas.ch

Genehmigt von der Philosophisch-Naturwissenschaftlichen Fakultät
auf Antrag von

Prof. Dr. Stefan Goedecker
Prof. Dr. Silvana Botti

Basel, 11.12.2018

Prof. Dr. Martin Spiess
Dekan

To my grandparents
For changing my life in ways you will never know.
Without you I would not be where I am.
May you rest in peace.

Acknowledgements

Foremost, I would like to express my gratitude towards my thesis advisor Prof. Stefan Goedecker for providing me with an opportunity to work in this vibrant scientific field. His knowledge and experience as well as his belief in providing his students with freedom in their scientific pursuits have been essential for all I have managed to produce in my four years as a doctoral student at the University of Basel. I would also like to thank Prof. Silvana Botti and Dr. José A. Flores-Livas for taking part in my defence and finding the time to read the thesis. I would further like to acknowledge all my experimental collaborators for sharing their valuable time and expertese with me: Dr. Aïcha Hessler-Wyser, Dr. Monica Morales-Masis, Dr. Quentin Jeangros, Federica Landucci and Esteban Rucavado, as well as Prof. Ashkan Salamat and Dr. Dean Smith.

I feel privileged to have learned along side all the people that were part of the Computational Physics group throughout my doctoral studies: Dr. Max Amsler, Deb Sankar De, Melania D'Aniello, Augustin Degomme, Jonas Finkler, Dr. Giuseppe Fisicaro, Dr. José A. Flores-Livas, Behnam Parsaeifard, Dr. Santanu Saha, Dr. Bastian Schaefer and Dr. Daniele Tomerini. I appreciate every valuable and each frivolous discussion alike. Each and everyone one of you have tought me something unique and have brought color into my day-to-day office life. I am also grateful to Barbara Kammermann and Astrid Kalt, the secretaries of the physics department, for making these four years simpler by providing endless support in all technicalities related to living and working in Basel.

I would like to acknowledge Dr. Daniele Tomerini and Dr. José A. Flores-Livas for their invaluable help in proofreading my thesis and many other works throughout the duration of my studies. I further appreciate the efforts of Caitlin, Raluca and Daniel in seeking out errors in my work and am grateful to all of my friends, near and far, for making the good times better and being supportive in the bad times. I would especially like to thank Daniel for making *everything* he touches just a little better and my family for believing in me and letting me believe in myself.

Last, but certainly not least, I would like to express my gratitude to Dr. José A. Flores-Livas for the time, patience and guidance he had lent me in the past few years. Thank you, José, for every occassion when you held not just the Ph.D. thesis, but me myself together. Certainly, without your kindness this work would not be half of what it is today.

Abstract

In this thesis a series of theoretical studies aimed at enhancing the optical and electrical properties of selected oxide and hydride materials *via* defect incorporation is presented. Large-scale screening for useful defects was performed on two transparent tin-based oxide materials: a natively p-type tin monoxide and an intrinsically n-type tin dioxide. Novel dopant candidates that promise amplified charge-carrier generation if incorporated successfully were uncovered for both compounds. We further showed that some of these dopant elements are able to maintain the optical properties displayed by the bulk phases of the oxides. The two studies revealed the affinity of tin monoxide for both hole and electron free-carriers when doped appropriately, while tin dioxide was shown to be a strictly n-type conductor. The posibility of improving both optical and electronic attributes of tin-oxide materials further was investigated by exploring the interactions between impurity atoms and intrinsic defects of the host. Isovalent silicon doping in tin dioxide was shown to suppress absorption states arising from oxygen deficiencies, thus, presenting a novel path for improving optical properties in transparent conductive oxide materials. In tin monoxide, halogen interstitials were observed to bond with native tin vacancies ionizing them to higher charge states, which result in improved p-type carrier generation. Finally, acceptor doping was also considered in large band gap hydride materials under compression. Defects in ice, H_2O, and polyethylene, $(H_2C)_n$, were studied by identifying high-pressure phases that display covalent bonding and can, therefore, be successfully doped. The possibility of such doped phases displaying a superconducting transition was addressed and a transition temperature of 60 K in ice-X and a 35 K in a polymeric high-pressure phase of polyethylene was estimated.

Contents

1. Introduction **1**
1.1. Transparent Conductors . . . 2
1.2. Superconductors . . . 3
1.3. Thesis Outline . . . 4

2. Theoretical Background **5**
2.1. Quantum Mechanical Framework . . . 5
2.1.1. Schrödinger equation . . . 5
2.1.2. Approximations . . . 6
2.1.3. Self-consistent field approach . . . 10
2.1.4. Density functional theory . . . 10
2.1.5. Exchange-correlation functionals . . . 12
2.2. Extended Systems . . . 15
2.2.1. Band structure . . . 16
2.2.2. Ionic potentials . . . 18

3. Defect Calculations **21**
3.1. Point Defects . . . 21
3.2. Defect Formation Energies . . . 23
3.3. Shallow and Deep Defects . . . 25
3.3.1. Thermodynamic and optical transition levels . . . 25
3.3.2. Electronic defect levels . . . 27
3.4. The Band Gap Problem . . . 28
3.5. External Reservoirs . . . 30
3.5.1. Chemical potentials . . . 30
3.5.2. The Fermi level . . . 32
3.6. Supercell Size Corrections . . . 33
3.6.1. Elastic corrections . . . 33
3.6.2. Magnetic corrections . . . 34
3.6.3. Electrostatic interactions . . . 34
3.6.4. Band filling corrections . . . 36
3.7. Binding Energies . . . 37

4. Dopant Screening **39**
4.1. Case A: Tin Dioxide . . . 42
4.1.1. Bulk properties . . . 43
4.1.2. Defect calculations . . . 44
4.1.3. n-type dopants . . . 46

4.1.4. *p*-type dopants 50
4.1.5. Electronic structure 52
4.1.6. Discussion 54
4.2. Case B: Tin Monoxide 54
4.2.1. Bulk structure 56
4.2.2. Defect calculations 58
4.2.3. Analysis of *p*-type dopants 60
4.2.4. Analysis of *n*-type dopants 64
4.2.5. Dopants and transparency 68
4.2.6. Effects of vdW and interstitials 69
4.2.7. Discussion 71
4.3. Common Trends 71

5. Defect Complexes 73
5.1. Case Study A - Silicon in Sn-based Oxides 74
5.1.1. Experimental basis 75
5.1.2. Computational assessment of Si-modification in SnO_2 77
5.1.3. Steric effects 81
5.1.4. Discussion 82
5.2. Case Study B - Defect Complexes in Tin Monoxide 82
5.2.1. Oxygen in SnO 83
5.2.2. Chalcogens in SnO 85
5.2.3. Halogens in SnO 87
5.2.4. Alternative defect sites 88
5.2.5. The effect of vdWs interactions 90
5.2.6. Discussion 91

6. Defects under Pressure 93
6.1. Defect Formation Volume 94
6.2. Case Study A - Superconducting H_2O 96
6.2.1. Electronic structure of doped ice under pressure 97
6.2.2. Stability of doped-ice under pressure 100
6.2.3. Defect formation energies 100
6.2.4. Superconducting properties 102
6.2.5. Discussion 103
6.3. Case Study B - Superconducting $(H_2C)_n$ 104
6.3.1. Electronic structure of doped polyethylene under pressure . . . 107
6.3.2. Superconducting properties 110
6.3.3. Discussion 110

7. Summary and Outlook 113
7.1. Outlook 115

Bibliography 133

A. Chemical reference **139**
A.1. Tin Dioxide 139
A.2. Tin Monoxide 140
A.3. Tin Monoxide – Complexes 142

B. Electronic Density of States **145**

C. HSE06 Relaxations **151**

D. Defect Concentrations in Thermal Equilibrium **153**

E. Shallow Acceptor Correction **155**

Publications **157**

1 Introduction

New and higher performance materials are necessary to enable the ever more ambitious feats of engineering. Copious experimental and theoretical efforts have, therefore, been exerted towards the realization of compounds that consistently outperform their predecessors. Methods for synthesizing new materials anywhere from nanometers to tens of meters in size have been developed [1] and characterization techniques have become routinely available to test and manipulate the properties of the deposited samples. Parallelly, computational methods have evolved from a tool that aids the aforementioned characterization to a level of maturity that permits purely computational design of novel materials [2].

It is now well understood that the properties of a given compound are determined by its atomic and electronic structure [3, 4]. Methods for computationally exploring the possible atomic arrangements of a material with a specific composition have been proposed, such as the minima hopping method [5], metadynamics [6], simulated annealing [7] and genetic algorithms [8]. Although such systematic structural searches routinely return thousands of candidate crystals, only a handful of them can be synthesized (or are even stable) at the thermodynamic conditions accessible in a laboratory [9, 10]. A smaller fraction still may display a desired, rare or exceptional property. It is, thus, imperative to maximize the potential of a useful compound once it is identified and defects are typically invoked to do this job. Furthermore, impurity incorporation can enable fine-tuning of specific features displayed by a material.

Though defects, as the name implies, are structural imperfections in the crystalline lattice, their presence is not necessarily detrimental to the performance of the material. In fact, many useful features of certain systems are a direct consequence of impurity incorporation, e.g., semiconductors. Defects can dramatically alter mechanical [11], optical [12, 13], electrical [14, 15], magnetic [16], and thermoelectric [17] properties. Furthermore, in thermodynamic equilibrium defects are ubiquitous in all materials even when not incorporated intentionally. Such unintentional defects can be key to understanding the behavior of a specific system.

When attempting to unravel the impact of a defect, computational studies can offer significant advantages over experimental work. Techniques, such as secondary ion mass spectroscopy (SIMS) [18] or Rutherford backscattering spectrometry (RBS) [19] for impurities, and electron paramagnetic resonance (EPR) [20] or positron annihilation spectroscopy (PAS) [21] for intrinsic defects, can permit the experimental determination of defect concentrations in a solid. However, most of these techniques provide very little information on the behavior of the defect on an atomistic level with only extended X-ray absorption fine structure (EXAFS) experiments lending insights into the average struc-

tures surrounding impurity atoms [22, 23]. In contrast, *ab initio*[†] simulations provide a tool that is able to identify the structural, electronic, magnetic, and optical behavior of a defect at a fraction of the cost. Theoretical models are also indispensable in interpreting experiments where the origin of an observed defect-induced transition needs to be identified, such as temperature dependent Hall conductivity [24], deep-level transient spectroscopy (DLTS) [25], photoluminescence and absorption measurements [26].

Furthermore, computational tools are now fast and reliable enough to allow the design of materials *in silico*, i.e. solely as a concept on a computer chip [2]. Metrics to evaluate a desired aspect of a system can be established and subsequently utilized to search for new materials specialized for a given task [27]. This has lead to high-throughput approaches that combine the use of large databases with advanced electronic-structure calculations to search for novel materials, such as new thermoelectric compounds [28], topological insulators [29], or to design new batteries [30]. This ideology can, in principle, be extended to design systems with coveted features *via* high-throughput searches for useful defects. Yet, only limited studies of this nature have been implemented to date despite the fact that in an experimental set up analogous tests are incredibly time-consuming and cost-inefficient to perform.

In this spirit, the DISCO project was established as a collaboration between the computational physics group at the University of Basel and the experimental teams at École Polytechnique Fédérale de Lausanne (EPFL), Photovoltaics and Thin Film Electronics Laboratory (PV-Lab) of EPFL and the Forschungszentrum Jülich. The overarching goal of the collaboration was to realize alternative transparent conductive oxide (TCO) materials that display optoelectronic properties competitive with those of the current industry standard – indium oxide, In_2O_3.

1.1. Transparent Conductors

Many emergent technologies make use of optoelectronic devices – instruments that are able to utilize both light and electricity. The prerequisite for such applications are efficient transparent conductor materials that, as the name suggests, are able to simultaneously transmit visible light and sustain an electric current despite the sizable electronic band gap implied by the transparency. Some of the most profitable optoelectronic industries include the production of organic light-emitting diode (OLED) displays [31], in which TCOs are utilized as transparent electrodes, and window coatings [32], which are typically used for efficient temperature regulation via infrared reflection. The transparent electrode technology currently used in OLED displays, however, could bring forth equally groundbreaking changes in photovoltaic (PV) applications [33] where significant current collection gains can be postulated. Tin-doped In_2O_3 is the current front-runner in the TCO race with resistivity on the order of 10^{-5} Ω cm and over 90% transparency in the visible range [31]. However, it is unable to accommodate PV applications as the wide spread usage of solar cells is not compatible with the low abundance of indium within the earths crust and its hefty market price [34]. Furthermore, stringent demands

[†]Latin for “from the beginning”, refers to calculations performed from *first principles* that only rely on basic and established laws of nature without the use of empirical models.

are placed on other properties of potential candidate PV compounds, such as good stability, sustainability, and non-toxicity [35].

Analogous to semiconductors, defects play a crucial role in transparent conductor materials [36]. Defect-induced electronic states near the conduction or valence band edges of the host are the source of the current generated under an applied electric field. The origin of these defect states is still widely debated in the scientific literature with both native defects and impurities implicated as the culprit for conduction [36–40]. Furthermore, only a handful of crystals (among them, In_2O_3, CdO, SnO_2, Ga_2O_3, ZnO, Sb_2O_5 and TiO_2) have been identified as good transparent conductors [35, 41] despite the numerous scientific interest in their discovery [41–44]. This fact combined with the knowledge that critical properties of TCOs are defect-induced makes them particularly amenable to a high-throughput defect study.

Additionally, finding highly efficient *p*-type transparent conductors is still a challenge in the scientific community [42, 43, 45], as most of the aforementioned oxide conductors are *n*-type. Successful synthesis of *p*-*n* junctions of transparent conductor materials would open up a path for entirely new optoelectronic devices [45]. A systematic way to search for *p*-type dopants could speed up the process of transparent conductor exploration and synthesis, allowing for a faster concept to production pathway.

1.2. Superconductors

Transparent conductors are not the only electronically relevant materials that can benefit from defect-induced free-carriers. Superconductors, if realized at room temperature, could result in an insurmountable increase in efficiency of most electronic devices. In conventional superconductors the presence of hydrogen seems to be fundamental to obtaining the large phonon frequencies and strong electron-phonon coupling required to achieve high superconducting temperatures [46–48]. Thus, major emphasis when searching for room-temperature superconductors has been given to hydrides, such as silane [49, 50], disilane [51], hydrogen sulfide [52–55], hydrogen selenide [56], phosphine [57, 58], etc. Unfortunately, most chemical compounds containing hydrogen only metalize at extremely high pressures. Furthermore, the metallic phases are often thermodynamically unstable and difficult to access experimentally.

A possible, but largely overlooked, alternative is to introduce charge carriers by doping and, thus, enable a superconducting transition. It is well known that by introducing enough electron- or hole-donating impurities one can render a semiconducting system metallic and even superconducting. This strategy was already successfully used to induce superconductivity in diamond (doped with boron) [59], silicon (doped with boron [60]), germanium (doped with gallium [61]), and silicon carbide (doped with boron [62]). The combination of high pressure and defect engineering could enable new pathways to induce superconductivity in many hydride materials that would otherwise remain insulating up to terapascal pressures.

1.3. Thesis Outline

It is the goal of this thesis to demonstrate how computational modelling tools can be used to inform targeted doping in experimentally synthesizable compounds. This is desirable for two reasons. First, targeted doping allows materials with superior properties to those nominally undoped to be created. Yet more importantly, computationally informed targeted doping can save millions in development costs when compared to blind testing in experimental laboratories. The thesis is structured as follows.

We start in **Chapter 2** with a brief introduction to the theoretical background needed to understand the modelling techniques employed. Basic quantum mechanical concepts for performing electronic structure calculations are covered together with the common approximations used and the limitations that they impose. A connection between finite size simulations and periodic extended systems is made. The chapter ends with a brief discussion of the ionic potential and its description in simulations.

Chapter 3 presents approaches specific to defect calculations. The concept of shallow and deep defects is introduced by way of thermodynamic transition levels. Ways of overcoming the band gap problem inherent to local density functional calculations when evaluating transition levels are enumerated. The supercell approach to defect calculations is explained and the periodic boundary related corrections are elucidated. We close the chapter with a quick glance at defect complex formation.

Chapter 4 is dedicated to defects in isolation - a methodology for high-throughput dopant searches in transparent conductor materials is presented. The potential pitfalls of the method are illustrated and discussed. The effectiveness of the presented approach is demonstrated for two example cases: tin dioxide (a successful *n*-type TCO) and tin monoxide (a native *p*-type TCO). Common trends and divergences among the two cases close this chapter.

Chapter 5 deals with defect complexes and the effects they can have on device performance. In particular, we focus on two scenarios where defect complex formation offers an improved performance of the underlying material: in one case optical properties and in the other electrical properties are enhanced.

In **Chapter 6** we extend our understanding of defect behavior to study defects under pressure. In particular, doping as a path for creating superconducting materials under high pressure is postulated. Again, two case studies are presented and the theoretical possibility of doping-induced superconductivity in hydrogen-based materials is addressed. Finally, we conclude the thesis in **Chapter 7** with an overview of our results and their implications. Further avenues for future studies are considered.

2 Theoretical Background

Employing modern computational modelling tools to advance the understanding of transparent conductor materials is the chief aim of the thesis. In order to guide the reader with ease through the results presented in the following chapters, we begin with a short self-contained introduction to the theoretical background needed to understand the methodologies presented later.

In the first section, the underlying quantum mechanical concepts are introduced. Then approximations required to perform *ab initio* simulations based on these concepts are presented and a discussion of their limitations is included where appropriate. Density functional theory is outlined in the following section and the performance of different exchange-correlation functionals within the formalism is assessed. The ideas key to modelling extended systems, i.e. infinite periodic crystals, and representations for the ionic potential conclude the chapter. Here, particular focus is placed on the methods employed throughout the work presented in the thesis.

2.1. Quantum Mechanical Framework

2.1.1. Schrödinger equation

The laws of quantum mechanics formulated in the beginning of the 20th century (1923–1925) [63–65] allow us to describe, in principle up to an arbitrary accuracy, a system of interacting nuclei and surrounding electrons. A many-body wavefunction $\Psi(\{\mathbf{R}_I, \mathbf{r}_i\})$ is constructed to describe the system under consideration, where $\{\mathbf{R}_I\}$ represent the positions of the ions and $\{\mathbf{r}_i\}$ the positions of the electrons. The total energy, E, of the electron-ion network can then be obtained by solving the Schrödinger Eq. 2.1. Throughout the body of the thesis we do not concern ourselves with properties that require a response (evolution in time) of the wavefunction to time-varying fields, such as electric or magnetic fields, and thus the following discussion is limited to the time-independent Schrödinger equation.

$$\mathcal{H}\Psi(\{\mathbf{R}_I, \mathbf{r}_i\}) = E\Psi(\{\mathbf{R}_I, \mathbf{r}_i\}) \tag{2.1}$$

The time-independent Hamiltonian, $\mathcal{H}$, contains within it the kinetic energy operators for the nuclei, $\mathcal{T}_n$, and the electrons, $\mathcal{T}_e$, as well as the potential energy terms arising from interactions present in the system. Here, namely the Coulomb interaction is considered, which introduces a repulsive potential for the electron-electron, $\mathcal{V}_{ee}$, and the nuclei-nuclei, $\mathcal{V}_{nn}$, interactions and an attractive potential for the nuclei-electron, $\mathcal{V}_{en}$, interactions.

$$\mathcal{H} = \underbrace{-\sum_{I} \frac{1}{2M_I} \nabla^2_{\mathbf{R}_I}}_{\mathcal{T}_n} + \underbrace{\sum_{I<J} \frac{Z_I Z_J}{|\mathbf{R}_I - \mathbf{R}_J|}}_{\mathcal{V}_{nn}} \underbrace{-\sum_{i} \frac{1}{2} \nabla^2_{\mathbf{r}_i}}_{\mathcal{T}_e} \underbrace{-\sum_{I,i} \frac{Z_I}{|\mathbf{R}_I - \mathbf{r}_i|}}_{\mathcal{V}_{en}} + \underbrace{\sum_{i<j} \frac{1}{|\mathbf{r}_i - \mathbf{r}_j|}}_{\mathcal{V}_{ee}} \tag{2.2}$$

In Eq. 2.2 the Hamiltonian is defined using atomic units, typical to the field of quantum physics. The units are defined such that the mass of the electron, m_e, and the charge of the electron, e, are equal to one. The Plank constant divided by 2π, $\hbar$, and the electric permittivity of the vacuum multiplied by 4π, $4\pi\epsilon_0$, are also set equal to one. The mass of the nuclei, M_I, and the ionic charges, Z_I, are then rescaled to reflect these units. The indexes I and J run over all nuclei, while i and j enumerate the electrons. The Laplace operator, ∇^2, represents a second order derivative of the position it is applied to.

$$\nabla^2_u = \frac{\partial^2}{\partial u_x^2} + \frac{\partial^2}{\partial u_y^2} + \frac{\partial^2}{\partial u_z^2} \tag{2.3}$$

Once the wavefunction corresponding to a given system is known, all the observable properties of that system can be extracted from the wavefunction by calculating the expectation values of the appropriate operators, $\mathcal{O}$. The Hamiltonian, $\mathcal{H}$, is itself an operator that corresponds to the total energy expectation value.

$$\langle \Psi | \mathcal{O} | \Psi \rangle = \int \Psi^*(\{\mathbf{R}_I, \mathbf{r}_i\}) \mathcal{O}(\{\mathbf{R}_I, \mathbf{r}_i\}) \Psi(\{\mathbf{R}_I, \mathbf{r}_i\}) d\mathbf{R}_1 ... d\mathbf{R}_N d\mathbf{r}_1 ... d\mathbf{r}_n \tag{2.4}$$

Other often encountered operators include the momentum operator, $-i\nabla_{\mathbf{r}}$, and the position operator, $\mathbf{r}$. As will be shown in further sections of this thesis, the electronic density operator, $\mathcal{N}(\mathbf{r})$, given by Eq. 2.5, is of particular interest. The expectation value of this operator gives the total number of electrons found at a given location $\mathbf{r}$ in space.

$$\mathcal{N}(\mathbf{r}) = \sum_i \delta(\mathbf{r} - \mathbf{r}_i) \tag{2.5}$$

Unfortunately, any of the above mentioned information about the system can only be extracted once the exact wavefunction is known. Yet, analytic solutions for the Schrödinger Eq. 2.1 and, hence, the corresponding wavefunction are only scarcely available. These solutions are generally limited to toy models, such as the free-electron gas model and particle in a potential well, or systems of restricted complexity, such as the hydrogen atom. For the quantum mechanical formalism to be useful in practice, even for systems made up of only a handful of atoms, approximations to the Schrödinger equation need to be introduced. In the following sections the most common approximations and their repercussions are discussed.

2.1.2. Approximations

The Born-Oppenheimer approximation

For all but the lightest of elements, such as hydrogen, the heavier nuclei can be anticipated to move on much longer time scales than the accompanying electrons. This is a

consequence of the large mass disparity between the heavy atomic cores and the light electrons. The use of this knowledge to decouple the electronic degrees of freedom from those of the nuclei is presently known as the Born-Oppenheimer or the adiabatic approximation [66]. Within the adiabatic approximation it is assumed that the wavefunction of the full system can be adequately described as a product of the ionic, $\phi(\{\mathbf{R}_I\})$, and the electronic, $\psi(\{\mathbf{r}_i\},\{\mathbf{R}_I\})$, wavefunctions.

$$\Psi(\{\mathbf{R}_I,\mathbf{r}_i\}) = \psi(\{\mathbf{r}_i\},\{\mathbf{R}_I\})\,\phi(\{\mathbf{R}_I\}) \tag{2.6}$$

The electronic wavefunction is taken to depend on the atomic positions only parametrically, thus, we will denote this term further as simply $\psi(\{\mathbf{r}_i\})$. In other words, it is presumed that the heavy ions are so slow that for each 'snap-shot' of the ionic motion the electrons have enough time to reach their ground state configuration. The instantaneous electronic ground state can be found by solving the electronic Schrödinger equation (2.7).

$$\mathcal{H}_e\psi(\{\mathbf{r}_i\}) = (\mathcal{T}_e + \mathcal{V}_{ee} + \mathcal{V}_{en})\psi(\{\mathbf{r}_i\}) = E_e\psi(\{\mathbf{r}_i\}) \tag{2.7}$$

The total energy of the system, at the fixed ionic positions, can then be recovered by adding the energy term arising from nuclear-nuclear, $\mathcal{V}_{nn}$, interactions. This additional term is simply a constant as far as the electrons are concerned.

$$E = E_e + E_{nn} \tag{2.8}$$

The complete wavefunction is obtained by applying the full Hamiltonian (Eq. 2.2) to the total ansatz wavefunction given by Eq. 2.6. Within the Born-Oppenheimer approximation, the cross-terms involving derivatives of the electronic wavefunction scaled by the inverse of the ionic masses are neglected. It is clear from the resulting Eq. 2.9 that the ionic wavefunction is only affected by the electrons through the $E_e(\{\mathbf{R}_I\})$ term. This term provides the adiabatic contribution of the electrons to the lattice energy and can be obtained by solving Eq. 2.7 for each fixed set of atomic positions $\{\mathbf{R}_I\}$.

$$\mathcal{H}_n\phi(\{\mathbf{R}_I\}) = (E_e(\{\mathbf{R}_I\}) + \mathcal{V}_{nn} + \mathcal{T}_{nn})\phi(\{\mathbf{R}_I\}) \tag{2.9}$$

To study phenomena where electron scattering by phonons offers significant contributions one needs to go beyond the Born-Oppenheimer approximation. Such phenomena, among others, typically include superconductivity, thermoelectricity, Raman scattering and polaron formation [67].

The Hartree approximation

Despite the simplifications provided by the adiabatic approximation, the ensuing electronic Schrödinger Eq. 2.7 is notoriously difficult to solve analytically. Numerical solutions could be attained, but even with the ever-growing computational power available to materials scientists only very small system sizes are tractable. The many-body nature of quantum systems implies that each individual electron impacts directly the motion of all other electrons within the system. An intuitive way to reduce the complexity of an N-electron many-body wavefunction was proposed by D. R. Hartree in 1928 [68]. He

suggested the use of an ansatz wavefunction consisting of a product of non-interacting single particle orbitals. This crude simplification permits a significant reduction in the complexity of the problem and is now known as the Hartree approximation [68]. The complex electron-electron interactions are not completely neglected within this approach, but are rather accounted for in some average fashion. In its simplest form a non-interacting wavefunction of this type can be written as a product of single particle states, $\phi_i(\mathbf{r}_i)$.

$$\psi(\{\mathbf{r}_i\}) = \phi_1(\mathbf{r}_1)\phi_2(\mathbf{r}_2)\dots\phi_{N-1}(\mathbf{r}_{N-1})\phi_N(\mathbf{r}_N) \tag{2.10}$$

The electronic energy of the system within this approximation is obtained by solving Eq. 2.7. Using a variational argument a single-particle Schrödinger equation for each individual orbital, $\phi_i(\mathbf{r})$, is found and takes the form of Eq. 2.11. The first term in the square brackets corresponds to the kinetic energy of the single orbital, the second term is the nuclear potential, $\mathcal{V}_{en}(\mathbf{r})$, acting on the electron placed at position $\mathbf{r}$, and the final term gives the Hartree potential, $\mathcal{V}_i^H$, a mean field approximation to the electron-electron interaction. While the potential arising from the presence of the ions is identical for each orbital $\phi_i(\mathbf{r})$, the Hartree-term is unique for every particle in the system.

$$\left[\frac{1}{2}\nabla^2_{\mathbf{r}} + \sum_I \frac{Z_I}{|\mathbf{R}_I - \mathbf{r}|} + \sum_{j\neq i}\langle\phi_j|\frac{1}{|\mathbf{r}_j - \mathbf{r}|}|\phi_j\rangle\right]\phi_i(\mathbf{r}) = \epsilon_i\phi_i(\mathbf{r}) \tag{2.11}$$

Thus, to obtain the complete electronic wavefunction within the Hartree approximation one only needs to solve a set of N single-particle equations. However, as evidenced by Eq. 2.11, the Hartree potential of a specific orbital $\phi_i(\mathbf{r})$ can only be evaluated once all the other orbitals $\phi_j(\mathbf{r}_j)$ are already known. Yet, typically neither the Hartree potential, nor the orbital wavefunctions are known prior to solving the Schrödinger equation. An iterative approach to obtaining the total electronic wavefunction proposed in order to circumvent this problem is discussed in more detail in Section 2.1.3.

Due to its simplicity the Hartree approximation fails to capture two key properties of interacting electrons: *correlation* and *exchange*. The first, addresses the inability of mean-field electrons to respond to the *instantaneous* positions of other particles. The motion of mean-field electrons is presumed to be governed by a Hartree-potential resultant from the average density of other electrons. The second, is a mathematical consequence of the Pauli exclusion principle. In relativistic quantum theory, the fermionic nature of electrons demands the wavefunction sign to be inverted upon the exchange of position between two electrons of the same spin. It is easily seen that this principle is not obeyed in the wavefunction form chosen in Eq. 2.10.

Hartree-Fock approximation

The quantum mechanical effects of the Pauli exclusion principle can be incorporated into the Hartree approximation by explicitly antisymmetrizing the wavefunction with respect to particle exchange. A convenient method to achieve this was first introduced by Slater [69] who proposed expressing the wavefunction as a determinant of the single particle orbitals. Combined with the self consistent field approach of Hartree this method is known as the Hartree-Fock approximation [70].

$$\psi(\{\mathbf{r}_i\}) = \frac{1}{\sqrt{(N!)}} \begin{vmatrix} \phi_1(\mathbf{r}_1) & \phi_1(\mathbf{r}_2) & \dots & \phi_1(\mathbf{r}_N) \\ \phi_2(\mathbf{r}_1) & \phi_2(\mathbf{r}_2) & \dots & \phi_2(\mathbf{r}_N) \\ \dots & \dots & \dots & \dots \\ \phi_N(\mathbf{r}_1) & \phi_N(\mathbf{r}_2) & \dots & \phi_N(\mathbf{r}_N) \end{vmatrix} \tag{2.12}$$

In this form, swapping the positions of two particles is equivalent to an interchange of two columns of the determinant, producing the desired change of sign. Using this ansatz for the wavefunction to solve the electronic Schrödinger equation results in a set of single-particle equations (Eq. 2.13), similar to those of the Hartree approximation.

$$\epsilon_i \phi_i(\mathbf{r}) = \left[\frac{1}{2}\nabla^2_{\mathbf{r}} + \mathcal{V}_{en}(\mathbf{r}) + \mathcal{V}_i^H\right] \phi_i(\mathbf{r}) - \sum_{j \neq i} \langle \phi_j | \frac{1}{|\mathbf{r}_j - \mathbf{r}|} | \phi_i \rangle \phi_j(\mathbf{r}) \tag{2.13}$$

However, the explicit antisymmetrizaton of the wavefunction elicits an additional term corresponding to the electronic exchange. This term, last on the right hand side of Eq. 2.13, is non-zero only for electrons of the same spin. The explicit inclusion of the electronic exchange in the construction of the wavefunction results in the lowering of the total energy of the system. We can reformulate this term in a more familiar form of a Hartree-Fock potential, $\mathcal{V}_i^{HF}(\mathbf{r})$, acting on a single orbital.

$$\mathcal{V}_i^{HF}(\mathbf{r}) = \int \frac{\rho(\mathbf{r}') - \rho_i^{HF}(\mathbf{r}, \mathbf{r}')}{|\mathbf{r} - \mathbf{r}'|} d\mathbf{r}' \tag{2.14}$$

The first term on the right hand side of Eq. 2.14 is the electrostatic potential arising form the *total* average particle-density, $\rho(\mathbf{r})$, obtained by applying the density operator defined in Eq. 2.5 to the Hartree-Fock wavefunction. This term differs slightly from $\mathcal{V}_i^H$ defined in Eq. 2.11 by also including the contribution of $j = i$ into the sum. Nevertheless, the Hartree-Fock formalism is completely self-interaction free as this contribution is canceled out by an identical contribution coming from the second term on the right hand side. This term corresponds to the electronic-exchange defined through the single-particle Hartree-Fock density (a single-particle exchange density) given in Eq. 2.15.

$$\rho_i^{HF}(\mathbf{r}, \mathbf{r}') = \sum_j \frac{\phi_i(\mathbf{r}')\phi_i^*(\mathbf{r})\phi_j(\mathbf{r})\phi_j^*(\mathbf{r}')}{\phi_i(\mathbf{r})\phi_i^*(\mathbf{r})} \tag{2.15}$$

Despite the inclusion of the electronic-exchange effects, the error coming from electron *correlation* discussed in the previous section is not alleviated by the Hartree-Fock approach. Thus, the method fails to accurately describe molecular bonding. The likelihood of finding two-electrons close to each other is, hence, anticipated to be lower in a realistic system than in Hartree-Fock predictions. This is particularly problematic for modelling delocalized electronic states and in the case of metals, where the Coulombic screening resulting from the highly mobile electrons remains unaccounted for. Furthermore, in some systems more than one Slater determinant may be needed to correctly describe the ground state properties. Here, static correlations play an important role. Post-Hartree-Fock quantum chemistry methods may be used to progress further in understanding such systems, e.g., configuration interaction approaches use a linear combination of determinants, weighted by some coefficients, to describe the wavefunction.

2.1.3. Self-consistent field approach

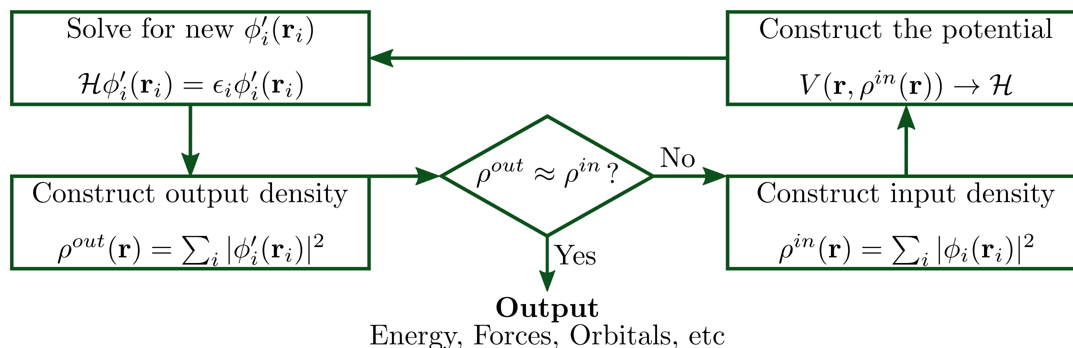

Figure 2.1. A schematic illustration of the iterative process used in the self-consistent field approach. The process begins with the construction of the input charge density based on an initial ansatz set of orbitals.

Both Hartree and Hartree-Fock approximations introduced above result in a set of equations that are dependent on a potential, which is itself dependent on the solutions to the equations. An iterative approach, such as the one illustrated in Fig. 2.1, can be used to overcome this issue.

Starting at the bottom right corner of the schematic, an initial input guess for the single-particle orbitals, $\phi_i(\mathbf{r}_i)$, is used to obtain an input density. A reasonable starting choice, for example, could be a linear combination of atomic orbitals. Consequently, the Hartree (or Hartree-Fock) potential can be constructed allowing the full Hamiltonian to be obtained. The resulting Hamiltonian can then be used to determine a new set of atomic orbitals, $\phi'_i(\mathbf{r}_i)$, and the new output density.

After comparing the old and new densities, the initial guess can be updated to coincide more closely with the output orbitals. The entire process is repeated until a desired level of self-consistency is achieved. In a computer simulation this is often measured by some tolerance criteria, Δ, that can be a change in total energy, a change in total particle-density or any other relevant parameter.

2.1.4. Density functional theory

An alternative path to tackling the many-body problem of the electronic Shrödinger equation has its roots in the pioneering work of Hohenberg and Kohn presented in 1964 [71]. The publication demonstrated that it is impossible for two external potentials differing by more that an additive constant to give rise to the same ground state particle density, $\rho_g(\mathbf{r})$. This implies that the external potential (and by extension the Hamiltonian) is fully determined by the ground state density alone. In fact, it should be sufficient to determine all the characteristics of the system [3, 72]. The complexity of the $3N$-dimensional many-body problem (where N is the number of constituents) could, thus, technically be reduced to a 3-dimensional problem of simply determining $\rho_g(\mathbf{r})$. A further advantage of such an approach is that the estimated property itself is an observable allowing for direct comparison to experiments.

From the proof demonstrated by Hohenberg and Kohn, it follows that all properties of the system can be regarded as functionals of $\rho_g(\mathbf{r})$, giving rise to the name density functional theory (DFT). The total energy of an electronic system within this formalism can, hence, be expressed in the form of Eq. 2.16.

$$E^{HK}[\rho(\mathbf{r})] = F[\rho(\mathbf{r})] + \int \mathcal{V}_{ext}(\mathbf{r})\rho(\mathbf{r})d\mathbf{r} \tag{2.16}$$

Here, $\mathcal{V}_{ext}(\mathbf{r})$ denotes the system-dependent external potential (throughout the rest of this work simply taken to be generated by the nuclei), while the $F[\rho_g(\mathbf{r})]$ term contains the kinetic contributions and the electron-electron interactions. In opposition to the external potential, $F[\rho_g(\mathbf{r})]$ should have the same functional form independent of the specific details of the system under consideration. Hence, it is often referred to as the *universal* functional. If $\rho_g(\mathbf{r})$ gives the ground state density of the system, then $E^{HK}[\rho_g(\mathbf{r})]$ must correspond to the minimum value of the functional in Eq. 2.16. As a consequence, the functional evaluated at any other density would provide an upper bound for the ground state energy, allowing minimization procedures to obtain good estimates for the energy when the ground state density is unknown.

A significant hindrance to utilizing this method in practice is the lack of obvious links between the ground state particle density and other observable properties, as well as the exact form of the universal functional. The key ideas allowing DFT approaches used in most electronic structure codes today to overcome this hurdle were presented in 1965 by Kohn and Sham [73]. Replacement of the original interacting system by an auxiliary one made up of non-interacting particles, which nevertheless give rise to the same density, was proposed. This is advantageous as a density functional form for the terms contained in the universal functional of a non-interacting system is known (see Section 2.1.2). The electron-electron interaction results in an average Coulombic energy given by Eq. 2.17, while the kinetic energy is given by Eq. 2.18.

$$E^{aux} = \frac{1}{2}\iint \frac{\rho(\mathbf{r}')\rho(\mathbf{r})}{|\mathbf{r}-\mathbf{r}'|}d\mathbf{r}'d\mathbf{r} \tag{2.17}$$

$$T^{aux} = -\frac{1}{2}\sum_j \langle\phi_j|\nabla^2_{\mathbf{r}}|\phi_j\rangle \tag{2.18}$$

Where $|\phi_j\rangle$ represent the orbitals of the non-interacting particles. An exchange-correlation energy, $E_{XC}[\rho_g(\mathbf{r})]$, defined by Eq. 2.19, needs to then be added to recover the total energy of the interacting system. Thus, the non-interacting particles give rise to an *interacting* density [3], where all of the many-body effects are grouped into a single contribution.

$$E_{XC}[\rho(\mathbf{r})] = F[\rho(\mathbf{r})] - T^{aux} - E^{aux}[\rho(\mathbf{r})] \tag{2.19}$$

Contrary to the Hartree approximation introduced previously, the solution obtained for the ground state energy through this approach is exact due to the additional $E_{XC}[\rho_g(\mathbf{r})]$ term. A Kohn-Sham Hamiltonian for the auxiliary system can be constructed by defining an exchange-correlation potential using a functional derivative of the exchange-correlation energy with respect to the density.

$$\mathcal{V}_{XC}(\mathbf{r}) = \frac{\delta E^{XC}[\rho(\mathbf{r})]}{\delta\rho(\mathbf{r})} \tag{2.20}$$

The independent particles are then taken to move in an effective potential, $\mathcal{V}_{KS}(\mathbf{r})$, given in Eq. 2.21. Analogous to the Hartree/Hartree-Fock approximations, this formulation allows a set of one-particle equations to be obtained for the auxiliary system via the variational principle. Solutions for the effective potential and the orbitals giving rise to it are found through the self-consistent iterative approach described in Section 2.1.3.

$$\mathcal{V}_{KS}(\mathbf{r}) = \mathcal{V}_{ext}(\mathbf{r}) + \mathcal{V}^{aux}(\mathbf{r}) + \mathcal{V}_{XC}(\mathbf{r}) \tag{2.21}$$

To construct the effective potential described above, a form for the exchange correlation term, $\mathcal{V}_{XC}(\mathbf{r})$, is needed. Just like before, the universal functional $F[\rho(\mathbf{r})]$ is unknown, we simply hid it in Eq. 2.19. However, this reformulation allows us to focus our attention on a much smaller set of attributes of the system – only the many-body corrections are missing. Various approximate forms for the functional have been proposed and are successfully in use today.

2.1.5. Exchange-correlation functionals

The success of density functional theory hinges upon the accuracy provided by the exchange-correlation (XC) functional employed. All the many-body modifications to the non-interacting Kohn-Sham system are condensed into a single energy term, $E_{XC}(\mathbf{r})$, that should account for the kinetic energy corrections, self-interaction, exchange and correlation. Unsurprisingly, finding the best approximation for this term is not a simple task and the search for improved forms of the functional is likely to remain an active field of research for years to come. A large variety of approximate solutions for $E_{XC}(\mathbf{r})$ has, therefore, been proposed and the most commonly used among them are introduced below.

Local density approximation

The simplest form of the XC-functional assumes only local dependence on the density at the coordinate at which it is evaluated, hence, acquiring the name local density approximation (LDA). Approaches of this type that are based on the homogeneous electron gas (HEG) model appear to be amidst the most successful.

$$E_{XC}(\mathbf{r}) = \int \epsilon^{XC}(\rho)\rho(\mathbf{r})d\mathbf{r} \tag{2.22}$$

Within the HEG, electrons are compensated by a positive homogeneous background charge resulting in a spatially uniform electron density, reminiscent of the behavior anticipated in metallic systems. For this simple model the XC energies can be tabulated with high accuracy using Monte Carlo simulations [74]. The exchange-correlation energy per particle, $\epsilon^{XC}(\rho)$, is then taken to be equivalent to that of a homogeneous electron gas with the same density $\rho(\mathbf{r})$. However, the integral is weighted by the actual particle density at each point.

LDA functionals typically provide accurate geometries, but tend to overeste the energies required to separate molecules into individual constituents. Nevertheless, when the electronic density is homogeneous any approximate exchange-correlation functional should reproduce the exact HEG result. As a consequence, LDA functionals are important for the construction of more sophisticated models of the XC energy.

Generalized gradient approximation

In real atomic systems the ground state electronic configurations are not homogeneous and LDA is likely to perform poorly if the density varies rapidly. A better approximation to the XC energy could, therefore, be achieved by considering its dependence on both the density, ρ, and the gradient of the density, $\bigtriangledown\rho$. Approximations of this form are known as generalized gradient approximations (GGA).

$$E_{XC}(\mathbf{r}) = \int \epsilon^{XC}(\rho, \nabla\rho)\rho(\mathbf{r})d\mathbf{r} \tag{2.23}$$

One of the most popular parametrizations of GGA is the functional proposed by Perdew-Burke-Erzernhof (PBE) [75] in 1996. GGA functionals tend to improve upon the total energies and atomization energies predicted by LDA and perform well in calculations of periodic systems.

Meta-GGA

Higher order terms can be continuously added to the XC energy to improve the approximation. As an example, Meta-GGA functionals include the single-particle kinetic energy density, $\tau^s(\mathbf{r})$, in the construction of $E_{XC}(\mathbf{r})$ [76]. This term contains second order derivatives with respect to the density as seen from Eq. 2.18.

$$E_{XC}(\mathbf{r}) = \int \epsilon^{XC}(\rho, \nabla\rho, \tau^s)\rho(\mathbf{r})d\mathbf{r} \tag{2.24}$$

Meta-GGA functionals require direct manipulation of the single-particle orbitals, from which the $\tau^s(\mathbf{r})$ is constructed, and are, thus, typically more computationally costly than the simpler GGA and LDA variants.

Hybrid functionals

The astonishing success of density functional theory in accurately capturing materials properties [77] sparked interest in the quantum chemistry community to combine the correlation energies obtained from DFT with the approaches of Hartree-Fock (HF) (discussed in Section 2.1.2), since HF methodology already contains the exact energy for electronic exchange, E_X^{HF}. Unfortunately, initial attempts of directly incorporating DFT correlation energies into HF did not fulfill the hopes of achieving superior accuracy. It was proposed by Becke in 1993 [78] that instead a fraction of *both* the correlation and exchange of DFT should be admixed to HF (as shown in Eq. 2.25). Becke based his reasoning on the idea of the adiabatic connection potential between the interacting and non-interacting electron systems [79].

$$E_{XC} = \alpha E_X^{HF} + (1-\alpha) E_{XC}^{DFT} \tag{2.25}$$

Originally, an equal split between the two contributions was suggested, but it was found that if fitted as a free parameter a lower value of α would result in better agreement with experiments. The rationale behind the success of the proposed method was explored further by Perdew *et al.* [80] determining that the fraction of the exact-exchange (HF) incorporated should depend on the curvature of the adiabatic potential connecting the interacting and non-interacting systems. For example strongly exchange dominated systems should have α close to one, while those with nearly-degenerate ground states should have small values of α.

A union with HF could also help to alleviate issues associated with DFT approaches, such as the self-interaction problem arising from the definition of the Coulombic potential. Eq. 2.17 implies that within DFT each electron responds not only to the potential generated by other electrons, but also by itself. This can be especially problematic for highly localized electron states, such as d- or f-electron orbitals. In contrast, HF is self-interaction free and its admixture improves significantly upon the DFT predicted electronic structures of insulators or semiconductors. The three most popular hybrid-functionals are described below.

PBE0: Perdew *et al.* [80] rationalized the mixing value $\alpha = 0.25$ between HF and DFT as the one most suitable for determining atomization energies of molecules, on the basis of fourth-order Møller–Plesset perturbation theory of HF typically providing sufficiently accurate results. Within this approach only the exchange energies of HF and DFT are mixed, while the correlation energy is fixed to that of the DFT functional.

$$E_{XC}^{PBE0} = \alpha E_X^{HF} + (1-\alpha) E_X^{PBE} + E_C^{PBE} \tag{2.26}$$

The use of such a fitted-parameter-free approach was thoroughly tested by Adamo and Barone in conjunction with the PBE functional [81] finding good agreement with experiments across a wide range of molecular systems and predicting remarkably accurate excitation energies across the periodic table. This simple hybrid-functional form given in Eq. 2.26, now known as PBE0, was later tested and found equally as successful at predicting the electronic properties of solids [82].

HSE: In metallic systems the energy contribution arising from the exact Hartree-Fock exchange convergences slowly with distance, r. Thus, creating difficulties in achieving full convergence in hybrid-functional calculations. To alleviate this problem, screening of the long-range electronic-exchange through range separation was suggested [83], resulting in a family of functionals of the form given by Eq. 2.27, named HSE after the initials of the authors proposing them.

$$E_{XC}^{HSE} = \alpha E_X^{HF,SR} + (1-\alpha) E_X^{PBE,SR} + E_X^{PBE,LR} + E_C^{PBE} \tag{2.27}$$

The screening is facilitated by the splitting of the $\frac{1}{r}$ dependence into a short-range (SR) and a long-range (LR) part using an error function as demonstrated in Eq. 2.28. The parameter w determines the extent of the short-range interaction, with $w \to \infty$ limit recovering the behavior of an unscreened PBE0-type functional.

$$\frac{1}{r} = \underbrace{\frac{\text{erfc}(wr)}{r}}_{\text{SR}} + \underbrace{\frac{\text{erf}(wr)}{r}}_{\text{LR}} \tag{2.28}$$

Fixing α to a value of 0.25 was also suggested for HSE functionals to create a fitted-parameter-free variant, though the screening precludes it from being justified by the same physical arguments as in the PBE0 case. Nevertheless, combining the fixed value of α with a default parameter $w = 0.106a_0^{-1}$ (where a_0 is the Bohr radius) one obtains the highly popular HSE06 functional. HSE06 shows excellent agreement with experimental measurements for semiconductor materials [83, 84] , similar to PBE0, but is often observed to converge quicker, therefore, requiring less computational power. The screening length w, however, is not universal and should in principle be determined from the dielectric properties of the specific material investigated.

B3LYP: One of the earliest parametrizations of hybrid-functionals still in use in the chemistry community is B3LYP [85]. Here, fractions of exchange and correlation functionals of both LDA and PBE are included with HF. However, no physical justification for the values of the parameters chosen has been attempted, with the fractions of each functional fitted empirically to reproduce experimental data. As a consequence, B3LYP can provide higher accuracy for certain materials, but offers less transferability than PBE0 or HSE06.

All hybrid-functional DFT calculations are significantly more expensive than methods employing only LDA or GGA. This is due to the fact that a typical DFT calculation scales as N^3, with N being the number of atoms in the system, while HF calculations scale as N^4, allowing only much smaller systems to be computed. Nevertheless, hybrid-functional calculations lead to, perhaps fortuitously, accurate description of the band-gaps of many semiconductor materials. Consequently, excitation behavior can be probed at a much lower cost than alternative (more accurate) approaches, such as e.g., the GW approach [86, 87].

2.2. Extended Systems

The quantum mechanical tools introduced thus far have focused on calculations of finite systems containing a fixed number of constituents – an approach appropriate for molecules or small clusters. Yet, typical solid state systems of interest, even in the fields of nanoscience and nanotechnology, consist of billions of atoms. If every atom were individually specified systems of this size would certainly not be tractable using the methodologies presented previously on any currently existing supercomputer. To successfully investigate bulk materials an additional feature of crystalline systems has to be exploited, i.e. its periodicity in space.

The bulk structure of a perfect crystal can be fully specified using a single unit cell, describing the smallest repeatable unit of the material. The extent of the unit cell is defined through three lattice vectors, $\mathbf{a}_1$, $\mathbf{a}_2$ and $\mathbf{a}_3$, resulting in a total volume $\Omega = \mathbf{a}_1 \cdot (\mathbf{a}_2 \times \mathbf{a}_3)$ and the atomic positions are specified as occupied crystalline lattice sites

within the cell [4]. The full crystal can then be recreated by periodically repeating the unit cell in every direction through a translation vector $\mathbf{R}$, that connects all equivalent points in space.

$$\mathbf{R} = n_1\mathbf{a}_1 + n_2\mathbf{a}_2 + n_3\mathbf{a}_3 \tag{2.29}$$

The integer values n_1, n_2 and n_3 range from 1 to the total number of unit cells (N_1, N_2 and N_3) in that direction of the crystal. If the values of N_1, N_2 and N_3 are very large an effectively infinite crystal is constructed. Of course, a realistic system is not infinite and the atoms on the surface will contribute towards experimentally measured properties. Nevertheless, one can (often reasonably) assume that the surface effects lead to small contributions that are overshadowed by the properties of the bulk. As a corollary, all properties of importance need only to be evaluated within the unit cell, as their value at any other position in the crystal can be simply obtained by applying the translation vector $\mathbf{R}$.

Alternatively, an infinite system can be constructed by reconnecting the edges of the unit cell with each other through periodic boundary conditions. In such a way the behavior of an infinitely large bulk material can be recovered by considering only the smallest repeatable unit containing a finite number of atoms, N_a. A unit cell of a crystal repeated periodically through space gives rise to an equally periodic potential. Bloch [88] has demonstrated that the single-particle electronic wavefunctions in such a potential can be expressed in the form of Eq. 2.30.

$$\psi(\mathbf{r}) = u_{n,\mathbf{k}}(\mathbf{r})e^{i\mathbf{k}\cdot\mathbf{r}} \tag{2.30}$$

The function $u_{n,\mathbf{k}}(\mathbf{r})$ is required to have the same periodicity as the underlying crystal lattice, with the quantum number n enumerating the distinct eigenvalue solutions corresponding to the same wave-vector $\mathbf{k}$. Here, we introduce the concept of a reciprocal lattice useful for dealing with periodic systems. The reciprocal lattice (an inverse of the real lattice) described by a translation vector $\mathbf{G}$ is related to the direct lattice through a relationship given in Eq. 2.31.

$$e^{i\mathbf{G}\cdot\mathbf{R}} = 1 \tag{2.31}$$

Given the definition, it is immediately apparent that reciprocal lattices provide a natural basis for expanding functions with the periodicity of the direct lattice, such as the ones introduced in Eq. 2.30. This makes the inverse lattice indispensable for studies of diffraction and related phenomena. An example of a reciprocal lattice corresponding to a face-centered cubic structure of a crystal is shown in Fig. 2.2(a) with some of the high symmetry points highlighted.

2.2.1. Band structure

In a finite system imposing boundary conditions on Eq. 2.30 would result in discretized values of $\mathbf{k}$, however, in an infinite crystal a continuum of values is allowed. Thus, in a periodically repeated system a plot of the eigenvalues corresponding to a specific quantum number n as a function of $\mathbf{k}$ results in a continuous band of energies. The plot of all energy bands against the wave-vector $\mathbf{k}$ along high-symmetry lines in the reciprocal space is referred to as the *bandstructure* plot of the system. An example of

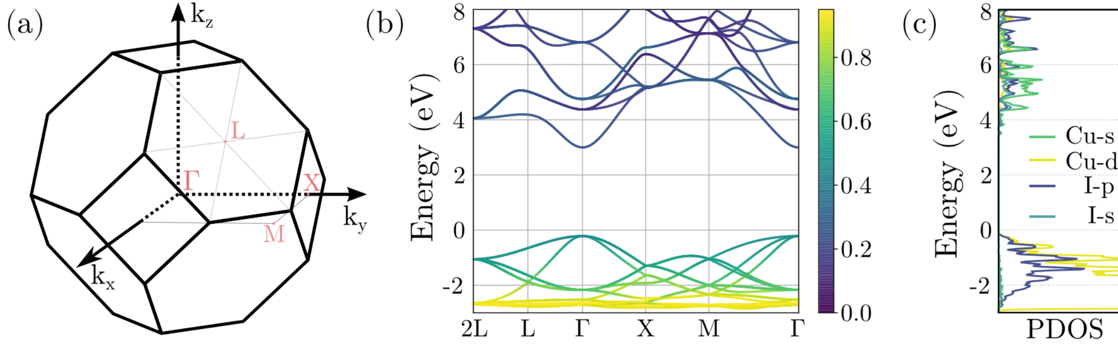

Figure 2.2. Example of band structure calculations for CuI. Left: the Brillouin zone corresponding to the face-centered cubic zinc blende structure of CuI. Some high-symmetry k-points are illustrated. Center: a calculated band-structure along high-symmetry points of CuI. Fermi level is set to 0 eV. The colour map shows the Cu-character in the specific bands: yellow - completely Cu derived, deep blue - I derived states. Right: partial density of states corresponding to the same bands. Only the orbits strongly contributing to the conduction and valence band edges are shown.

a bandstructure plot calculated with the PBE0 hybrid functional is shown for the zinc blende structure of cuprous iodide (CuI) in panel (b) of Fig. 2.2.

The bandstructure of a crystal can reveal various important attributes of the material. First, the system can be immediately classified as an insulator, a metal or a semiconductor based on the existence (or lack) of an electronic band gap. The dispersion (curvature) of the valence and conduction bands permits the calculation of the effective mass of the corresponding free charge-carriers. Furthermore, the atomic and orbital character of the bands in question can be identified by projecting the corresponding wavefunctions onto localized atomic orbitals. As an example, the fractional contribution of copper-states is colour coded in the bandstructure shown in Fig. 2.2(b), revealing that deep states around -3 eV below the valence band edge are purely copper based, while both the valence band maximum and conduction band minimum are a result of significant hybridization between the electronic states of both Cu and I. In addition, the electronic band gap allows one to gauge the optical appearance of the material.

The integral of the bandstructure over all values of $\mathbf{k}$ results in the electronic density of states (DOS). An example of a DOS is shown in the right panel of Fig. 2.2 for the CuI system. Here, only partial densities of states are plotted corresponding to the atomic orbital character of I-s, I-p, Cu-s and Cu-d states. Knowledge of the s-/p-/d-orbital band character and which atoms provide the highest contributions allows for informed material design, where atoms exhibiting the desired orbital behavior can be preselected.

Finally, for doped semiconductors that are a major focus of this thesis analysis of the band structure can help to understand the characteristic behavior of different impurities. A bandstructure plot is typically sufficient to assess if the carriers introduced by an impurity atom would be localized/delocalized and if the defect would cause changes to the optical properties of the material (see Section 3.3 for an in-depth discussion).

2.2.2. Ionic potentials

Previous sections have focused on tools and approximations used for solving the electronic Schrödinger equation in some external potential, $\mathcal{V}$, arising from the nuclei. Naturally, for actual calculations to be performed this potential needs to be explicitly specified. Here, as previously, simplifications can be sought after to lighten the computational load.

While a part of the electrons rearrange to form bonds in molecules or solids, many electrons of an atom remain strongly bound to the nucleus in highly localized core states. The requirement that the electronic wavefunctions should be orthogonal to one another leads to their rapid oscillations in the region close to the nucleus. In addition, the nuclear potential ($\propto -\frac{Z}{r}$) decays rapidly in this region. This is problematic in practical calculations as high spatial resolution is required to capture such behavior resulting in hefty computational costs. Since only a few electrons, known as valence electrons, actively participate in the formation of chemical bonds methods differentiating between them and the inert core electrons can be used to speed up calculations.

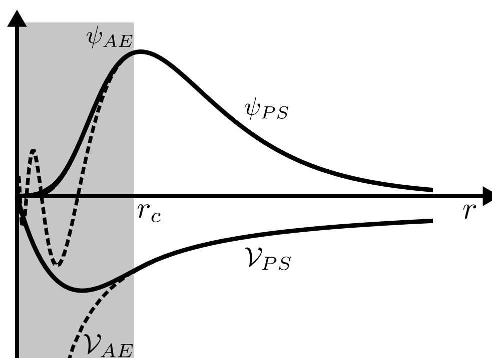

Figure 2.3. Schematic illustration of the pseudopotential method applied to an all electron state ψ_{AE}. The all electron potential, $\mathcal{V}_{AE}$, in the core region, r_c, is replaced by a pseudopotential, $\mathcal{V}_{PS}$, that gives rise to a smoother pseudized wavefunction, ψ_{PS}.

In a pseudopotential approach illustrated in Fig. 2.3, a core region within a distance r_c from the nucleus is defined, such that outside r_c wavefunctions belonging to the strongly-bound core electrons decay quickly. As the core electrons play no significant role in bond formation, they can be treated as fixed (frozen), resulting in the frozen core approximation. The frozen core can be eliminated from further calculations and replaced by a weak effective potential (since core-electrons act to shield the nuclear potential) that mimics the effect of the frozen core on the valence electrons. This can be interpreted as a replacement of the all-electron Coulomb potential, $\mathcal{V}_{AE}$, by a pseudopotential, $\mathcal{V}_{PS}$. The true wavefunction, ψ_{AE}, of a valence electron exhibiting oscillatory behavior below r_c is then replaced by an appropriately normalized smooth pseudowavefunction, ψ_{PS}, [89] generated by the potential $\mathcal{V}_{PS}$. Though distinct in shape, both ψ_{AE} and ψ_{PS} satisfy charge conservation within r_c and match at and outside this boundary. It was later proposed by Vanderbilt [90] that the requirement for the charge conservation (also known as norm conservation) could be relaxed. In this scheme, the depletion in charge density due to the relaxation of norm conservation is taken care of

by a post treatment of augmentation charge. This has lead to the development of new ultasoft pseudopotentials that offer a further increase in computational efficiency.

Various parametrizations for the pseudopotentials, such as Vanderbilt [90], GTH [91], Schlipf-Gygi [92] etc., have been suggested and the existence of pseudopotentials has become paramount to fast processing of large solid state systems. Nevertheless, full all-electron calculations are necessary to present a reference for pseudopotential fitting. All-electron methods also commonly partition the simulation space into core and valence regions similar to the pseudopotential approach. Slater [93] proposed the use of two different basis sets: one to represent the core region and one to represent the valence region, with the wavefunctions and their derivatives matched at the boundary between the regions. A prominent example is the linearized augmented plane wave (LAPW) method [94]. Here, the atomic core is expanded in a basis of spherical atomic-like partial wave states, while outside the core region wavefunctions are expressed as plane waves. Since, according to the Bloch theorem (see Section 2.2) plane waves are a natural choice for representation of electrons in solids, but are not a good choice for describing spatially localized functions.

An alternative to the pseudopotential method is the projector augmented-wave method (PAW) proposed by Blöchl [95] in 1994. It relies heavily on the LAPW method discussed previously, but here the core electrons expressed in a localized basis set are frozen. The fixed PAW states are generated from all-electron calculations and their effects are simply projected onto the potential, influencing the valence electrons behavior analogously to a pseudopotential. The use of pseudopotential and PAW methods helps to alleviate significantly the computational costs associated with the calculation of an all-electron DFT ground state, as only the valence electrons need to be considered in forming the ground-state particle density.

3 Defect Calculations

The work presented throughout this thesis revolves around the alteration of materials properties via point defect incorporation. Consequently, in the following sections the computational methods discussed in the previous chapter are expanded upon and an introduction to the concepts and terminology relevant for defect calculations in bulk semiconductors is presented.

We begin with the definition of a point defect and enumerate its most common types. The free energy of formation is introduced and its significance to the study of defects is discussed. Common approximations used when calculating this quantity are explored. Optical and thermodynamic transition levels are elucidated and their link to the identification of shallow and deep defects is explained. The remainder of the chapter focuses on corrections elicited by the supercell approach used for calculating defect formation energies. In the final section, we venture beyond point defects and probe clustering effects using the concept of defect binding energies.

3.1. Point Defects

Point defects, unlike interfaces, grain boundaries or dislocations, are associated with a single crystalline lattice site. This does not, however, imply that local atomic relaxations involving surrounding atoms are excluded, only that the extent of such relaxations should be limited. Typically, only a few atomic shells surrounding the imperfection site are affected. Point defects are often grouped into: *native* (intrinsic) and *impurity*-related (extrinsic), based on the atom type associated with the defective lattice site. Native point defects only involve elements that make up the bulk material, i.e. they can also exist in the lattice of the pure host. Impurity defects, on the other hand, consist of elements external to the bulk composition.

Point defects can be further classified into **vacancies**, **interstitials** and **substitutionals**. All three types are illustrated in Fig. 3.1 using a model lattice of sodium chloride (NaCl). Vacancy defects, as the name implies, are formed by vacant crystalline lattice sites. The shorthand – V_D – will be used when discussing defects of this type, where V stands for the vacancy and D identifies the element missing from the lattice site. A chlorine vacancy, V_{Cl}, is illustrated in Fig. 3.1(a). By definition all vacancy defects are intrinsic.

Interstitials are formed by atoms that incorporate themselves in between occupied lattice sites of the perfect crystal. Intuitively, these defects, further denoted D^i where D is the atomic species, are easier to form in materials with porous open structures and are less likely to incorporate in close-packed crystals. A sodium interstitial, Na^i, is illustrated in Fig. 3.1(b). Native interstitials are often referred to as self-interstitials.

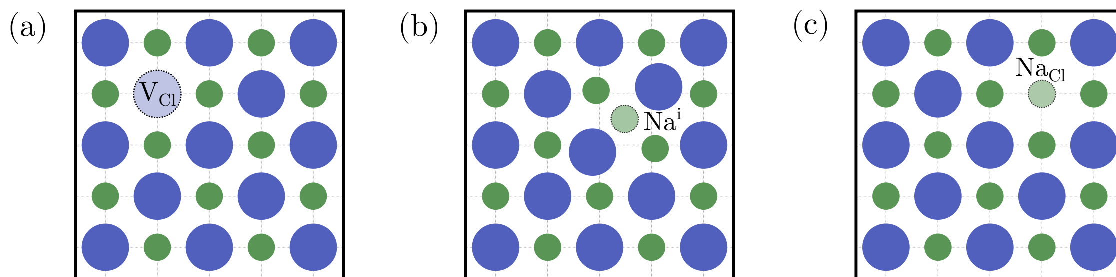

Figure 3.1. A schematic illustration of different defect types inside a crystalline lattice of NaCl: (a) chlorine vacancy, V_{Cl}; (b) sodium interstitial, Na^{i}; (c) sodium substitutional, Na_{Cl}.

Substitutional defects are created when a lattice site belonging to a specific atomic species is occupied by a different element. Native substitutional defects can, thus, only exist in non-elemental solids. A notation similar to V_D will be used to denote substitutional defects, where V is replaced by the elemental species occupying the lattice site. A substitutional defect with a Na atom occupying a site belonging to a Cl, Na_{Cl}, is illustrated in Fig. 3.1(c).

As alluded to above, a single element can form multiple defect types that may induce disparate effects on the characteristics of the host. The ability to determine the lattice site into which the defect is most likely to incorporate is, therefore, highly important to the study of defects. Here, accurate estimation of the energy of formation is essential as it gives insights into what defect concentrations can be achieved at a specific temperature, T, and consequently permits knowledge of what defect types will be most prominent in a given compound. At low concentrations impurities are anticipated to have no observable effects on the properties of the bulk material, since defects with the smallest formation energies will dominate.

In thermodynamic equilibrium a defect X is expected to incorporate into a material with a concentration, C_X^{eq}, according to the Boltzmann distribution. The concentration of lattice sites available to form the defect is denoted by C_0; N_X gives the number of internal degrees of freedom (e.g. spin degeneracy) available at the lattice site; k_B is the Boltzmann constant 8.617×10^{-5}(eV/K) and T is the temperature in Kelvin.

$$C_X^{eq} = C_0 N_X \exp\left(-\frac{G_X^F}{k_B T}\right) = C_0 N_X \exp\left(\frac{S_X^F}{k_B}\right) \exp\left(-\frac{H_X^F}{k_B T}\right) \tag{3.1}$$

As defect concentrations depend exponentially on the Gibbs free-energy associated with the formation of the defect, G_X^F, very high accuracy in estimating this quantity is required to attain concentrations with a correct order of magnitude. Eq. 3.1 is only applicable in the dilute limit[†], where the configurational entropy of each defect is assumed to be unaffected by the presence of others. While growth of a (defective) host

[†]In the study of defects the dilute limit refers to conditions where defects are spaced far enough away from each other to be safely regarded as completely non-interacting.

material is certainly not an equilibrium process, if activation barriers for diffusion are low equilibrium defect distributions are, nevertheless, likely to be applicable [96].

3.2. Defect Formation Energies

On the right hand side of Eq. 3.1, the Gibbs free energy is explicitly separated into its entropic, S_X^F, and enthalpic, H_X^F, contributions. Here, S_X^F denotes only the entropy not associated with configurational multiplicity as this is explicitly included in the construction of Eq. 3.1. Instead, it contains terms arising from electronic and vibrational entropy, as well as contributions from magnetic excitations [97]. Typically, configurational entropy dominates these effects and for semiconductor materials the band gap underestimation, discussed in detail in Section 3.4, results in sizable errors that render the inclusion of entropic corrections meaningless. As a result, the vast majority of defect formation energy calculations is performed with the $T = 0\,\mathrm{K}$ assumption. This is also the case for all formation energies reported in the following chapters. Nevertheless, quasi-harmonic approaches for including vibration entropy contributions into defect formation energies have been explored in the literature, demonstrating that in metallic systems such effects can be important and need to be considered [98, 99].

The enthalpy of formation, H_X^F, takes the form of Eq. 3.2, where $E_X^F(v_F)$ is the energy required to create a defect X with a formation volume, v_F, at a given pressure, P. The formation volume is defined as the change in volume introduced by the presence of a defect X.

$$H_X^F(v_F) = E_X^F(v_F) + Pv_F \tag{3.2}$$

At ambient conditions, in which most technological applications are operated, the Pv_F contribution can be considered negligible since volumetric changes induced by a point defect are small. Under high pressure, however, the term becomes important and should be included in formation energy calculations. Evaluation of the Pv_F contribution is addressed in more detail in Chapter 6, where doping under high pressure is investigated. In the remainder of this section, we focus on zero pressure calculations and use the assumption $E_X^F(v_F \to 0)$.

The energetic cost of neglecting volume relaxations in evaluating $E_X^F(v_F)$ can be estimated [97] using Eq. 3.3. Here, B is the bulk modulus of the host material and V is the volume of the supercell used in the calculation. For typical semiconductor values of B, v_F and V this correction corresponds to $\sim$30 meV [97], making it negligible in comparison to typical errors associated with band gap underestimation or charge corrections, discussed in later sections.

$$\Delta E \approx \frac{1}{2} B \frac{v_F^2}{V} \tag{3.3}$$

As alluded to above, a supercell approach was used to perform the calculations of defects presented in the thesis. Within this approach a single point defect is modelled inside a large (super)cell of the crystalline host, constructed from multiple unit cells. The entire structure is then evaluated in a periodic density functional theory (DFT) calculation. The available computational resources often constrict the possible choices of supercell size, leading to errors in the resulting defect formation energies due to the

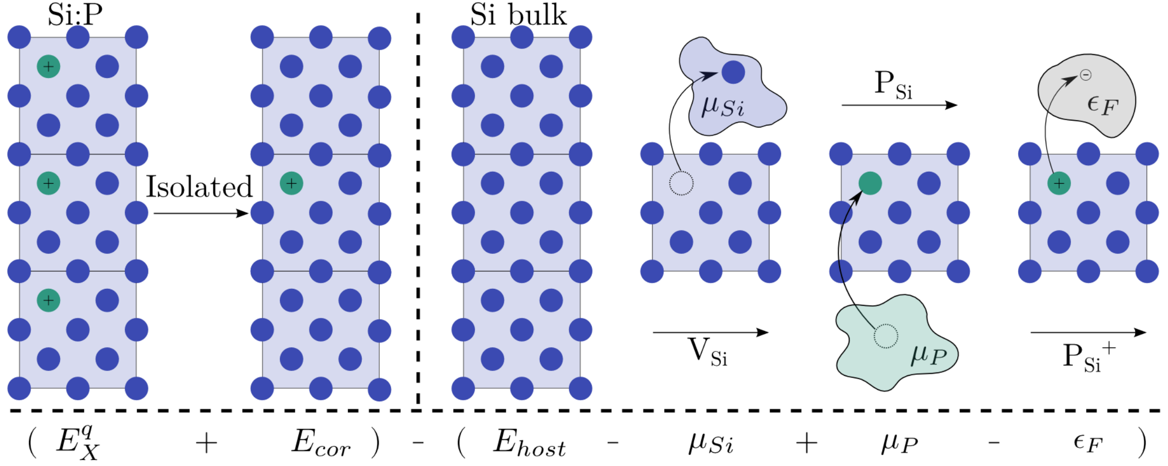

Figure 3.2. Schematic illustration of a defect formation energy calculation for a P_{Si} substitutional in a $q = 1$ charge state. Left side shows the supercell cell correction. Right side depicts the individual constituent terms that make up the defect.

limited extent between periodically repeated constituents. Methods for correcting these errors have been suggested and will be addressed in detail in Section 3.6. It is worth mentioning that alternative approaches for investigating defects in bulk crystals, such as embedded cluster method or Green's function approach [100, 101], are available, but are plagued by their own challenges and pitfalls [97].

The formation energy of a defect, E_X^F, within the supercell approach is calculated using Eq. 3.4. Here, E_X^q is the energy of a cell containing a defect of type X in a charge state q, while E_{cor} contains all correction terms applied in order to counter the errors in the calculation of E_X^q introduced by the periodic boundary. E_{host} is the energy of the same size supercell of the pure host material. The number of atoms of species i, n_i, is used to count the atoms that were added to ($n_i > 0$) or subtracted from ($n_i < 0$) the bulk in order to create the desired defect; μ_i is the chemical potential of species i and ϵ_F is the position of the Fermi level in the material.

$$E_X^F = (E_X^q + E_{cor}) - (E_{host} + \sum_i n_i \mu_i - q\epsilon_F) \tag{3.4}$$

Eq. 3.4 corresponds to a grand canonical approach used to evaluate E_X^F [97], i.e. the system is considered to be freely exchanging atoms with multiple external particle reservoirs and to be exchanging charge with an external electron reservoir. Interactions of the system with the reservoirs, that are in thermal equilibrium with the bulk, are mediated via chemical (μ_i) and electronic (ϵ_F) potentials. Evaluation of these potentials and their significance in defect formation energy calculations are discussed in Section 3.5.

Formation energy calculations are exemplified in Fig. 3.2 for a positively charged phosphorus substitutional, P_{Si}, in bulk silicon. Here, each term required to evaluate E_X^F using Eq. 3.4 is illustrated schematically. First, the energy of a defect, E_X^q, in a periodic supercell is evaluated. Supercell sizes used in typical defect calculations correspond to defect concentrations of 1-5%. The energy E_X^q is, thus, brought closer to the dilute limit by adding correction terms able to counteract periodic boundary effects.

The adjusted energy is then compared with the sum of the corresponding individual constituent energies that make up the defect site. First, the energy of the host is evaluated in the same size supercell. From this, an energy corresponding to a Si atom residing in a particle reservoir with the chemical potential μ_{Si} is subtracted. An energy of placing a phosphorus in a reservoir with a chemical potential μ_P is added and, finally, an electron is removed from the defect and placed into an electron reservoir with the Fermi energy ϵ_F. Given that q denotes the charge of the supercell it is equivalent to the number of electrons placed in the reservoir.

3.3. Shallow and Deep Defects

Eq. 3.4 reveals that the formation energy of a specific defect X depends on the charge state, q, in which the defect is found. Inversely, knowledge of the formation energy permits the identification of the stable charge state, allowing us to further classify defects based on their electronic behavior. In particular, impurity atoms that can be ionized inside a semiconductor bulk, enhancing the free-carrier concentration of the host, belong to a specific class of defects known as *dopants*. The notion of dopants has become almost synonymous with the field of semiconductor physics. To distinguish this important class of impurities, defects are often categorized as **shallow** (easy to ionize, i.e. good dopants) or **deep** (hard to ionize, i.e. bad dopants). This distinction is often made by evaluating the stability of the ionized charge state via thermodynamic transition levels or by examining the electronic defect levels inside the band structure of the semiconductor host.

3.3.1. Thermodynamic and optical transition levels

A given defect will alternate between different ionization states with some characteristic time length, dependent on the specific energetics of the system under consideration. However, a transition into a new charge state can also be induced by an external perturbation, e.g., an optical excitation or through the application of an electric field. A change in the charge state usually brings forth a change in the local atomic environment surrounding the defect, such that the ground state atomic positions of different charge states of the same defect, X, are nonequivalent, $\{R\}_{q_1} \neq \{R\}_{q_2}$.

Two transition timescales can, therefore, be distinguished [102]: (i) the new charge state is allowed to equilibrate on the phonon timescale relaxing into a new ground state geometry. Formation energies of defects in their relaxed geometries, $E^q(\{R\}_q)$, are shown by solid lines in Fig. 3.3(a); (ii) the change in charge state is mediated through an absorption/emission of a photon and the atomic geometry remains fixed (in that of the former charge state). Formation energies of ionized defects frozen in the charge neutral atomic configuration, $E^q(\{R\}_0)$, are shown by dotted lines in Fig. 3.3(a).

When defect geometries are allowed to relax, the transition is termed thermodynamic. Such transitions can be observed in deep-level transient spectroscopy experiments [96]. The thermodynamic (ionization) level, $\epsilon(q_1/q_2)$, between two charged states q_1 and q_2 can be calculated using Eq. 3.5.

$$\epsilon(q_1/q_2) = \frac{E_X^F(q_1, \epsilon_F = \epsilon_{VBM}) - E_X^F(q_2, \epsilon_F = \epsilon_{VBM})}{q_2 - q_1} \tag{3.5}$$

Setting the Fermi level equal to ϵ_{VBM}, where ϵ_{VBM} is the energy of the valence band maximum (VBM) of the pristine host, defines the transition level with respect to the valence band edge, i.e. inside the electronic gap. Since the Fermi level of a typical semiconductor lies within the band gap, such a definition of $\epsilon(q_1/q_2)$ hones in on the ϵ_F range of interest.

Thermodynamic transitions indicate the value of the Fermi level at which a defect changes its stable charge state as exemplified by solid black arrows in Fig. 3.3(a) for a system with three stable charge states. Since all formation energies are evaluated using ground state geometries, these transitions are independent of the direction of charge transfer, i.e. whether an electron is added or removed from the impurity. The exact position of the thermodynamic transition level within the band gap allows the separation of defects into the aforementioned shallow and deep dopants. To be electrically active (shallow), the defect should be ionizable at room temperature or the temperature of device operation. Therefore, the ionization level must lie no further than a few k_BT from the relevant host band edge.

In n-type conductors the Fermi level resides near the conduction band minimum (CBM). A potential dopant under these conditions should be stable in a positive charge state (donated one or more electrons into the conduction band). In p-type conductors ϵ_F lies close to the valence band maximum and a potential dopant should be stable in a negative charge state (donated one or more holes into the valence band). Temperature dependent Hall data can be used to identify thermal defect ionization energies corresponding to shallow transition levels [96].

Shallow dopants generally introduce minimal distortions to the bulk, while deeper defect behavior is typically associated with strong local relaxations with respect to the host lattice [103]. In the model system of Fig. 3.3(a) the defect displays both deep acceptor and deep donor transition levels. A defect of this type is classified as *amphoteric*, characterized by adopting a charge state that always counters the majority carriers of the bulk. Other defects can remain completely electrically inactive, such as impurities (ordinarily those isovalent to the host) that are exclusively stable in a charge neutral state.

Charge state transitions corresponding to frozen atomic geometries are called optical. These transitions are of interest when comparing calculated results with photoluminescence and optical absorption experiments. Optical transitions from a charge neutral defect state to a positively or negatively charged one for the same three-charge-state system are indicated by dashed blue arrows in Fig. 3.3(a). The larger the difference between the solid black and the dashed black lines, the stronger the structural relaxation effects, and, consequently, the bigger the disparity between optical and thermodynamic transition levels [96]. The presence of strong structural relaxations between different charge states can create kinetic barriers that stabilize an excited charge state beyond its thermodynamic transition level, resulting in photo-induced conductivity [104].

In contrast to thermodynamic transitions, optical transitions are path dependent due to the difference in relaxed atomic geometries between charged states. This is illustrated in the configurational coordinate diagram shown in Fig. 3.3(b), representing a defect

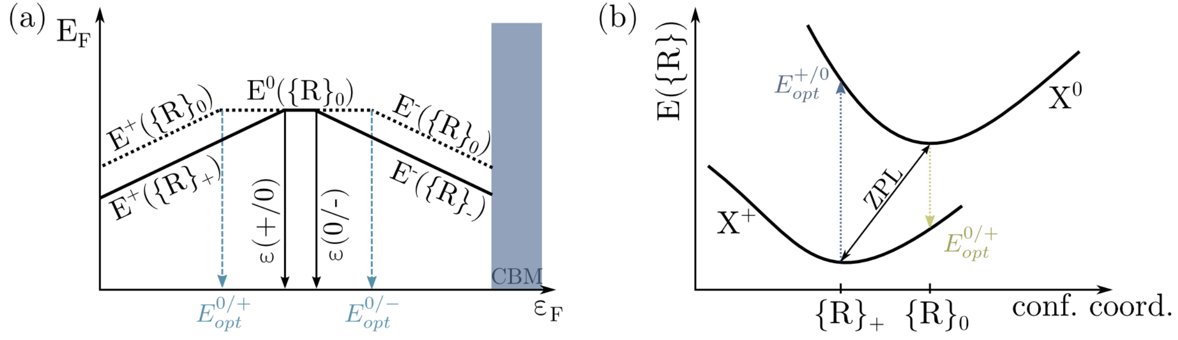

Figure 3.3. Schematic illustration of thermodynamic and optical transition levels: (a) defect formation energies corresponding to relaxed (solid black) and frozen (dotted black) atomic geometries depicted for a system with three stable charge states. Thermodynamic transitions are marked by black arrows, optical transitions are marked by blue arrows; (b) configurational coordinate $\{R\}$ diagram for a defect, X. Energy dependence on the configurational coordinate for different charge states is shown by solid black lines. Optical transitions are marked by dotted arrows. The zero phonon line (ZPL) is indicated.

X, stable in two charge states $q = +1$ and $q = 0$. The charge state $q = +1$ relaxes to the atomic geometry $\{R\}_{+1}$ and $q = 0$ relaxes to the atomic geometry $\{R\}_0$. Here, the x-axis represents some generalized configurational coordinate defined to connect $\{R\}_0$ and $\{R\}_{+1}$ using a single dimension. The difference between the indicated $E_{opt}^{(+/0)}$ and $E_{opt}^{(0/+)}$ transitions is the difference between optical absorption and emission peaks corresponding to this transition [97, 102]. The zero phonon line (ZPL) is also indicated in the plot. The ZPL is a phonon-assisted transition between the local minima of the two charge states and is energetically similar to the thermodynamic transition level. Calculations of optical transition levels are more involved than those of thermodynamic transitions, since excited electronic states need to be evaluated – a challenge for the standard DFT formalism, due to the band gap and self interaction problems that will be discussed in more detail in Section 3.4.

3.3.2. Electronic defect levels

The presence of a defect within a semiconductor host results in the appearance of a defect localized electronic state (DLS) [103]. For deep dopants these states reside within the fundamental band gap of the host. Such states, often associated with unfulfilled coordination originating from broken or dangling bonds, are typically well localized spatially. The localized nature of the wavefunction corresponding to this deep-state suggests that it will respond only weakly to outside perturbations (such as temperature and pressure) [97]. Furthermore, high activation energies would be required to ionize an electron/hole residing in this deep energy level to a bulk band edge, making conductivity via such defects unlikely.

In contrast, for shallow dopants the DLS creates a resonance within the bulk bands of the host material [105]. Instead of occupying the localized state, in this case, the

electrons/holes will occupy a perturbed host state (PHS) at the conduction/valence band edge. The PHS, formed from the conduction (valence) bands of the host, is a hydrogen-like state – the free-carrier is bound to the defect atom by a screened Coulombic potential and responds with an effective mass equal to that of the bulk host bands [4]. Such a state is much more responsive to external influences and can be easily ionized to result in successful conductivity in the material.

As a result, a shallow or deep character of a defect can also be assessed from the resultant electronic band structure. However, certain defects can manifest as both a DLS or a PHS depending on the charge state in which the defect is formed. Such defects are known as DX centers [103] and are typically characterized by a large energy difference between the optical and thermal ionization levels. The properties of the deep state arise from a strong coupling with the crystal lattice [106]. Consequently, a DX center can induce persistent photo-conductivity [103, 104]. If the deep defect state is ionized into a metastable PHS state, for example, through an absorption of a photon, the PHS can be frozen in thermodynamically due to strong atomic relaxations associated with the change in charge state.

3.4. The Band Gap Problem

One of the most notorious difficulties associated with *ab initio* defect calculations is the band gap problem of DFT. It is well known, that the electronic gaps of semiconductor and insulator materials are significantly underestimated by Kohn-Sham DFT [107]. Two sources of error are typically cited: the self-interaction present in the Kohn-Sham Hartree energy (see Section 2.1) and the lack of discontinuity in the functional-derivative of the exchange-correlation energy with respect to the particle number [108]. Such derivative discontinuity associated errors have been demonstrated to persist even if the exact exchange-correlation functional, able to counter the self-interaction energy, was used [109].

Errors in defect calculations resultant from a too small band gap are two fold in nature: (i) if the true band gap and the calculated one differ by ΔE_G, the energy of the DLS induced by a defect can be altered by up to the same amount. In cases where this state is occupied by an electron, the formation energy of the defect can be significantly affected by the shift. This scenario is illustrated in Fig. 3.4(a) for a charge neutral Te_{Sn} impurity in SnO_2. In compounds where the band edge shifts are extreme, the DLS can even be erroneously predicted to lie resonant with the valence or conduction bands, resulting in fictitious hybridization between the bulk and defect states, and an incorrect characterization of the defect; (ii) the determination of thermodynamic transition levels (described in Section 3.3.1) with respect to the host band edges is prohibited. Fig. 3.4(b) illustrates how the inaccurate assessment of the conduction band minimum can lead to the prediction of shallow donor character for a deep donor defect. As a consequence, only semi-quantitative interpretation of the electric and optical activity of a defect is provided by LDA and GGA calculations [110].

The self-interaction error of DFT presents an additional challenge as it tends to result in charge delocalization [111]. This effect can lead to changes in local atomic geometries surrounding a defect and the prediction of fictitiously delocalized states.

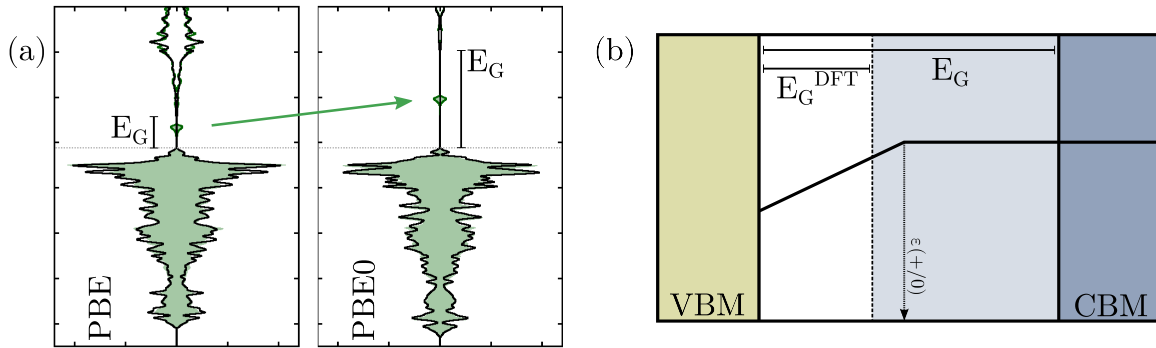

Figure 3.4. The effect of band gap changes on defect calculations: (a) Shift of the defect level inside the fundamental band gap, associated with the band gap opening resultant from PBE0 calculations, illustrated for Te-doped SnO_2 and (b) misclassification of a deep donor based on inaccurate band gap estimation. The light-blue shaded area shows the calculated and the dark-blue – the true conduction band edge.

Various approaches to overcome the above shortcomings of DFT have been proposed [97, 105] and are briefly summarized below.

The simplest approach suggests recovering the correct electronic band gap through the use of scissor-operators [112]. Scissor-operator based schemes shift rigidly only the respective band edges in order to open up the band gap [113]. Within this approach the structure of the bands (their width and dispersion) is assumed to be accurately represented by the underlying DFT calculations. A more sophisticated approach attempts to also shift the defect states accordingly [105, 114] by decomposing them based on their valence and conduction band character [115]. Such a correction, while simple and, hence, computationally favorable does nothing to account for the self-interaction error and further offers no capacity to deal with situations where fictitious hybridization between the host and the defect states occurs [116].

The self-interaction error of density functional theory affects most prominently states that are strongly localized, such as the semicore *d*- or *f*-electrons of an atom. The method known as DFT + U [117, 118] attempts to reduce this interaction by introducing an on-site attractive Coulombic potential, U. To obtain the parameter U a variety of first-principles [117, 119] and empirical fitting [120, 121] approaches have been proposed. This, however, makes the method problematic to apply in general as it is not straightforwardly transferable between systems. In particular, systems with no *a priori* experimental information cannot be studied if fitting approaches are to be used. Worse still, chemical reference phases cannot be treated on the same footing as the host since the parameter U should reflect the dielectric screening of the material [119] and, thus, differs between systems. Additionally, although the self-interaction error may be countered, the band gap, while improved, typically remains underestimated [97, 120, 121], requiring further extrapolation schemes to be adopted.

Modified pseudopotentials, similar in spirit to the DFT + U approach, offer a further alternative to account for the self-interaction. Here, a self-interaction correction (SIC) is incorporated directly into the construction of a pseudopotential [122]. The great advantage of the SIC approach is that once fitted the calculations are as cost efficient

as standard LDA/GGA methods [75, 123]. The drawbacks are the lack of predictive power outside of the fitted system and the lack of transferability, in particular, to reference phase calculations.

Many-body methods, such as GW [86, 87], are also available and can predict accurately the quasiparticle energies of a system. In this way, accurate calculations of not only the band gap, but also of the defect levels within it are permitted. However, such approaches are challenging to apply to large supercells, which are frequently required to converge defect calculations, due to their hefty computational cost. Furthermore, local relaxations cannot yet be performed using GW approaches, therefore, geometry inaccuracies inherent to self-interaction of DFT would still need to be circumvented by an alternative method [124]. Nevertheless, significant progress has been made in this direction and such calculations are usually informative in the evaluation of "lower-level" calculation performance. If the high computational cost can be afforded, quantum Monte Carlo simulations [125] for point defects in solids [126] offer a final alternative.

In this thesis, we chose to use the hybrid-functional approach to overcome the band gap problem. Hybrid-functionals are discussed at length in Section 2.1.5, where we demonstrate how the admixture of the exact-exchange of Hartree-Fock theory helps to counter the self-interaction problem of DFT. Despite having no fitted parameters, functionals such as PBE0 and HSE06, seem to result in electronic band gaps that offer astonishingly accurate agreement with experimental results, as demonstrated in Chapter 4. Furthermore, hybrid functionals have been ubiquitously cited to compare well with both experimental observations and the predictions provided by higher levels of theory, such as GW or quantum Monte Carlo [97].

3.5. External Reservoirs

A supercell approach for calculating defect formation energies was presented in Section 3.2. Within this approach, a defect is created through the exchange of particles and charge with external reservoirs. Characterization of such external reservoirs is, therefore, critical for accurate defect formation energy evaluations and is discussed in more detail below.

3.5.1. Chemical potentials

Chemical potentials are invoked to describe the exchange of particles between a host system and a particle bath. The value of a chemical potential, μ_i, of a particle i is simply the energy required to extract it from the reservoir. The reservoir is assumed to be in thermal equilibrium with the host system, thus, in order to ensure the stability of the bulk crystal constraints are placed on the possible values the potentials can take. Additional requirements are introduced by the possibility of elemental decomposition and ternary phase formation. This is illustrated further using an example case of tin dioxide.

To successfully incorporate defects the crystalline SnO_2 host must be stable. As a consequence, the chemical potential of the host phase should be equivalent to the chemical potentials of its constituent particles in the reservoirs, leading to the Eq. 3.6.

$$\mu_{Sn} + 2\mu_O = \mu(\mathrm{SnO_2}) \tag{3.6}$$

A lower bound on the chemical potential values, μ_i, of the atoms forming the bulk phase is placed by Eq. 3.6. Otherwise, particles would defuse out of the bulk into the reservoirs until equilibrium was reached. An upper bound to the chemical potential values is introduced by the most stable elemental phase available to the corresponding atomic species. If this bound is exceeded precipitation of elemental phases inside the host compound becomes likely. In the case of SnO_2, the most stable elemental phases under ambient conditions are metallic α-Sn and isolated O_2 molecules.

$$\begin{aligned} \mu_{Sn} &\leq \mu(\alpha\mathrm{Sn}) \\ \mu_O &\leq \frac{1}{2}\mu(\mathrm{O_2}) \end{aligned} \tag{3.7}$$

For a host crystal that is not a compound material the upper and lower bounds coincide and only one value of the chemical potential is available. For a system made up of two or more constituents, some variability in the chemical potential values is permitted. As a result, it is often more convenient to rewrite the total chemical potential of a species i, as a sum of the most stable elemental reference phase, μ_i^0, and the deviation of the chemical potential from the elemental phase, $\Delta\mu_i$.

$$\mu_i = \mu_i^0 + \Delta\mu_i \tag{3.8}$$

Defined in this way $\Delta\mu_i$ can be viewed as reflecting experimental conditions, such as a SnO_2 sample placed in oxygen-rich conditions ($\Delta\mu_O = 0$), or oxygen-poor conditions ($\Delta\mu_{Sn} = 0$). In the latter case, $\Delta\mu_O$ attains a negative value corresponding to half the chemical potential of the host $\mu(\mathrm{SnO_2})$. Using the newly defined $\Delta\mu_i$, Eq. 3.6 can be rewritten in the form of Eq. 3.9. Where $E^F_{\mathrm{SnO_2}}$ is the formation energy of SnO_2 per formula unit, defined as the difference between the chemical potential of a SnO_2 unit and the sum of the potentials of individual constituent elemental phases.

$$\Delta\mu_{Sn} + 2\Delta\mu_O = E^F_{\mathrm{SnO_2}} \tag{3.9}$$

Similar considerations to those above can be extended to chemical potentials of impurity atoms. No intrinsic lower bounds are placed on external elements, yet, if impurity incorporation is to be achieved, the highest possible chemical potential for the atomic reservoir is desirable. Here, it is also useful to separate the chemical potential in the form of Eq. 3.8. In the case of external defects, $\Delta\mu_i$ accounts for variations introduced by secondary (ternary, etc.) phase formation, which can often impose a stricter upper bound on the impurity potential than the elemental phase. This bound is not strictly fixed due to the possible variations in the chemical potentials of the host atoms.

In the case of tin dioxide, secondary oxide phase formation ($\mathrm{D_mO_n}$), for example, might play an important role. In this case, the following relationship should be addressed in the evaluation of chemical potentials.

$$m\Delta\mu_D + n\Delta\mu_O \leq \Delta E^F_{\mathrm{D_mO_n}} \tag{3.10}$$

In principle, any phase that is stable on the convex hull (made of the host and impurity elements) could affect the allowed range of the chemical potentials. Tools for automatizing the process of evaluating the chemical potential bounds have been proposed [127], but typically require *a priori* knowledge of the most stable phases. Recently, a tool for defect calculations PYCDT [128] has been presented with the capacity to access the Materials Project database [129] in order to extract the most relevant phase information from a vast range of computationally and experimentally proposed structures. One should be careful, however, to ensure that all electronic structure calculations performed use the same criteria. Since chemical potentials are dependent on pressure and temperature, such effects should in principle also be included in their evaluation. However, if the formation energies are estimated at 0 K and/or ambient pressure, the same theoretical footing should be maintained when phase stability is considered.

From a computational point of view, as long as conditions required for phase stability are upheld, the choice of the precise chemical potential value is arbitrary. As a result, in the following chapters chemical potential variations are treated as free-parameters that reflect the experimental environment. Nevertheless, the specific choice of potential influences defect formation energies directly. Intuitively, in oxygen rich conditions, oxygen vacancies are less likely to form than in oxygen-poor conditions. In multicomponent systems, computational investigations can often help to design experiments with the conditions most likely to result in a desired outcome [130, 131].

3.5.2. The Fermi level

The Fermi level, ϵ_F, is useful for describing the exchange of charge between a host system and an electron reservoir. Naturally, it is easier to extract an electron from a reservoir with a high ϵ_F and more challenging to place an electron into a reservoir with a high ϵ_F. Therefore, the formation energy of a charged defect is dependent on the position of the Fermi level, as can be further seen from Eq. 3.4. Since the electron reservoir and the system are in thermal equilibrium, the Fermi level of the bath is simply equivalent to the Fermi level of the host.

In an undoped semiconductor ϵ_F is defined to lie midway between the conduction and the valence band edges. If the number of free carriers is increased, for example via external doping, the Fermi level moves closer towards the corresponding band edge. It is thus convenient to rewrite ϵ_F in the form of Eq. 3.11, such that $\Delta\epsilon_F$ describes the values of the Fermi level within the band gap, E_G, of the semiconductor.

$$\epsilon_F = \epsilon_{VBM} + \Delta\epsilon_F \tag{3.11}$$

The Fermi level of the host is established by the cumulative effect of all the defects and defect clusters present inside the semiconductor and is, therefore, dependent on the free-carrier concentrations provided by *all* defects. However, defect concentrations are themselves dependent on ϵ_F. This suggests that thermal equilibrium values of the Fermi level should be obtained self-consistently through the charge-neutrality relation given in Eq. 3.12, where C_X is the concentration of a defect X in a charge state q_X determined by Eq. 3.1. The sum runs over all possible defect types X, as well as all of their available charge states.

$$\sum_X q_X C_X - c_e + c_h = 0 \tag{3.12}$$

The concentration of electrons, c_e, in the conduction band and the concentration of holes, c_h, in the valence band are obtained by integrating the Fermi-Dirac distribution, f, as shown in Eq. 3.13. This equation allows for the number of electrons, n_e, and the number of holes, n_h, at a fixed value of ϵ_F to be computed. These values are then normalized by the volume of the crystal. Here, $D(\epsilon)$ is the density of states at a given energy ϵ.

$$\begin{aligned} n_e &= \int_{\epsilon_{CBM}}^{\infty} D(\epsilon) f d\epsilon \\ n_h &= \int_{-\infty}^{\epsilon_{VBM}} D(\epsilon)(1-f) d\epsilon \end{aligned} \tag{3.13}$$

In a practical calculation, the integral can be replaced by a sum over one-electron energies obtained in a unit cell DFT calculation, assuming an appropriately dense choice of a k-point mesh [132]. Nevertheless, caution should be taken when determining the Fermi level through Eq. 3.12, as overlooking important compensating defects can alter significantly the position of the Fermi level and, hence, the calculated equilibrium defect concentrations. Due to the difficulty of knowing all relevant defects *a priori* and the computational cost of calculating them, most modern calculations treat $\Delta\epsilon_F$ as a free-parameter. Variation of this parameter, then, reflects a p-type ($\Delta\epsilon_F \sim 0$) or an n-type ($\Delta\epsilon_F \sim E_G$) character of the semiconductor.

3.6. Supercell Size Corrections

In Section 3.2 the supercell approach to defect formation energy calculations was elucidated. Within this approach, in a host supercell of a computationally tractable size (of the order of 10 Å) a periodically repeated defect will inevitably interact with itself. Such (self-)interactions can be further subdivided into elastic, magnetic and electrostatic. In principle, with increasing supercell size these effects should become negligible and, eventually, fall below the limit of chemical accuracy. However, this limit is typically not reached in computationally feasible calculations. To overcome this difficulty, various *a posteriori* corrections have been proposed that can be introduced after a calculation is performed. These corrections and their scaling as a function of the supercell dimension, L, are discussed in more detail below.

3.6.1. Elastic corrections

A defect, introduced into a crystalline host, typically results in structural distortions surrounding the defective lattice site (as discussed in more detail in Sec. 3.3.1). If the extent of the distortions exceeds $L/2$, alterations produced by the periodic images of the defect will affect the structural rearrangements around the defect site. Such elastic interactions as well as the energy resulting from them have been demonstrated to scale as L^{-3} [133, 134]. However, no *a posteriori* correction methods to account for these effects have been proposed.

A possible route to eliminate elastic effects (or any other supercell size dependent inaccuracies [97]) is to perform formation energy calculations using a range of varying supercell sizes and to extrapolate the results to the limit $L \rightarrow \infty$. Here, knowledge of the physical dependence of the correction on the cell dimension L is important for meaningful interpolation. Such an approach is computationally costly and given the rather rapid convergence of elastic interactions is rarely used for their evaluation.

3.6.2. Magnetic corrections

Magnetic defect self-interactions can be mediated via a magnetic host lattice. Intuitively, the largest errors of this nature are anticipated in compounds containing strongly magnetic atoms, such as Fe, Ni, Cr, etc. However, defect mediated magnetism has been predicted for many non-magnetic semiconductor hosts, including SnO_2 [135, 136], a compound explored in this thesis.

An L^{-3} scaling, analogous to the elastic interactions above, has been proposed for the interactions between dilute magnetic defects [137], suggesting that in reasonably sized cells the energy of this interaction decays fairly rapidly. However, particular care should be taken to ensure supercell size convergence in calculations where magnetic defect behavior is observed. Fortuitously, spin polarization typically results in the introduction of defect energy levels inside the band gap of the host. Such levels are unfavorable for maintaining the optical transparency displayed by TCO materials and, thus, result in immediate disqualification of magnetic dopants in our targeted doping approaches.

3.6.3. Electrostatic interactions

A charged point defect will interact with its periodically repeated images through a long-range Coulomb potential. In this case, the total electrostatic energy of the charged periodic cell becomes divergent, precluding formation energy calculations. Conventionally, this issue is circumvented by setting the average electrostatic potential of the supercell to zero [138]. The omission of the $G = 0$ term in the Fourier expansion of the electrostatic potential in a charged defect calculation is analogous to the introduction of a compensating uniform background charge. This compensating charge, of course, is only present in the electrostatic potential and is not explicitly introduced into the computation. As a result, the calculated eigenvalues are determined only up to an additive constant. To account for a potential offset between the unknown constants of the charged and neutral supercells, an alignment energy is introduced that attempts to restore the relative positions of the average electrostatic potentials.

$$\Delta E = q\Delta V \tag{3.14}$$

The difference in local atomic-site electrostatic potentials (far away from the defect) between the defective cell and the host cell can be used to determine the potential difference, ΔV [97, 138]. However, the determination of alignment terms in this way is challenging as it has been demonstrated that the potential alignment and the charge corrections, discussed next, are not independent of each other [105, 138–140].

The direct charge-charge interaction as well as the charge-background interaction should be accounted for in periodic calculations containing charged defects. Setting the average electrostatic potential to zero results in a uniform compensating background charge, i.e. the jellium model. For point charges in a jellium model a correction term, with $\frac{1}{L}$ scaling, has been proposed by Leslie and Gillan [133] and later extended by Makov and Payne [141] to include a contribution for the delocalized part of the charged defect (Eq. 3.15).

$$\Delta E = \frac{q^2\alpha}{2L\epsilon} + \frac{2\pi qQ}{3L^3\epsilon} + \mathcal{O}(L^{-5}) \tag{3.15}$$

Where q is the charge of the defect, α is the lattice dependent Madelung constant of the material and Q is the electrostatic dipole moment. The dielectric constant, ϵ, is included to account for the screening effects of the material. A modified version of the correction in Eq. 3.15 has been proposed by Lany and Zunger [105, 138], where the dipole moment is calculated using the full defect-induced charge density, $\Delta\rho = \rho_X - \rho_H$ (ρ_X is the charge density obtained in the calculation of the defective supercell and ρ_H is the charge density of the pure host supercell), including the contributions arising from the dielectric screening.

An alternative approach has been proposed by Freysoldt *et al.* [139, 142] arguing that the macroscopic screening is not appropriate for defects separated by short ranges and can often lead to over-corrections. In the Freysoldt approach, the long range (microscopically screened) Madelung term is subtracted from the defective cell potential, which is then aligned at a distance far from the defect with that of a bulk calculation. Here, the planar-averaged electrostatic potentials from the *ab initio* calculations are used, not the atomic-site potentials as was the case for the previously discussed potential alignment approaches. This is problematic in the presence of strong atomic relaxations that create a non-smooth defect potential [140], which is difficult to align to the bulk with high accuracy.

The approach of Freysoldt *et al.* has been further extended by Kumagai and Oba [140] to utilize the dielectric tensor, instead of the macroscopic dielectric constant. Such extension permits the treatment of systems with non-isotropic dielectric properties. Furthermore, they suggest the use of atomic-site potentials averaged in a sampling region away from the defect site to estimate the potential alignment term. This permits more accurate estimation of the alignment term in cases where atomic relaxations are included in the defective cell calculations. The inclusion of such relaxation is relatively important for ionic materials (such as the ones presented in this thesis), since much of the Coulombic screening is due to the dipoles of polarizable ions.

A review of the performance of different methodologies has been presented by Komsa *et al.* [143] in 2012 (before the extension suggested by Kumagai and Oba), concluding that the Freysoldt scheme offers most robust performance for defect states with well-behaved localization. It is evident that the electrostatic energy, scaling as $\frac{1}{L}$, is the most important long-range correction to be accounted for and, thus, gives the strongest contribution. In our calculations, both Freysoldt and Kumagai approaches have been used to evaluate the electrostatic corrections as implemented in the PYCDT code [128].

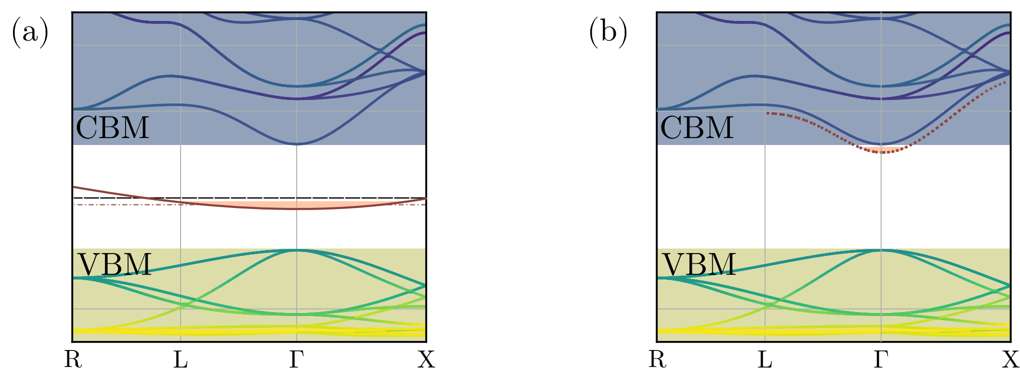

Figure 3.5. Schematic illustration of band dispersion effects for (a) a deep localized defect level and (b) a perturbed host state corresponding to a shallow delocalized defect level.

3.6.4. Band filling corrections

When an electronic localized defect state is formed inside the band gap of an infinite semiconductor it gives rise to a single energy level in the infinitesimal Brillouin zone (reciprocal k-space). In a periodically repeated finite-size supercell corresponding to the same crystal, this energy level is represented in k-space as a single flat band. Any calculated dispersion of this band arises from defect wavefunction overlap across different cells and is a consequence of the fictitious defect-periodic-image interactions.

If sampled perfectly the average of the disperse band should result in the correct defect energy level. In most calculations, however, a finite size k-point mesh is used to sample the reciprocal space and, consequently, the corresponding defect band. For large supercells a common choice is Γ-point-only sampling. At this point of high symmetry the artificial dispersion of the defective band is largest and could lead to inaccuracies in total energy estimation [97]. Methods for choosing k-point meshes based on the symmetry of the underlying unit cell have, therefore, been proposed in order to accelerate the convergence of the defect band energy [144].

Even with an appropriate k-point mesh one runs into difficulties in situations where the localized defect state is only partially occupied by charge carriers, as illustrated in Fig. 3.5(a). The variational nature of DFT calculations ensures that only the lowest lying energy levels of the defective state will be occupied, precluding successful averaging of the band even with perfect k-point sampling. A possible solution to this issue is to ensure that energy states at different k-points corresponding to the same defect level are equally occupied [96]. This approach, however, is applicable only with *a priori* knowledge of the behavior of a specific defect.

Band filling related issues also arise in shallow defect calculations. A shallow defect in a semiconductor results in a hydrogen-like state formed from the perturbed host conduction (or valence) bands. In the dilute limit, this hydrogenic state would only be occupied at the lowest energy level below the CBM (or unoccupied above the VBM). In a charge neutral supercell calculation, however, due to the high defect concentration a Burstein-Moss-like [145, 146] band filling results. This scenario is shown in Fig. 3.5(b) for a shallow donor. An electron, that should lie in the bottom of the shallow energy

band, fills the conduction band and raises the overall energy of the supercell.

Shallow band filling can be corrected for *a posteriori* by estimating the band filling energy, ΔE_D, using Eq. 3.16. Here, $f_{\mathbf{k}}$ are the occupation values of the state $\epsilon(\mathbf{k})$, at the k-point $\mathbf{k}$, with a weight $w_{\mathbf{k}}$. The sum runs over all k-points, but only includes energies $\epsilon(\mathbf{k})$ that are above the (aligned) conduction band minimum, ϵ_{CBM}, of the host. This is equivalent to moving the electrons from k-points with higher eigenvalues to the CBM.

$$\Delta E_D = -\sum_{\mathbf{k}} w_{\mathbf{k}} f_{\mathbf{k}} \left(\epsilon(\mathbf{k}) - \epsilon_{CBM}\right) \tag{3.16}$$

$$\Delta E_A = \sum_{\mathbf{k}} w_{\mathbf{k}} (1 - f_{\mathbf{k}}) \left(\epsilon(\mathbf{k}) - \epsilon_{VBM}\right) \tag{3.17}$$

An inverse argument applies to shallow acceptors, where a hole should be extracted from a single energy level above the (aligned) valence band maximum energy, ϵ_{VBM}, of the host. In a periodic calculation a part of the host valence band is depleted and a correction term, ΔE_A, should be applied. In evaluating this term, the sum only runs over energies up to the value of ϵ_{VBM}. In contrast to deep defects, when a Γ-point only sampling is used the shallow defect band filling is eliminated completely, resulting in the most accurate defect energies.

3.7. Binding Energies

In the previous section methods for extrapolating supercell defect calculations to the dilute limit have been presented. In the dilute limit, defects are considered to be **isolated**, i.e. far enough away from all other defects that no defect-defect interactions are present. Most of the work in this thesis focuses on isolated defects. Under certain conditions, such as at high concentrations or at low temperatures, however, effects of defect-defect interactions can become significant. Two defects are considered **associated** when the separation between them is small enough to non-trivially influence each others formation energies or other properties of importance. When two defects are close enough to form a direct bond they can be considered as a single extended unit – a **defect complex**. In the following, the notation $X + Y$ is used to address the combined properties of the two isolated defects, namely X and Y, while the notation $(X + Y)$ is reserved for a complex formed by X and Y. The concentration, $C_{(X+Y)}$, of a defect complex $(X + Y)$ is directly proportional to the availability of defects of type X and type Y as demonstrated by Eq. 3.18.

$$C_{(X+Y)} = N_{(X+Y)} \frac{C_X C_Y}{C_0} \exp\left(\frac{E^B}{k_B T}\right) \tag{3.18}$$

Here, $N_{(X+Y)}$ gives the internal degrees of freedom available to the defect complex (per defect site), C_X and C_Y are the concentrations of isolated defects defined by Eq. 3.1 and E^B is the binding energy of the cluster $(X + Y)$. A comparison between Eq. 3.18 and Eq. 3.1 defines the binding energy (Eq. 3.19). A positive binding energy, defined in this way, implies that energy can be gained by complex formation, while a negative binding energy suggests that the defects are likely to repel each other.

$$E^B = E^F_X + E^F_Y - E^F_{(X+Y)} \tag{3.19}$$

Typically, positive binding energies are found between defects in opposing charge states, where strong electrostatic interactions are the driving force behind complex formation. Acceptor dopants are, therefore, likely to attract defects that behave as donors and vice versa, creating complexes that are overall charge-neutral (electrically inactive) [147]. The removal of the doping character of an impurity through complex formation is known as *defect passivation*.

Electrostatics is not the only way for two defects to interact, steric (spacial) effects can also significantly impact the affinity of two defects to cluster. For example, interstitial atoms may preferentially form next to vacancy sites, due to the additional volumetric space available that would help to reduce the overall strain on the host lattice introduced by the defect pair.

$$E^A = E^B + E^M \tag{3.20}$$

In order for two defects that favor complex formation to be separated, a minimum activation energy E^A of the form of Eq. 3.20 is required. Where E^M is the lowest energy barrier for migration of either defect X or defect Y that allows the two imperfections to diffuse away from each other.

4 Dopant Screening

In Chapter 1 the importance of understanding defects in semiconductors and wide-band gap insulators was highlighted and in Chapter 2 and 3 computational tools that can be used to attain this understanding were presented. In the following chapters we aim to demonstrate how the aforementioned tools can be further utilized to enhance the desired attributes of existing transparent conductor materials through targeted doping. Our goal is to be able to inform our experimental colleagues on how improvements on existing approaches can be made in order to realize transparent conductive oxides with exceptional performance.

The aim of targeted doping is, perhaps obviously, to improve or induce a chosen attribute in a material in a way that is beneficial for the intended application. In a computational study, this implies that the term *useful* has to be defined in a way that is measurable through some property, which can be obtained from a calculation. As our interests lie in transparent conductors, in this chapter we focus on quantifying their useful aspects, though the proposed scheme can be easily expanded to accommodate any number of coveted properties.

For optoelectronic applications two clear requirements can be distinguished: good conductivity and optical transparency. Conductivity, σ, is a result of both free-carrier concentrations (n_e for electrons and n_h for holes) and mobility, μ, of these carriers. The mobility, in turn depends on the effective mass, m^*, of the carrier and its average scattering time, $\overline{\tau}$.

$$\begin{aligned} \sigma &= e(n_e\mu_e + n_h\mu_h) \\ \mu &= \frac{q}{m^*}\overline{\tau} \end{aligned} \tag{4.1}$$

Where e is the elementary charge and q is the charge of the free carrier: $-e$ for electrons and e for holes. Thus, in principle, multiple avenues for improving conductivity by defect incorporation are available. However, the mobility is unlikely to be enhanced by the presence of external impurities. By definition defects create structural faults that result in increased scattering of free carriers, i.e. shorter scattering time-lengths. Furthermore, the effective mass is a feature of the bulk electronic structure that would have to be strongly altered to impact the mobility in a meaningful way. To this end very high defect concentrations would be needed, likely resulting in significant scattering of the charge-carries. Given the above, the best way to improve conductivity is doping, i.e. magnifying the free-carrier concentrations. An additional advantage of doping is

Research presented in this chapter was adapted with permission from: Graužinytė M., *et al.*, Chem. Mater. **29**, 10095–10103 (2017). Copyright © 2017 American Chemical Society. Graužinytė M., *et al.*, Phys. Rev. Mater. **2**, 104604. (2018) © 2018 American Physical Society.

that, as outlined in Section 3.3.2, shallow defects typically have minimal impact on the underlying host structure.

To successfully generate free-carriers an impurity element needs to be stable in a suitable charge state. n-type conductivity is enhanced if the dopant favors a positive charge state (donated one or more electrons into the conduction band) when the Fermi level, ϵ_F, is in the vicinity of the conduction band. p-type conductivity is enhanced if the dopant favors a negative charge state (donated one or more holes into the valence band) when ϵ_F is close to the valence band. Such behavior can be easily quantified by thermodynamic transition (ionization) levels that indicate the value of ϵ_F at which the defect changes its stable charge state (see Section 3.3.1). To evaluate the ionization level of a defect X and assess its suitability for doping, formation energies, E_X^F, as a function of charge, q, need to be determined. Eq. 3.4 and Eq. 3.5 with the methodology described at length in Chapter 3 were used to evaluate the formation energies and ionization levels of all defects.

Just like the effective mass of charge-carriers, optical transparency is strongly linked to the electronic structure of the host. A straightforward way to quantify optical appearance is, thus, through the evaluation of the band-structure. Though in principle the electronic band gap can be tuned by external doping [13, 148], typically a host material that already has a sufficiently large electronic gap ($> 2.8\,\text{eV}$) to allow optical transparency in the visible range is chosen. In this case the only requirement to minimize absorption is that the impurity introduces no deep-lying electronic defect levels. All defects resulting in defect localized states are not only likely to act as color centers, but also as charge trapping centers. Another way to easily distinguish the presence of new states within the band gap, that is computationally cheaper than calculating the bandstructure, is to evaluate the electronic density of states (DOS). Two features of a defect were, therefore, chosen to represent the requirements of a good TCO: (i) the relevant thermodynamic transition levels and (ii) the electronic density of states.

Conventionally, dopant elements are chosen by relying on some *a priori* chemical knowledge or intuition that indicates which elements are likely to act as successful donors or acceptors. This is a powerful approach that is often successful and therefore plays an important role in experiment design, as testing dopant candidates costs valuable resources and time. However, chemical intuition is limited in its predictive power. The impact of either structural changes, solubility limits or the affinity for incorporating in the anticipated site are difficult to guess without explicit calculations or experimentation. Additionally, and perhaps more importantly, it is the opinion of the author of this thesis that only searching for what we already know limits our potential for discovery and that novel physics emerges out of the unexpected. As a consequence, a screening approach that checks **all** elements as potential candidates to act as useful defects is employed in this chapter.

As was shown in Section 3.4, the band gap problem of local density functional theory is a big hindrance in evaluating defect formation energies accurately. In this chapter, we will demonstrate that (at least for tin-based oxides) this problem can be successfully mitigated by employing hybrid exchange-correlation functionals. However, it is evident that accessing the formation energies of each charge state of all available defects for every element in the periodic table using hybrid functional calculations is computationally prohibitive, especially if more than one host compound is to be considered. In order

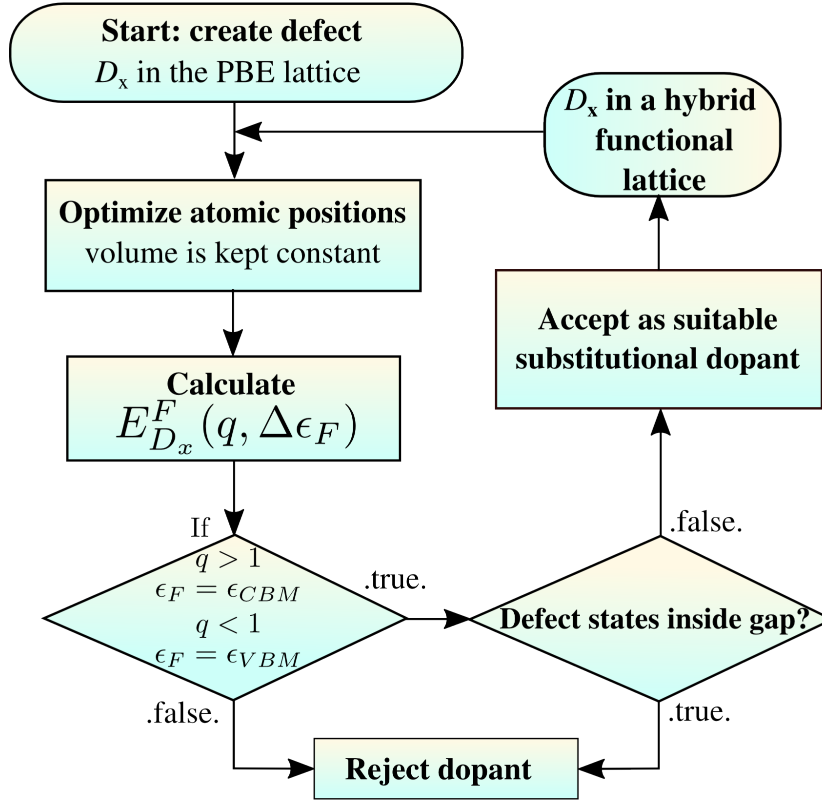

Figure 4.1. A schematic illustration of the calculation recipe used for useful dopant screening in transparent conductive oxide materials.

to circumvent this issue the computational work-flow illustrated in Fig. 4.1 was implemented. All dopant ionization levels were first calculated with a local functional (PBE) level of theory and if both criteria – desired stable charge state and a defect-free band gap – were fulfilled, a subsequent hybrid functional calculation cycle was performed to verify the result. To expedite the computations, the second cycle of calculations was performed by compressing the PBE lattice to the relaxed hybrid functional lattice, with no further atomic relaxations. As will be demonstrated later in this chapter, changes induced from the neglect of these small local relaxations on the hybrid functional level did not affect the results significantly. In stark contrast, the correct lattice size is crucial for accurate electronic band gap (and consequently defect formation energy) evaluation.

Our proposed approach could be easily generalized to account for alternative quantities, however, the crucial pre-screening step that enables a large scale defect study in a specific compound to be performed has to be considered carefully. Indeed, it is of great importance that on the local functional level of theory all useful defects are categorized correctly. Nevertheless, in Section 3.4 we indicated that transition levels predicted by PBE are not reliable. How then can a PBE pre-screening step be justified?

Hybrid functional calculations open up the electronic band gap of the host crystal by shifting the valence and conduction band edges predicted by PBE. In this context, PBE calculations are qualitatively similar to hybrid ones for any emergent defect states that are rigidly shifted together with the relevant band edge. This should always be the case for a perturbed host state that indicates a shallow donor or acceptor – the

ideal doping scenario – as the shallow level is host bands derived. In contrast, when a localized defect state is formed this condition is no longer guaranteed. Nevertheless, the reduced band-gap of PBE suggests a tendency for predicted transition levels to be shallower, i.e. closer to the band edges, thus preferentially stabilizing donating charge states when compared to hybrid functionals. The opposite behavior – a charge neutral PBE state becoming a shallow dopant on a hybrid level of theory – is extremely unlikely, as this would require the defect state energy to be shifted by an amount larger than the relevant band-edge shift itself. As a result, all true shallow dopants should always be categorized correctly using the local PBE functional.

We demonstrate the effectiveness of our proposed work-flow for two test cases: (i) an already established *n*-type TCO tin dioxide. SnO_2 is a strong contender to the current industry favorite In_2O_3 and is, consequently, a well-studied material that has received much theoretical and experimental attention over the years. It, thus, presents a great test case to validate our method and to explore any interesting dopants, which may have been previously overlooked; (ii) a metastable stoichiometry of the same elements – tin monoxide, SnO. Only stable up to 500 K, crystalline SnO exhibits strikingly different properties to those of SnO_2. It presents native *p*-type conductivity, but has been suggested as promising for ambipolar behavior [149, 150]. SnO showcases a rather small fundamental band gap, yet is nearly transparent due to its indirect nature.

We begin our case studies by providing an overview of the theoretical and experimental knowledge gathered so far. We then address the properties of the bulk crystalline phases by exploring the use of different functionals and identifying the most appropriate choice for describing each compound. A computationally tractable supercell size, which nevertheless allows for appropriately converged properties of importance, is then chosen and the calculation recipe outlined in Fig. 4.1 is followed. Useful acceptor and donor impurities are identified and presented for each stoichiometry. We conclude the chapter by comparing the results between the two study cases.

4.1. Case A: Tin Dioxide

The combination of optical transparency and high electrical conductivity enables transparent conductive oxide materials to be used for a wide range of applications - from simple smart window coatings to OLEDs and futuristic see-through displays [41, 151–153]. The niche of these futuristic materials is heavily dominated by electron (*n*-) doped SnO_2, In_2O_3 and ZnO. Currently, many optoelectronic applications are primarily based on indium oxide [154, 155], this material is taking the lead thanks to its superior conductivity, while tin and zinc oxides are close runner-ups, having promising yet not quite sufficient properties for widespread use as electronic materials [156, 157]. In spite of that, the advantage of earth abundance (and, hence, lower cost than indium) has spurred a large experimental and computational effort into understanding and enhancing the properties of Zn- and Sn-oxides [39, 119, 158–167]. In order to bring SnO_2 on a level playing field with indium based TCOs a thorough understanding of useful dopants is needed. Unfortunately, the use of different codes (i.e. basis sets), exchange-correlation functionals, and approaches used to overcome deficiencies inherent to the level of theory has generated a large scatter of results that are hardly, if at all, comparable with each

other. Even the cause for unintentional n-type doping is still an open debate in the scientific community [36, 38–40]. With contradicting predictions reported for oxygen vacancies and cation interstitials – that have been blamed for decades for the intrinsic n-type TCO conductivity. This has even led to the proposal of hydrogen interstitials and hydrogen trapped in oxygen vacancy sites as an alternative explanation for the intrinsic n-type character of conductive oxides [38]. Needless to say, examination of external dopants suffers from similar issues.

It is well known that Kohn-Sham density functional theory band structures systematically underestimate the band gap for semiconductor materials. The band gap problem of standard density functionals is particularly troublesome in the case of TCOs [39, 168]. For instance, the calculated generalized gradient approximation (GGA-PBE) band gap of SnO_2 is 0.6 eV, while experimental results indicate a direct gap of 3.6 eV [169]. Different approaches have been used to alleviate this problem. *A posteriori* corrections, such as the use of scissor operators or alignment schemes, simple extrapolation [36] or different variants of DFT+U [170] are a major cause for the conflicting results in current literature. Moreover, the validity of many such approaches has been called into question when it comes to accurate prediction of defect levels [171].

Hybrid functional HSE calculations, which include a fraction of the exact Hartree-Fock exchange, are often seen to improve the band gaps of semi-conducting materials. However, for SnO_2 a further increase in the standard $\alpha = 0.25$ fraction of the exact-exchange is required to recover the experimental band gap [37, 163] - a necessity for accurate defect formation energy calculations. While fitting the band-gap via α might be justified for the SnO_2 host, the resultant parameter could easily be inappropriate when other substitutional elements are considered. In fact, in the case of zinc oxide recent G_0W_0 'single-shot' calculations have shown that the increased fraction of exact-exchange, while capturing the experimental band gap leads to worse predictions of thermodynamic transition levels, than the standard HSE functional [167]. And further works by Lany and Zunger [172, 173] conclude that the generalized Koopman's theorem and not the experimental band gap should be used for finding an appropriate choice of α in metal-oxide materials.

While all the above methods for band gap correction require adjustable parameters, in stark contrast, the PBE0 hybrid functional predicts the correct band gap of SnO_2 without any adjustments. This allows, in principle, *ab initio* defect calculations in SnO_2 that are completely parameter free, yet has only been utilized in a single p-type dopant study [166]. Incongruous to the various studies, even if often limited to a handful of defects each, of n-type dopants that have been considered by different groups using variants of the HSE hybrid functional [37, 163–165]. In this work we use PBE0 to perform a parameter-free large-scale defect study of SnO_2. This allows us to bring the pre-existing dopant studies on a comparable level of theory and, more significantly, to deepen our understanding of this important TCO material as we shed light not only on the behavior of isolated defects, but overall doping trends.

4.1.1. Bulk properties

First, the volume dependence of the rutile SnO_2 structure on the functional employed was assessed. All calculations were performed using the projector augmented wave

method (PAW) [95, 174] as implemented in the VASP [175, 176] code. A plane wave energy cutoff of 700 eV was used to obtain energy convergence up to 1 meV/atom. POTCAR files with Sn *d*-shell electrons included as valence were used. Volumes of the unit cell structures were obtained by performing a Burch-Murnagham [177] fit to the energy-volume curves, as predicted with PBE, PBE0 and HSE06 exchange-correlation functionals. For PBE [75] primitive cell calculations a $k = 4 \times 4 \times 6$ mesh was used, while for hybrid functionals [81, 82] a larger $k = 6 \times 6 \times 8$ mesh was required. Table 4.1 summarizes the results.

	Exp.	PBE	HSE06	PBE0
a (Å)	4.73 [a]	4.82	4.75	4.75
c (Å)	3.18 [a]	3.24	3.19	3.19
x	0.307 [a]	0.306	0.306	0.306
E^F (eV)	-6.0 [b]	-4.9	-5.2	-5.2
B_0 (GPa)	205 [a]	165	203	204
B'_0	7.4 [a]	5	5	5
E_G (eV)	3.6 [c]	0.63	2.8	3.6

[a] Reference [178] [b] Reference [179] [c] Reference [169]

Table 4.1. Lattice parameters, bulk modulus and electronic gap of rutile SnO_2 calculated using different exchange-correlation functionals.

Clearly, both hybrid functionals greatly improve over the PBE results when comparing experimental and calculated structural parameters as well as the bulk moduli. However, only PBE0 reproduces accurately the experimental band gap without the need for further adjustments to the fraction of exact-exchange. It is worth mentioning, that independently of the functional used, a marked dependence between the volume and the band gap is found. This is particularly evident for hybrid functionals - the use of PBE instead of PBE0 optimized lattice results in a drastic 0.6 eV change in the band gap calculated by PBE0. The large lattice constant variation of approximately 2% between PBE and PBE0 corresponds to a pressure of the order of 10 GPa. This pressure is of the same magnitude as the lattice strain induced by the substitutional elements studied in this work. Thus, in order to have a correct and accurate result not only electronic PBE0 band calculations are necessary, but also the PBE0 volumes are mandatory (i.e. it is not consistent to use PBE volumes with hybrid-functional calculations for these materials, as has been previously attempted [165]). For completeness, we further compare the PBE0 heat of formation and find it in nice agreement with the previous (-5.29 eV) value reported by Scanlon *et al.* [166]. HSE06 values reported by Varley *et al.* [37] are also within 0.2 eV of our result. All functionals are seen to significantly underestimate the experimentally measured value.

4.1.2. Defect calculations

A total of 63 atoms acting as Sn-site substitutionals, D_{Sn}, were considered as potential dopants in this study. An extensive search for D_O substitutionals was not performed, as only elements with an ionic radius similar to that of oxygen are likely to incorporate on

an O-site without causing strong distortions in the lattice and, hence, being energetically expensive. Small ionic-radii, however, would also lead to a smaller cost of interstitial incorporation. This is both a disadvantage for experimental realization of the material and problematic from the theory-modeling point of view, as all potential competing sites should be included in the calculations before any realistic conclusions could be drawn. In contrast, dopants preferentially incorporating as D_{Sn} are generally expected to be larger in size and, therefore, significantly more expensive to incorporate on other (potentially electrically inactive) sites. This choice is further motivated by the intended use of the results for informing our experimental colleagues on defects suitable for doping the thin-film samples they deposit, which are primarily amorphous. Elements that strongly favor Sn-site substitution are less likely to be impacted by small local changes in the atomic environment and can be more reasonably speculated to successfully dope an amorphous film. We stress here, however, that there are certainly elements, such as fluorine (F) – a well established donor [180, 181] for SnO_2, that could act as dopants on a D_O site, but be non-donating on a D_{Sn} position. Impurities of this type would be overlooked in the following work.

A $2 \times 2 \times 3$ supercell (72 atom) of rutile SnO_2 was used for all defect calculations performed in this study. All calculations were spin polarized and magnetism was checked for all systems. The supercell lattice parameters were fixed to those of the expanded primitive cell, while the atomic positions were allowed to relax until the forces on the atoms were below 0.002 eV/Å. All formation energy calculations using PBE0, the exchange-correlation functional identified as the most suitable for describing SnO_2, were performed by compressing the PBE-relaxed defect structures to the correct PBE0 lattice constant. No further PBE0 atomic relaxations were performed. The influence of further relaxation was tested for a subset of defects and the total energies were found to not be affected by more than 0.15 eV.

All supercell relaxations were performed using $k = 2 \times 2 \times 2$ Monkhorst-Pack meshes, while $k = 3 \times 3 \times 4$ (PBE) and $k = 3 \times 3 \times 3$ (PBE0) Γ-centered meshes were employed for final DOS calculations. For each defect formation energies of $q = -1$, $q = 0$ and $q = 1$ charge states were calculated using Eq. 3.4 and the methodologies explained in Chapter 3. Elements identified as shallow dopants were checked for higher stable charge states in the cases where filled states at the conduction band minimum (CBM) were found for donors or empty states at the valence band maximum (VBM) were observed for acceptors. The results are shown in the O-rich limit - the most favorable experimental conditions for Sn-site substitution to take place. Under these conditions, when a stable binary-oxide reference phase exists the formation energies are completely independent of the individual metallic references. As the use of PBE0 hybrid-functional for metallic reference phase calculations may be inappropriate, we would like to stress here that such deficiencies are circumvented in the work presented. Structural information pertaining to all the phases used in determining the chemical potentials is listed in Appendix A.1.

Electrostatic correction terms were evaluated using the Freysoldt approach (see Section 3.6) as implemented in SXDEFECTALIGN [142] code. The static dielectric constant of rutile SnO_2 for use in electrostatic corrections of charged defect supercells was calculated. Both electronic and ionic contributions of the dielectric constant of SnO_2 were evaluated using PBE, obtaining the values $\epsilon_{\parallel} = 4.677(9.054)$ and

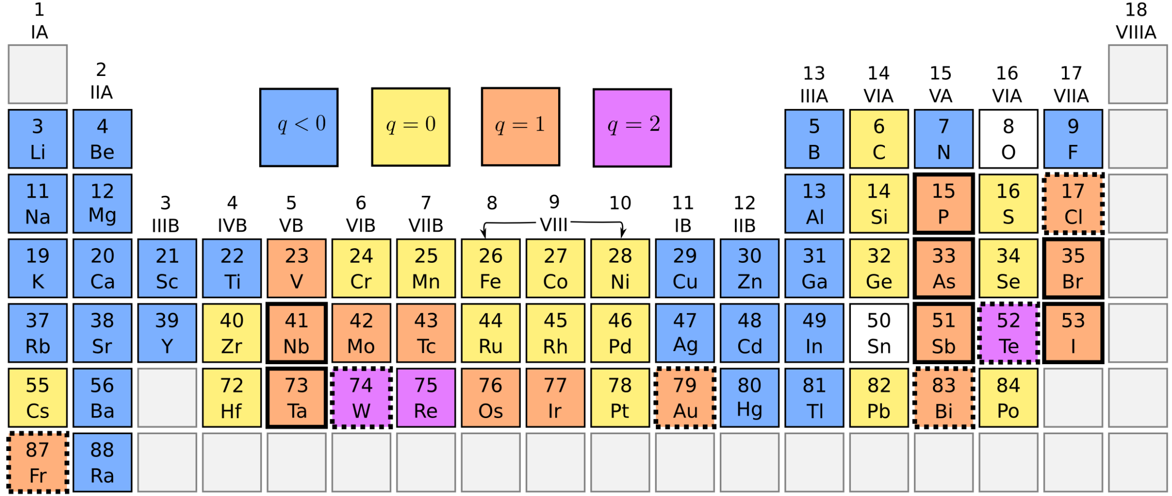

Figure 4.2. Stable PBE charge state of a substitutional atom on a Sn-site, when $\Delta\epsilon_F$ is at the conduction band minimum (CBM): blue < 0, yellow 0, orange +1 and purple +2. Black outline - no localized defect states, dashed outline - elements with intriguing behavior at the CBM (see Appendix B).

$\epsilon_\perp = 4.907(5.604)$. For PBE0 only the electronic contribution including local field effects was calculated, obtaining $\epsilon_\parallel = 3.627$ and $\epsilon_\perp = 4.013$. PBE ratios of electronic and ionic contributions were then used to estimate the ionic contribution for PBE0, recovering $\epsilon_\parallel = (7.020)$ and $\epsilon_\perp = (4.582)$ and obtaining a total value of the averaged dielectric constant of 9.96 (comparable to 9.86 value obtained by Varley *et al.* [163]). The final corrections are, however, not strongly dependent on the precise value of the dielectric constant - not more than 80 meV changes are seen when the PBE dielectric constants are used instead.

4.1.3. *n*-type dopants

In Fig. 4.2 pre-screening results for n-type dopants are summarized by showing the calculated stable charge states for a Fermi level, $\Delta\epsilon_F$, lying at the conduction band minimum. PBE calculations predict nineteen elements as potential n-type donors (shown in orange ($q = 1$) and purple ($q = 2$) in Fig. 4.2). Based on their densities of states these elements were separated into three categories: (a) elements that do not strongly affect the electronic structure of SnO_2 and should act as good n-type donors, highlighted by a solid black outline in Fig. 4.2; (b) elements that do not form defect states inside the band gap, but induce strong distortions close to the CBM that warrant further investigation, marked by a dashed outline in Fig. 4.2; (c) transition d-metals resulting in defect states lying inside the band gap due to metal-d and O-2p orbital interactions (plots of the DOS can be found in Appendix B).

Clear trends across the periodic table can be identified with donor impurity regions seen within the transition metals and the elements of group V and VII. Two intriguing outliers to the general trend can also be spotted: (i) Te - the only element of those in group VI acting as a double donor in a $q = 2$ charge state; (ii) Au - offering up

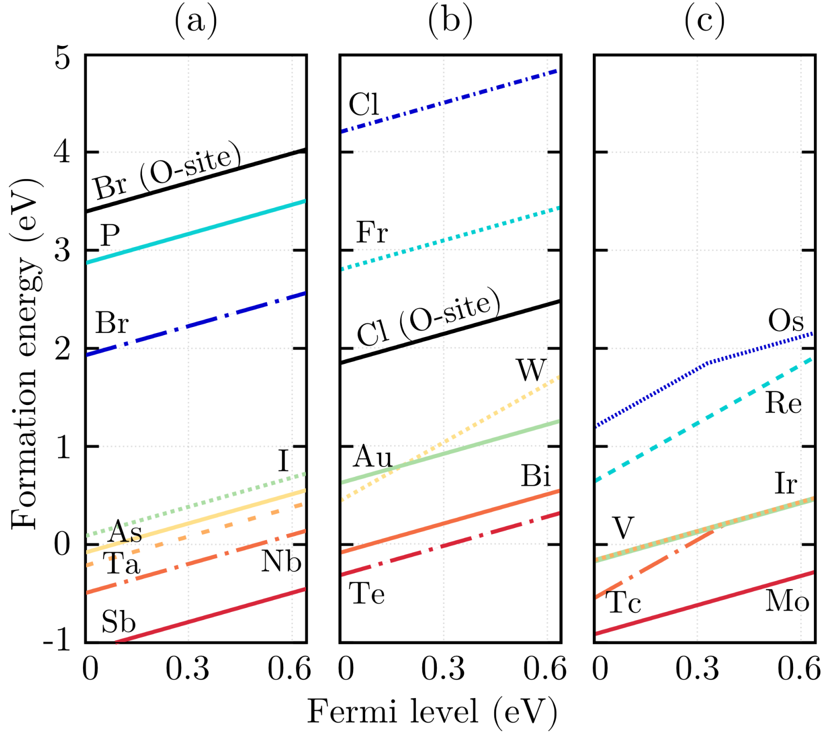

Figure 4.3. PBE formation energies of selected substitutional defects as a function of the Fermi level in the O-rich limit. Colored lines show D_{Sn} substitution for different atoms, while black solid lines show D_O. Only the stable charge state is shown. (a) elements outlined in solid-black lines in Fig. 4.2, (b) elements highlighted by dashes in Fig. 4.2, (c) all remaining donors.

an electron despite its typical +3 oxidation state. This, as will be shown later, is an artifact of the PBE functional preferentially stabilizing electron donating states. Due to the small band gap, induced defect-states for these two elements are predicted to be energetically close to the CBM, artificially increasing the total energy of the charge neutral state. With the use of hybrid-functionals calculations the outliers are seen to disappear acquiring the same charge state as the rest of the elements in the group - Te is found to be charge neutral, while Au is stable in the negative charge state.

PBE formation energies under Sn-poor conditions, when D_{Sn} formation is favourable, are shown in Fig. 4.3 as a function of $\Delta\epsilon_F$ for all nineteen n-type dopants. Panels (a), (b) and (c) correspond to the three categories outlined previously. The points at which a change in slope is seen for Os and Tc indicate the thermodynamic transition levels. Both elements undergo a $q = +2$ to $q = +1$ transition as the Fermi level passes the mid-gap region. However, as mentioned previously the localized defect states seen inside the band-gap for elements of panel (c) are likely to negatively impact both the optical and electronic properties of SnO_2. These elements were, thus, excluded from more detailed investigations.

To check if the Sn-site substitutions of the potential dopant impurities are in fact stable, O-site formation energies, D_O, were calculated for all elements in panel (a) and (b) of Fig. 4.3 and are shown in the plot as solid black lines. For all but two elements

– Br and Cl – the oxygen-site formation energies are so much higher in energy they lie above the 5 eV range of the plot. For these elements, in the oxygen-rich growth conditions considered throughout this work D_O substitutions are extremely unlikely.

Chlorine, as seen in Fig. 4.3(b), is the only element of those identified as suitable Sn-site dopants to have a lower formation energy of D_O than D_{Sn}. Nevertheless, all D_O substitutions were also found to be exclusively stable in a positive charge state for the elements considered. We conclude, that even if the dopant atoms were to incorporate at a more energetically expensive (except for Cl) O-site location, they would still act as free-carrier donors. On the other hand, in many of the cases – as is also observed for unoccupied anion vacancies – oxygen site substitution results in localized defect states inside the band gap and as such is less favorable.

In a second step, formation energy calculations for elements from panels (a) and (b) in Fig. 4.3 were repeated using the PBE0 functional. The results are shown in Fig. 4.4. To place our work in the context of preceding publications we have also included in panel (c) the formation energies of previously purported unintentional n-type conductivity culprits: oxygen vacancies, V_O, hydrogen interstitials, H_i, and substitutional hydrogen, H_O. Our calculated formation energies in panel (c) compare favorably with the previous works using the PBE0 functional [39, 166]. We see both H_i and H_O to be exclusively stable in an electron donor state, while V_O is seen to prefer the charge-neutral configuration once the Fermi level approaches the CBM.

In panel (a) – the case with no localized defect states – little change when going from PBE to hybrid functional calculations is observed. The relative energetic ordering of the defects is mostly maintained, with Br and P costing significantly (~ 2 eV) more energy to incorporate in the SnO_2 lattice than the other defects. Br is the only element observed not to maintain the positive charge state near the CBM and would result in self-compensation as the Fermi level approaches the conduction band. In flagrant contrast none of the panel (b) elements maintain their PBE predicted charge states, with thermodynamic transitions to a lower charge state occurring more than 0.5 eV below the CBM. Of all the elements in panel (b) only tungsten is still predicted to act as a donor. The different behavior of the two sets of elements further supports the idea that panel (a) dopants result in a perturbed host state, while elements of panel (b) form localized defect states that do not follow the behavior of the host conduction band[†]. Density of states plots of the elements in panel (b), shown in Appendix B, clearly illustrate this behavior – even those electronic defect states that are predicted to lie above the CBM using the PBE exchange-correlation functional are seen to shift into the band gap region when calculated with hybrid functionals.

Interestingly, for the case of Br a k-point mesh dependent energy splitting between spin-up and spin-down states was observed in the $q = -1$ charge state. This leads to a relative lowering of the energy of the $q = -1$ charge state, when a Γ-centered mesh is used. Using this mesh we predict the thermodynamic transition level $\epsilon(+/-)$ for Br at -0.3 eV below the CBM (-0.9 eV in previous GW calculations [182]). In contrast, a the smaller off-Γ mesh leads to n-type behavior all the way at the conduction band minimum. All other element results were not affected by the k-mesh choice.

The $\epsilon(+/-)$ thermodynamic transition for As was seen to occur just above the CBM

[†]Revisit Section 3.3 for an in depth discussion on the differences between deep and shallow defects

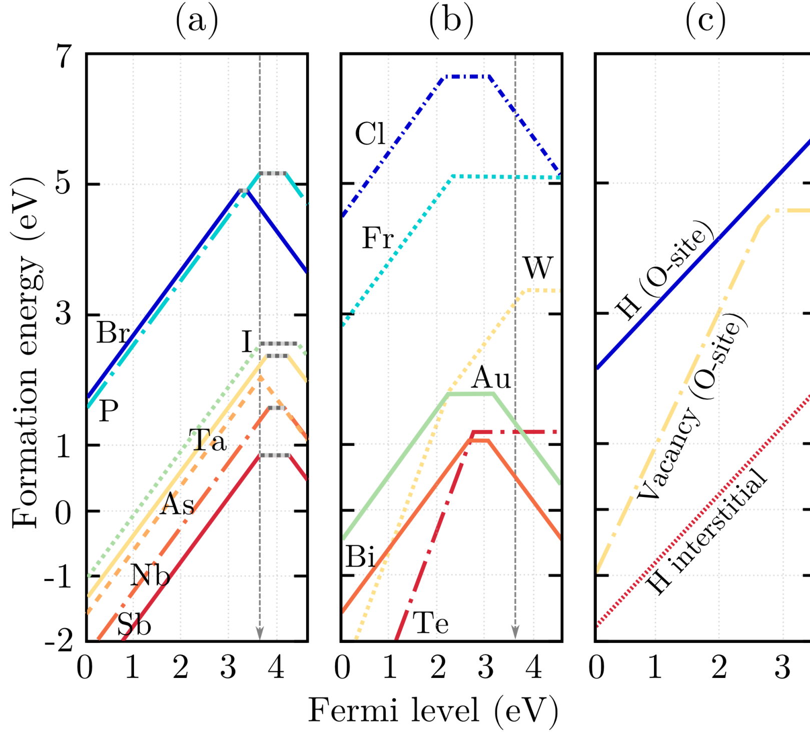

Figure 4.4. PBE0 formation energies of Sn-site substitutional defects as a function of the Fermi level in the O-rich limit. Only the stable charge state is shown. Grey dashed lines indicate formation energies for defect-state-free charge neutral states. (a) elements outlined in black in Fig. 4.2, (b) elements outlined by dashes in Fig. 4.2, (c) other defects: oxygen vacancy and hydrogen-related defects.

(-0.1 eV reported in a GW study [182]). The same $\epsilon(+/-)$ thermodynamic transition level for both Sb and P was predicted at +0.4 eV in GW calculations [182], which is in close agreement with our PBE0 results of +0.3 eV. However, the direct $\epsilon(+/-)$ transition is not predicted to occur for the later two elements in our calculations. We find that the neutral charge state becomes stable just above the CBM instead and a subsequent $\epsilon(0/-)$ transition occurs at 0.6 eV (Sb) and 0.5 eV (P) above the CBM. For shallow donors, however, the neutral charge state calculations result in a defect state that has an energy above the CBM of SnO_2 and the additional electron occupies instead a perturbed host state. In this state the electron is usually highly delocalized, resulting in an environment analogous to the ionized defect in a jellium background. In this case, applying a similar charge correction to the neutral charge state may be pertinent. This suggests that our calculated $q = 0$ values are more indicative of the lower bound to the formation energy of this charge state. Regardless, for these two dopant elements quite high Fermi levels could be reached before the onset of self-compensation. Both Sb and P have been shown to act as donors, when substituting on a Sn-site, experimentally [183, 184]. Our results also confirm previous HSE calculations [163].

As far as the authors are aware no thermodynamic transition energies are available for the remaining elements of panel (a), nevertheless, similar qualitative agreement with GW could be expected. Tantalum exhibits a thermodynamic $\epsilon(+/-)$ transition at just

0.1 eV above the CBM. While iodine and niobium behave similarly to Sb. Iodine shows the deepest $\epsilon(0/-)$ transition level at 0.8 eV above the conduction band edge. The same transition for Nb occurs at around 0.5 eV, however, it remains an active electron donor the longest out of all the dopants in this category, with a $\epsilon(+/0)$ transition at 0.2 eV above the band egde. Previous theoretical work using the HSE functional [165], considering only charge neutral defects, has speculated that Nb should not act as an electron donor based on the existence of occupied spin-down defect states at the CBM. Yet, such states are eliminated when Nb is ionized to a $q = 1$ charge state suggesting that it, in fact, forms a DX-center[†] and is able to donate charge carriers. This further highlights the importance of considering formation energies as a function of charge. Our results for Nb are also in good agreement with experimental findings [185] that observe low dopant concentrations improving the sheet-resistance for SnO_2, and subsequent worsening when high dopant concentrations are used.

We predict tantalum (see Fig. 4.4) to also exhibit donor behavior in SnO_2. Unfortunately, the DOS of the stable $q = 1$ charge state (Appendix B) reveals localized defect states in the middle of the band gap, likely to act as a scattering or a color center. This is in agreement with experimental findings [186] that find a constant decrease in mobility with increasing tungsten concentration. Nevertheless, a peak in free-carrier concentration is seen at around 3% doping, hinting that up to a certain Fermi-level value tungsten does indeed act as an electron donor.

Defect calculations for the O-site substitution were not pursued on the PBE0 level, given the fact that strong preference for Sn-site formation was demonstrated by all but one impurity species. The agreement of relative defect formation energies between the two different functionals leads us to expect similarly high formation energies for O-site defects also on a PBE0 level of theory. It is, nevertheless, worth mentioning that three elements - Br, Cl and I - were seen (on the PBE level of theory) to occupy the O-site without introducing any defect-states into the band gap. These elements may, therefore, be worthwhile to investigate in a further study. On the other hand, previous experimental investigations [187] confirm our prediction that the D_O site solubility of these elements would be low, with iodine showcasing a prohibitively high energy for O-site incorporation, resulting in extremely low solubilities.

4.1.4. *p*-type dopants

Acceptor doping is a contentious subject in SnO_2. In contrast to the *n*-type results, our PBE calculations predict only two elements to act as potential *p*-type dopants, despite the large number of metals considered in this work that prefer lower oxidation states than that of Sn. The affinity for *n*-type conductivity of SnO_2 (as well as many other TCOs) is readily explainable by the relative alignment of the band edges of the material with respect to the vacuum level [188]. Scanlon *et al.* [166] suggest that the combination of a low-lying CBM together with a large band gap result in a VBM too deep for *p*-type conductivity to become realizable in practice. Our pre-screening formation energy results summarized in Fig. 4.5 are in full support of this suggestion. The viable *p*-type dopants for SnO_2 are shown in blue, indicating a negative stable charge state when $\Delta\epsilon_F$

[†]see Section 3.3.2 for more information on DX-centers

Figure 4.5. Stable PBE charge state of a substitutional atom on a Sn-site, when $\Delta\epsilon_F$ is at the valence band maximum: blue < 0, yellow 0, orange +1 and purple +2. Potential p-type dopants are outlined in black.

is at the valence band maximum.

Some experimental studies have reported measuring p-type conductivity in tin dioxide [189–195], yet these results are not well supported by the existing theoretical calculations [163, 166]. As an example, previous computations predict nitrogen to be an extremely deep acceptor when doping on an oxygen site. Still, limited hole densities of the order of 10^{14} cm^{-3} have been reported via N substitution [189]. Most commonly, however, p-type conductivities are achieved by replacing 20-30% [190, 191, 194, 195] of the original Sn atoms. While these approaches are successful, at high doping levels new phase formation may need to be considered to find an agreement between theory and experiments.

The DOS of the two p-type dopants, plotted in Fig. 4.6, reveal an energy splitting between the spin-up and spin-down states. A single unoccupied spin down defect-state close to the VBM was seen in both beryllium and magnesium doped SnO_2 using PBE level of theory. Yet, defect states so close to the band edge should have no strong affect on the optical transparency of the TCO. However, a qualitative change in the DOS is seen using the PBE0 level of theory. An energetic splitting between states in the two spin channels is still seen using hybrid-functionals, however, all the defect induced states close to the valence band are now fully occupied. Furthermore, in the case of Mg_{Sn} a deep localized defect state appears about 1 eV inside the electronic band gap.

Additionally, PBE0 calculations reveal that for Be the $\epsilon(+/-)$ transition level actually occurs 0.6 eV above the valence band maximum. Hence, pining the Fermi level above the VBM and prohibiting any acceptor doping due to self-compensation. For Mg the $\epsilon(+/-)$ transition is predicted to be lower (at 0.45 eV) but is still too deep for any ionized free-carriers to be expected. The combined PBE/PBE0 formation energy calculations show that not only is it difficult to achieve p-type conductivity in SnO_2, but that there is, in fact, no single element in the entire periodic table (excluding lanthanides not considered in this study) with which tin dioxide could be acceptor doped via Sn-site

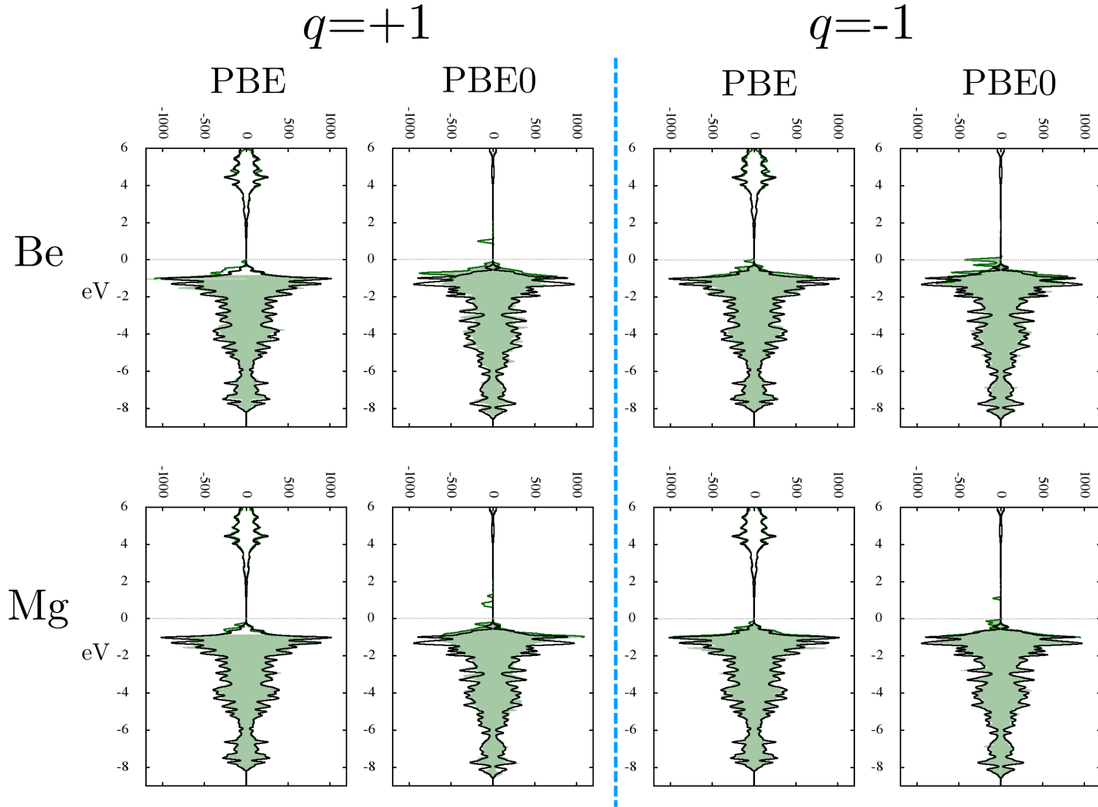

Figure 4.6. Electronic density of states corresponding to Mg and Be impurities in SnO_2. The PBE stable $q = -1$ charge state (two left side panels) and the PBE0 stable $q = 1$ charge state (two right side panels) when the Fermi level is at the VBM is shown. Black solid line shows the DOS of pure SnO_2, with the Fermi level of the pure SnO_2 crystal aligned to zero. Green solid line shows the DOS of the doped system, with shaded area indicating the occupied states only.

substitution.

4.1.5. Electronic structure

The electronic structure arising from doping by substitution was closely investigated for every element considered throughout this work. We separated all n-type dopants into three categories based on their DOS as described in the previous section and condensed in Fig. 4.3. Left panel on Fig. 4.7 compares the electronic structure of tantalum doped SnO_2 with the undoped case by showing the band structure around the high-curvature directions of the conduction band minimum. The highly-dispersive CBM of SnO_2 is responsible for the high mobility of electron carriers in this material, thus, changes around the CBM could have a large impact on the conductivity, especially when no other defect states arise. The BANDUP [196, 197] code was used to unfold the Ta-doped (supercell) electronic structure (green) for direct comparison with the undoped case (orange). Here, PBE results are shown.

Our calculations indicate that tantalum doping preserves the features of SnO_2 and

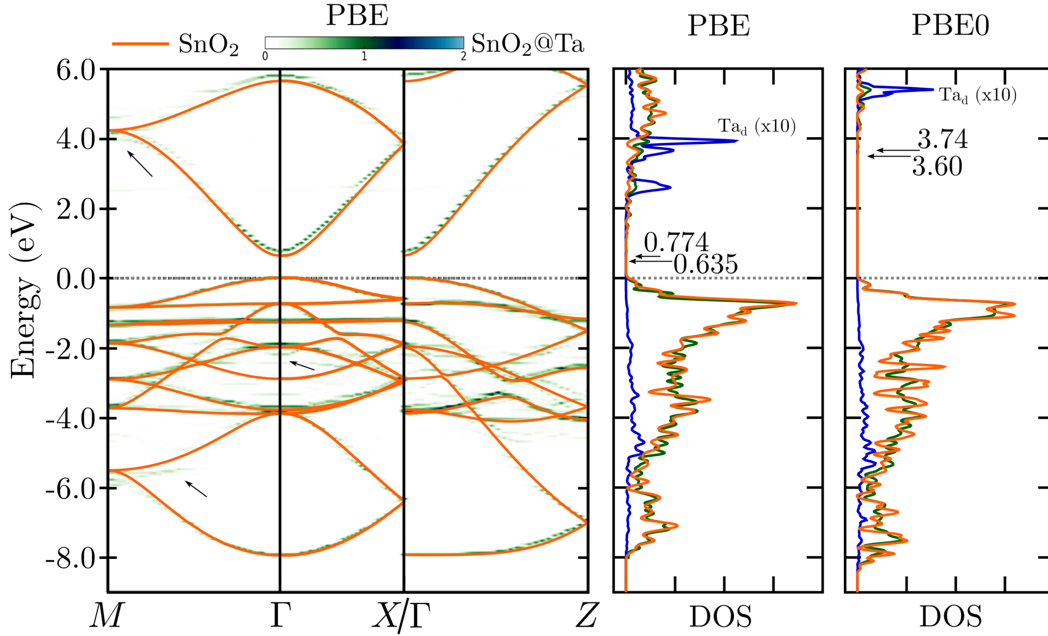

Figure 4.7. Left panel: PBE electronic band structure of SnO_2 (orange) and SnO_2 doped with tantalum (green) for the $q = 1$ charge state. Center and right panels: corresponding DOS calculated with PBE and hybrid-functionals. The partial DOS of Ta-d states (x10) are shown by solid blue lines. Band gaps are indicated for the undoped and the doped cases in both PBE and PBE0. The VBM of SnO_2 was aligned to zero (dashed gray line) in all plots.

a close inspection of the electronic structure reveals the most prominent effects of Ta, indicated by arrows in Fig. 4.7. Breaking of degeneracy at high symmetry points is seen, for example the in-plane dispersion from $M \rightarrow \Gamma$ at -6 eV below the VBM and at 4 eV above the CBM. Additionally, the appearance of states, like those at -2.2 eV at Γ-points can be identified. The band splittings at 2.6 eV and at 4 eV above the CBM are clearly linked to Ta-d states, shown in the central panel of Fig. 4.7. A slight opening of the band gap upon Ta doping is also observed, with a calculated $\sim$ 140 meV change (with both PBE and PBE0). The renormalization of the gap is nevertheless not significant enough to substantially affect the optical properties, affirming the conclusion that Ta is a suitable dopant for n-type SnO_2. In agreement with our results an experimental band gap of 3.78 eV upon 10% Ta doping has also been reported [198] for thin-films of larger thickness, where bulk like properties are expected to dominate.

The two right-side panels on Fig. 4.7 compare the DOS of PBE and PBE0 functionals. Overall, the features of the electronic structure are well captured with PBE and PBE0 represents an effective rigid shift of the band gap. Similar behavior is seen for all other defects in panel (a) of Fig 4.4 identified as suitable dopants. Two notable exceptions - Br_{Sn} and I_{Sn} - are seen to introduce a localized occupied defect state close to the valence band maximum. These defect-states are shifted deeper into the band gap using PBE0 level of theory, however, remain shallow enough to not be significantly detrimental to the optical transparency given the large electronic band gap of n-doped SnO_2. Furthermore, occupied defect-states could only act as scattering centers, but should not be expected

to act as electron traps.

4.1.6. Discussion

We conducted a thorough investigation of Sn-site substitutional dopants in rutile SnO_2. Only 6 elements – P, I, Ta, As, Nb and Sb – are predicted to dope SnO_2 n-type while preserving its good optoelectronic properties. Tungsten is also predicted to act as a free-carrier donor, yet likely at the cost of mobility. In contrast, we show that there exists no single element in the entire periodic table (excluding lanthanides and noble gases not examined in this study) that can dope SnO_2 p-type via Sn-site substitution. We compared our results with the relevant literature on SnO_2 and found that many of the suitable dopants identified in the study have been previously synthesized experimentally. We find our predictions to be in good agreement with experiments, providing consistent explanation for the observations seen. We, therefore, conclude that iodine doping could also significantly improve carrier concentrations of SnO_2 if grown under suitable experimental conditions (such that Sn-site substitution is favored).

As the work was built on a parameter-free, well-converged study of defects that showed good agreement with experimental results, we have to unfortunately conclude that the limits of electrical conductivity via cation doping in crystalline SnO_2 have been reached. While some elements like iodine or niobium will only reach self-compensation at Fermi levels deep inside the conduction band, all of the elements are expected to stop providing free carriers at a few hundred meV above the CBM. This indicates, that novel approaches would be required to bring earth-abundant crystalline oxides into competition with indium based materials.

4.2. Case B: Tin Monoxide

Tin monoxide (SnO), the *less coveted brother* of the well established n-type transparent conductor tin dioxide (SnO_2), has recently recaptured the attention of the scientific community due to its p-type properties and the promise of ambipolar doping [132, 149, 150, 199, 200]. The layered crystalline structure of SnO results in a fundamental band gap of only 0.7 eV [200]. Yet, its indirect nature implies a much larger optical gap of 2.7 eV [200, 201] – close to the requirements for transparency in the visible spectrum. As a consequence, this oxide material shows potential for diverse applications, such as novel optoelectronic devices, thin film transistors (TFT), thermoelectric devices and transparent flexible circuits [202–206]. Moreover, a methodology for harvesting single monolayers of optically transparent semiconducting SnO from an interfacial oxide layer of liquid tin has recently been demonstrated and used to fabricate a p-type field-effect transistor [207].

Oxide semiconductors offer advantages over amorphous silicon in use for TFTs as they are generally more uniform and can be used with established methods for large-area and low temperature deposition [208]. However, p-type channel oxide materials have proven elusive with the family of Cu_2O-based materials garnering most of the attention. While hybridization of Cu-d and O-p orbitals allows for p-type conductivity, difficulties with generating appropriate hole densities and mobilities remain [209].

The existence of ambipolar semiconductors, materials that can exhibit both *p*-type and *n*-type behavior within a single phase, suggests an alternative route to attaining *p*-type conductivity in transparent materials. Acceptor doping of a transparent conductive oxide that exhibits native *n*-type character, such as SnO_2 and ZnO, would not only result in a transparent *p*-type conductor, but would allow for the first fully transparent *p*-*n* homojunction to be realized. Synthesizing such homojunctions is crucial for the functionality of the next-generation optoelectronics [45, 210]. Unfortunately, only limited success in creating *p*-type TCOs in such a way has been achieved, with hole concentrations in the materials remaining discouragingly low [211, 212].

In comparison, SnO has been successfully demonstrated as a transparent *p*-type TFT [205] and the possibility of doping SnO *n*-type with antimony has been shown as early as 2010 [149]. Furthermore, *n*-type doping of SnO is theoretically predicted to be beneficial for thermoelectric applications [204]. Despite this, the full range of possibilities for bipolar doping of tin monoxide remains, to this day, largely unexplored.

The ambipolar nature of SnO is explained by the ionization potential of the material (experimentally reported to lie in the range of 4.9–5.8 eV [149, 213]) similar to other *p*-type semiconductors. Unlike most Cu_2O-based *p*-type TCOs with band gaps of over 2 eV, the fundamental band gap of SnO is strikingly small and, hence, allows for an electron affinity similar to that of *n*-type conductors to be simultaneously attained. Furthermore, the sizable band dispersion around both the conduction band minimum and the valence band maximum, shown in the left panel of Fig. 4.8, result in moderate effective masses for charge carriers of either flavor [132]. In addition, a large gap of about 4 eV between the lowest and the second lowest unoccupied bands in SnO prevents strong degradation of transparency due to free-carrier absorption, when electron concentrations are increased [214]. All of the above characteristics hint towards an excellent ambipolar TCO candidate.

Previous studies using Kohn-Sham density-functional theory unanimously agree that cation vacancies, V_{Sn}, act as shallow acceptors in SnO [132, 150, 201]. Although, most authors claim this to be the source of the unintentional *p*-type conductivity, Varley *et al.* [150] point out that the shallow behavior of tin vacancies is an insufficient criteria for copious charge-carrier generation, as the high formation energy would limit the equilibrium concentration of this defect. The authors further hint that unintentional hydrogen incorporation may be key to understanding the electronic properties of SnO. Hydrogen impurities can form complexes with tin vacancies, lowering the formation energy of these defects, while maintaining their acceptor nature. The same research group was the only one to date to provide theoretical insights into external doping of tin monoxide with the aim of improving electrical properties, though only H and Sb were considered [150].

Experimentally, the story is less transparent. A link between cation deficiency and an increase in conductivity, which would support the theoretical studies above, has been reported [215]. On the other hand, cation excess resulting in Sn-metal cluster formation inside the SnO thin films was also demonstrated to lead to significantly improved *p*-type properties [202, 205]. Both yttrium and antimony doping have been reported to enhance the *p*-type conductivity of SnO by Guo *et al.* [215], while Hosono *et al.* [149] established the ambipolar nature of tin monoxide by *n*-type antimony doping. Such inconsistencies provide a glimpse into the challenging nature of high quality doped SnO

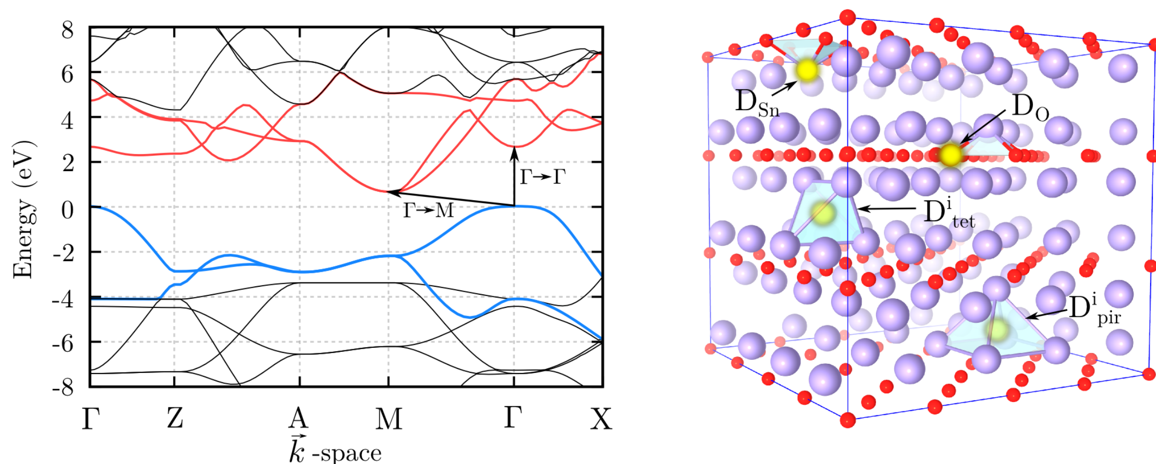

Figure 4.8. Left panel: the electronic band structure of SnO (HSE06). Arrows show the indirect($\Gamma \rightarrow$ M) and the direct ($\Gamma \rightarrow \Gamma$) band gap. Right: nomenclature for the different doping sites in crystalline SnO. Oxygen atoms are represented in red, tin atoms in light-purple, yellow spheres highlight the defect sites.

thin film production. In contrast, the advances in theoretical methodologies [2] and computational power in the past decades has made it feasible to study doped materials *in silico*. The information gained from such an exploratory work could reduce significantly the experimental efforts needed to produce n-/p-type SnO films, by guiding the material synthesis towards the subspace of elements with the most enticing properties.

Notwithstanding, computational modeling of tin monoxide posses its own challenges. Standard exchange-correlation functionals, such as the generalized gradient approximation, are known to underestimate the band gaps of semiconductors. Yet, obtaining an accurate band gap is crucial for calculating reliable defect formation energies. Furthermore, the layered structure of SnO with inter-layer interactions mediated via van der Waals (vdWs) forces is not well described by standard DFT, as dispersion interactions are not present in the exchange-correlation functionals [201].

In this work, we demonstrate that the screened hybrid HSE06 exchange-correlation functional accurately captures the band-gap and the intra-layer structure of tin monoxide. We further prove that the fundamental band gap of tin monoxide is not strongly dependent on the inter-layer distances suggesting that HSE06 establishes a suitable level of theory for calculating defect formation energies. The above knowledge is utilized to perform a thorough scan of the entire periodic table of elements in search of useful n- and p-type dopants. The success of doping and its repercussions on the structural, electronic and optical properties of SnO are discussed. This search sheds light on the possibilities of enhancing the properties of tin monoxide through targeted substitutional doping, providing a useful reference for future experiments.

4.2.1. Bulk structure

The projector augmented-wave method [95, 174] as implemented in the VASP [175, 176] code was used to perform the calculations. Structural parameters of the litharge

(P4/nmm) structure of SnO, as calculated using different exchange-correlation functionals, are summarized in Table 4.2. The PBE [75], PBE0 [81, 82], HSE06 [83, 84] and DFT-D2 as parametrized by Grimme [216] exchange-correlation functionals were tested, with calculations performed using a $k = 6 \times 6 \times 6$ Monkhorst-Pack mesh, an energy cutoff of 700 eV and Sn-d electrons included as valence states in the PAW potentials.

A clear improvement in the agreement of theoretically predicted and experimentally measured structural parameters can be noted, when moving from a generalized gradient approximation to a hybrid-functional level of theory. The intra-layer distances are captured perfectly by both the HSE06 and the PBE0 functionals. In contrast, the inter-layer distances, where vdWs interactions dominate, show little improvement and remain $\sim$3% larger than the experimental values. The DFT-D2 method, which includes approximate corrections for the dispersion forces, resulted in inter-layer distances closer to the experimental values than the hybrid functionals, but was found to over-estimate the intra-layer distances.

In the left panel of Fig. 4.8 the calculated electronic bandstructure of litharge SnO is depicted. As is typical of semi-local functionals, PBE is seen to underestimate the electronic band gap by 35 % when compared to values measured experimentally. Despite their agreement on the structural parameters, the two hybrid-functionals result in very different electronic gaps. While HSE06 improves upon the PBE values, giving excellent agreement with the experimental results, the PBE0 hybrid-functional overestimates both the indirect ($\Gamma \rightarrow M$) and the direct ($\Gamma \rightarrow \Gamma$) gaps by over 0.6 eV. Even more surprisingly while providing great improvement in the lattice parameters, the vdWs functional produces an even smaller band gap than that found with PBE. In fact, a semi-metallic band structure of SnO is predicted with a band gap of merely 0.025 eV.

Table 4.2. Lattice parameters, formation energies and electronic band gaps of SnO calculated with different exchange-correlation functionals.

	Exp.	PBE	HSE06	PBE0	vdW-D2
a (Å)	3.8011 [a]	3.867	3.801	3.800	3.842
c (Å)	4.8351 [a]	5.042	4.984	4.984	4.820
u	0.2381 [a]	0.231	0.231	0.231	0.242
E^F (eV)	-2.96 [b]	-2.59	-2.505	-2.517	–
E_G^{ind}(eV)	0.7 [c]	0.45	0.677	1.305	0.025
E_G^{dir}(eV)	2.6 [c]	1.93	2.677	3.325	2.123

[a] Reference [201] [b] Reference [217] [c] Reference [213]

In many ionic (and non-ionic) materials, including SnO_2 [14], the size of the band gap is seen to be highly sensitive to lattice vector changes. To estimate the magnitude of the error, which may arise from the 3 % change in the inter-layer distances calculated by HSE06, we investigated the dependence of the fundamental (indirect) band-gap of SnO on the lattice constants of the litharge structure. The results are summarized in Fig. 4.9. We observe that for any fixed value of the intra-layer (a) distance the fundamental band gap of SnO is almost independent of the inter-layer (c) distance. In fact, at the ideal value of $a = 3.801$ Å determined by HSE06, the band gap lies in the range of 0.67 – 0.70 eV throughout a variation of c by ± 2 %, in excellent agreement

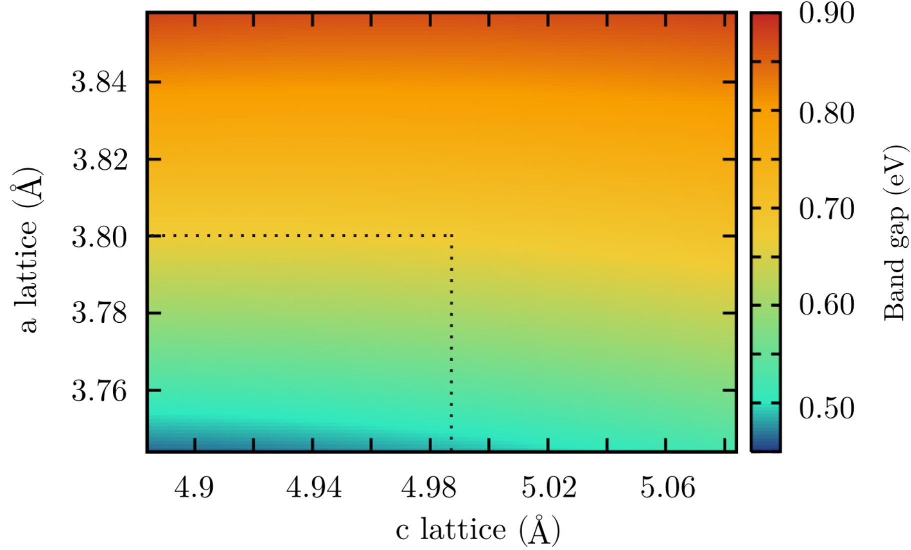

Figure 4.9. The dependence of the indirect electronic energy gap (HSE06) on the lattice parameters of the litharge SnO.

with the experimental value of 0.7 eV. Furthermore, a difference of less than 10 meV was found between the indirect band gaps obtained using the experimental lattice and the HSE06 relaxed lattice.

According to Fig. 4.9, the over-estimation of inter-layer distances by the HSE06 functional would introduce negligible errors to the band gap and, consequently, to the defect levels inside the gap. Despite this, inconsistencies in the structural parameters could still result in sizable errors. Local atomic relaxations following the introduction of a dopant element, for example, could be affected by the proximity of the SnO layers. In particular, where interstitial atoms are concerned strong inter-layer distance dependence could be expected. Such concerns will be addressed in more detail in Section 4.2.6.

4.2.2. Defect calculations

A total of 64 elements was investigated for substitutional doping in the crystalline structure of SnO, using the work-flow proposed in Fig. 4.1. Two different substitutional sites were investigated for each defect species: (i) a Sn-site, further noted as D_{Sn}, where D stands for the defect species; (ii) an O-site, further noted as D_O. Two additional interstitial sites were checked for atoms identified as suitable dopants in the substitutional sites, namely: (iii) a site in the middle of a pyramid formed by five Sn atoms, further noted as D^{i}_{pir}; and (iv) a site in the middle of a tetrahedron formed by four Sn atoms, further noted as D^{i}_{tet}. The four defect sites considered throughout the work are shown in the right panel of Fig. 4.8.

A 192 atom supercell (4×4×3) of SnO was used for all defect calculations performed in the study, corresponding to a defect concentration of ∼0.5 %. All supercell calculations performed using a single Γ-point were spin-polarized. The supercell lattice parameters were fixed to those of the expanded primitive cell and the atomic positions were allowed to relax until the forces on the atoms were below 0.002 eV/Å. Defect formation energies

were calculated using Eq. 3.4 and the methodologies explained in Chapter 3. For each defect charge states $q = -1$, $q = 0$ and $q = 1$ were considered. Elements identified as shallow dopants were checked for higher stable charge states in the cases where filled states at the CBM were found for donors or empty states at the VBM were observed for acceptors. In the pre-screening step, only impurities resulting in localized defect states inside the fundamental (and not the direct) band gap were eliminated.

All HSE06 formation energies reported throughout this work were calculated by compressing the PBE-relaxed defect structures to the HSE06 lattice constant. No further HSE06 atomic relaxations were performed. A test of the influence of HSE06 relaxations on a subset of defects revealed them to be negligible on the calculated thermodynamic transition energies (see Appendix C). Additional correction terms included a potential alignment term and an anisotropic electrostatic correction term for all charged defect calculations. The electrostatic correction terms applied were evaluated using the approach proposed by Kumagai and Oba [140] as implemented in the PYCDT code [128]. For shallow donor/acceptor elements an electrostatic correction was added to all charge states exhibiting shallow behavior (including the charge neutral calculations).

Estimation of the electrostatic correction term requires the evaluation of the static dielectric constant of SnO. Both electronic (and ionic) contributions of the dielectric constant were evaluated using the PBE functional. The values $\epsilon_{\parallel} = 7.405(15.054)$ and $\epsilon_{\perp} = 6.739(5.221)$ were obtained. Only the electronic contribution including local field effects, was evaluated using the HSE06 functional, resulting in $\epsilon_{\parallel} = 6.974$ and $\epsilon_{\perp} = 6.096$. PBE ratios between the electronic and ionic contributions were then used to estimate the ionic contribution for HSE06, resulting in the values $\epsilon_{\parallel} = (14.177)$ and $\epsilon_{\perp} = (4.722)$. Our estimated average dielectric constant of 17.7 is within the range of experimentally reported relative permittivities of 15-18.8 [218, 219]. We note, that at such large sizes of the supercell and values of the average dielectric constant the final results are not strongly sensitive to the exact value used for the dielectric constant. A change of $\sim$23 meV in the electrostatic charge correction was calculated for the singly ionized and $\sim$81 meV for the doubly ionized cells, when the dielectric constant was replaced by the lower bound experimental value of 15.

Chemical potentials $\Delta\mu_O$ and $\Delta\mu_{Sn}$ are bound by SnO stability and limited by the possibility of oxidation into SnO_2. These two criteria (summarized in the equations underneath) require $\Delta\mu_O$ to lie below the difference between the formation enthalpies of SnO_2 and SnO.

$$\begin{aligned} \Delta\mu_{Sn} + \Delta\mu_O &= \Delta H^F(\mathrm{SnO}) \\ \Delta\mu_{Sn} + 2\Delta\mu_O &\leq \Delta H^F(\mathrm{SnO_2}) \end{aligned}$$

Using enthalpy values calculated with the HSE06 functional we find $\Delta\mu_O = -2.7$ eV and $\Delta\mu_{Sn} = 0.2$ eV. The positive (unphysical) chemical potential of Sn is consistent with the experimental observations that SnO is metastable with respect to decomposition into SnO_2 and metallic Sn at high temperatures [220]. As a consequence, the chemical potentials were set to $\Delta\mu_{Sn} = 0$ and $\Delta\mu_O = \Delta H^F(\mathrm{SnO_2})/2 = -2.6$ eV, i.e. the intersection between metallic Sn and the stable SnO_2 phase, following the approach of Ref. [201]. For all other dopant species i the chemical potential, μ_i, was evaluated using the stable crystalline elemental phase. Secondary phase formation was considered only

for those elements that were identified as successful substitutional dopants. Structural information pertaining to all the phases used in determining the chemical potentials is listed in Appendix A.2.

The Fermi level was regarded as a free parameter throughout the majority of the work, reflecting the *n*- or *p*-type environments in SnO. For impurity atoms deemed as useful dopants, however, the Fermi level was also evaluated self-consistently, according to the approach described in Section 3.5.2, and used to obtain equilibrium defect and charge carrier concentrations.

4.2.3. Analysis of *p*-type dopants

The PBE pre-screening results for *p*-type dopants in tin monoxide are summarized in Fig. 4.10. Geometric shapes identify the stable substitutional site of each element, while the color of the geometric shape shows the ionization state of the defect on this site. Here, the Fermi level is fixed at the valence band maximum. Acceptor doping is achieved if the impurity atom is negatively charged under these conditions (identified by a blue color in Fig. 4.10). Although no elements were found to act as acceptors for Fermi levels at the valence band maximum (i.e. degenerate *p*-type conductivity could not be achieved), six defect species showing promising shallow acceptor behavior were discovered. These impurities – Li, Na, K, Rb, Cs and Ag – highlighted by a dashed outline in Fig. 4.10 were found to result in an unoccupied perturbed host state, with no localized electronic defect states within the fundamental band gap. Similar to the activation energy of 96 meV reported experimentally for the tin vacancy [149], the ionization levels for these proposed acceptors evaluated with the PBE level of theory were estimated to lie within 100 meV above the VBM.

In addition to the elements above, the charge states of the less favorable substitutions (indicated in Fig. 4.10 via small colored circles), revealed that Os_O and In_O should also result in hole generation. Unfortunately, for both of these elements even under Sn-rich growth conditions O-site substitution is found to be extremely unfavorable when compared to Sn-site substitution. An extra 1.7 eV is required to form Os_O and an extra 4.2 eV to form I_O. We can hypothesize that apart from sophisticated chemical growth techniques, allowing for targeted site substitution, *p*-type doping with these two elements would be exceedingly challenging to achieve in practice. In particular, if reactive methodologies that are important for large scale thin-film deposition, such as sputtering, were used.

We note that the majority of the elements seem to favor the substitutional Sn-site, D_{Sn}, marked by triangles in Fig. 4.10. However, for some atoms, shaded in light-gray in Fig. 4.10, Sn-site substitution could not be successfully stabilized. For this subset of elements, strong local atomic relaxations following the introduction of the defect lead to structural environments that should be more aptly regarded as defect complexes. The lightest of these elements – hydrogen – when substituted for tin moves out of the central four oxygen coordinated position (shown in Fig. 4.8) and forms instead a single O-H bond with one of the neighboring oxygen atoms. The calculated bond length in the stable charge state was found to be 0.98 Å, comparable to the bond length of 0.97 Å in an H_2O molecule (obtained from a reference phase calculation). The resulting defect, therefore, resembles more closely a hydrogen interstitial neighboring a tin vacancy, than

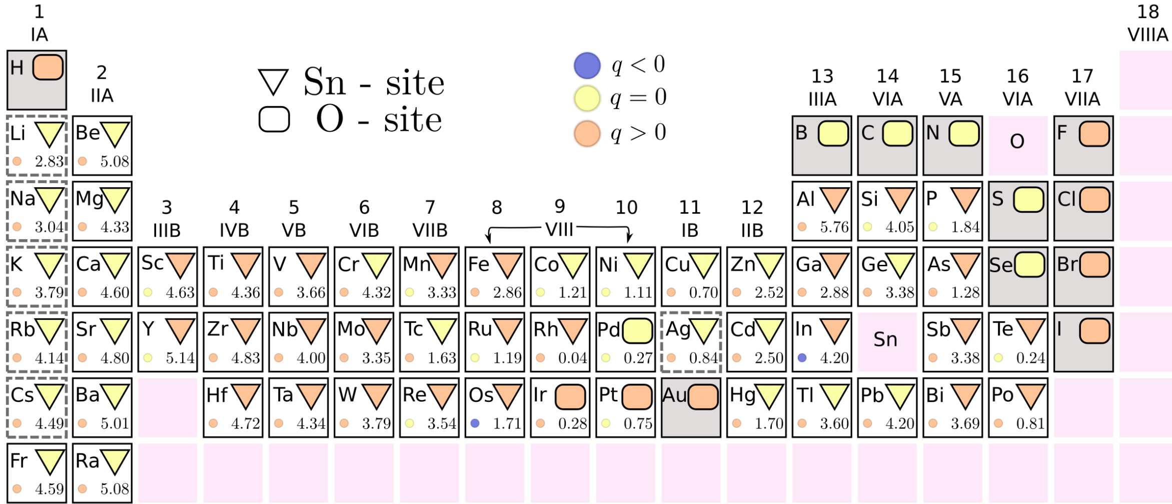

Figure 4.10. PBE pre-screening results for p-type dopants in SnO. Geometric shapes indicate the energetically favored substitution of the two sites available. D_{Sn} site is marked by a triangle, D_O - by a rectangle. The color of the shape indicates the charge state (stable when the Fermi level is at the VBM): rose - positive, yellow - neutral, blue - negative. For each element the energy difference (in eV) between the two substitutional sites is indicated in the bottom right corner. The stable charge state of the alternative site is indicated by the small colored circle. Elements with thermodynamic transition levels to an acceptor state close to the VBM are indicated by a dashed outline. Elements with no stable D_{Sn} substitution are shaded in gray.

a H_{Sn}. Carbon, introduced into a tin site, rejects the tetrahedral oxygen coordination in favor of a CO_2 molecule formation, but unlike hydrogen remains in the central position. Two oxygens are acquired from the neighboring tins by breaking the corresponding Sn-O bonds, while the other two oxygens are pushed away from the defect site. The C-O bond length calculated in this configuration is 1.17 Å, akin to the distance in an isolated CO_2 molecule of 1.16 Å [221]. Boron is seen to adopt a mixture of the two atomic structures formed by carbon and hydrogen. The element migrates towards one of the neighboring oxygens, forming a bond at a distance of 1.43 Å. Simultaneously, two additional oxygens are pulled away from their respective tins, following the boron to form a borate (BO_3) type environment. These additional oxygen atoms form slightly shorter B-O bonds at a distance of 1.38 Å. For comparison, bond distances of 1.38 Å are reported for an isolated BO_3 molecule and 1.47 Å for an isolated BO_4 [222] molecule.

Intriguingly, the formation of these heavily altered local environments is still found to be energetically favored over the simple O-site substitution – for hydrogen by 0.01 eV, carbon by 0.18 eV and boron by an astonishing 5.08 eV. In all three cases, the resulting defect clusters are found to be stable in a $q = 1$ charge state at the VBM, that would counter rather than enhance p-type conductivity.

The remaining atoms that fail to form Sn-site substitutions (halogens, chalcogens, nitrogen and gold) are expelled from the substitutional site into the interstitial space. These configurations are more appropriately described as $(D^{i}_{pir}+V_{Sn})$ defect complexes. In all cases, the resulting atomic arrangements were found to be stable in a negative

charge state, indicating that such defect clusters could enhance *p*-type conductivity. Moreover, formation energies competitive with simple O-site substitution were observed for iodine, bromine, chlorine and gold. A detailed analysis of the cause for the energetic favoring of these clusters will be addressed in Chapter 5.

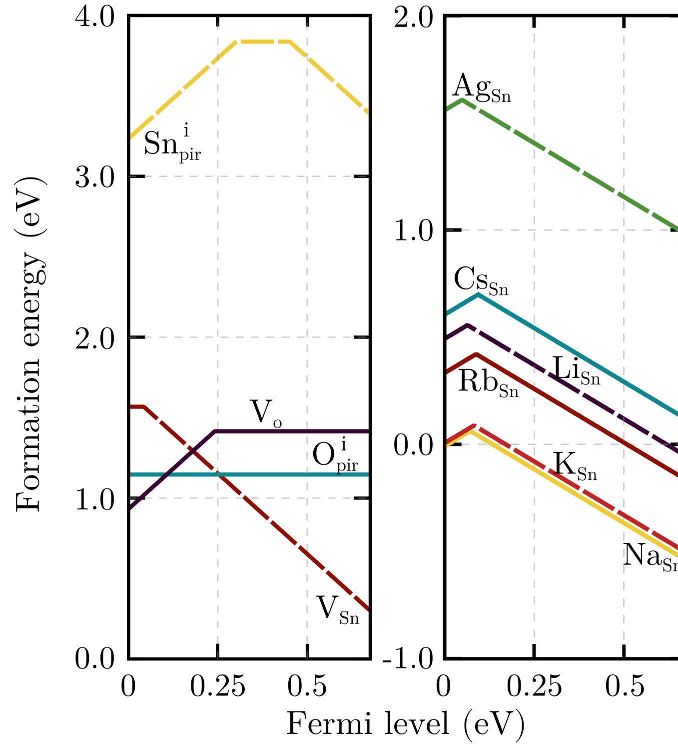

Figure 4.11. Defect formation energies as a function of the Fermi level inside the band gap of SnO (HSE06). Left panel shows intrinsic defects in SnO, right panel shows the pre-selected *p*-type dopants. Sn-rich conditions are assumed. Only the stable charge state is shown.

The acceptor character of the six substitutional elements identified in Fig. 4.10 was verified using hybrid functional level of theory. The formation energies, as a function of the Fermi level, calculated using the HSE06 functional are shown in the right panel of Fig. 4.11. All six elements are observed to retain their shallow acceptor behavior using the higher level of theory. In opposition to the PBE results, the charge neutral state is not found to be stable at the VBM using hybrid calculations, instead a direct $\epsilon(+/-)$ thermodynamic transition is seen. The shallowest transition level is observed to belong to silver at 49 meV and the deepest to cesium at 93 meV above the valence band edge. Small activation energies for *p*-type conductivity are, hence, expected with any of these dopant elements.

Formation energies of the most common intrinsic defects in tin monoxide were also calculated and are shown in the left panel of Fig. 4.11. Oxygen vacancy, V_O, formation is found to be favorable over V_{Sn} formation for Fermi levels near the valence band. In contrast, all alkali impurities are predicted to have formation energies lower than the compensating V_O defect. Our calculated $\epsilon(2+/0)$ transition level for V_O at 0.24 eV is in agreement with the study in Ref. [150]. The work of Allen *et al.* [201], using a

fitted PBE0-vdWs type functional, finds the same ionization level to be shifted below the valence band edge. This appears to be inconsistent with experimental observations that report the Fermi level of nominally undoped SnO to be pinned at 0.1-0.2 eV above the VBM [219].

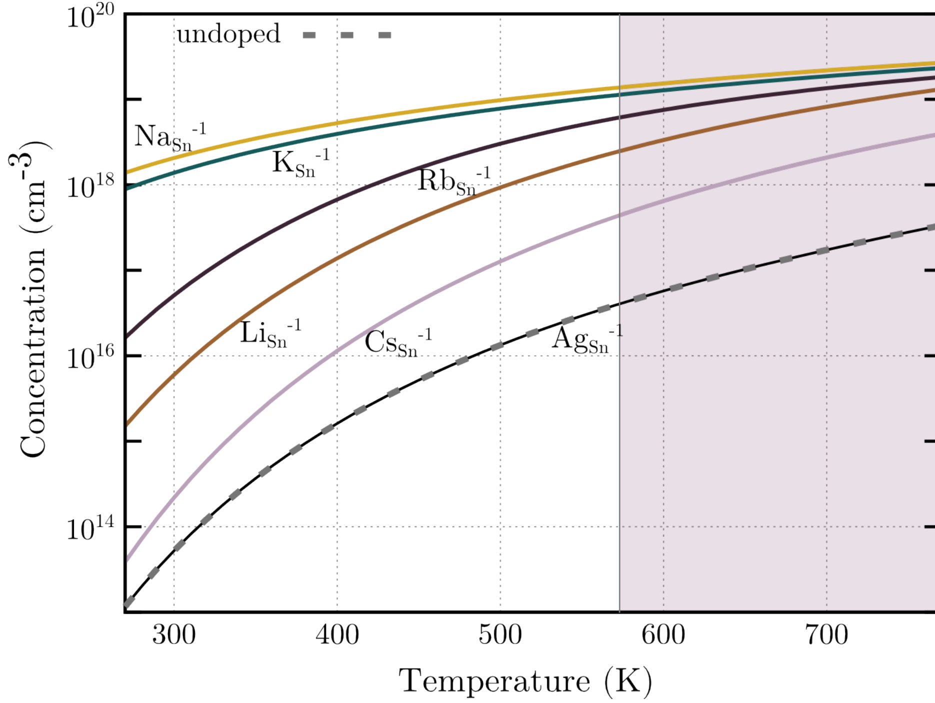

Figure 4.12. Majority carrier (hole) concentrations for *p*-type doped SnO in thermal equilibrium calculated as a function of temperature. The undoped film hole concentrations are also indicated by dashed gray lines. Pink shaded area marks experimentally identified temperatures where crystallites of SnO_2 phase start emerging in SnO.

From the suggested *p*-type impurities, silver is found to require the most energy to incorporate, yet still offers formation energies competitive with the tin vacancy. In agreement with previous studies [132, 150, 201], we observe shallow defect behavior for V_{Sn}. Our reported acceptor ionization level is the shallowest, when compared to the two preceding hybrid functional studies of tin monoxide [150, 201]. We estimate the $\epsilon(0/2-)$ transition at just 40 meV above the VBM, lower than the $\epsilon(0/-)$ transition at 120 meV predicted by the work of Varley *et al.* [150], where the HSE functional with an increased 32 % fraction of the exact-exchange was employed. In Ref. [201] an even deeper (390 meV) ionization level was suggested, again appearing to be at odds with the low activation energies (<100 meV) reported experimentally [149, 219].

The alkali metals were found to have low formation energies, with exothermic defect formation predicted in *n*-type SnO for all elements, except cesium. As such, the incorporation of the alkali metals into the host lattice appears to be easily realizable experimentally. To further validate our results, we calculated the expected hole concentrations in thermal equilibrium for SnO films containing acceptor impurities together with the native defects shown in the left panel of Fig. 4.11. The resulting majority

carrier concentrations in thermal equilibrium are shown in Fig. 4.12. The region of stability for SnO, as reported in Ref. [223], is also indicated by a shaded pink area marking the temperature range in which SnO_2 phase starts appearing in SnO. Acceptor concentrations in the nominally undoped SnO due to the native p-type defect, V_{Sn}^{-2}, formation are shown for comparison as a dashed gray line. V_{Sn}^{-2} is the dominant intrinsic defect, out of those considered, in undoped SnO. Concentrations of other native defects in thermal equilibrium as a function of temperature can be found in Appendix D. In the temperature range where SnO is stable, intrinsic carriers are predicted to dominate those produced by native defects – a consequence of the small fundamental band gap of SnO and the rather large formation energies of V_{Sn}^{-2}. This suggests that the (V_{Sn}-H_i) clusters, proposed by Varley *et al.* [150], are likely responsible for the unintentional p-type conductivity in SnO, as dopant-free SnO is expected to act as an intrinsic semiconductor. For simplicity, only the p-type carrier concentrations are depicted in Fig. 4.12, though thermal equilibrium was evaluated including all the native defects from Fig. 4.11 together with each impurity. We find that all alkali metals increase the free-charge-carrier densities by orders of magnitude, when compared to the nominally undoped host. Silver, however, was observed to offer no significant improvement to carrier concentrations.

4.2.4. Analysis of *n*-type dopants

The PBE pre-screening results for n-type dopants in tin monoxide are summarized in Fig. 4.13. Analogous to p-type results, the geometric shapes identify the stable substitutional site (the Fermi level is fixed at the conduction band minimum), while the color of the shape shows the stable charge state of the defect. The light-gray shading indicates defect elements where Sn-site substitution could not be stabilized as discussed at length in the preceding section.

The formation energy of a charged defect depends on the position of the Fermi level. It follows, that a change in the energy difference between the two substitutional sites, $E^F_{D_{\mathrm{Sn}}}(q, \Delta\epsilon_F) - E^F_{D_{\mathrm{O}}}(q', \Delta\epsilon_F)$, for elements with $q \neq q'$ is seen. As a consequence, the stable substitutional site in n-type SnO may be different from p-type SnO. In fact, both ($\mathrm{Cl}^{i}_{\mathrm{pir}}$+$V_{Sn}$) and ($\mathrm{Au}^{i}_{\mathrm{pir}}$+$V_{Sn}$) defect clusters become favorable over O-site substitution, when the Fermi level is at the CBM. In opposition, C_O substitution becomes energetically favorable over the CO_2 molecule formation in the Sn-site.

Electrons are successfully donated into the host material if a substitutional element is positively charged, when the Fermi level lies at the conduction band edge (identified by a rose color in Fig. 4.13). The strict requirement of degenerate n-type doping, however, as seen from the figure would result in no suitable donors for SnO. Nevertheless, n-type tin monoxide was demonstrated experimentally by Hosono *et al.* [149] using antimony doping, with activation energies of 92 meV. The shallow donor behavior of the Sb impurities was later verified by the computational work of Varley *et al.* [150], with an estimated ionization level at 120 meV below the CBM. Given the above information, we conclude that elements with thermodynamic transition levels below the CBM but close to those of antimony could also successfully dope SnO n-type. A total of fifteen defects was identified to fall into this category. The corresponding atoms are marked by a dashed outline in Fig. 4.13.

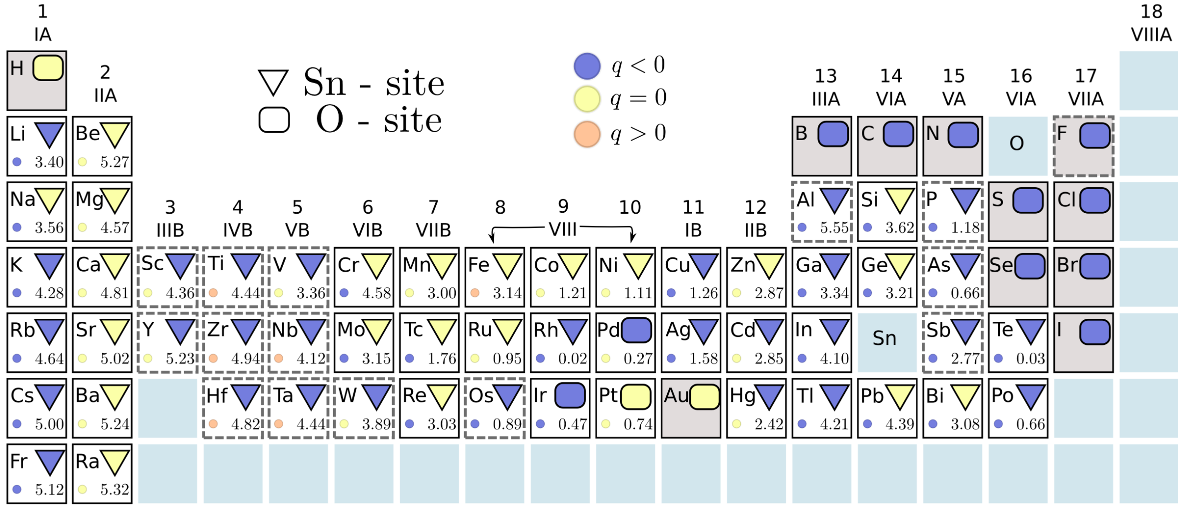

Figure 4.13. PBE pre-screening results for n-type dopants in SnO. Geometric shapes indicate the energetically favored substitution of the two sites available. D_{Sn} site is marked by a triangle, D_O by a rectangle. The color of the shape indicates the charge state (stable when the Fermi level is at the CBM): rose - positive, yellow - neutral, blue - negative. For each element the energy difference (in eV) between the two substitutional sites is indicated in the bottom right corner. The stable charge state of the alternative site is indicated by the small colored circle. Elements with thermodynamic transition levels to a donor state close to the CBM are indicated by a dashed outline. Elements with no stable D_{Sn} substitution are shaded in gray.

Most of the donor impurities selected demonstrate shallow behavior, i.e. the additional electrons are seen to occupy a perturbed host state, with localized electronic defect levels only forming above the conduction band minimum of the host [103]. Just like in the case of acceptor defects, elements that appear to be suitable donors on the less energetically favorable site were found. These include most of the transition metals in groups IV-B and V-B. However, as seen in Fig. 4.13 elements that show n-type behavior when substituting on an oxygen site, also require over 3 eV more energy to form this substitution. Regrettably, such defects would be very difficult to realize in practice and, as a consequence, were excluded from further investigations.

Formation energies of potential n-type dopants calculated using hybrid-functional level of theory are summarized in Fig. 4.14. Elements with lower formation energies are shown in the left panel of the figure, while those with relatively high formation energies are shown on the right hand side. Substitutional vanadium, Vd_{Sn}[†], is the only defect that displays a change of character (shallow to deep donor) between hybrid functional and generalized gradient approximation levels of theory. The energy required to form the neutral charge state of this element is significantly lowered by spin-polarization using HSE06. In contrast, a non-polarized ground state is found by PBE. All other elements are seen to retain their shallow donor character.

Most of the identified n-type impurities undergo a direct $\epsilon(+/-)$ transition at Fermi levels less than 100 meV below the CBM. Al_{Sn}, Sc_{Sn} and Y_{Sn} exhibit shallowest ionization

[†]Notation Vd_{Sn} is used to differentiate a Sn-site vanadium substitutional, from the tin vacancy V_{Sn}.

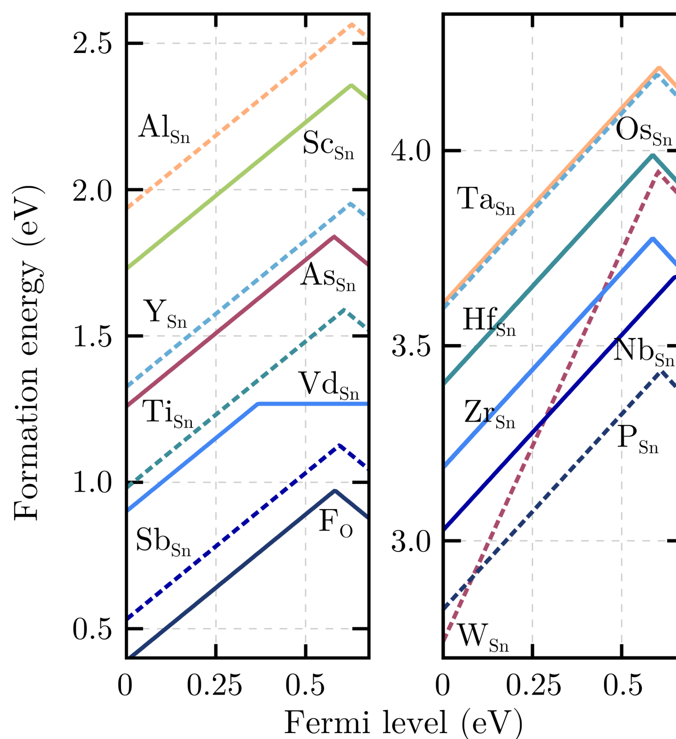

Figure 4.14. Defect formation energies as a function of the Fermi level for preselected n-type dopants (obtained using the HSE06 xc-functional). Vd_{Sn} here stands for vanadium on a Sn-site to avoid confusion with a tin vacancy. Sn-rich conditions are assumed. Only the stable charge state is shown.

levels just ∼ 50 meV below the CBM, closely followed by P_{Sn}, Ti_{Sn}, Ta_{Sn}, Os_{Sn} and W_{Sn}. All of the aforementioned defects are predicted to have thermodynamic transition levels closer to the conduction band than antimony – the only element previously reported to successfully dope SnO n-type [149]. Zr_{Sn}, Hf_{Sn}, F_O and As_{Sn} exhibit thermodynamic transition levels slightly deeper than those of Sb_{Sn} by roughly 10 meV. All of these defects are deemed likely to act as shallow donors in tin monoxide if incorporated successfully. The exact values of all thermodynamic transition levels are summarized in Table 4.3.

The thermodynamic transition from a donor into an acceptor state close to the conduction band edge suggests that, after a certain dopant concentration is exceeded, the Fermi level of the system will be pinned below the CBM. Nb_{Sn} is, notably, the only shallow donor with a stable neutral charge state: the $\epsilon(+/0)$ transition is calculated to lie only 30 meV below the conduction band and self-compensation is anticipated at 130 meV above the CBM. The shallow acceptor transition and the delayed onset of self-compensation suggest niobium as a very promising n-type dopant.

So far donor formation has only been considered in isolation, however in a realistic material different types of defects coexist. While compensation via extrinsic defects may be avoided with careful control of the experimental conditions, native defect formation is much more challenging to suppress. As seen from the left panel of Fig. 4.11, oxygen related defects do not hinder the creation of n-type carriers, but the low formation

Table 4.3. Thermodynamic transition levels for n-type dopant elements in SnO evaluated with hybrid functional theory. Values are shown in meV, as distance away from the conduction band edge. Vd_{Sn} here stands for vanadium on a Sn-site to avoid confusion with a tin vacancy.

Dopant element	(+/-)	Dopant element	(+/-)
Al_{Sn}	47	Os_{Sn}	77
Sc_{Sn}	52	Sb_{Sn}	83
Y_{Sn}	52	Zr_{Sn}	90
P_{Sn}	66	Hf_{Sn}	90
Ti_{Sn}	70	F_O	95
Ta_{Sn}	74	As_{Sn}	96
Dopant element	**(+/0)**	**(0/-)**	**(2+/-)**
Vd_{Sn}	311	-144	N/A
Nb_{Sn}	30	-130	N/A
W_{Sn}	N/A	N/A	75

energy of V_{Sn} suggests strong compensation of the donated electrons, especially in n-type SnO.

Our estimated defect concentrations, shown in Fig. 4.15, reveal that Sb_{Sn} and F_O are the only two donor elements that are dominant over V_{Sn} in thermal equilibrium. The lower formation energy of F_O, when compared to Sb_{Sn}, suggests the former to be a more effective donor. Furthermore, oxygen-poor conditions that favor F_O creation, are most appropriate for minimizing the concentration of compensating V_{Sn} defects. Unfortunately, in thermal equilibrium low defect concentrations are predicted for both of these donor impurities resulting in intrinsic carrier dominated films. For donors with even higher formation energies, holes introduced by V_{Sn} defects are expected to completely surpass the carriers introduced by the donor impurities, as is demonstrated in the case of Vd_{Sn} in the right most panel of Fig. 4.15.

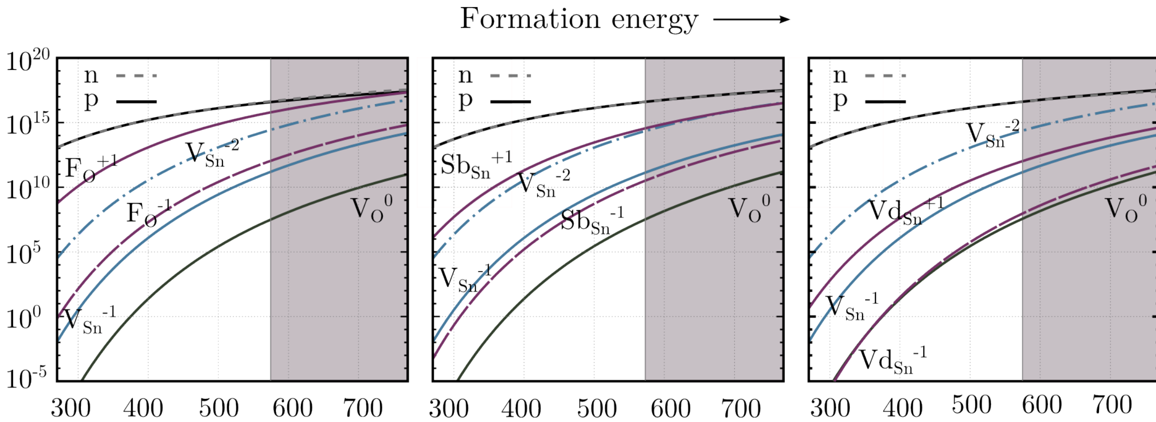

Figure 4.15. Selected defect concentrations for n-type doped SnO calculated as a function of temperature. Gray area marks temperatures where crystallites of SnO_2 phases start emerging in SnO. From left to right the formation energy of the n-type dopant is increasing.

Nevertheless, Hosono *et al.* [149] report successful n-type doping of SnO with Sb by incorporating $1.1\times10^{20}\,\mathrm{cm}^{-3}$ defects, more than ten orders of magnitude larger than our predicted thermal equilibrium values. One could, therefore, speculate that off-equilibrium deposition processes are still able to result in successful n-type doping. If formed, $\mathrm{D_{Sn}}$ defects would have to overcome an energy barrier to be able to dissociate and diffuse out of the film. The dissociation barrier for $\mathrm{D_{Sn}} \rightarrow \mathrm{V_{Sn}} + \mathrm{D^i}$ is equal to the sum between the defect binding energy and the migration barrier of $\mathrm{D^i}$. If the formation energy on an interstitial site is significantly higher than the substitutional site, the defect will not dissociate. We illustrate this with an example, using the shallowest predicted donor – niobium. The calculated formation energy of $\mathrm{Nb^i_{pir}}$ in n-type SnO with PBE level of theory is 4.032 eV. An O-site substitution, $\mathrm{Nb_O}$, is even more unfavorable at 7.245 eV. On the same level of theory, $\mathrm{V_{Sn}}$ formation requires 0.873 eV of energy and $\mathrm{Nb_{Sn}}$ – 3.059 eV. A dissociation barrier of at least 1.85 eV is therefore expected, preventing $\mathrm{Nb_{Sn}}$ from diffusing out of the material at room temperature. The possibility of interstitial incorporation for other atoms is discussed in detail in Section 4.2.6.

4.2.5. Dopants and transparency

Ample experimental studies of nano- and poly-crystalline tin monoxide report transparency of 70 % or greater in the visible range [209]. Optical properties can also be enhanced further via applied stress/strain or through external doping [13, 148, 224]. As such, the preservation of transparency may also be a relevant criteria when selecting dopants for SnO targeted towards specific applications. In this section we comment on the defect energy levels, introduced into the optical band gap via external doping, that could have a disruptive impact on the transparency of the material. Such defect levels are illustrated in Fig. 4.16 for all acceptor and donor impurities found. We note that the folding of the band structure – a by-product of the large supercell size used – introduces energy states below the first conduction band of tin monoxide at Γ. Such states in regions more than ∼ 2 eV above the valence band maximum (indicated by dark blue in Fig. 4.16) arise from indirect conduction band edges. A newly incorporated defect state in this energy range is, therefore, challenging to distinguish from the host states. Such distinction was not attempted in this work and we focus our attention only on the region up to 2.1 eV inside the optical band gap.

We observe that six out of the fourteen n-type defects (vanadium is concluded not to be an effective dopant) introduce defect states outside of the fundamental band gap, but close to the mid-region of the direct optical ($\Gamma \rightarrow \Gamma$) gap of SnO. A likely ramification of such defect states are color centers, which could negatively effect the transparency. Upon zirconium doping, states inside the fundamental band gap are seen to emerge. The close proximity of the defect states to the valence band edge suggests that they would not play a significant role in optical absorption, if only direct $\Gamma \rightarrow \Gamma$ transitions were considered. Nevertheless, defect states near the valence band edge at Γ lie close to the middle of the direct $\mathrm{M} \rightarrow \mathrm{M}$ gap. In a similar fashion to Zr, tin monoxide doping with Ta, Hf and Nb would trigger defect state formation in the neighborhood of the valence band, closing the transparency window at the M point. Fortunately, four of the n-type dopant elements – $\mathrm{F_O}$, $\mathrm{P_{Sn}}$, $\mathrm{Sb_{Sn}}$, $\mathrm{As_{Sn}}$ – are observed to result in a mostly unaltered host band structure. These elements are suitable candidates for synthesizing

a transparent n-type SnO.

In the case of acceptors, doping with Ag_{Sn}, Li_{Sn} and Na_{Sn} induces defect state formation deep inside the optical band gap at Γ. Just like in the case of donors, such unoccupied defect states are likely to be detrimental to optical transparency. The three heavier alkali metals are seen, however, to create no defect states inside the optical band gap of SnO and leave the host bandstructure unaltered upon incorporation. These three substitutional defects – K_{Sn}, Rb_{Sn} and Cs_{Sn} – are excellent candidates for enhancing the number of free-charge-carriers, while simultaneously maintaining the transparency of p-type tin monoxide in the visible range.

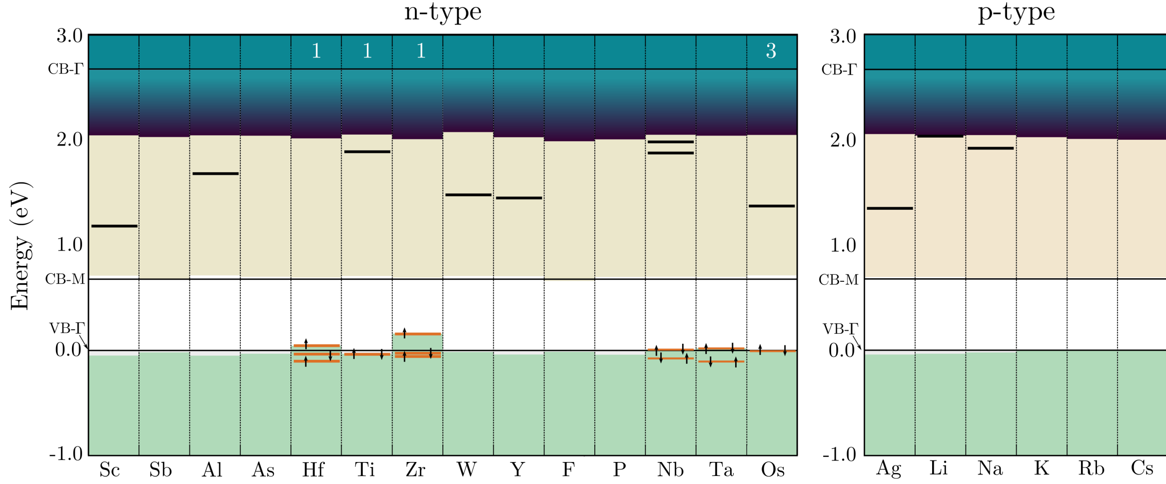

Figure 4.16. Mid-gap electronic defects states of dopant elements in SnO. For donors a charge state of $q = +1$ is shown, except for tungsten ($q = +2$). For acceptors a charge state of $q = -1$ is shown. Black lines indicate the energetic positions of defect states. For defect states close to the valence band their occupation by spin is shown. Changes in valence and conduction band edges (after band alignment) of the host upon doping are indicated by the edges of the light green and sand colored areas, respectively. Bright blue areas show the onset of the region below the optical band gap edge in which electronic defect states could not be distinguished. Differences in the spin channel occupation, for structures where spin polarized solutions were found, are indicated by the numbers at the top of the chart.

4.2.6. Effects of vdW and interstitials

As was outlined in previous sections, the layered structure of tin monoxide is held together by dispersion forces that are not accounted for in standard DFT functionals. In Section 4.2.1 we demonstrated that the intra-layer distances are captured remarkably well by HSE06 (as well as PBE0) but the shortcomings become apparent in the inter-layer distances – approximately 3 % shorter than the experimental values. Despite the correct representation of the band structure by the HSE06 functional (evidenced by Fig. 4.8), questions pertaining to structural relaxations remain. For a substitutional defect, even with significant reduction in the distances between the layers, strong changes

are unlikely to result. The much greater proximity of the atoms within the layer suggests they should account for the majority of local relaxations. On the other hand, for interstitial defects the separation between the layers is anticipated to play a role.

Consequently, the PBE (and HSE06) functionals are speculated to perform poorly in evaluating the energetics of interstitial defects. Unfortunately, as shown in Table 4.2, the vdW-type functional produces a semi-metallic SnO band structure and, thus, does not offer an improved description. Erroneous electronic structure could equally result in inaccurate atomic forces and hence incorrect geometries. The almost non-existent band gap also rules out the possibility of using such a functional to obtain reliable formation energy information. These issues prevent us from performing a *sensible* pre-screening for interstitial dopant elements in SnO.

Nonetheless, the layered nature of tin monoxide offers plenty of space for interstitial incorporation. These alternative defect sites could be competitive with the substitutional locations investigated in this work. The energetics of such interstitials are, therefore, significant when considering paths to successful doping of tin monoxide. To support our assertions of having found useful *p*-type and *n*-type dopants we investigated the interstitial positions of those elements using PBE only. The results provide insights on the competition between substitutional and interstitial sites for a given element.

Amongst *n*-type impurities, Os_{Sn} was the only element with competitive interstitial incorporation. In a *p*-type SnO we found the substitutional site to be more stable, however in *n*-type SnO the interstitial location is favored by 60 meV. The close competition between the substitutional and interstitial sites makes this element unsuitable for doping. All other donors presented were found to be stable on the substitutional site. The lowest relative interstitial energies were calculated for the fluorine atom, requiring an extra 450 meV of energy, and tungsten, requiring an extra 650 meV for interstitial incorporation. The rest of the interstitial defects were found lying over 1 eV higher in energy than the corresponding substitutional sites. The elements for which interstitial incorporation was found to be extremely unlikely were Al (3.75 eV more energy), Y (3.28 eV) and Sc (2.26 eV). In view of these results, it is reasonable to conclude that even if large discrepancies in the calculated formation energies arose from the PBE functional, the *n*-type dopants would still favor substitutional sites.

Most of the donor impurities exhibit amphoteric behavior when incorporated on interstitial sites, i.e. act as compensating defects to the majority free-carriers in both an *n*-type and a *p*-type doped material. However, some exceptions are present. On the PBE level of theory we observe Sb^{i}_{pir}, C^{i}_{pir}, P^{i}_{pir}, F^{i}_{tet} and Y^{i}_{pir} to show shallow acceptor behavior. This may offer a potential explanation for the experimental reports of *p*-type properties in SnO enhanced by both Sb and Y doping [215]. However, one needs to keep in mind that the interstitial incorporation is predicted to be extremely unfavorable > 3 eV for Y^{i}_{pir} and ~ 2 eV for Sb^{i}_{pir}.

Silver was the only acceptor found to be more stable in the interstitial site by 550 meV, and the only acceptor found to favor the tetrahedral rather than the piramidal interstitial site. The Ag^{i}_{tet} was predicted to act as a shallow donor by PBE, countering the desired *p*-type conductivity. The preference of silver to form interstitials, as well as its hefty market value, makes this element unlikely to be a useful dopant. Substitution on a Sn-site was seen to be the most energetically favored position for all alkali metals. The smallest energy difference of ~ 1 eV was found between the Li_{Sn} and Li^{i}_{pir}. This

energy divide was observed to increase with the size of the alkali metal, with cesium interstitial found to be over 3 eV more expensive to create than the substitution. The alkali metals incorporated on the interstitial sites were seen to act as electron donors with $\epsilon(0/+)$ transition levels 100 meV below the conduction band. This suggests that dopant elements incorporated on the wrong site would act as compensating centers and should be mitigated.

4.2.7. Discussion

In this work a thorough search of useful dopants in SnO aimed at improving the conductivity of the material was presented. The affinity of an element for donating free-carriers when incorporated as a substitutional defect was assessed for every atom in the periodic table. The stability of the substitutional defects, established as useful, was compared with alternative defect locations, eliminating the elements that are not likely to be stable dopants. In this way, five alkali metals – Li, Na, K, Rb and Cs – were identified as prospective *p*-type carrier generators. Furthermore, thirteen elements acting as shallow donors – eight transition metals: Sc, Y, Ti, Zr, Hf, Nb, Ta, W as well as As, Al, P, Sb and F (the only O-site dopant) – were found suitable for enhancing charge-carrier concentrations in *n*-type SnO.

After a close inspection of the optical properties of doped tin monoxide, we further verified that both *n*- and *p*-type conductivities could be improved by doping without detrimental repercussions to transparency. Three of the heavier alkali acceptor impurities (K, Rb, Cs) were observed to result in free-carrier generation without altering the bulk band structure. The same conclusions were drawn for P, Sb, As and F electron-doped SnO films. Our considerations of interstitial incorporation point towards interstitial elements commonly acting to counter/compensate the carriers donated by the substitutional defects of the same species. Consequently, such off-site defect incorporation should be strictly avoided if doping is to be successfully achieved. Defects with most unfavorable interstitial incorporation were identified as the heaviest alkali metals (for *p*-type dopants) and Al, Y, Sc for (*n*-type dopants).

Our methodology shows results in good agreement with previous studies of the native defects in SnO using the same level of theory and is in line with the experimental findings on both *p*-type and *n*-type SnO. The large variety of potential dopant elements (not yet experimentally explored) discovered through this study, demonstrates tin monoxides' potential for high technological relevance. The strong agreement between our results and previous studies hints that many of the doped SnO variants suggested could be physically synthesized.

4.3. Common Trends

Some interesting observations can be made by comparing the doping trends among the two stoichiometries of tin oxide. First, less donor elements have been predicted for tin monoxide in the initial PBE pre-screening step than for tin dioxide. Even though intuitively the lower Sn(II) oxidation state, when compared to Sn(IV), suggests more substitutional elements in the periodic table should have higher oxidation states and

thus be available for electron-doping, such as Sc, Y, Ti, Zr and Hf, etc. However, we observe that impurities which differ too greatly in their valence from Sn(II), such as Re and Mo, do not offer any free-carrier generation. The same behavior is observed for halogen substitutionals predicted to act as donor impurities in SnO_2. Sn-site halogen substitutions could not be stabilized in our investigations of tin monoxide. This indicates that when utilizing halogen dopants only phase-pure SnO_2 crystals should be used that contain no admixture of SnO. In contrast, all transparent donors (P, Sb, As and F) in SnO appear to be able to also dope SnO_2 successfully. Finally, tin monoxide was observed to be the only stoichiometry that permits *p*-type doping via impurity incorporation – a result that seems to be a consequence of the strikingly different ionization potentials [149, 213] of the two compounds.

5 Defect Complexes

In the preceding chapter we demonstrated that impurity incorporation is a powerful tool for enhancing the properties of perfect crystalline systems. Unfortunately, real bulk materials are rarely pristine and growing flawless crystals is challenging. As a result, typical materials contain sizable amounts of both native and extrinsic imperfections. Such imperfections can play a dominant role in the properties of a material, as exemplified by both tin dioxide, where unintentional n-type conductivity is observed, and tin monoxide, where unintentional p-type conductivity is reported. Thus, simply addressing defect behavior in isolation is not always sufficient and investigating how incorporated impurities might interact with other defects already present is the system can be truly informative.

In this chapter, we will study SnO_2 and SnO, previously screened for useful substitutional dopants, and demonstrate how their attributes can be altered further by introducing impurity atoms that interact with the most abundant native defects. Successfully improving the properties of a material via defect complex engineering is substantially more challenging than simply selecting isolated dopants. In order to form complexes, defects not only need to incorporate into the material easily, but further result in strong binding energies that stabilize the complex, and have favorable migration pathways that allow the complex to form. The pre-screening step utilized in the previous chapter is eliminated, here, and all calculations are performed using a hybrid functional level of theory only. This is crucial for addressing defect complexes, as local atomic environments surrounding the defects are key to the stability and bond formation of the complex.

In the first case study, we return to tin dioxide, SnO_2. It has been experimentally observed, by our collaborators at EPFL, that optical properties in Sn-based transparent conductive oxides (TCOs) are improved significantly when co-doped with silicon. The same behavior was identified both in the case of amorphous zinc-tin-oxide (ZTO) and in rutile SnO_2. Yet, the mechanism responsible for this improvement could not be uncovered from experimental observations alone. Although optical absorption within the band gap of these oxides has been linked to intrinsic oxygen vacancies, suppressing the presence of the vacancies alone does not seem to recover the same behavior. In our study we investigate the interaction of silicon with these native defects and elucidate the origins of the experimental observations.

The second case study is tin monoxide, SnO. As we have seen in the previous chapter, certain impurity elements in SnO could result in complex formation. Here, these defect

Research presented in this chapter was adapted with permission from: Rucavado E., Graužinytė M., *et al.*, J. Chem. Phys. C **122**(31), 17612-17620 (2018) Copyright © 2018 American Chemical Society (ACS Authors Choice).

complexes are studied in detail and their promise to further increase p-type conductivity in tin monoxide is demonstrated. We will show that this intriguing behavior is enabled by the double valency of tin that permits highly charged native tin vacancies to be created, which can then be stabilized by impurity incorporation.

5.1. Case Study A - Silicon in Sn-based Oxides

Optoelectronic properties of tin dioxide can be tuned over a wide range of conductivity and transparency and can, hence, be adapted to the requirements of a variety of technologies from smart windows to batteries and solar cells. For example, reported electrical conductivity values span from $\sim 10^{-6}$ S† cm^{-1} [225] to 10^4 S cm^{-1} [226]. This is achieved by tuning the density of oxygen deficiencies, V_O, or by adding dopants, as demonstrated in the previous chapter and explored experimentally [45, 148, 155, 227, 228]. Other elements may be added to modify the microstructure and thermal stability [229]. In that regard, the addition of zinc to SnO_2 to create ZTO yields thin films with attractive properties such as a total transmittance higher than 75 % in the visible and near-infrared spectral range [230–232] and an amorphous microstructure when deposited at room temperature, which is preferable for applications in flexible and organic devices [233]. Furthermore, this microstructure remains stable up to temperatures as high as 550°C [23, 232]. Due to these properties, ZTO has already been applied as a transparent contact in organic light emitting diodes (OLED) [233, 234], as a channel in thin film transistors (TFT) [235, 236] and as a recombination layer in silicon-perovskite tandem solar cells [237].

Theoretical and experimental evidence suggests that the presence of oxygen deficiencies, V_O, in ZTO creates both shallow and deep subgap states, with the latter acting as absorption centers in the visible part of the spectrum [232, 238, 239]. Even though these defects can be passivated by post-deposition treatments in air at temperatures greater than 400°C [232], annealing in these conditions is thermally costly and/or not convenient for devices with low thermal budgets, such as solar cells based on thin hydrogenated amorphous silicon layers or hybrid organic-inorganic perovskite materials [240–242].

Alternatively, previous investigations have shown that the co-deposition of silicon dioxide, SiO_2, with different transparent conductive oxides (mainly ZnO) may decrease the density of V_O defects [243–246], but also lower the refractive index [243, 247], decrease the resistivity [247–249] and amorphize the TCO [248, 250, 251]. For the case of Si in Sn-based TCOs, Kang and coworkers [246] used first-principle calculations to suggest that silicon atoms alter the coordination number of Sn, leading to an increase in the formation energy of V_O deficiencies. Yet, this passivation mechanism would lead to a strong decrease in electrical conductivity as these deficiencies are also the source of the free-carriers.

Furthermore, it was recently proposed that Si modifies the band gap of ZTO, resulting in improved TFT performance [252]. However, the role of Si in the subgap structure of ZTO was not fully clarified at the atomistic level in this study. In contrast to previous reports, we use computational techniques informed by experimental observations to explain the effect of Si on the optoelectronic properties of SnO_2-based

†Siemens is an SI unit used to measure conductance. $S = \Omega^{-1}$ with units ($kg^{-1}m^{-2}s^3A^2$).

materials. Our experimental colleagues demonstrate that adding SiO_2 during deposition of Sn-based TCOs (using ZTO and SnO_2 as case examples) results in a decrease of subgap absorption, while keeping electrical properties unchanged. Simultaneously, we use density functional theory (DFT) calculations to bring insights into this intriguing behavior. Combining experimental results and theoretical predictions we found that, while the oxygen from SiO_2 passivates deep sub-gap defects, the addition of Si decreases the ionization energy of V_O and shifts the corresponding subgap defect states close to the conduction band minimum. Thanks to this effect, the defect no longer contributes to the formation of detrimental subgap absorption centers and provides free-carriers.

5.1.1. Experimental basis

Our experimental colleagues at EPFL demonstrated that properties of tin-based oxides can be altered by tuning the oxygen content in the material. To this end, the absorption and conductivity of ZTO films was studied as a function of O_2 flow during deposition. It was observed, that a low O_2 flow results in low conductivity and high optical absorption in the measured spectral range. Initially, increasing the O_2 content improves the film transparency and conductivity, reaching a maximum value of 456 S cm^{-1}. Increasing the O_2 flow further reduces the optical absorptance, but at the expense of conductivity, which drops by 62%. A trade-off often observed in TCOs is reached: improving the optical properties worsens the electrical ones and vice versa. Indeed, analogous behavior was also observed for pure thin films of SnO_2. Thus, optimizing the oxygen flow during deposition does not yield a film that combines a conductivity above 400 S cm^{-1} and a low absorptance at 500 nm ($\leq$ 5%). Alternative approaches are, hence, required to control the amount of oxygen in the films and to ensure both high conductivity and transparency.

To introduce oxygen into Sn-based TCOs in a precise manner, while avoiding high temperature steps [232], ZTO or SnO_2 were co-sputtered with SiO_2. The undoped ZTO/SnO_2 film with highest conductivity was used as a reference to assess the effectiveness of co-sputtering deposition with SiO_2. Optimal deposition conditions were determined by comparing a simplified figure of merit (FOM) of films sputtered under different conditions. The FOM was calculated as follows: $FOM = \frac{\sigma}{A_{400\text{-}800}}$, where σ is the electrical conductivity and $A_{400\text{-}800}$ is the average absorptance from 400 nm to 800 nm. A high FOM is indicative of films with high electrical conductivity and/or low absorptance in the visible spectral range.

To highlight the effect of SiO_2 addition, a comparison between the best (highest FOM) SiO_2-SnO_2 ($SiSnO_2$) and pure SnO_2 thin films is shown in Fig. 5.1. It is worth noting, that only a slight difference in conductivity between the films with and without silicon is seen, while the absorptance in the visible and near infrared decreases simultaneously from 6% to 3% at 500 nm. Analogous results were observed for the SiZTO vs ZTO films: ZTO at a wavelength of 500 nm, has a measured 5.5% absorptance, while SiZTO has an absorptance of only 2.5%. Thus, unlike variation of O_2 flow during deposition, silicon addition allows a control of optical absorption that does not impact electrical conductivity. Some further clues as to the origin of this effect were provided by the following experimental observations:

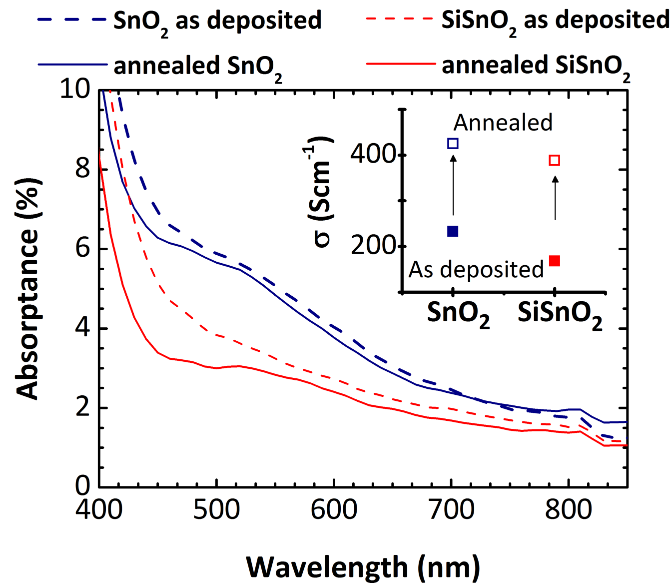

Figure 5.1. Absorptance and conductivity (inset) of as-deposited and annealed $SiSnO_2$ and SnO_2 films, deposited at the optimal conditions. Both films display similar conductivities. The main advantage of $SiSnO_2$ films is their lower absorption in the visible range.

- The composition of the optimized SiZTO film determined by Rutherford backscattering spectrometry (RBS) is $Si_{0.02}Zn_{0.04}Sn_{0.27}O_{0.67}$, indicating an absolute increase in oxygen concentration of 2 at%, when compared to the reference ZTO ($Zn_{0.05}Sn_{0.30}O_{0.65}$). A small increase in oxygen content is also observed for $SiSnO_2$ when compared to SnO_2. Thus, additional oxygen is brought into the films by SiO_2 co-sputtering. This suggests that at least some V_O defects could be passivated directly, contributing to the observed reduction in the absorption at 500 nm.

- Measurements of film microstructure performed using scanning transmission electron microscopy reveal a dense and homogeneous microstructure for SiZTO. Undoped ZTO forms an amorphous film and no obvious changes in this microstructure with silicon addition could be identified. In the case of SnO_2, the presence of silicon atoms is seen to retard the onset of crystallization: crystalline grains start to appear closer to the top surface in $SiSnO_2$ than in SnO_2. The section of $SiSnO_2$ film in contact with the substrate is amorphous, however, as the material thickens it crystallizes into the rutile SnO_2 structure.

- Energy dispersive X-ray (EDX) spectroscopy analysis line profiles demonstrate that Si atoms do not accumulate at grain boundaries or inside the bulk (amorphous or crystalline) of $SiSnO_2$. No Si-rich clusters are observed, particularly towards the top of the film, where the film is composed of crystallites. The same is observed for the amorphous films of SiZTO, i.e. the distribution of all elements is uniform within the film.

- Possible changes in the oxidation state of the elements with SiO_2 addition, which

could explain the observed changes in optoelectronic properties, were investigated using X-ray photoelectron spectroscopy. However, calculated binding energies and the full width at half maximum for O-1*s*, Sn-3*d*, and Zn-2*p* bands displayed no important differences in the fitted values between the different samples.

5.1.2. Computational assessment of Si-modification in SnO_2

The addition of a small SiO_2 amount does not modify the microstructure of ZTO, which remains amorphous, yet improves the optical properties of the film. The gain in optical properties takes place irrespective of whether the microstructure is fully amorphous (SiZTO) or an amorphous/polycrystalline mixture ($SiSnO_2$), suggesting that the passivation mechanism is independent of the underlying microstructure. Moreover, both Si and O are found by EDX to be homogeneously distributed within the thin films and show no segregation. These observations indicate that the addition of SiO_2 is modifying the nature of point defects within the films, point defects that must be present in both amorphous and crystalline structures.

To understand in detail the nature of these defects and their passivation mechanism by Si addition, density functional theory calculations were performed. For these calculations, the rutile crystal structure of SnO_2 was used as a starting point, since: (i) the same effect was observed for amorphous and polycrystalline structures; (ii) the amorphous ZTO phase crystallizes into rutile SnO_2 and has first coordination shells very close to this atomic structure [23]; (iii) Zn does not appear to modify the Si-passivation mechanism as it is analogous in both ZTO and SnO_2; (iv) in a crystalline structure changes induced by point defects can be isolated, whereas in an amorphous material a convolution of different effects is present (eg., induced by the aperiodic structure and/or locally missing atoms) and may blur the contribution of individual point defects; (v) in a crystalline lattice only a limited number of defect sites needs to be considered.

The stoichiometric phase of crystalline SnO_2 has a defect-free band gap of 3.6 eV with no parasitic absorption in the visible range (see previous chapter) [253] . One possible cause for the optical absorption feature shown in Fig. 5.1 is deep defect states, predicted by theoretical models to arise from the presence of charge neutral oxygen vacancies [238, 239]. A similar role of oxygen deficiency related defects in subgap absorptance was demonstrated for the amorphous ZTO films in Ref. [232]. The link between V_O-related defects and the absorptance features at 600 nm [13] is further supported by the observation that increasing oxygen partial pressure during deposition suppresses absorption. The central role of oxygen deficiencies in subgap absorption and its reduction in the presence of silicon suggests that silicon must be interacting with the native V_O defects in some unique way, since the same results are not reproducible by simply increasing O_2 flow during deposition. In the following, we present one possible mechanism for this interaction to take place. First, the contribution of oxygen vacancies to the parasitic absorption in SnO_2 is described in detail and then the impact of Si addition is elucidated.

Calculation Details

Density functional theory calculations were performed using the PBE0 hybrid functional [81, 82] as implemented in the VASP electronic structure code [175, 176]. Si $3s$ and $3p$ (4), O $2s$ and $2p$ (6) and Sn $5s$, $5p$ and $4d$ (14) electrons were included as valence. All defects were investigated inside a $2\times2\times3$ (72 atom) supercell of rutile SnO_2 phase (discussed in detail in Section 4.1.1). Atomic positions for all defects were relaxed using a $2\times2\times2$ Monkhorst-Pack k-point mesh until forces below 0.02 eV/Å were obtained, while the volume of the supercell was fixed to that of the (expanded) perfect crystal calculated by fitting the Birch-Murnaghan [177] equation of state. Since SnO_2 has a direct electronic gap at Γ, a Γ-centered $3\times3\times3$ k-point mesh was used to obtain the plotted densities of states, in order to observe any changes nearby the extrema of the valence and conduction bands.

Defect properties were calculated using the methodology described in detail in Chapter 3. Defect formation energies were evaluated using Eq. 3.4, thermodynamic transition levels using Eq. 3.5 and binding energies using Eq. 3.19. Electrostatic correction terms analogous to the ones used in Section 4.1.2 were applied. Chemical potential bounds were imposed by SnO_2 and SiO_2 formation. Finally, a $3\times3\times4$ (216 atoms) supercell was tested to verify convergence of the above properties with respect to supercell size and good qualitative agreement with the results presented was found.

Oxygen Vacancies

The rutile structure of a SnO_2 crystal containing an oxygen vacancy is shown in Fig. 5.2(a). Local relaxations of the three neighboring tin atoms following the creation of an oxygen vacancy result in two symmetrically nonequivalent Sn-sites labeled site A and site B in the inset of Fig. 5.2(a). An isolated V_O is seen to be stable in two charge states in the crystalline SnO_2 film (see Fig. 5.2(b)): an ionized $q = 2$ charge state when the Fermi level is below 2.77 eV and in a charge neutral $q = 0$ state when the Fermi level is approaching the conduction band.

In agreement with previous studies [14, 36, 254], we observe electronic defect states in the mid-gap region for a charge neutral V_O shown in Fig. 5.3(a), which would contribute to parasitic absorption. In contrast, a doubly ionized V_O results in electronic states at the edge of the conduction band minimum (CBM) of stoichiometric SnO_2 shown in Fig. 5.3(b), which would not detrimentally affect the optical properties of the TCO. This transition of electronic defect states from deep to shallow (DX-center behavior†) is a result of local atomic relaxations that follow the ionization of the vacancy. Similar metastable shallow donor state formation via ionization has also been reported for other TCOs, namely ZnO and In_2O_3 [40, 103].

Whether an oxygen vacancy contributes to parasitic absorption or not is, therefore, determined by the position of the Fermi level, ϵ_F. The Fermi energy at which two different charge states of a given defect have the same formation energy (i.e. form in equal concentrations according to Boltzmann statistics) is known as the thermodynamic transition level. The calculated thermodynamic transition levels, $\epsilon(2/0)$, are indicated by gray lines in Fig. 5.2. In the case of an isolated oxygen vacancy the $\epsilon(2/0)$ transition

†See Section 3.3.2 for a more detailed discussion of DX-centers

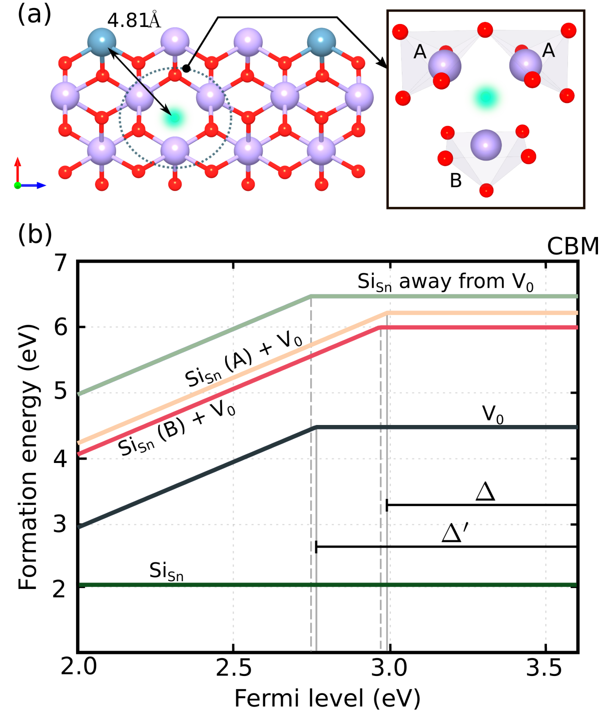

Figure 5.2. (a) SnO_2 surrounding an oxygen vacancy defect. Sn atoms are shown as purple spheres, oxygen - red, silicon - blue, the vacancy is indicated in green. Right panel: A and B distinguish the two substitutional Si sites neighboring the vacancy. Left panel: the distance between a substitutional Si_{Sn} far from V_O is indicated; (b) Formation energies (O-rich) of isolated defects and defect complexes as a function of the Fermi level. $\epsilon(2/0)$ transitions are indicated by light gray lines. Δ marks the distance between $\epsilon(2/0)$ transition and the conduction band minimum (CBM). This distance, important in determining the ratio between different charge states, is shifted towards the CBM in the presence of Si.

was found to occur at a Fermi level of 2.77 eV above the valence band. However, in an n-type TCO material ϵ_F is expected to lie at or above the conduction band minimum. The distance, Δ, between the CBM and the thermodynamic transition level is, therefore, the quantity that determines the ratio between the concentrations, C^q, in which the different charge states, q, will form.

$$\frac{C^0}{C^2} = \exp\left(\frac{2\Delta}{k_B T}\right) \tag{5.1}$$

In the case of an isolated V_O a value of 0.855 eV for Δ was obtained. As a consequence, in an n-type SnO_2 the majority of oxygen vacancies are expected to be charge neutral and likely to result in parasitic absorption.

Addition of Silicon

EDX measurements revealed a uniform distribution of Si atoms in the SnO_2 and ZTO atomic networks, hence, Si clustering was not considered in the modeling process. The

rutile structure of SnO_2 offers two obvious substitutional sites for Si incorporation: the oxygen, Si_O, or the tin, Si_{Sn}, site. We found that silicon preferentially substitutes Sn with a formation energy of 2.04 eV and remains electrically inactive for Fermi levels across the band gap, as demonstrated in Fig. 5.2(b). O-site substitution, on the other hand, results in a formation energy over 10 eV higher than that of a Sn-site (not-shown), which suggests this defect-type is extremely unlikely to occur. As a result, it is clear that silicon does not passivate oxygen vacancies by directly occupying the lattice site.

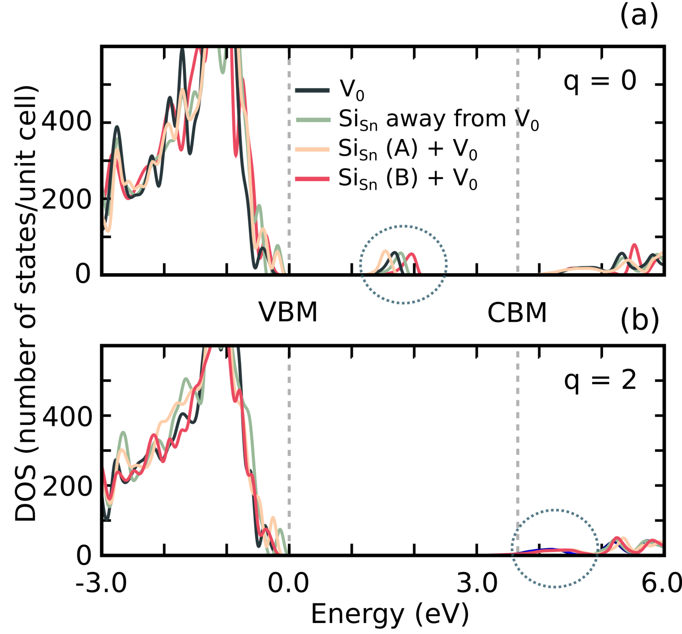

Figure 5.3. Electronic densities of states for oxygen vacancy related defects in SnO_2. Results for (a) the charge neutral ($q = 0$) and for (b) the doubly ionized ($q = 2$) supercells are shown. Colored lines correspond to defect geometries described in detail in the main text. Defect induced states are highlighted by dashed circles.

We considered the formation of (Si_{Sn}-V_O) defect complexes, where the Si atom takes one of the two symmetrically nonequivalent Sn-sites neighboring the oxygen vacancy, marked by A and B in the right panel of Fig. 5.2(a). The calculated binding energies of the ionized (Si_{Sn}-V_O) complexes were found to be 0.757 eV on site A and 0.927 eV on site B. These positive binding energies suggests that silicon substitutionals prefer to incorporate nearby under-coordinated Sn atoms.

As Fig. 5.3 demonstrates, in all cases, the electronic defect states associated with a V_O formation are not strongly affected by the presence of a neighboring Si atom. However, Fig. 5.2(b) reveals that when the (Si_{Sn}-V_O) complex is formed the thermodynamic transition energies $\epsilon(2/0)$ are shifted closer to the conduction band and values of Δ equal to 0.635 eV (site B) and 0.655 eV (site A) are obtained. The exponential dependence on the value of Δ suggests that a 25% shift observed in the presence of Si could significantly affect the ratio between the different charge states of oxygen vacancies present in the TCO. The presence of silicon is, accordingly, seen to promote the formation of ionized oxygen vacancies, i.e. charge states that do not contribute to parasitic absorption, but do contribute to free-carrier generation.

Finally, we validate our results by placing the Si_{Sn} and the V_O defects inside the same cell, but as far away from each other as the cell size allows. This defect geometry is depicted in the left panel of Fig. 5.2(a). In the limit of an infinite cell, one should recover the exact sum of the behaviors of the two defects in isolation. Instead, Fig. 5.2(b) reveals a small shift of 20 meV in the thermodynamic transition level $\epsilon(2/0)$, when compared to isolated V_O. Changes of similar magnitude are seen in the electronic defect states shown in Fig. 5.3. These shifts reflect the size of the error that results from the choice of the supercell and demonstrate the validity of the (Si_{Sn}-V_O) complex calculations.

5.1.3. Steric effects

Silicon has four valence electrons and, thus, forms charge neutral substitutional defects when replacing a tin atom inside the crystalline SnO_2 structure, as shown in Fig. 5.2(b). As a consequence, the interaction resulting in the positive binding energy of the (Si_{Sn}-V_O) complex cannot be Coulombic in nature. What is then the origin of the attraction between these two defects? Furthermore, why does silicon preferentially stabilize the doubly charged oxygen deficiency and not the neutral one?

Si has a demonstrably strong preference for four-fold coordination. In fact, despite the isovalence with tin, it is only four-fold oxygen coordinated in SiO_2 in contrast to the six-fold oxygen coordination of tin in SnO_2. Furthermore, this lower coordination environment is retained even when amorphous silica phases are formed [255, 256]. It is feasible that the preference for oxygen deficiencies in SnO_2 shown by silicon is rather simple in origin. The formation nearby an oxygen vacancy site is favored, as it results in a decrease in the over-coordination experienced by the silicon atom.

Further insights into the stabilization of the $q = -2$ charge state of the neighboring oxygen vacancy are provided by the local atomic structures associated with the V_O defect. The $q = -2$ and $q = 0$ charge states result in opposing effects on the atoms neighbouring the defect site. In the $q = 0$ case, surrounding tin atoms are pulled towards the empty lattice site, while in the $q = -2$ case they are strongly pushed outwards. Since, silicon forms stronger bonds with the neighboring oxygen atoms and has a smaller ionic radius than Sn, it enforces a $q = -2$ like separation from V_O, regardless of the charge state of this defect. Consequently, the $q = 0$ state becomes more energetically costly to form.

If such a steric effect is indeed responsible for the observed phenomena, other elements along the series should behave in a similar fashion. Germanium and carbon were, therefore, investigated for analogous interactions with V_O. A stronger stabilization of the $q = -2$ charge state was anticipated in the presence of carbon and a weaker effect in the vicinity of germanium. Our preliminary results, using a local PBE functional (PBE was observed to show stronger $q = -2$ stabilization when compared to hybrid functionals), indicated that germanium does indeed behave comparably to silicon. As predicted, however, the shift in the thermodynamic transition levels was 70 meV smaller, than that found with Si using the same functional. Thus, optical absorption improvements should also be observable in germanium co-sputtered tin-based oxides. Though the presence of germanium may result in lesser numbers of ionized V_O, advantages over silicon can still be speculated. For example, the smaller disparity between the ionic sizes of Ge and Sn could offer a reduced impact on the mobility of the free-carriers. Carbon, on

the other hand, was found to be unable to successfully replace Sn, i.e. it resulted in both strong structural changes around the substitutional site and the introduction of deep electronic defect-states inside the band gap. Such states are certain to result in increased parasitic absorption. We conclude that silicon remains the most favorable element for optical absorption reduction, at least if using the mechanism elucidated above.

5.1.4. Discussion

The observed increase in oxygen content in Sn-based thin films when co-sputtering with SiO_2 eliminates some V_O related defects, subsequently improving the transparency of Sn-based TCOs. As the same optical/electrical trade-off cannot be achieved solely by tuning the oxygen partial pressure during deposition or by mild annealing in air [13, 232], some additional effects linked to the presence of Si atoms are expected. Our DFT calculations show that the incorporation of Si atoms nearby oxygen deficient sites is energetically favored, at least in the rutile SnO_2 lattice. This is due to a positive binding energy between a substitutional Si atom and a V_O. The binding of Si is further seen to promote the ionization of the oxygen defect, releasing charge carriers into the host material. Local structural relaxations following the ionization of V_O lead to electronic defect states at the edge of the optical band gap range and, thus, provide a potential explanation for the success of silicon in passivating optically detrimental states in Sn-based TCOs. A combination of the two phenomena, namely a direct passivation of V_O by the oxygen atoms of SiO_2 and an indirect passivation of V_O due to a shift of the electronic defect states to higher energies close to the band gap edge, could explain the experimental results shown in Fig. 5.1.

Interestingly, the addition of SiO_2 is experimentally seen to be equally effective for amorphous and mixed phase amorphous/polycrystalline microstructures, demonstrating the generality of the ‘cold-passivation’ approach. The approach simultaneously preserves the electrical conductivity and improves the transparency of the films, opening new perspectives on low-temperature defect-selective passivation. The compatibility of this co-sputtering methodology with temperature-sensitive processes and substrates (< 200 °C) enables its application in transparent and flexible electronics. Finally, this approach should serve as an inspiration to design and discover oxides that could potentially play a similar role in other TCOs as SiO_2 does in SnO_2 and ZTO.

5.2. Case Study B - Defect Complexes in Tin Monoxide

The layered litharge structure of SnO is a metastable stoichiometry of the more established rutile tin dioxide and is reported to disproportionate into metallic Sn and SnO_2 at elevated temperatures [220]. The two readily available stoichiometries of the oxide reveal a feature of tin, that is common among the group-IV elements, the capacity for double valency. The four valence electrons in the $5s^2 5p^2$ configuration of the metal atom allow the element to share only two (SnO) or all four (SnO_2) electrons when forming ionic bonds. As a consequence, tin is four-fold coordinated by oxygen in SnO, but six-fold coordinated in SnO_2, resulting not only in different crystal structures,

but also in opposing electronic properties [14, 15]. In SnO, the stability of the cation vacancy, V_{Sn}, in a $q = -2$ charge state, for Fermi levels close to the valence band maximum, is speculated to be the source of the experimentally measured p-type conductivity [132, 150, 201]. In contrast, nominally undoped SnO_2 displays n-type character, that is unaffected by V_{Sn} formation due to the high energy required to incorporate this defect and the associated ultra-deep acceptor ionization levels [166].

The multivalency of Sn is often cited as a drawback of p-type SnO, as the excessive removal of cations required for hole formation may result instead in the creation of a SnO_2-like n-type environment, as is observed for lead oxide [257]. In this work, we evidence how the lamented complications associated with cation divalency, can instead be exploited as an advantage for p-type SnO formation. The possibility of oxidizing Sn(IV) is demonstrated to correspondingly permit $q = -4$ charged tin vacancies to be formed. We prove that these highly charged vacancies can be stabilized by binding to interstitial elements that display strong electronegativity. The resultant defect complexes are seen to not only enhance the number of available free-carriers, but to also stabilize a charge donating state even when the Fermi level lies below the valence band edge, preventing self-compensation. This novel defect complex mechanism for boosting carrier concentrations is likely to be applicable in other Sn(II)-based materials, such as SnS, a p-type absorption layer used for solar cells [258], or SnSe, an exceptional thermoelectric compound [259].

5.2.1. Oxygen in SnO

Contrary to what one would expect from a highly electronegative element, previous computational investigations in SnO report a charge neutral state as the most stable for the oxygen interstitial, O^i, concluding that this defect would be electrically inactive [132, 150, 201]. Such behavior conflicts with the anticipated n-type environment creation facilitated by the excess of oxygen. We investigate this inconsistency by performing density-functional theory calculations using HSE06 hybrid exchange-correlation functional [83, 84] with a projector augmented-wave [95, 174] basis set as implemented in the VASP code [175, 176]. Spin polarized calculations were performed using a plane wave energy cutoff of 700 eV and PAW potentials including Sn-d electrons as valence states. This methodology closely reproduces the experimental properties of the bulk: a fundamental band gap of 0.68 eV (experiment: 0.7 eV [213]) and optimized lattice constants of 3.80/4.98 Å (experiment: 3.80/4.84 Å [201]). A more detailed description of the bulk properties using this functional was presented in Section 4.2.1.

The most stable location to incorporate excess oxygen, as reported in previous studies [132, 201, 260], is the pyramidal (coordinated by five Sn atoms) interstitial site, shown in Fig. 5.4. This interstitial was investigated here using a 192 atom supercell ($4 \times 4 \times 3$) containing one isolated defect, resulting in a defect concentration of less than ~1 %. To determine the stable charge state associated with a defect X (in this instance $X = O^i$) the formation energy, E_X^F, as a function of the Fermi level, ϵ_F, and the chemical potentials, μ_i, was calculated using Eq. 3.4. Reference phases used to calculate the chemical potentials in evaluating E_X^F are described in Appendix A.3. The electrostatic correction terms, E_{cor}, were implemented following the work presented in Section 4.2.2. In the cases where shallow acceptor behavior was identified the same

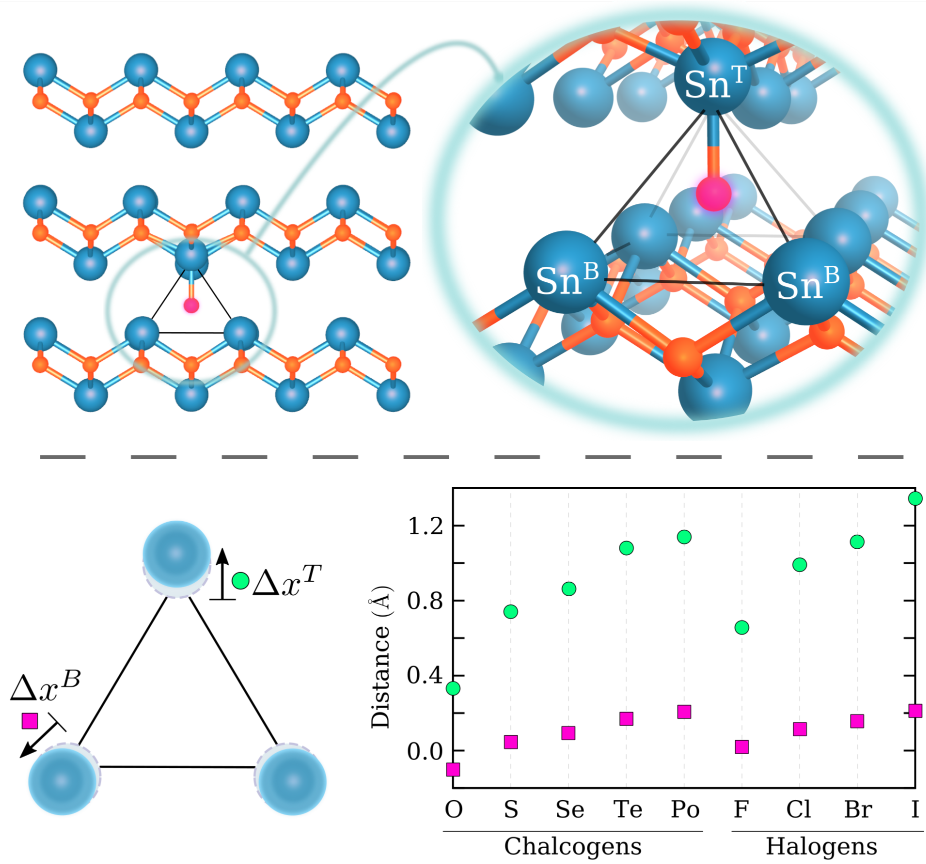

Figure 5.4. (Top) Atomistic model of the litharge SnO crystal with Sn atoms represented in blue and oxygen in vermilion. The favored position for an interstitial oxygen atom is indicated in pink. The close-up figure marks the symmetrically nonequivalent Sn-sites in the upper/lower parts of the pyramid formed by the interstitial. (Bottom) Left panel illustrates the nomenclature for changes in the positions of tin atoms when neighboring a D^{i} defect: green, Sn^{T}; pink, Sn^{B}. Right panel shows these calculated distances in Å found for chalcogen and halogen interstitials.

electrostatic correction was also applied to the charge neutral defect state. The effect of this choice is elucidated in greater detail in Appendix E. Defective supercells were investigated using a single Γ-point in k-space. The lattice of the supercell was fixed to the values obtained for bulk SnO, while the atomic positions were allowed to relax until forces below 0.02 eV/Å were obtained.

Our calculated O^{i} formation energy, shown in Fig. 5.5, confirms that the configuration corresponding to the $Q = 0$ charge state† is the most stable one, for values of ϵ_F within the band gap. However, a closer Bader charge [261] inspection reveals that while the overall configuration is charge neutral, the interstitial oxygen is not. The O^{i} possesses a Bader charge of −1.28, close to the value of −1.36 for oxygen in the bulk. As seen from Table 5.1, the majority of this charge originates from the Sn atom at the top of the pyramid formed by the defect (Sn^{T} in Fig. 5.4), while the charges of the Sn atoms

†Here, we introduce the notation Q to distinguish the charge state of the supercell, from the charge state of the defect q, assessed by Bader charge evaluation.

at the base of the pyramid (Sn^B in Fig. 5.4) are largely unaffected. The Sn^T cation has a Bader charge of +2.44 (compared to +1.36 in bulk SnO), a value that is close to that of bulk SnO_2 [158]. These observations suggest Sn(IV) formation with the following charge equilibration (in Kröger-Vink notation [262]) taking place:

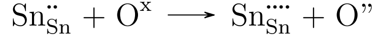

$$Sn_{Sn}^{\cdot\cdot} + O^{x} \longrightarrow Sn_{Sn}^{\cdot\cdot\cdot\cdot} + O''$$

The above result confirms that, as previously hypothesized, a SnO_2-like environment is exceedingly easy to form in SnO. In fact, the presence of even a single additional oxygen is sufficient to promote Sn(IV) oxidation. However, as the stable $Q = 0$ charge state reveals, Sn(IV) formation does not generate free-carriers: the electrons stripped from the cation are bound to the interstitial site, and are not detrimental for p-type conductivity. Furthermore, O^i does not introduce electronic defect states within the band gap, which could negatively impact the optical transparency of SnO.

The observed oxidation state of Sn^T, nevertheless, alludes to a tantalizing possibility: a vacancy formed on this site could attain a $Q = -4$ charge state, resulting in the formation of twice as many holes as a typical tin vacancy. Indeed, it is conceivable that a careful choice of the interstitial species could promote the ionization of tin vacancies, rather than tin atoms. To investigate this possibility, we calculated the formation energies associated with V_{Sn^T} formation neighboring an interstitial. We denote the resulting configuration as a $(V_{Sn^T} + D^i)$ defect complex, where D is the atomic species of the interstitial impurity. Due to their mono-valence with oxygen, all chalcogens were considered in the initial screening step.

5.2.2. Chalcogens in SnO

From an electronic point of view, heavier chalcogen interstitials were found to induce effects analogous to O^i. As shown in Fig. 5.5, an overall charge neutral supercell is favored, while Bader charge analysis reveals that the impurity atom imposes a significant electronic uptake from the neighboring Sn^T. Table 5.1 demonstrates, that the charge transfer decreases along the series, with Po displaying a Bader charge of −0.41, only a third of that of oxygen. Concurrently, the base layer tins retain their Sn(II) oxidation state.

Upon removal of the neighboring Sn^T atom, to form a $(V_{Sn^T} + D^i)$ complex, the Bader charge of the impurity is observed to be largely unaffected (Table 5.1). However, in this case the charge is no longer transferred from a Sn atom, since the Bader charges of Sn^B reflect an unchanged Sn(II) nature. The additional electrons are extracted from the now vacant Sn^T site, resulting in a V_{Sn}^{-4}, that is only permitted to form due to the divalent character of tin. This $Q = -4$ ionization state, as shown in Fig. 5.5, is stable for all Fermi levels within the band gap, regardless of the chalcogen impurity species. Hence, a V_{Sn} bound to an interstitial impurity demonstrably generates twice the free-carriers of isolated V_{Sn} (shown in the right panel of Fig. 5.5). Furthermore, the highly ionized state of the $(V_{Sn^T} + D^i)$ complex remains favorable for Fermi levels beyond the valence band edge in contrast to V_{Sn}, that is observed to transition to a $Q = 0$ state. As a consequence, interstitial impurity assisted hole generation could persist even in a p-type material.

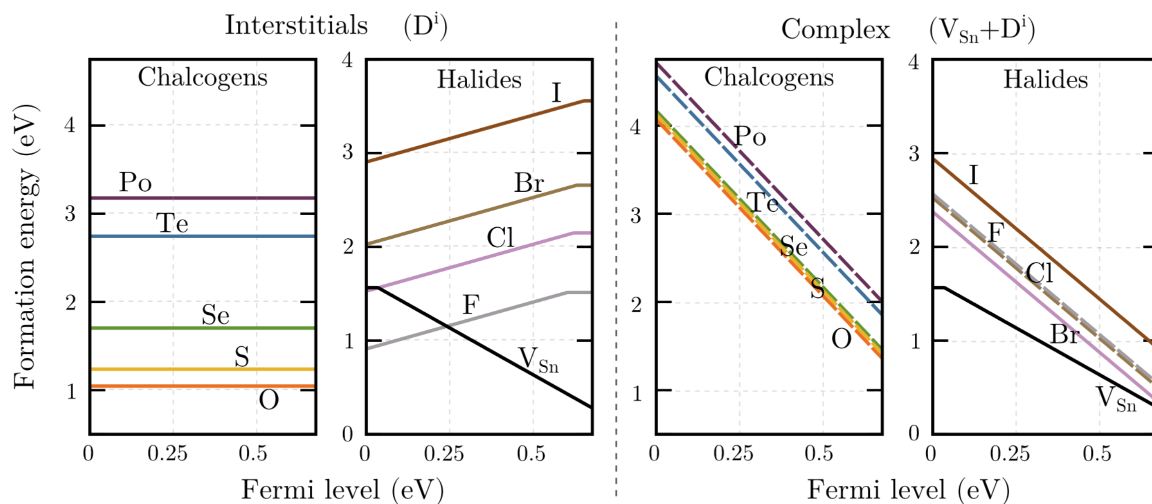

Figure 5.5. Defect formation energies as a function of the Fermi level, $\Delta\epsilon_F$, under Sn-rich conditions. Left panel: interstitial defect formation energies. Right panel: energy corresponding to an interstitial defect neighboring a V_{Sn^T}. Only the stable charge state is shown.

These results showcase the potential of defect complex formation for enhancing free-carrier generation. Yet, assessing the stability of the complex towards dissolution is crucial for justifying the utility of the method. To this end, a quantity, E_B^v, analogous to the binding energy introduced in Section 3.7 is defined according to Eq. 5.2.

$$E_B^v = E^F[D_\mathrm{i}] + E^F[V_\mathrm{Sn}] - E^F[D^\mathrm{i} + V_\mathrm{Sn}] \tag{5.2}$$

The superscript v indicates, that all formation energies used were of the stable charge state, evaluated at the valence band maximum. E_B^v defined in this way contains the energy gained by both separating the defect complex into its individual constituents and allowing the constituents to further decay into their respective ground states.

For oxygen a binding energy of -1.6 eV is obtained. The negative value reveals the complex configuration to be unfavorable under p-type conditions. Similar conclusions were reached by Togo *et al.* [132], using the PBE exchange correlation functional. While complex formation becomes increasingly favorable along the chalcogen series, it remains uncompetitive with dissolution for all impurities, except polonium. This result is not entirely surprising: the creation of a V_{Sn^T} requires the removal of a cation, that leads to a negatively charged ($Q = -2$) environment, into which a further anion is introduced. The lack of an intermediary cation results in a strong electrostatic repulsion, which is only compensated for by structural (steric) effects.

Structural changes in the local atomic environment induced by an interstitial impurity are surveyed in the bottom panel of Fig. 5.4. Oxygen is the only element that attracts the Sn^B, while all other impurities push them outwards. Evidently, the Sn^T cation, to which the interstitial is bonded directly, is displaced much further from its bulk equilibrium position, than the other neighbors. Thus, a significant structural strain is expected to be alleviated, upon removal of the strongly distorted Sn^T when forming a (V_{Sn^T} + D^i) complex. Indeed, it is this effect that is seen to stabilize the complex

formed by larger chalcogen atoms. Local distortions are observed to increase with the size of the anion impurity, consequently raising the formation energy of interstitials, as seen in Fig. 5.5. Simultaneously, the formation energy of the complex changes only slightly. This is reflected in the calculated binding energies, summarized in Table 5.1. Unfortunately, as no heavier chalcogens are available, no further steric energy gain can be obtained by increasing atomic radii.

Table 5.1. Summary of the relevant information on the interstitial and the interstitial-vacancy defect complex. For each impurity species D, we report the formation energy of the defect in the stable charge state Q and the Bader charges, q, of elements in the vicinity of the defect. For the defect complexes the binding energy at the valence band maximum, E_B^v, is also reported.

	interstitial (D^i)			complex (V_{Sn^T} + D^i)		
D	q_D	q_{Sn^T}	q_{Sn^B}	E_B^v	q_D	q_{Sn^B}
O	-1.3	2.4	1.39	**-1.6**	-1.4	1.35
S	-1.0	2.3	1.37	**-1.3**	-1.1	1.31
Se	-0.9	2.2	1.36	**-0.9**	-1.0	1.29
Te	-0.6	2.1	1.34	**-0.3**	-0.8	1.27
Po	-0.4	2.0	1.33	**+0.0**	-0.6	1.26
F	-0.8	2.6	1.39	**-0.1**	-0.9	1.40
Cl	-0.7	2.4	1.39	**0.7**	-0.8	1.37
Br	-0.6	2.4	1.38	**1.0**	-0.7	1.36
I	-0.5	2.3	1.37	**1.5**	-0.6	1.34

Given this, an alternative route to stabilizing complex formation must be sought. One possibility is the reduction of the unfavorable electrostatic interactions through lowering of the impurity charge state. With this goal in mind, we turn towards halogens. The strong electronegativity of these elements is expected to still result in successful electron depletion from the neighboring Sn^T, yet when formed next to V_{Sn^T} the lower charge state of the impurity should reduce the electrostatic repulsion.

5.2.3. Halogens in SnO

First, isolated halogen impurities were verified to successfully ionize Sn^T. The corresponding formation energies are shown in Fig. 5.5. Shallow donor behavior, with a stable $Q = 1$ charge state, is found for all halogen interstitials. This unexpected result is, once again, illuminated by the Bader charge analysis summarized in Table 5.1. In all cases, the Sn^T atom displays a charge indicative of the formal Sn(IV) oxidation state, while the impurity atom takes only a single electron. We propose the following mechanism as responsible for the surprising generation of a free-electron in the presence of a halogen, confirming Sn(IV) ionization:

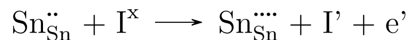

$$\mathrm{Sn}_{\mathrm{Sn}}^{\cdot\cdot} + \mathrm{I}^{\mathrm{x}} \longrightarrow \mathrm{Sn}_{\mathrm{Sn}}^{\cdot\cdot\cdot\cdot} + \mathrm{I}' + \mathrm{e}'$$

Furthermore, halogens are observed to incur similar structural distortions to chalcogens (see bottom panel of Fig. 5.4). In fact, stronger displacements of the Sn^T atom are

induced by halogens of the same row. Therefore, eliminating this cation would again alleviate significant structural stress. Three (rather than four) shallow acceptor states are created with the (V_{Sn^T} + D^i) complex formed with a halogen, as is demonstrated by the stable charge state of $Q = -3$ found for this defect. These findings confirm the speculated lowering of electrostatic interactions. Nevertheless, an additional free carrier is generated per each defect of this type. The holes are observed to occupy perturbed host like states (see Appendix E) [103], further confirming the shallow character of the complex. The highly ionized state of the complex is again favored below the valence band edge, resulting in more stable hole generation when compared to isolated V_{Sn}.

Evaluation of E_B^v for halogens (see Table 5.1) reveals that these defect complexes are strongly favored, with the exception of fluorine, where a small amount of energy can be gained by dissolution. Thus, at least three elements: Cl, Br and I, are identified as capable of interacting with the native defects of SnO lattice in a way that not only successfully generates additional free-carriers, but also acts to counter the pinning of the Fermi level.

5.2.4. Alternative defect sites

An important concern to address is the possibility of alternative-site occupation by the proposed impurities. Formation of D_{Sn}, D_O and D^i_{tet} (as defined in Section 4.2) was considered as an alternative for the pyramidal D^i site discussed throughout this work. Exact formation energies of all alternative-sites are tabulated in Table 5.2, with the stable supercell charge state for each defect site shown in brackets.

Table 5.2. Impurity and the impurity-vacancy defect complex formation energies, E_X^F, of the stable supercell charge states, (Q), at the valence band maximum. The most stable configuration is highlighted in bold. N/S marks defect configurations that could not be stabilized. For reference V_{Sn} formation energy is 1.563 eV ($Q = 0$).

D	$E^F_{D_O}(Q)$	$E^F_{D_{Sn}}(Q)$	$E^F_{D^i_{tet}}(Q)$	$E^F_{D^i}(Q)$	$E^F_{V+D^i}(Q)$
O	–	N/S	2.53 (0)	**1.05** (0)	4.13 (-4)
S	1.69 (0)	N/S	3.95 (0)	**1.37** (0)	4.20 (-4)
Se	2.36 (0)	N/S	4.97 (0)	**1.70** (0)	4.17 (-4)
Te	3.87 (0)	3.04 (2)	5.23 (0)	**2.74** (0)	4.56 (-4)
Po	4.46 (0)	3.21 (2)	5.37 (0)	**3.18** (0)	4.71 (-4)
F	**0.39** (1)	N/S	1.60 (0)	0.91 (1)	2.56 (-3)
Cl	2.15 (1)	N/S	3.30 (0)	**1.53** (1)	2.37 (-3)
Br	3.03 (1)	N/S	4.05 (0)	**2.03** (1)	2.52 (-3)
I	4.44 (1)	N/S	5.27 (0)	**2.91** (1)	2.99 (-3)

Sn-site substitution was found to be unstable, relaxing into (V_{Sn^T} + D^i) for all impurities considered, except the heaviest chalcogens – Te and Po. Though, interstitial pyramidal site is still preferred over the tin substitution, a ($V_{Sn} + D_i$) complex formed with these elements is likely to recombine to form a much more energetically favorable D_{Sn}. For both elements, this would result in a release of electrons, thus, making these

elements unsuitable for the proposed defect-complex doping approach. Fluorine is the only element to prefer oxygen-site, F_O, substitution, again enhancing n-type conductivity. The remaining elements – O, S, Se, Cl, Br and I – all favor interstitial formation over any of the alternatives. Particularly noteworthy, is the formation energy of the $(V_{Sn^T} + I^i)$ complex. Not only is it 1.5 eV lower than the sum of isolated defects, but it is also directly competitive with the energy of the I^i alone, implying a negligible cost for the removal of the Sn^T neighbor.

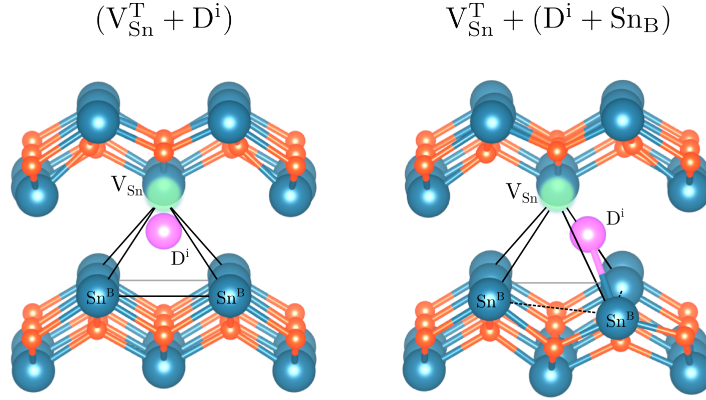

Figure 5.6. The structure of the proposed complex (left) and an alternative metastable complex (right) for $(V_{Sn} + D^i)$ defects. In the metastable complex the impurity atom (shown in pink) forms a direct ionic bond with a new Sn atom (shown in blue). The neighboring tin vacancy is shown as a green sphere, while oxygen atoms are shown in vermilion.

For the halogens stable in the $(V_{Sn} + D^i)$ complex configuration, a further possibility of the impurity migrating away from the vacancy and bonding to an alternative nearby tin site, such as one of the neighboring Sn^B atoms, was also investigated. In the highly ionized $(Q = -3)$ charge state a bond of this type could not be formed, but with a capture of two holes $(Q = -1)$ a metastable bonded configuration was observed. The structure of this alternative complex is depicted in the right panel of Fig. 5.6. The left panel of the figure displays the original complex for comparison. We note that significant structural distortions of the original complex are required for the bonded complex to form. The formation of an ionic bond between the tin and the migrated impurity is supported by the Bader charge analysis summarized in Table 5.3. The Bader charge associated with the Sn^B to which the impurity is bonded increases to ≈2.4, indicating a Sn(IV) ionization state of this atom, while the remaining three Sn^B atoms forming the base of the pyramid retain their Sn(II) states.

The bonded complex is stable in an overall $Q = 1$ charge state at the valence band, corresponding to a sum of a neutral V^T_{Sn} and an ionized D^i. However a shallow acceptor transition for this new defect complex is obseved, linked to the $Q = -2$ charge state of the tin vacancy. Although more stable than V_{Sn^T} and D^i in isolation, this defect complex is significantly less favorable than the original $(V_{Sn^T} + D^i)$ complex. For typical values (100 meV above the VBM) of the Fermi level in SnO, our original complexes are favored

energetically by 0.38 eV (Cl), 0.49 eV (Br) and 0.51 eV (I).

Table 5.3. Comparison between the two interstitial-vacancy defect complexes shown in Fig. 5.6. For each elemental species D, we report the stable charge state Q at the VBM and the Bader charges associated with the defect environment.

	original complex			alternative complex		
D	Q	q_D	q_{Sn^B}	Q	q_D	q_{Sn^B}
Cl	-3	-0.8	1.37	1	-0.6	2.44
Br	-3	-0.7	1.36	1	-0.5	2.35
I	-3	-0.6	1.34	1	-0.3	2.22

Given the above, we propose that incorporation of halogens in the SnO matrix, under careful growth conditions, could lead to significantly enhanced p-type properties. Methodologies for growing SnO via sputtering (and subsequent annealing) are readily available [202, 203] and could, in principle, be extended to include halogen co-sputtering. Additional iodine, for example, with a much higher (1.5 eV) formation energy of I_O substitution and the unstable I_{Sn} substitution, is most likely to form interstitial defects. A post-deposition annealing of tin monoxide doped with iodine, that already contains native V_{Sn} defects, could offer one successful strategy for bringing the two defects together. Once formed such defect complexes would be extremely stable due to the very high activation energy ($E_A = E_B + E_M > 1.5$ eV, where E_M is the energy of the lowest migration pathway of either constituent) required to separate the complex.

5.2.5. The effect of vdWs interactions

As discussed at length in Section 4.2.6 van der Waals interactions are not captured by typical DFT exchange-correlation functionals, including HSE06. This results in the overestimation of predicted distances between the monolayers of SnO. The error in evaluating the spacing between the layers might affect the formation energies of interstitial defects residing in this space. To further verify the validity of our calculations we also investigated the effect the reduction of the inter-layer spacing would have on our results. The case of iodine, the element identified as the most promising for p-type carrier enhancement, was considered.

The intra-layer bond distances in our calculations matched perfectly the experimental values reported in Ref [263]. Thus, simple reduction of the lattice parameter (c) along the stacking direction would lead to bond distortion. Instead, complete monolayers were moved closer to each other, such that the inter-layer bond distances corresponding to experimental observations reported in Ref [263] were reproduced for bulk SnO. Defective supercells (with relaxed atomic geometries) were then used as a starting point and each monolayer was individually moved by the same fixed amount determined for the bulk. Naturally, the supercell lattice was reduced to account for the aforementioned shifts. Further atomic relaxations within the compressed defective supercells were not performed. The results obtained are summarized in Table 5.4.

We estimated the energy increase upon inter-layer reduction for bulk SnO to be 0.42 eV. Intriguingly, the energy corresponding to the iodine interstitial is not signif-

Table 5.4. Summary of the supercell energies for a selection of defects, using different lattice sizes: a computationally optimized and the experimentally measured. The total energy difference between the two cells is also reported.

Structure	Q	E[c=HSE06] (eV)	E[c=EXP] (eV)	E_{diff} (eV)
SnO bulk	0	-1348.688	-1348.265	0.423
I^i	1	-1355.400	-1354.860	0.540
V_{Sn^T}	-2	-1329.699	-1328.641	1.058
$(V_{Sn^T} + I^i)$	-3	-1324.687	-1323.122	1.565

icantly altered when compared to the bulk (0.12 eV). In stark contrast, the energy of the V_{Sn} is affected by a further 0.6 eV. However, the overall shift for the defect complex $(V_{Sn^T} + I^i)$, is found to be roughly equal to the sum of the effects on the isolated defects. As such, the binding energy, E_B^v, evaluated previously remains largely unaffected. Furthermore, such a shift in the formation energy of V_{Sn^T} as the one found in Table 5.4 might help explain why n-type doping in SnO seems to be feasible despite the high compensation by tin vacancies anticipated from most theoretical studies [14, 150].

5.2.6. Discussion

To conclude, $(V_{Sn} + D^i)$ complexes formed by halogens and chalcogens were investigated as potential sources for improved p-type conductivity in SnO. The complexes were observed to be stable in an acceptor state below the valence band edge, providing improved acceptor state stability over isolated V_{Sn}, as well as an amplified number of free-carriers. While, O^i, S^i and Se^i can be incorporated into the film they are energetically unlikely to bind with a tin vacancy, suggesting that achieving enhancement of acceptor donation is improbable. In contrast, halogen impurities offer positive binding energies with the tin vacancy, resulting in three holes generated in the valence band for each complex.

These high ionization states that incur no detrimental effects to the optical properties of tin monoxide are made possible by the double valency of the Sn cation. The proposed mechanism offers a promising method to circumvent the pinning of the Fermi level in tin monoxide allowing for a high performance p-type transparent conductor to be realized with large carrier concentrations. Furthermore, this defect complex strategy offers a viable path for improving the electric properties of other Sn(II)-based materials or alternative multivalent cation containing compounds.

6 Defects under Pressure

A room temperature superconductor has been a century-old dream of the high pressure scientific community that appears to finally be on the verge of being reached [264]. The theoretical prediction [265] and subsequent experimental discovery [266] of superconductivity in H_3S at 200 GPa with a critical temperature, T_C, of 203 K has lead to active research of superconductivity in many other hydride materials [49–58]. Indeed, as of writing this thesis, a new record high T_C of 260 K has been reported for LaH_x at 190 GPa [264].

High pressure (HP) is an exciting field that has evolved incredibly far since the original works of Cailletet, Amagat and Bridgman [267]. The landscape of the high-pressure field changed drastically in 2004 when in his pioneering work Ashcroft suggested chemically precompressed materials as an alternative route to decrease the tremendous pressure necessary to metalize hydrogen [268]. Eremets *et al.* [49] successfully proved the principle in 2008 by metalizing silane. Although subsequent studies attributed these results to probable decomposition or the existence of other stoichiometries [50, 269–273], this work remains the first solid evidence of chemically precompressed materials at high pressure.

Many – if not all – of the structures under high pressure are metastable, i.e. out of thermodynamic equilibrium, at ambient conditions [274]. Consequently, many of the HP phases cannot be recovered at zero applied pressure. This translates to one of the greatest challenges of using pressure in practical applications [275]. Different strategies to aid stabilization of HP structures have been proposed, where a major role is played by the precise control of thermodynamic conditions [276–278]. It is well understood, that compression of molecular systems increases the electron-orbital overlap between neighboring atoms resulting in an increase of the band dispersion, eventually completely closing the electronic band gap. Chemical precompression [268] is certainly one promising route to reduce the metalization pressure in insulating materials [279], but not the only one. Another method to reach metalization is *chemical doping under pressure* – a path previously used at ambient pressures to render standard insulators superconducting [59, 60, 280]. This represents a promising avenue that could be explored for high T_C candidates.

In the following work, we combine the tools used to enhance electronic conductivity in Chapter 4 with pressure, in order to investigate the possibility of attaining high-temperature superconductivity in hydrides via external doping. Two distinct case stud-

---

Research presented in this chapter was adapted with permission from Springer Nature: Flores-Livas J. A., Graužinytė M., *et al.*, Eur. Phys. J. B **91(8)**, 176 (2018). © 2018 EDP Sciences, SIF, Springer-Verlag GmbH Germany, part of Springer Nature. Flores-Livas J. A., Sanna A., Graužinytė M., *et al.*, Sci. Rep. **7(1)**, 6825 (2017). Creative Commons Attribution 4.0 International License.

ies are presented: (i) we look at one of the most abundant and best studied hydrides – H_2O. Undoped ice remains insulating in the terapascal (TPa) pressure range, with metalization predicted to occur beyond 5 TPa [281–284], however, above 100 GPa a covalently bonded phase of the molecular crystal suitable for doping emerges; (ii) we look at another incredibly abundant material – the common plastic (polyethylene, $(H_2C)_n$). This compound is far less studied under pressure and structure prediction methods are utilized prior to doping to determine the stable high pressure phases of this compound.

The questions we aimed to address were: do stable phases of these materials that can be doped under pressure exist? And if so, can these phases, when doped, display superconductivity? Both studies presented were performed in a collaboration with Dr. José A. Flores-Livas and Dr. Antonio Sanna, who performed and analyzed the calculations related to answering the latter question.

6.1. Defect Formation Volume

Thus far the formation volume, v_F, associated with the introduction of a given defect was considered to play a negligible role (see Chapter 3). Straying away from ambient conditions the validity of such an assumption comes into question and a new relevant quantity – the formation enthalpy – emerges. In order to investigate defect formation under high pressures ($P > 100\,\text{GPa}$) properly, the methodology introduced in Chapter 3 needs to be revisited. We return to the formation enthalpy, H_X^F, of a defect, X, as defined through Eq. 3.2.

$$H_X^F = E_X^F(v_F) + Pv_F$$

Here, two new contributions are seen. First, a direct Pv_F term is introduced, for which the volume associated with the formation of the defect needs to be established. Second, the formation energy, E_X^F, obtained by Eq. 3.4, discussed in detail in previous chapters, is now evaluated by relaxing both the atomic positions *and* the lattice of the defective supercell. Thus, the term $E_X^F(v_F)$ also depends (indirectly) on the formation volume as demonstrated by Eq. 6.1. The energy of a supercell containing a defect X in a charge state q that has been allowed to relax from the pure host volume Ω (at an applied pressure P) to a defect equilibrium volume Ω' is denoted here by $E_X^q(\Omega')$.

$$E_X^F(v_F) = (E_X^q(\Omega') + E_{cor}) - (E_{host}(\Omega) + \sum_i n_i\mu_i - q\epsilon_F) \tag{6.1}$$

We can then define a relaxation volume, Ω^{rel}, as the difference between Ω' and Ω. The volume of formation, v_F, on the other hand, represents the size associated with the lattice imperfection excluding the volume of the element creating it. It is, thus, not straightforward to evaluate and is ill-defined in non-elemental systems. To illustrate this we draw an analogy between the notion of chemical potentials (addressed in Section 3.5.1) and the volume of formation.

In an elemental solid of N total atoms, the formation energy of an intrinsic charge neutral defect, X, resulting in a total of $N' = N + n_i$ atoms can be defined through Eq. 6.2. In the case of a vacancy ($n_i = -1$) or an interstitial ($n_i = +1$), the energy ϵ is

clearly defined as the energy per particle, i.e. $\epsilon = \frac{E(N)}{N}$.

$$E^F = E(N') - \frac{N'}{N} E(N) = [E(N') - E(N)] - [N' - N]\epsilon \tag{6.2}$$

In multicomponent materials or when n_i denotes a defect of an impurity species, the second term on the right hand side of Eq. 6.2 is replaced by a chemical potential contribution $[N' - N]\epsilon \rightarrow n_i \mu_i$. This is equivalent to the grand canonical approach, discussed at length in Chapter 3, and ensures that the impurity atoms n_i removed (added) from the cell did not simply disappear (spawn), but were rather put in a different environment with an energy μ_i. It is convenient to rewrite the chemical potential of species i in two terms $\mu_i = \mu_i^0 + \Delta\mu_i$, where $\mu_i^0 = \epsilon_i$, to highlight the fact that there is some flexibility in the chemical potentials of individual species as long as phase-stability conditions are respected. In the case of H_2O, for example, $\Delta\mu_{\mathrm{O}} + 2\Delta\mu_{\mathrm{H}} = \Delta E^F(\mathrm{H_2O})$. The choice of which element takes up more of the contribution is simply representative of different experimental conditions.

Analogously, the formation volume v_F can be defined for an elemental solid using Eq. 6.3. The first term on the right-hand side of Eq. 6.3 is the relaxation volume Ω^{rel} introduced previously and v is the volume per atom inside the elemental solid $v = \frac{\Omega(N)}{N}$.

$$v_F = \Omega(N') - \frac{N'}{N} \Omega(N) = [\Omega(N') - \Omega(N)] - [N' - N]v \tag{6.3}$$

Here, again if n_i denotes a defect of an impurity species, it is possible to select a reference system from which the newly added atom is extracted. Thus, a volume per atom v_i is established, such that $[N' - N]v \rightarrow n_i v_i$. Reasonably, the volume reference system should be taken as the same phase that was used to evaluate the chemical potential (the atom is placed into the same particle reservoir). We can then analogously rewrite v_i as $v_i = v_i^0 + \Delta v_i$, where v_i^0 is the volume per atom of the most stable elemental phase (maximizing the chemical potential), while Δv_i is introduced to account for the possibility of alternative phase formation.

Returning to the example case of ice under pressure, all calculations that obey the volume conservation $\Delta v_{\mathrm{O}} + 2\Delta v_{\mathrm{H}} = \Delta v_F(\mathrm{H_2O})$, correspond to the situation where the removed atoms are forming new layers of H_2O on the surface. Let us imagine a scenario in which the bulk sample is submerged in a pure H_2 environment. We anticipate each removed hydrogen to simply join the H_2 phase, thus $\Delta v_{\mathrm{H}} = 0$. On the other hand, each oxygen atom removed from the bulk may utilize the surrounding H_2 to form an ice-like structure, thus, we can set $\Delta v_{\mathrm{O}} = \Delta v_F(\mathrm{H_2O})$. Though, volume conservation does not have to be strictly obeyed for the bulk material to remain stable, we favor conditions where the host structure is energetically preferred. We can, therefore, assume that when possible removed atoms will tend towards rejoining the structure by forming new layers on the surface.

Defect formation volumes evaluated in this way are directly related to the chemical potentials. As we will see in Case Study A, the formation volume v_F plays a crucial role in defect enthalpies evaluated under pressure. The above approach is, thus, used to estimate a reasonable range of v_F values in order to gain insight into the effects of this contribution for binary systems, where the term is not strictly defined.

6.2. Case Study A - Superconducting H_2O

Despite its simple chemical formula, H_2O appears to have one of the most complex phase diagrams known to man [285]. Over a dozen different crystallographic phases have been reported or predicted in a wide range of temperatures and pressures [281–300]. At ambient pressure and low temperatures ice assumes [286] its phase I, where oxygen has four hydrogen neighbors: two covalently bonded (forming the H_2O molecule) and two connected by hydrogen bonds to neighboring H_2O molecules. Below 200 K, phase I transforms to phase XI, and under compression to phase IX, stable in the range from 0.1 to 1 GPa. Under further compression and at very low temperatures, the phase VIII dominates up to 60–80 GPa. This molecular crystal can be seen as an ordered and symmetric version of phase VII that occurs at high temperatures. At 80–90 GPa the cuprite-type ice-X, characterized by static, symmetric O–H bonds emerges [301–303]. This phase is shown in the right panel of Fig. 6.1.

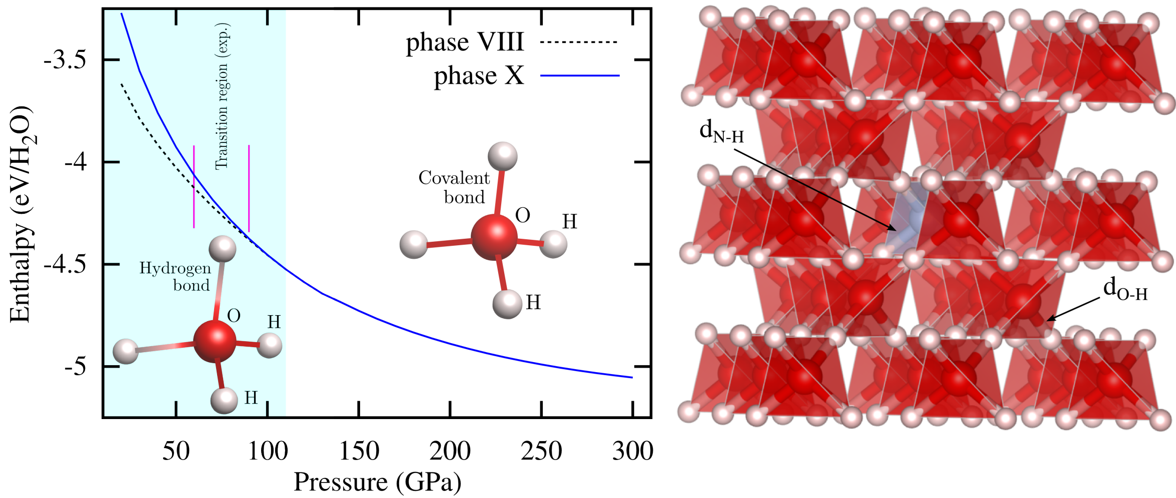

Figure 6.1. Left: Calculated enthalpy for the VIII and X phases of H_2O. Values are given with respect to the elemental decomposition into H_2 + O. The experimental transition region between phases VIII and X, according to Goncharov *et al.* [304], is marked by pink lines. Right: Relaxed atomic structure of N-doped ice phase X at 150 GPa. Oxygen atoms are in red, hydrogen in light pink, nitrogen dopant is indicated by light blue. Nitrogen-hydrogen distances, d_{N-H}, are reduced by 0.1Å when compared to oxygen-hydrogen distances, d_{O-H}.

We investigated ice under pressure by performing density functional theory calculations with the projector augmented wave method as implemented in the Vienna Ab Initio Simulation Package VASP [174, 175]. The energies, atomic forces and stresses were evaluated with the PBE [75] approximation to the exchange-correlation functional. A plane wave basis set with a high cutoff energy of 1000 eV was used and all geometry relaxations were performed with tight convergence criteria such that the forces on the atoms were less than 2 meV/Å and the stresses were less than 0.1 meV/Å^3.

In agreement with experimental knowledge [302, 303], we find that at low pressure

phase VIII dominates (see left panel of Fig. 6.1). Above 110 GPa phase VIII undergoes a transition to the proton-symmetric and experimentally confirmed phase X. Benoit *et al.* [305] have shown that from 102 GPa onwards the proton-ordered symmetric ice-X emerges, i.e. protons are localized at the bond mid-points. At these pressures, quantum effects do not play as crucial a role as they do for the molecular "antiferroelectric" ice-VIII and "paraelectric" ice-VII [306]. Phase X remains the dominant structure up to 210 GPa [307] and is of great interest, as it is no longer a molecular crystal, but a fully covalently bonded material [308]. This is essential for doping induced superconductivity, otherwise impurities would simply result in localized electronic states that cannot participate in the formation of Cooper pairs.

6.2.1. Electronic structure of doped ice under pressure

In order to study doping in H_2O, supercells of ice-X under pressure were created for a range of doping concentrations $H_2O_{1-x}D_x$, with $x = 25\%$, 12.5%, 6.25%, and 4.16%, where D represents the dopant element. Acceptor doping with four different impurity atoms – B, C, N and P – was attempted. A nitrogen doped supercell of ice-X is illustrated in Fig. 6.1. Full structural relaxations (volume and lattice vectors) of the supercells (12 atoms cell for $x = 25\%$, 24 atoms cell for 12.5%, 48 atoms cell for 6.25% and 72 atoms cell for 4.16%) were carried out at 150 GPa. The following k-meshes were used in performing calculations of different supercell sizes: 25% doping, $k = 16\times16\times16$, 12.5% doping, $k = 8 \times 8 \times 8$, 6.25% doping, $k = 4 \times 4 \times 4$, 4.16% doping, $k = 2 \times 2 \times 2$. For low doping (4.16–6.25%), fairly small modifications of the crystal structure of ice-X were found. In contrast, larger doping levels (25%) induced strong deformations around the dopant sites, even if the cuprite-type ice-X global structure was preserved.

Fig. 6.2 depicts the electronic band structures of doped ice-X obtained at 150 GPa with varying impurity concentrations along selected high-symmetry directions. A color scale is used to represent the overlap between the Kohn-Sham states and the atomic orbitals of the impurity atom: red signifies a large overlap (dopant states are dominant), gray shows intermediate overlap, while blue suggests a small overlap (bulk states are dominant). At large doping concentrations (12.5% and 25%), boron and phosphorous induced dispersive defect bands close the electronic gap in ice-X, while at 4.16% and 6.25% the dopant states form localized impurity bands. These atoms are, therefore, not suitable to hole-dope ice-X.

At low doping levels, analogous impurity band formation is also observed with the introduction of carbon, while at higher levels some hybridization between the disperse carbon bands and the host is seen at the top of the valence band. In general a higher density of states at the Fermi level is found with B, C and P impurity incorporation. However, the band structure reveals that these are mostly localized molecular states detrimental to superconductivity, where the dispersion of the band arises from impurity-impurity interactions, rather than hybridization with the host structure. It is important to mention that ice-X has a highly symmetric cubic (P-43m, space group 215) structure with a single unique oxygen substitutional site, which was used here to also investigate high doping levels (i.e. 12.5% and 25%). This corresponds to a dense grid of uniformly spaced impurities, yet many nonequivalent distributions of the defects are, in principle, available to the system at high doping concentrations and could even result in defect

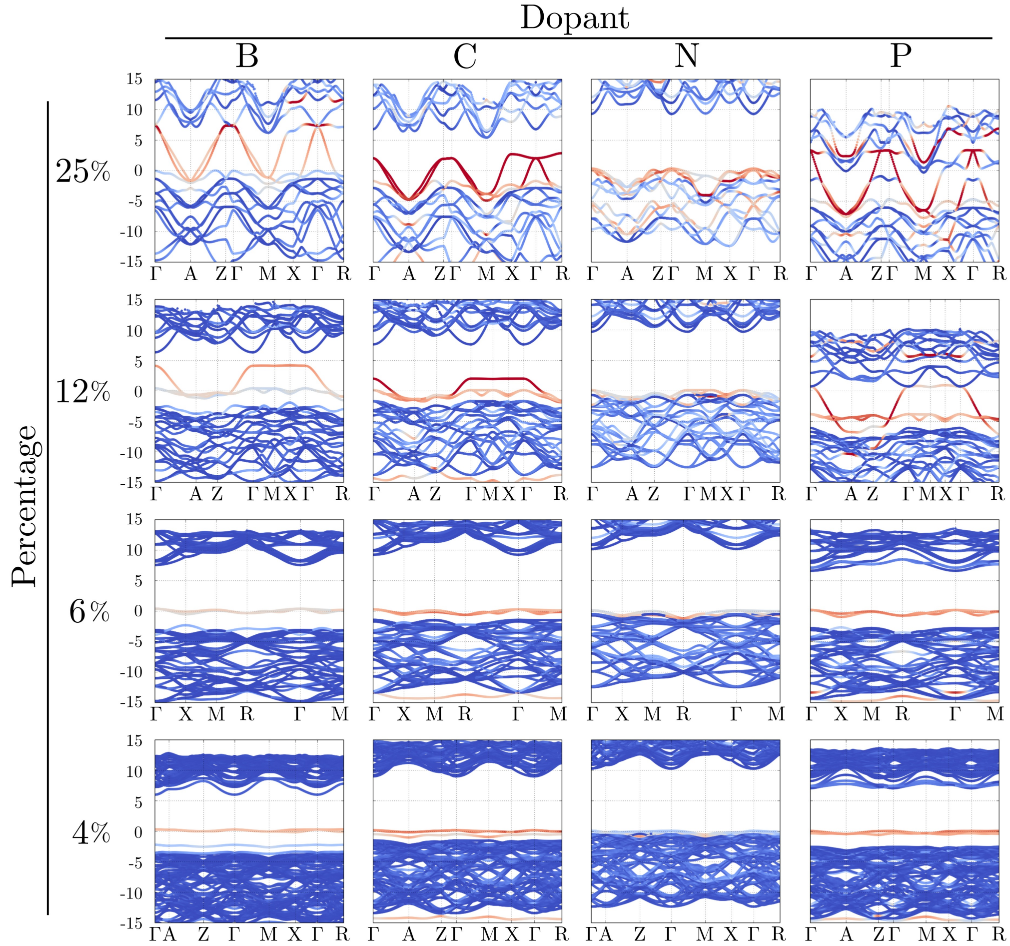

Figure 6.2. Electronic band structure for different dopants (B, C, N and P) in the phase-X of ice at 150 GPa. The Fermi level is set to 0 eV. Color scale represents the overlap of the Kohn-Sham states with the atomic orbitals of the dopant: red means large overlap (dopant states are dominant), gray – intermediate, blue – small (hydrogen and oxygen states dominant).

clustering. A study of all possible combinations of oxygen substitutions is beyond the scope of this work (and would require more advanced techniques, such as cluster expansion [309–311]). Nevertheless, our results are sufficient to provide a general trend of the physics of doped ice under pressure.

In contrast to other impurities, nitrogen induces hole doping in ice-X (see Fig. 6.2) and, as shown in the Supplemental Material of Ref. [312], is also the most likely non-isovalent element to result in stable oxygen substitution. The bottom panel in Fig. 6.3 shows the electronic density of states of undoped ice-X: revealing its insulator behavior, with a PBE electronic band gap of about 10 eV that is not observed to undergo any major modifications at least up to 300 GPa. According to our calculations, the insulator-metal transition is achievable starting from values of 4% nitrogen doping (as seen in Fig. 6.2). For 25% doping, the top valence is mostly dominated by nitrogen states forming a fairly dispersive band. For values between 4% and 12.5%, oxygen and nitrogen strongly

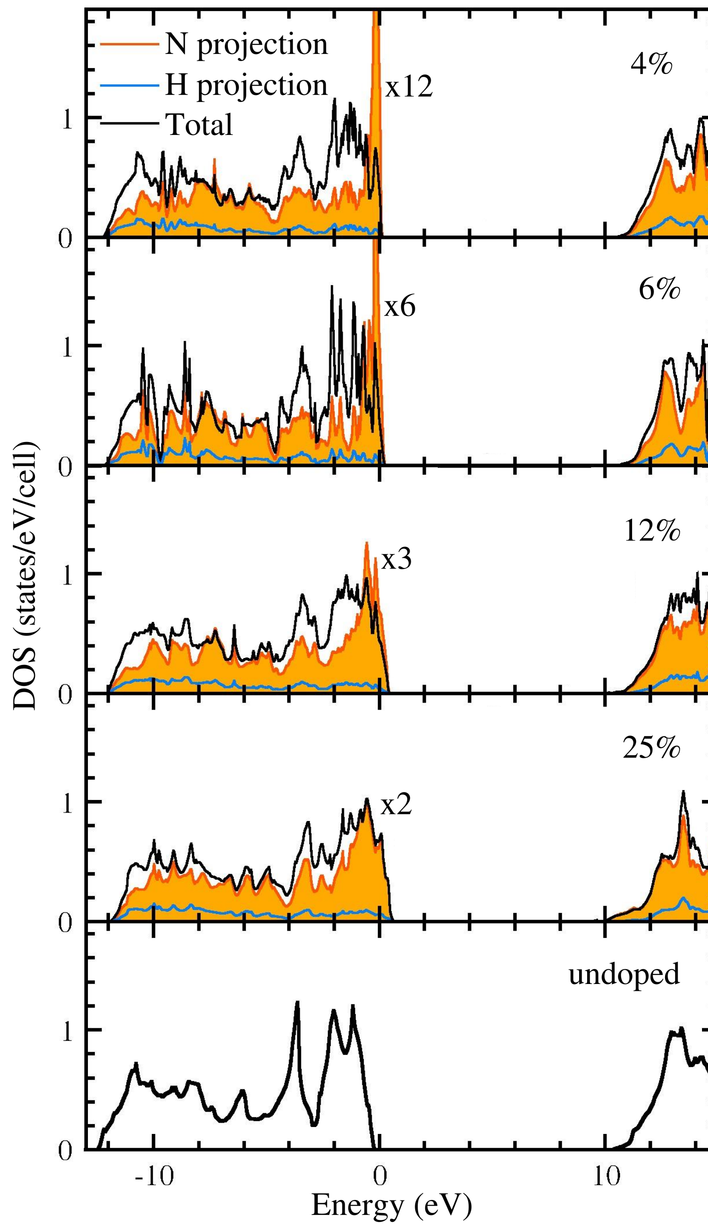

Figure 6.3. Density of states (DOS) of undoped and N-doped ice-X at 150 GPa. Thick black lines show the total DOS, light-blue lines the H-projected DOS and filled orange curves the projection on nitrogen atomic states. Nitrogen states are scaled by the factor indicated in each plot.

hybridize in the top valence forming metallic states (gray colors in Fig. 6.2).

The hybrid O–N nature of the empty states at the valence band is further verified by the projected density of states, shown in Fig. 6.3. At high doping (12.5% and 25%) the density of states at the Fermi level is simply proportional to the fraction of N atoms. On the other hand, at lower doping values (4.16% and 6.25%) the N-projected DOS, although reduced overall, are larger than the N/O fraction. Furthermore, a sharper peak close to the Fermi level can be identified at lower doping, indicating that the

induced holes are more localized on the N-site. We note that the latter concentrations are similar to the doping values used to render diamond or silicon superconducting at ambient pressure [313] and should be realizable experimentally.

6.2.2. Stability of doped-ice under pressure

Phonon band-structures of B, C, N, and P doped ice-X were calculated to evaluate the dynamic stability of these atomic structures. All doped systems were found to be highly unstable with large imaginary frequencies, with the exception of nitrogen, which led to dynamically stable structures in the doping range studied [308]. The stability of nitrogen doped compositions was, therefore, analyzed further. The right panel of Fig. 6.4 shows the calculated formation energy including zero point energy (ZPE) corrections for ice-X as a function of nitrogen content. The inclusion of ZPE has been show to be fundamental for accurate description of the energetics of hydrogen-based systems, especially at high pressures [314, 315].

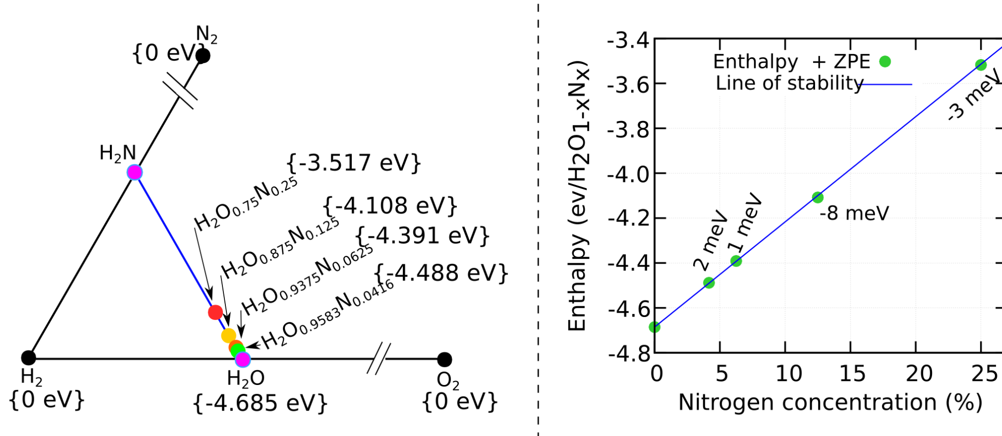

Figure 6.4. Left panel: part of the ternary phase diagram under consideration in this work, solid black dots represent the ground-state of experimentally know structures of H_2, O_2 and N_2 occurring at 150 GPa. Right panel: calculated formation energy and stability line including ZPE corrections for ice-X as function of nitrogen content.

Our systems lie on a straight-line drawn between H_2O and the hypothetical H_2N system where all oxygen in ice-X is replaced by nitrogen. Doped structures of ice-X are enthalpically stable towards decomposition to their elemental solids and all the compositions lie within a couple meV per formula unit above the stability line. The left panel in Fig. 6.4 shows the area of the ternary phase diagram under consideration in this work, with solid black dots representing the ground-state enthalpy of experimentally known structures of H_2, O_2 and N_2 occurring at 150 GPa.

6.2.3. Defect formation energies

We now investigate the acceptor character of substitutional nitrogen, N_O, in greater detail by calculating its defect formation energy and enthalpy and comparing it to

intrinsic defects, such as oxygen, V_O, and hydrogen, V_H, vacancies.

Defect formation energy calculations were performed at a single pressure point of 150 GPa, i.e. the same pressure as was used to obtain the electronic band structures displayed in Fig. 6.2. A $3 \times 3 \times 3$ supercell of ice-X with a k-mesh of $2 \times 2 \times 2$ was used. Formation energies were evaluated using Eq. 3.4 where only local atomic environment relaxations were included, while formation enthalpies were obtained using Eq. 3.2, where the $E_X^F(v_F)$ term was calculated via Eq. 6.1 including volume relaxations. The reference phase used for oxygen was the $C2/m$, ζ structure [316–318], for hydrogen the $C2/c$ (stable in 120–300 GPa range) [319] and for nitrogen the cubic gauche [320]. An electrostatic correction term as implemented in the SXDEFECTALIGN [142] code was applied to all charged defects. The dielectric constant used for electrostatic corrections included both the static dielectric and the ionic contributions. Changes in the dielectric constant with the relaxation volume were not considered.

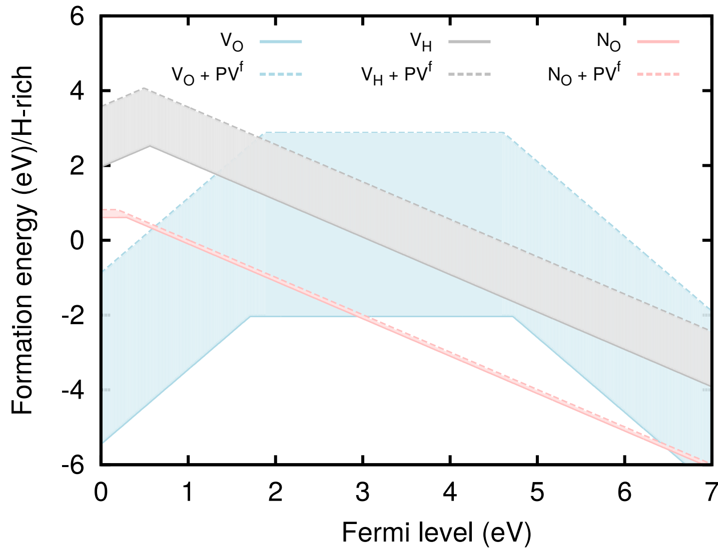

Figure 6.5. Defect formation energies at $P = 150\,\text{GPa}$ in ice-X as a function of Fermi level for oxygen vacancy, V_O, hydrogen vacancy, V_H and nitrogen substitutional on an O-site, N_O, under H-rich conditions. Solid lines show the calculated formation energies, while the dashed lines show the formation enthalpies (including the Pv_F contribution).

The PBE exchange-correlation functional was used to perform defect formation energy calculations in this study. Local exchange-correlation functionals, as discussed at length in Chapter 3, tend to underestimate the electronic band gaps of semiconductors and insulators. However, in this particular case, we focus on acceptor defects and, thus, the underestimation of the band gap is anticipated to play an insignificant role. Any hole states generated should follow the behavior of the valence band and be largely independent of the position of the conduction band. This is no longer the case, for the donor character displaying oxygen vacancies, where the V_O^{+2} compensating defect is likely over-stabilized by PBE†. Nevertheless, the qualitative trends displayed by V_O

†The over-stabilization of dopant states by local functionals when compared to hybrid functionals is discussed in Chapter 4

are informative.

Fig. 6.5 summarizes the calculated formation energies and enthalpies for H-rich experimental conditions as a function of the Fermi level inside the band gap. H-rich conditions are the most favorable for V_O and, hence, N_O formation. The slopes in the formation energy plot show the stable charge state of each defect. For Fermi energies close to the valence band maximum (relevant for hole conductivity) Fig. 6.5 indicates that the most likely defect is V_O^{+2} with N_O^0 found approximately 1 eV higher in energy. The low overall value of the formation enthalpy indicates N incorporation to be plausible, and the fairly shallow acceptor ionization level corresponding to this defect suggests that ionization of nitrogen impurities is achievable. However, our study also suggests that hole compensation by electrons provided by oxygen vacancies in ice-X cannot be ruled out.

Shaded areas outline the large impact that the inclusion of the Pv_F term has on the formation energies at these pressures. At 150 GPa the difference in volumes $\Delta v_F(H_2O)$ between H_2O and elemental H and O phases is 0.66Å, only a fraction of the reference volumes obtained for both V_O ($v_O^0 = 5.44$Å) and V_H ($v_H^0 = 1.94$Å) defects. Thus, the biggest contribution to the formation enthalpy coming from the Pv_F term is a result of the elemental reference phases. However, as cautioned by Bruneval *et al.* [321] volume relaxations of periodic charged calculations cannot be relied upon blindly, as the potential alignment contribution can skew the resultant formation volumes. This suggests that the most definitive information under pressure is obtained from the charge neutral defect formation enthalpies.

6.2.4. Superconducting properties

Different theoretical approaches for studying the effects of doping on the superconducting properties are available. The simplest among them uses a rigidly shifted Fermi level, but leaves both Kohn-Sham eigenvalues and eigenfunctions unchanged. The resulting phonon spectrum and electron-phonon scattering amplitude can then be used within an Eliashberg [322, 323] scheme to compute the superconducting critical temperature as a function of the Fermi level. For the ice-X phase of H_2O at 150 GPa, within this procedure, an astonishingly high phononic superconducting coupling was computed, predicting room-temperature superconductivity already at doping concentrations of a few percent. Although widely used in literature, such a rigid shift approach cannot be expected to yield more than an estimate of the order of magnitude of the critical temperature induced by doping. In fact, the extreme electron-phonon coupling obtained by the rigid shift would induce a strong electronic response, leading to a complete breakdown of the rigid shift approximation. Moreover, the method does not account for the important physical effects stemming from the metallic part of the electronic screening, such as the mechanism responsible for Kohn anomalies [324] that can significantly modify the phonon spectrum.

A more realistic route to theoretical understanding of the effect of doping on superconducting properties is calculating the phonon and electron-phonon matrix elements. Details on the phonon spectra and the electron-phonon matrix elements calculations can be found in Ref. [308]. Comparing these calculations with previous results, a complete restructuring of the phonon energies and the coupling strength is observed. Metaliza-

tion is seen to provide a significant screening causing both a softening of the phonon frequencies and a reduction of the deformation potential. Nevertheless, a significant electron-phonon coupling, λ, was found.

	Doping			
	4.16%	6.25%	12.5%	25%
λ	0.64	0.85	0.67	0.66
T_C (K)	34.4	60.4	33.3	25.6

Table 6.1. Electron-phonon coupling constant (λ) and the calculated superconducting critical temperature (T_C) at different nitrogen doping concentrations [308].

The estimated critical temperatures at different nitrogen concentrations are summarized in Table 6.1. The values of T_C in the range from 20 to 60 K, with the maximum value reached for a doping level of 6.25%, were obtained. Although lower than the astonishing value observed in sulphur hydride (200 K) and considerably lower than the rigid shift prediction (300 K) this is still a sizable T_C, which is much higher than the $\lesssim 4$ K values found in doped semiconductors at ambient pressure.

6.2.5. Discussion

In this study, the possibility of inducing high-temperature superconductivity by doping insulating hydrides under pressure was investigated, using an example case of ice in phase X. Several dopants were analyzed, with the conclusion that only nitrogen leads to dynamically stable hole-doped structures. A possible path to realize such doped phases of ice-X under pressure is high pressure synthesis, similar to the one used to obtain H_2+H_2O clathrates [295]. This method involves room temperature H_2 molecule insertion into a crystalline C_1 (clathrate) phase of water at 0.7 GPa. Experimentally, the unit cell of the C_1 phase contains 36 water molecules in a channel-like arrangement, which can host up to six hydrogen molecules [325, 326]. An analogous synthesis path starting with a N_2+H_2O clathrate (C_1) can be hypothesized, where the percentage of the original N_2 molecules will determine the doping level at high pressure [327]. Unfortunately, it is well-known that N_2 is a very stable molecule, thus, such a synthesis path would likely require high energies to break the strong N–N covalent bonds, achievable perhaps only through laser heating.

An alternative possibility is to start with a less stable molecule, such as ammonia (NH_3). The stability of ammonia is greatly reduced under pressure and, indeed, it has been reported to form super-ionic phases [328]. These compositions have been extensively studied and are well documented, however, only up to relatively low pressures of 50 GPa [329]. A final possibility is to start the synthesis with admixtures of other molecules, such as nitric oxide, NO, nitrogen dioxide, NO_2, or azanide, H_2N. Regrettably, just like amonia all of these compounds have been scarcely studied at high pressures.

Irrespective of the exact experimental method, if doped ice-X structures were successfully synthesized, we predict that for reasonable values of doping a superconducting

transition temperature as high as 60 K at 150 GPa could be reached. Considering the vast number of hydrides that remain insulating under pressure and that can be doped, this result opens up a number of possibilities for the exploration of high-temperature superconductivity.

6.3. Case Study B - Superconducting $(H_2C)_n$

Among polymers, polyethylene is one of the most common and widely produced [330]. Low-density polyethylene, for instance, can be obtained at room temperature by compressing (above 3 GPa) the ordered crystal phase of ethylene with a continuous-wave laser used as an optical catalyst [331]. Highly crystalline polymers can be produced by a similar approach. For pressures up to $\sim$ 40 GPa, polyethylene has been subject to detailed experimental [330, 332] and theoretical studies [333] and the sequence of structural transformations at relatively low pressures is well documented. Furthermore, it was recently shown that the ambient structural properties of polyethylene can be fully recovered after sequential compression/decompression cycles, indicating that polymers are structurally and chemically stable at least up to 50 GPa [334].

Experimental evidence suggests that benzene, C_6H_6, decomposes at pressures above $\sim$ 50 GPa [335, 336]. In fact, it was demonstrated that in its crystalline to amorphous hydrogenated carbon transformation the intermolecular C–C distance always remains the same ($\sim$ 2.6 Å) [337]. This suggests, that the $(H_6C_6)_n$ molecular systems are unstable with respect to the saturated, four-fold carbon coordination at high pressure. As such, independently of benzene or ethylene groups the formation of polymeric phases under high compression seems unavoidable [331, 338]. Yet, further information on structures available to $(H_2C)_n$ compounds under compression is lacking. Investigation of high pressure doping in polyethylene was, thus, started with a structural search in order to identify stable polymorphs of $(H_2C)_n$ at pressures above 50 GPa.

The enthalpy landscape was sampled with the minima hopping method (MHM) [5, 339], using unit cells containing two formula units, $(H_2C)_2$, for a selection of pressures in the range of 50 to 200 GPa. The MHM method has been successfully used for global optimization of an ample number of materials [340, 341] and was designed to thoroughly scan the low-lying energy landscape of any compound. Within this method, stable phases are identified by performing short consecutive molecular dynamics escape steps, followed by local geometry relaxations. The enthalpy surface is efficiently mapped by aligning the velocities in initial molecular dynamics steps approximately along the soft-mode directions [342]. In this way, the Bell-Evans-Polanyi [343] principle is exploited to steer the search towards low energy structures. Energy, atomic forces and stresses within this approach were evaluated at the density functional theory level with the PBE [75] parametrization of the exchange-correlation functional. A plane wave basis-set with a high cutoff energy of 900 eV was used to expand the wavefunction together with the projector augmented wave method, as implemented in the Vienna Ab Initio Simulation Package VASP [174, 175]. Reciprocal space k-grids were generated using the Monkhorst-Pack method with a spacing of 0.3.

Structural search results are summarized in Fig. 6.6, where selected (optimized) polymeric structures are shown, and in Fig. 6.7, where the enthalpy of formation for the se-

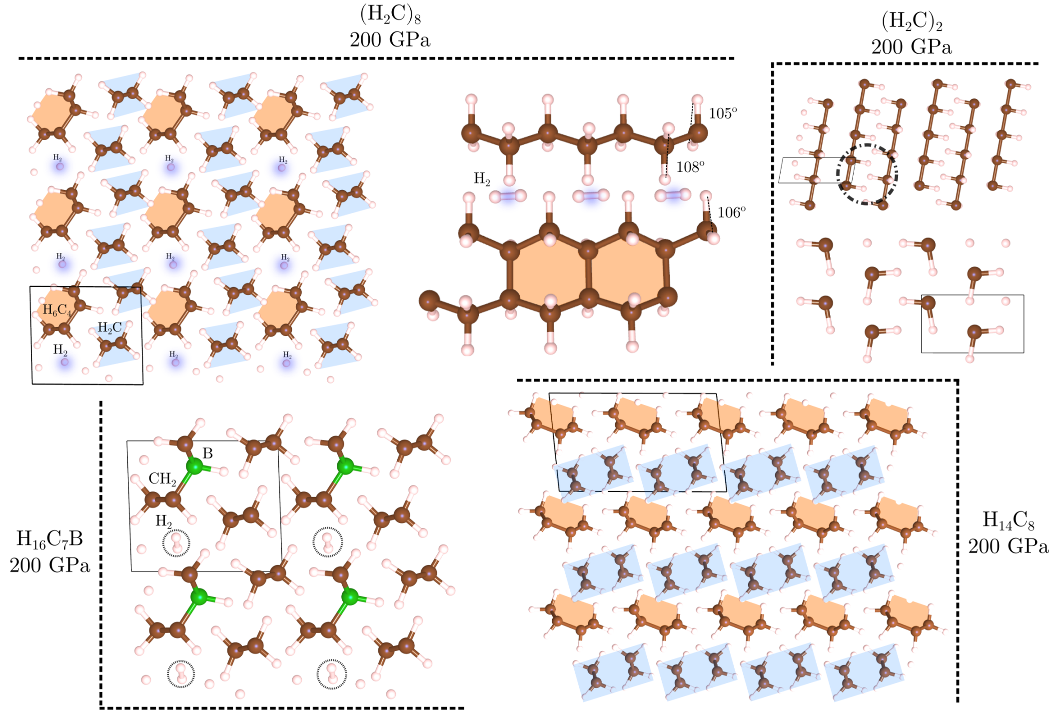

Figure 6.6. Polymeric polyethylene phases at high pressure. Top right: lowest Minima Hopping identified $(H_2C)_2$ structure. Top left: the high pressure $(H_2C)_8$ phase found in this work: two distinct polymeric lines are depicted in orange (H_6C_4) and blue (H_2C), H_2 molecules are also highlighted. Bottom right: the same high pressure $(H_2C)_8$ phase without the H_2 components: two distinct polymeric lines of H_2C are depicted in orange and blue. Bottom left: doped phase of polyethylene with 12% boron.

lected polymeric phases with respect to decomposition towards elemental carbon and hydrogen is summarized. Elemental phases $P6_3m$ (0–120 GPa) and $C2/c$ (120–200 GPa) of solid hydrogen were taken from Ref. [319]. Cubic structure of diamond $Fd\overline{3}m$ was taken as the most stable allotrope in the 50–200 GPa range for carbon. Structural search results, obtained for $(H_2C)_2$ (6 atoms cell), provide a glimpse to the complexity of the system. No stable structure, i.e. lower than the formation enthalpy of individual constituents (zero line in Fig. 6.7), was found. The lowest allotrope identified lies almost 1.7 eV above the stability line. This lowest structure, consistent of *intercalated* polymeric H_2C, is shown in the top right panel of Fig. 6.6 along two different directions.

Evidently, the number of atoms considered within the relatively small cell is not sufficient to rule out the possibility of thermodynamically stable polyethylene phases at high pressure. However, the complexity of the global minimum search increases exponentially with the number of atoms within the unit cell. The problem is no longer tractable even for tens of atoms when density functional level of theory is used. To circumvent this issue in an efficient and timely manner, supercells of the local minima (found with small cells) were constructed using CIF2CELL code [344] and subsequently relaxed along soft-phonon directions. Geometry relaxations were performed with tight parameters such that the forces acting on the atoms were below 2 meV/Å and the stresses were less than 0.1 eV/Å^3. With this procedure a novel polymeric phase, which

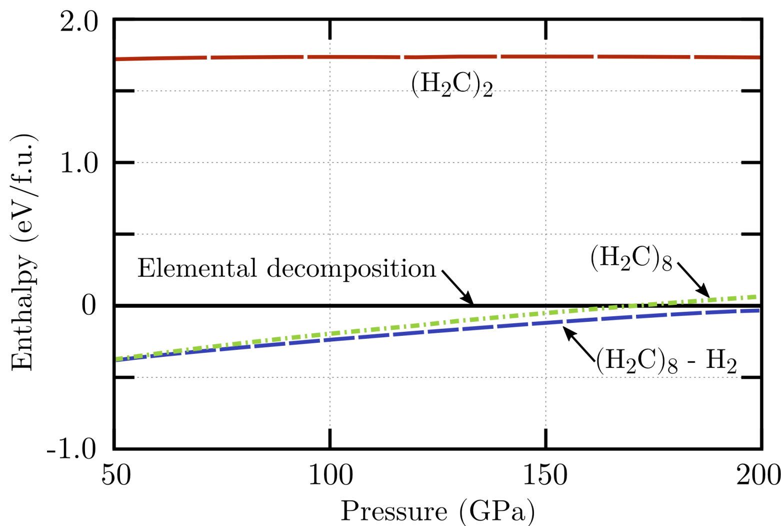

Figure 6.7. Calculated formation enthalpy for H_2C as function of pressure towards elemental decomposition into H_2 and C. Small simulation cells of $(H_2C)_2$ are thermodynamically unstable in the pressure range studied. Large simulation cells $(H_2C)_8$ are considerably more stable towards decomposition.

is thermodynamically stable against elemental decomposition, was identified.

The structural motif can be seen in the top left panel of Fig. 6.6. Interestingly, the new phase (marked $(H_2C)_8$ at 200 GPa) consists of two distinct polymeric groups: polymerized cyclohexanes in 'boat' configurations [345] (colored in orange) and interconnected methylene groups (colored in blue). The two units form a polymeric crystal with $P1$ symmetry, that lies considerably lower in the enthalpy plot (see the green line in Fig. 6.7) than the small $(H_2C)_2$ structure. A quick comparison with enthalpies computed by Wen-Hoffmann-Ashcroft [346] for predicted phases of polymeric benzene and layered graphane under pressure suggests that the newly identified structure is enthalpically lower. While not exact, the comparison is appropriate as the same Kohn-Sham functional (PBE) was used in their calculations and the zero reference line was computed with respect to elemental decomposition (carbon + hydrogen) into the same crystal structures.

A notable feature of the newly identified structure is the H_2 molecules occupying voids between the two polymeric groups. Hence, a logical question arises, what is the role played by the H_2 molecules in the system? To address this question, the H_2 components were removed from the low-enthalpy structure of polyethylene $(H_2C)_8$ and a further geometry optimization was performed. The computed enthalpy is shown in Fig. 6.7 as a dashed blue line. At low pressures, the stability is not strongly affected by the lack of H_2 and similar enthalpies are found when compared to polyethylene. Compressing the system further, however, results in increased stabilization of the polymeric phase by the removal of H_2. This is not a surprising outcome, one could simply imagine that under compression the reduction of volume brings the two main polymeric groups closer together, pushing out the H_2 molecules due to repulsive Coulomb interactions (dehydrogenating the polyethylene at high pressure). The resulting structural motif,

following the removal of H_2, can be seen in the bottom-right panel of Fig. 6.6. At 200 GPa, a 6 % reduction in volume results from the H_2 component removal, however, the overall C–H distances and angles within the polymeric motifs are preserved.

6.3.1. Electronic structure of doped polyethylene under pressure

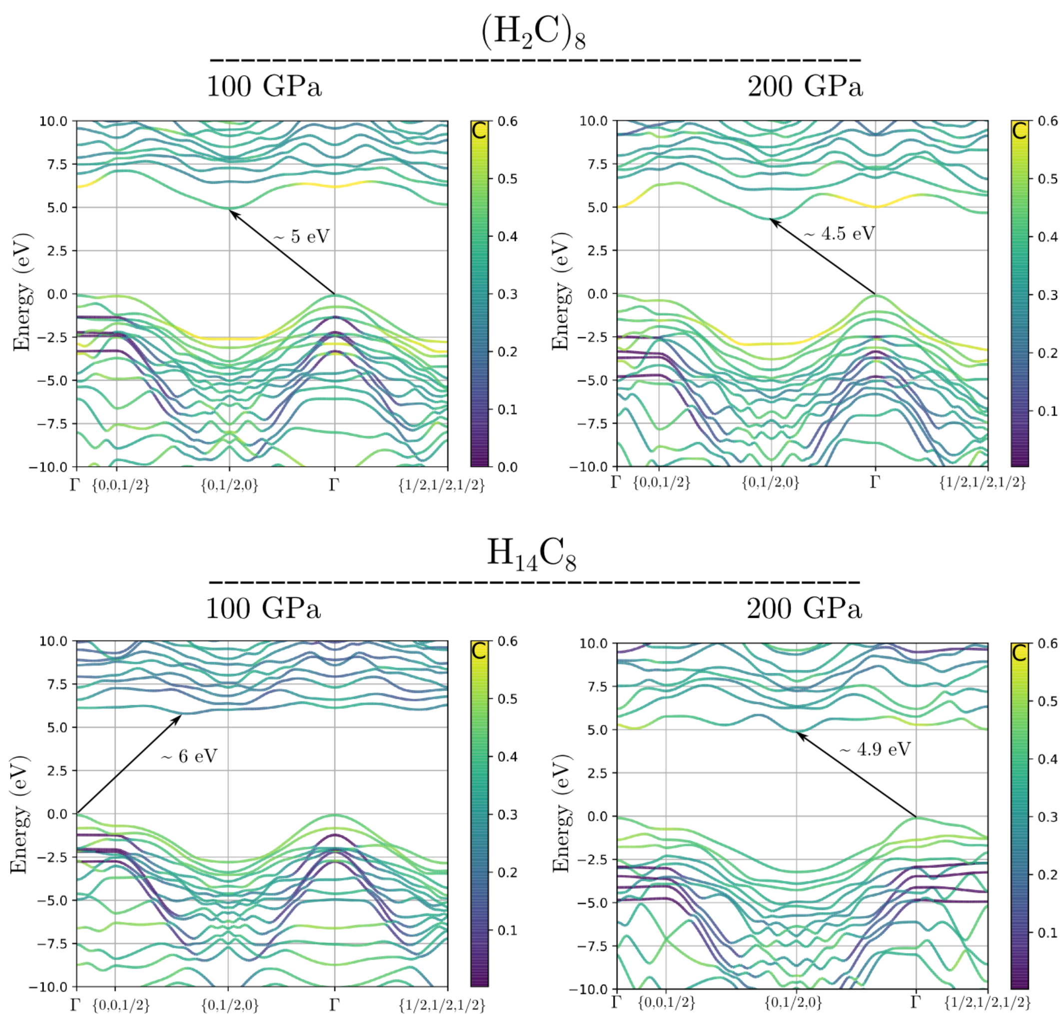

Figure 6.8. Electronic band structures computed for polymeric phases of polyethylene at different pressures. Polyethylene at 100 GPa is an insulator with a indirect band gap of 5 eV that closes to 4.5 at 200 GPa. By removing the H_2 components in polyethylene the gap increases to 6 eV at 100 GPa.

The electronic band structures calculated for the stable high pressure polymeric phases with and without interstitial H_2 are summarized in Fig. 6.8 (only two pressure points are shown). Polyethylene at 100 GPa is an insulator with an indirect band gap of 5 eV that closes by 0.5 eV at 200 GPa. Assuming a linear dependence of the band gap, pressures above a terapascal would be necessary to fully close the gap. The same phase without H_2 (marked as $H_{14}C_8$) possesses a larger indirect band gap of 6 eV at 100 GPa. Interestingly, the top of the conduction band shows decreased dispersion when

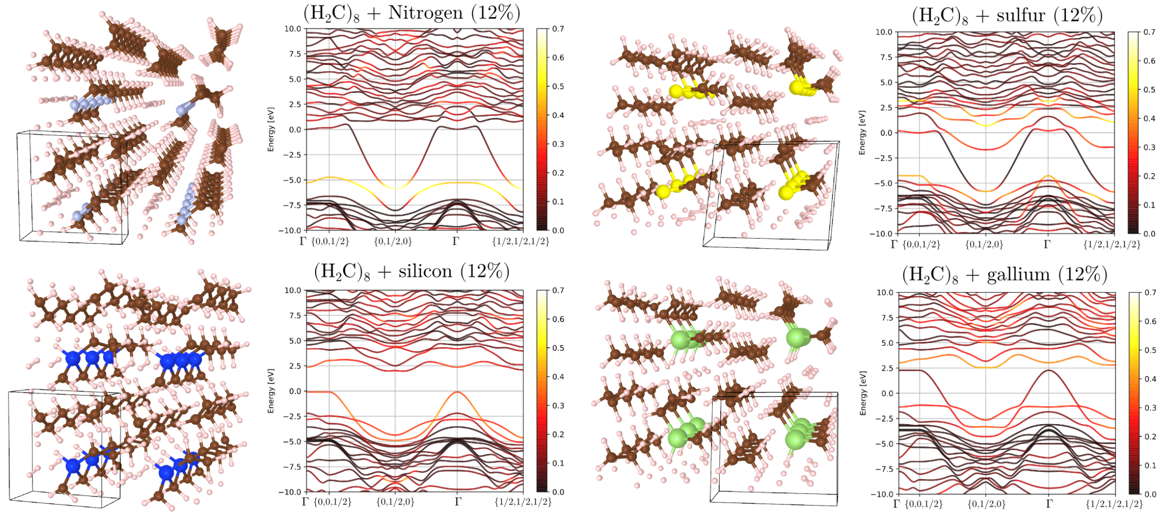

Figure 6.9. Crystal structures of $(H_2C)_8$ doped with N, Si, S and Ga, and the corresponding electronic band structures. Colour scale indicates Kohn-Sham states projected onto hydrogen orbitals.

compared to the conduction band of $H_{16}C_8$. This is due to the increase in repulsive forces between the two main polymeric chains, while in $H_{16}C_8$ these are mediated via H_2 molecules. The gap closes to a value of 4.9 eV at 200 GPa, but still an enormous pressure would be necessary to metalize this system.

Ten different elements (Li, Be, Na, B, N, Al, Si, Ga, P, S) were tested as possible acceptor dopants for the identified stable structure of $(H_2C)_8$. The study was conducted at the lowest pressure (50 GPa), where the phase is most stable against elemental decomposition. Substitutional doping on a single carbon-site belonging to the main polymeric chain of H_6C_4 (shown in orange in Fig. 6.6) was considered initially. In this pre-screening step we were interested only in elements that do not strongly *disrupt* the local environment (i.e. destroy the polymeric chains). The elements that were found to preserve the overall structural motif of polyethylene are shown in Fig. 6.9. The elements – Li, Na, Be, Al, P – are not shown, as they appear to significantly alter the host structure of polyethylene and produce dimerization of the polymeric chains that suggests amorphization. Such behavior is not suitable for doping and, as such, these elements were excluded from further consideration.

Interestingly, we observe nitrogen substitution to induce a structural distortion that leads to the formation of H_2 chains along the polymeric lines (see Fig. 6.9). These resemble the linear chains of hydrogen formed in H_3S [265, 266] and may offer an interesting avenue for future explorations. Silicon, since it is isovalent to carbon, does not dope the system. However, volumetric effects result in a drastic reduction of the electronic gap from 6 eV to 2.5 eV. Nevertheless, not sufficient to induce metalization. Sulfur and gallium lead to volume expansion and are seen to result in the presence of a very dispersive band that heavily modifies the electronic structure. This highly dispersive band found below the Fermi level (0 to -5 eV) with N, S and Ga doping, is seen to have strong contributions arising from the H_2 molecule/chain states, as demonstrated

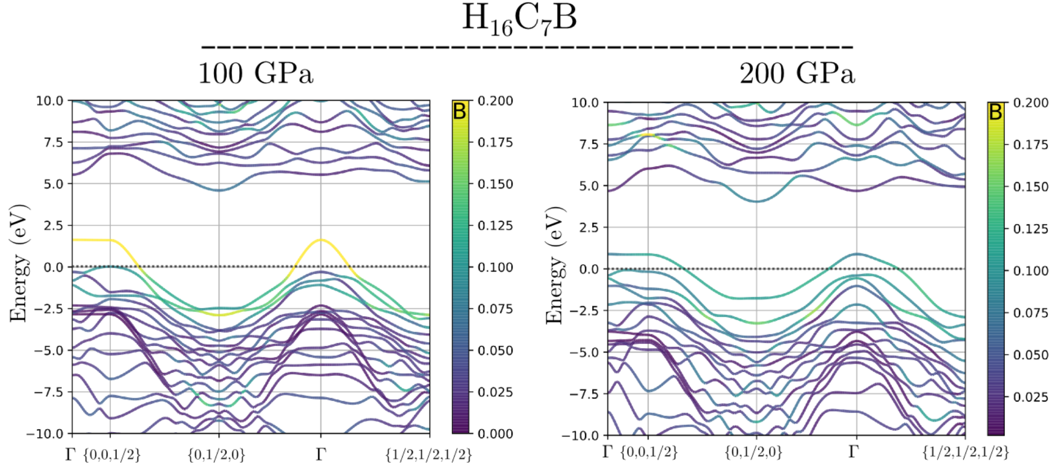

Figure 6.10. Electronic band structure computed for polymeric phases of polyethylene doped with boron at different pressures. Sufficient holes are produced in the band structure to demonstrate metallic behavior. Colour scale shows Kohn-Sham projected states onto boron orbitals.

by the projected Kohn-Sham states shown in Fig. 6.9.

Finally, boron, was identified as the impurity element most promising to act as a shallow acceptor. For this element all available substitutions at different carbon-sites were tested (full optimization of atomic positions and lattice vectors) and ranked energetically. The structural motif of $H_{16}BC_7$ with the lowest enthalpy at 200 GPa is shown in the bottom left panel of Fig. 6.6, equivalent to 12 % boron doping. The corresponding electronic structure is shown in Fig. 6.10. The color in the band structure plot highlights the projected Kohn-Sham states corresponding to boron (normalized to the value of 0.2 for clarity), identifying the energy regions in which boron-derived states offer the strongest contributions. We observe that in the proposed polymeric high-pressure phase, boron could hole-dope polyethylene, turning it metallic, in a pressure range of 100-200 GPa.

Explicit formation energy calculations were not performed for this system, due to the unknown high pressure reference phases for the ternary B-C-N system. As was shown in the previous case study of doped water under pressure, the formation volume plays an extremely important role in defect formation energetics. Thus, without adequate identification of reference formation volumes, meaningful insights from the calculated formation enthalpies could not be extracted. Nevertheless, the lack of localized boron bands in the electronic structure of polyethylene clearly hints to shallow acceptor behavior of the impurity.

The thermodynamic stability of polyethylene and the possibility of its metalization upon doping have been addressed so far. Another, essential quality to consider is the structural stability of the suggested phases. This was addressed by verifying that all calculated phonon frequencies for the doped-phases are real. The non-doped case was, of course, dynamically stable by construction. The H_2-poor variant was also confirmed to be structurally sound. In contrast, the doped $H_{16}BC_7$ was found to be dynamically unstable along finite q-vectors in the Brillouin zone at lower pressures (<100 GPa),

however, the phase becomes stable at elevated compression (200 GPa) [347].

6.3.2. Superconducting properties

Different theoretical methods for studying the effect of doping on the superconducting properties are available. The simplest – a rigid shift of the Fermi level leaving both Kohn-Sham eigenvalues and eigenfunctions unchanged is computationally cheap, but ignores the effects of structural relaxations on electronic states and does not account for changes in the phonon spectrum induced by excess charge. An alternative approach, manipulates the number of electrons directly in the simulations. Extra electrons are compensated for by a uniform (jellium) background to ensure charge neutrality. This method properly accounts for metalization and lattice relaxations in the doped system and is physically similar to doping by an intense electrostatic field [348]. A third approach, simulates chemical doping by using a doped supercell of the host material that results in hole or electron creation. Chemical doping is complex and cumbersome to simulate as it involves local structural relaxations of large supercells. Furthermore, in order to find suitable elements different doping locations, such as inequivalent site-substitutions, interstitials, etc., has to be consider before a prediction can be attempted.

The third approach was chosen in our work, as the two proposed structures, $(H_2C)_8$ and $H_{14}C_8$, have been verified as dynamically stable and boron substitution, as shown in the previous section, was checked for all sites and found to induce metalization on the thermodynamically stable position. Thus, superconducting properties using the chemically doped supercell $H_{16}BC_7$ were calculated. The electron-phonon spectral function obtained within linear-response for the doped $(H_2C)_8$ polymer reveals that the system possesses a moderate electron-phonon coupling, λ, calculated between 0.77 and 0.8 depending on the pressure. The calculated transition temperature is non-negligible and oscillates between the values of 35 to 42 K in the range between 180 GPa to 250 GPa. Details on the phonon spectra and the electron-phonon matrix elements calculations can be found in Ref. [347].

The calculated values of T_C depend on the parametrization chosen for the Coulomb pseudopotential, where a standard value ($\mu^* = 0.1$) was used [323]. It is possible that this assumption becomes inapplicable in the high pressure regime. Yet, further assessments of the exact value of the Coulomb pseudopotential on polymeric systems are difficult to make. If instead, a very strong Coulomb repulsion was chosen, in principle, the superconducting phase could vanish completely. While using values of 0.2 for μ^*, reduces the T_C by roughly a half: 15 K at 180 GPa and 200 GPa and 17 K at 250 GPa. These would, nevertheless, be well measurable values of T_C.

6.3.3. Discussion

No experimental or theoretical work on the high pressure domain (above 50 GPa) of polyethylene has been previously reported. In this study, we investigated the potential energy surface of $(H_2C)_n$, using a small unit cell that resulted in a prediction of two new polymeric phases. Interestingly, the postulated structures are considerably lower in enthalpy than those studied by Fontana *et al.* [333] ($Pnam$, $A2/m$ and $P2_1/m$ phases at 40 GPa) and the same two phases, $(H_2C)_8$ and $H_{14}C_8$, are comparable (or lower) in

enthalpy than benzene polymorphs and graphane phases at the same pressure [346]. Further experimental studies at pressures above 50 GPa could be used to verify our findings, perhaps the predicted polymeric phase is the product of compressed polyethylene/benzene? Our calculations point towards a low-symmetry phase comprised of H_6C_4 and H_2C groups stabilized by interstitial H_2 molecules, while further compression may result in the release of the H_2 from the main host. Metalization of polyethylene by boron doping of the newly predicted phase was also investigated. However, the range of stability identified for the boron doped ($H_{16}BC_7$) phase is relatively narrow, with dynamical stability observed in the 170 GPa to 250 GPa range and enthalpic stability (towards elemental decomposition) found only below 200 GPa. This limits the range of suitable synthesis conditions to a window of $\sim$ 30 GPa. To achieve doping under pressure, one could hypothesize methods analogous to those proposed for ice doping in Section 6.2.5, such as laser-heating aided decomposition of molecules that releases agents (doping elements) which target native vacancies or incorporate as interstitials at high pressure. If synthesized, we predict boron doping to induce metallic behavior in the insulating organic-polymeric polyethylene under pressure that leads to superconductivity with a T_C of $\sim$ 35 K at 180 GPa.

7 Summary and Outlook

In this thesis, enhancement of materials properties using carefully selected defect incorporation was investigated. In order to improve conductivity an efficient dopant screening-approach was designed that allows for all elements in the periodic table to be quickly examined as candidates for free-carrier generation. Applying this approach to substitutional defects in two different materials we revealed multiple novel dopant elements for each compound. Additional paths for improving the features of transparent conductive oxides were explored by examining the interactions between an important (ubiquitous) native defect and a selection of impurity atoms in either compound. We demonstrated that in this way both optical absorption properties and carrier generation can be boosted outside the range of control permitted by tuning only intrinsic defects. Finally, we looked into the possibility of doping under high pressure. We developed an approach for quantifying reference formation volumes and explored the dependence of defect formation enthalpies on the formation volume in ice under pressure. We demonstrated that measurable superconductivity could be induced by doping in common hydride materials at pressures significantly lower than those required for the undoped metalization transition. Below we review the main results.

Screening of useful dopants. A comprehensive scheme for useful dopant screening in semiconductor materials was presented. Within this scheme, a pre-screening step employing local density functional theory calculations was used with two parameters chosen for quantifying enhancement in optical properties and carrier generation. The approach was successfully applied in two (n-type and p-type) test cases of tin-based oxide materials and was demonstrated to work equally well in a layered compound. Our investigations identified 6 elements – Nb, Ta, P, As, Sb and I – that are able to dope SnO_2 n-type, while preserving its good optoelectronic properties. Thirteen elements acting as shallow donors were found suitable for doping SnO n-type: Nb, Ta, P, As, Sb (the same dopants are effective in SnO_2) and Sc, Y, Ti, Zr, Hf, W, Al, F. However, only four of them, P, As, Sb and F, preserved the optical transparency displayed by undoped SnO films. We excluded the possibility of p-type doping in SnO_2 via Sn-site substitution, but for SnO five alkali metals – Li, Na, K, Rb and Cs – were identified as prospective acceptors on this site. The large variety of potential dopant elements (not yet experimentally explored) discovered through these studies, demonstrates the relevance of such a large-scale dopant screening methodology in designing materials for industrial applications.

Improved optical absorptance. A computational defect study was employed to explain the experimentally observed optical improvements in tin-based oxide materi-

als resulting from silicon incorporation. We demonstrated that silicon impurities in the rutile SnO_2 lattice preferentially incorporate on those Sn-sites that neighbour an oxygen deficiency (V_O). This is a result of the significant binding energy between a substitutional silicon atom and a V_O. We revealed that the presence of a neighboring silicon promotes the ionization of oxygen vacancies releasing charge carriers into the host. The ionization of V_O is accompanied by structural relaxations that push electronic defect states close to the edge of the band gap and, thus, result in a passivation of optically detrimental states in Sn-based TCOs. The tendency for V_O ionization by silicon incorporation was linked to local structural strain created by the presence of silicon impurities. Similar strain induced changes were explored using other group IV-A elements. We speculate that native defects in n-type TCOs formed by other metals, that nevertheless display similar DX-center behavior, could be analogously manipulated by the addition of isovalent impurities.

Divalency of tin. The prospect of utilizing the divalency of tin, i.e. its ability to exist in both a Sn(IV) and a Sn(II) state, to enhance free-carrier generation in SnO was investigated. We proposed the possibility that the double valency of tin could equally result in elevated ionization states of the native V_{Sn} defect. We demonstrated that these higher charge states can indeed be stabilized by binding the vacancy to a halogen interstitial to form (V_{Sn} + D^i). Halogen complexes resulted in an amplified number of holes generated in the valence band, without significantly impacting the electronic band structure of the material. The higher charge state ($q = -3$) remained stable for Fermi levels below the valence band edge, providing improved acceptor state stability over isolated V_{Sn}. Tin vacancy interactions with chalcogen interstitials were also considered. While elevated charge states ($q = -4$) of the defect complex were observed, negative binding energies for the complexes were found. The proposed mechanism offers a unique method for enhancing the characteristics of this material and suggests a viable path for improving the electric properties of other double-valent metal compounds and further Sn(II)-based materials, such as SnS or SnSe.

Defects under pressure. Doping-induced superconductivity in otherwise insulating hydrides under pressure was investigated. Phase X of ice, H_2O, and a phase of polyethylene, $(H_2C)_n$, predicted in a structural search were considered as example cases. Two polymeric high-structure phases were identified for $(H_2C)_n$ under pressure and calculated to lie considerably lower in enthalpy than those suggested in previous studies [333, 346]. Several dopant atoms were analyzed for each compound, yet only a single element was identified to result in a dynamically stable acceptor doped structure: nitrogen in ice, and boron in polyethylene. For reasonable values of doping, ice-X structures were predicted to have a superconducting transition temperature as high as 60 K at 150 GPa. We predicted boron doping to induce metallicity in polyethylene under a pressure of 200 GPa that could lead to superconductivity with a T_C of $\sim$ 35 K. Unfortunately, the range of stability identified for the boron-doped ($H_{16}BC_7$) phase is relatively narrow, with a window of only $\sim$ 30 GPa. Considering the vast number of hydrides that remain insulating under extreme pressure, these example results showcase new possibilities for the exploration of high-temperature superconductivity presented by doping.

7.1. Outlook

Preliminary results of our experimental colleagues at EPFL seem to indicate that, indeed, in an amorphous tin-based oxide (which crystallizes into a rutile SnO_2 structure) iodine doping could result in an enhanced number of charge carriers, confirming one of our novel theoretically predicted dopants. This suggests that an analogous screening-approach could successfully improve properties of a large variety of alternative compounds. Thus, a natural extension of the current work would be to scan for useful dopants in other oxides, such as TiO_2 [349], expanded phases of ZnO [350], or even In_2O_3 [32], where large scope defect investigations are of relevance. Furthermore, such investigations could be made even more impactful when combined with high-throughput structural search results for new transparent conductor compounds [42–45]. One such study is already underway for a potential ambipolar transparent conductor – cuprous iodide, CuI – that displays an appropriate band gap and significant dispersion in both conduction and valence bands [351]. Our initial results for this compound suggest that both donor and acceptor dopants can be successfully incorporated. Furthermore, the method presented in Chapter 4 can be just as easily adopted for dopant studies of any semiconducting material, where electrical property improvement is important, e.g., in thermoelectrics [28].

In Chapter 5 we demonstrated that impurity interactions with native defects are very important. Interestingly, in both cases we illustrate an effect arising from a non-obvious defect interaction, i.e. one not mediated through electrostatics. The role of defect induced strain/stress is, thus, revealed to be significant when considering defect complexes. In particular, the consequences of isovalent Si interactions with V_O in SnO_2 are observable experimentally. This demonstrates that local strain effects can really change intrinsic defect behavior in a way that is technologically beneficial. Similar intriguing behavior for native defects has also been predicted in the presence of external strain [352, 353]. A natural question to ask is, thus, if other TCO materials could benefit from isovalent doping? In a future publication we intend to demonstrate the generality of the isovalent-doping approach by investigating a variety of wide band gap TCO compounds, where native defects are predicted to be the leading cause of carrier-generation. Additionally, follow-up work investigating divalency assisted doping in alternative Sn(II)-compounds, such as SnS and SnSe, could be of interest.

Finally, we discussed the possibility of dopant-induced superconductivity under pressure. We speculated that doped phases at high-pressure could be achieved in experiments by laser-heating aided decomposition of molecules, which subsequently release agents (doping elements) that target native vacancies or incorporate as interstitials. This, however, suggests that a somewhat simpler problem should be addressed first: how can control over vacancies or formation of native defects be achieved under high pressure? The evolution of crystalline defects under pressure, especially high pressure, is a field with many open questions that still remains poorly studied [321]. Thus, investigation of native defect formation energies and their dependence on pressure and the volumes of formation for various technologically relevant hydride compounds is an avenue that certainly warrants further exploration in the nearby future.

Bibliography

[1] S. M. George, Chem. Rev. **110**, 111 (2009).

[2] F. Oba and Y. Kumagai, Appl. Phys. Express **11**, 060101 (2018).

[3] R. M. Martin, *Electronic structure: basic theory and practical methods* (Cambridge university press, 2004).

[4] N. W. Ashcroft and N. D. Mermin, *Solid state physics* (Saunders College Publishing, 1976).

[5] M. Amsler and S. Goedecker, J. Chem. Phys. **133**, 224104 (2010).

[6] R. Martoňák, A. Laio, and M. Parrinello, Phys. Rev. Lett. **90**, 075503 (2003).

[7] M. Deem and J. Newsam, Nature **342**, 260 (1989).

[8] T. Bush, C. R. A. Catlow, and P. Battle, J. Mater. Chem. **5**, 1269 (1995).

[9] M. Jansen, Angew. Chem. Int. Ed. **41**, 3746 (2002).

[10] M. Aykol, S. S. Dwaraknath, W. Sun, and K. A. Persson, Sci. Adv. **4**, eaaq0148 (2018).

[11] C. Beachem, Metall. Mater. Trans. B **3**, 441 (1972).

[12] B. D. Evans, G. J. Pogatshnik, and Y. Chen, Nucl. Instrum. Methods Phys. Res. B **91**, 258 (1994).

[13] E. Rucavado, M. Graužinytė, J. A. Flores-Livas, Q. Jeangros, F. Landucci, Y. Lee, T. Koida, S. Goedecker, A. Hessler-Wyser, C. Ballif, *et al.*, J. Phys. Chem. C **122**, 17612 (2018).

[14] M. Graužinytė, S. Goedecker, and J. A. Flores-Livas, Chem. Mater. **29**, 10095 (2017).

[15] M. Graužinytė, S. Goedecker, and J. A. Flores-Livas, Phys. Rev. Mater. **2**, 104604 (2018).

[16] C. Lue, J. H. Ross Jr, K. Rathnayaka, D. Naugle, S. Wu, and W. Li, J. Phys. Condens. Matter **13**, 1585 (2001).

[17] G. Jiang, J. He, T. Zhu, C. Fu, X. Liu, L. Hu, and X. Zhao, Adv. Funct. Mater. **24**, 3776 (2014).

[18] N. p Johnson, F. Ponce, R. Street, and R. Nemanich, Phys. Rev. B **35**, 4166 (1987).

[19] M. Fujinami, A. Tsuge, and K. Tanaka, J. Appl. Phys. **79**, 9017 (1996).

[20] G. Watkins and J. Corbett, Phys. Rev. **138**, A543 (1965).

[21] R. Krause-Rehberg and H. S. Leipner, *Positron annihilation in semiconductors: defect studies*, Vol. 127 (Springer Science & Business Media, 1999).

[22] M. Islam, R. Davies, C. Fisher, and A. Chadwick, Solid State Ionics **145**, 333 (2001).

[23] Q. Zhu, Q. Ma, D. B. Buchholz, R. P. H. Chang, M. J. Bedzyk, and T. O. Mason, J. Appl. Phys. **115**, 033512 (2014).

[24] A. Catalano and R. Hall, J. Phys. Chem. Solids **41**, 635 (1980).

[25] T. Dalibor, G. Pensl, H. Matsunami, T. Kimoto, W. Choyke, A. Schöner, and N. Nordell, Phys. Status Solidi (a) **162**, 199 (1997).

[26] S. Tongay, J. Suh, C. Ataca, W. Fan, A. Luce, J. S. Kang, J. Liu, C. Ko, R. Raghunathanan, J. Zhou, *et al.*, Sci. Rep. **3**, 2657 (2013).

[27] S. Curtarolo, G. L. Hart, M. B. Nardelli, N. Mingo, S. Sanvito, and O. Levy, Nature Mater. **12**, 191 (2013).

[28] S. Wang, Z. Wang, W. Setyawan, N. Mingo, and S. Curtarolo, Phys. Rev. X **1**, 021012 (2011).

[29] K. Yang, W. Setyawan, S. Wang, M. B. Nardelli, and S. Curtarolo, Nature Mater. **11**, 614 (2012).

[30] G. Ceder, MRS Bull. **35**, 693 (2010).

[31] T. Minami, Semicond. Sci. Technol. **20**, S35 (2005).

[32] G. Bühler, D. Thölmann, and C. Feldmann, Adv. Mater. **19**, 2224 (2007).

[33] E. Fortunato, D. Ginley, H. Hosono, and D. C. Paine, MRS Bull. **32**, 242 (2007).

[34] L. Wang, D. W. Matson, E. Polikarpov, J. S. Swensen, C. C. Bonham, L. Cosimbescu, J. J. Berry, D. S. Ginley, D. J. Gaspar, and A. B. Padmaperuma, J. Appl. Phys. **107**, 043103 (2010).

[35] B. G. Lewis and D. C. Paine, MRS Bull. **25**, 22 (2000).

[36] Ç. Kılıç and A. Zunger, Phys. Rev. Lett. **88**, 095501 (2002).

[37] J. Varley, A. Janotti, A. Singh, and C. Van de Walle, Phys. Rev. B **79**, 245206 (2009).

[38] A. K. Singh, A. Janotti, M. Scheffler, and C. G. Van de Walle, Phys. Rev. Lett. **101**, 055502 (2008).

[39] P. Ágoston, K. Albe, R. M. Nieminen, and M. J. Puska, Phys. Rev. Lett. **103**, 245501 (2009).

[40] S. Lany and A. Zunger, Phys. Rev. Lett. **98**, 045501 (2007).

[41] K. Ellmer, Nat. Photonics **6**, 809 (2012).

[42] G. Hautier, A. Miglio, G. Ceder, G.-M. Rignanese, and X. Gonze, Nat. Commun. **4**, 2292 (2013).

[43] A. Bhatia, G. Hautier, T. Nilgianskul, A. Miglio, J. Sun, H. J. Kim, K. H. Kim, S. Chen, G.-M. Rignanese, X. Gonze, *et al.*, Chem. Mater. **28**, 30 (2015).

[44] J. B. Varley, A. Miglio, V.-A. Ha, M. J. van Setten, G.-M. Rignanese, and G. Hautier, Chem. Mater **29**, 2568 (2017).

[45] T. Arai, S. Iimura, J. Kim, Y. Toda, S. Ueda, and H. Hosono, J. Am. Chem. Soc **139**, 17175 (2017).

[46] N. Ashcroft, Phys. Rev. Lett. **21**, 1748 (1968).

[47] C. F. Richardson and N. W. Ashcroft, Phys. Rev. Lett. **78**, 118 (1997).

[48] J. M. McMahon and D. M. Ceperley, Phys. Rev. B **84**, 144515 (2011).

[49] M. I. Eremets, I. A. Trojan, S. A. Medvedev, J. S. Tse, and Y. Yao, Science **319**, 1506 (2008).

[50] X.-J. Chen, V. V. Struzhkin, Y. Song, A. F. Goncharov, M. Ahart, Z. Liu, H.-k. Mao, and R. J. Hemley, Proc. Natl. Acad. Sci. U.S.A **105**, 20 (2008).

[51] J. A. Flores-Livas, M. Amsler, T. J. Lenosky, L. Lehtovaara, S. Botti, M. A. L. Marques, and S. Goedecker, Phys. Rev. Lett. **108**, 117004 (2012).

[52] I. Errea, M. Calandra, C. J. Pickard, J. R. Nelson, R. J. Needs, Y. Li, H. Liu, Y. Zhang, Y. Ma, and F. Mauri, Nature **532**, 81 (2016).

[53] I. Errea, M. Calandra, C. J. Pickard, J. Nelson, R. J. Needs, Y. Li, H. Liu, Y. Zhang, Y. Ma, and F. Mauri, Phys. Rev. Lett. **114**, 157004 (2015).

[54] C. Heil and L. Boeri, Phys. Rev. B **92**, 060508 (2015).

[55] R. Akashi, W. Sano, R. Arita, and S. Tsuneyuki, Phys. Rev. Lett. **117**, 075503 (2016).

[56] A. J. Flores-Livas, A. Sanna, and E. Gross, Eur. Phys. J. B **89**, 1 (2016).

[57] A. Drozdov, M. I. Eremets, and I. A. Troyan, arXiv: 1508.06224 [cond-mat.supr-con] (2015).

[58] J. A. Flores-Livas, M. Amsler, C. Heil, A. Sanna, L. Boeri, G. Profeta, C. Wolverton, S. Goedecker, and E. K. U. Gross, Phys. Rev. B **93**, 020508 (2016).

[59] E. A. Ekimov, V. A. Sidorov, E. D. Bauer, N. N. Mel'nik, N. J. Curro, J. D. Thompson, and S. M. Stishov, Nature **428**, 542 (2004).

[60] E. Bustarret, C. Marcenat, P. Achatz, J. Kačmarčik, F. Lévy, A. Huxley, L. Ortéga, E. Bourgeois, X. Blase, D. Débarre, *et al.*, Nature **444**, 465 (2006).

[61] T. Herrmannsdörfer, V. Heera, O. Ignatchik, M. Uhlarz, A. Mücklich, M. Posselt, H. Reuther, B. Schmidt, K.-H. Heinig, W. Skorupa, M. Voelskow, C. Wündisch, R. Skrotzki, M. Helm, and J. Wosnitza, Phys. Rev. Lett. **102**, 217003 (2009).

[62] M. Kriener, T. Muranaka, J. Kato, Z.-A. Ren, J. Akimitsu, and Y. Maeno, Sci. Technol. Adv. Mater. **9**, 044205 (2008).

[63] E. Schrödinger, Phys. Rev. **28**, 1049 (1926).

[64] L. De Broglie, in *Annales de Physique*, Vol. 10 (1925) pp. 22–128.

[65] W. Heisenberg, in *Original Scientific Papers Wissenschaftliche Originalarbeiten* (Springer, 1985) pp. 382–396.

[66] M. Born and R. Oppenheimer, Ann. Phys. **389**, 457 (1927).

[67] J.-T. Lü, H. Zhou, J.-W. Jiang, and J.-S. Wang, AIP Adv. **5**, 053204 (2015).

[68] D. R. Hartree, Math. Proc. Camb. Philos. Soc. **24**, 89–110 (1928).

[69] J. C. Slater, Phys. Rev. **34**, 1293 (1929).

[70] V. Fock, Z. Phys. **61**, 126 (1930).

[71] P. Hohenberg and W. Kohn, Phys. Rev. **136**, B864 (1964).

[72] E. Kaxiras, *Atomic and electronic structure of solids* (Cambridge University Press, 2003).

[73] W. Kohn and L. J. Sham, Phys. Rev. **140**, A1133 (1965).

[74] D. M. Ceperley and B. Alder, Phys. Rev. Lett. **45**, 566 (1980).

[75] J. P. Perdew, K. Burke, and M. Ernzerhof, Phys. Rev. Lett. **77**, 3865 (1996).

[76] S. K. Ghosh and R. G. Parr, Phys. Rev. A **34**, 785 (1986).

[77] A. St.-Amant, W. D. Cornell, P. A. Kollman, and T. A. Halgren, J. Comput. Chem. **16**, 1483 (1995).

[78] A. D. Becke, J. Chem. Phys. **98**, 1372 (1993).

[79] J. Harris, Phys. Rev. A **29**, 1648 (1984).

[80] J. P. Perdew, M. Ernzerhof, and K. Burke, J. Chem. Phys. **105**, 9982 (1996).

[81] C. Adamo and V. Barone, J. Chem. Phys. **110**, 6158 (1999).

[82] J. Paier, M. Marsman, K. Hummer, G. Kresse, I. C. Gerber, and J. G. Ángyán, J. Chem. Phys. **124**, 154709 (2006).

[83] J. Heyd, G. E. Scuseria, and M. Ernzerhof, J. Chem. Phys. **118**, 8207 (2003).

[84] J. Heyd, G. E. Scuseria, and M. Ernzerhof, J. Chem. Phys. **124**, 219906 (2006).

[85] A. D. Becke, J. Chem. Phys. **98**, 5648 (1993).

[86] L. Hedin, Phys. Rev. **139**, A796 (1965).

[87] A. L. Fetter and J. D. Walecka, *Quantum theory of many-particle systems* (Courier Corporation, 2012).

[88] F. Bloch, Z. Phys. **52**, 555 (1929).

[89] D. Hamann, M. Schlüter, and C. Chiang, Phys. Rev. Lett. **43**, 1494 (1979).

[90] D. Vanderbilt, Phys. Rev. B **41**, 7892 (1990).

[91] S. Goedecker, M. Teter, and J. Hutter, Phys. Rev. B **54**, 1703 (1996).

[92] M. Schlipf and F. Gygi, Comput. Phys. Commun **196**, 36 (2015).

[93] J. C. Slater, Phys. Rev. **51**, 846 (1937).

[94] D. J. Singh, in *Planewaves, Pseudopotentials and the LAPW Method* (Springer, 1994) pp. 35–43.

[95] P. E. Blöchl, Phys. Rev. B **50**, 17953 (1994).

[96] C. G. Van de Walle and J. Neugebauer, J. Appl. Phys. **95**, 3851 (2004).

[97] C. Freysoldt, B. Grabowski, T. Hickel, J. Neugebauer, G. Kresse, A. Janotti, and C. G. Van de Walle, Rev. Mod. Phys. **86**, 253 (2014).

[98] G. Lucas and R. Schäublin, Nucl. Instrum. Methods Phys. Res. B **267**, 3009 (2009).

[99] B. Grabowski, T. Hickel, and J. Neugebauer, Phys. Status Solidi (b) **248**, 1295 (2011).

[100] G. Pacchioni, Solid State Sci. **2**, 161 (2000).

[101] P. Deak, Phys. Status Solidi (b) **217**, 9 (2000).

[102] A. Alkauskas, M. D. McCluskey, and C. G. Van de Walle, J. Appl. Phys. **119**, 181101 (2016).

[103] S. Lany and A. Zunger, Phys. Rev. B **72**, 035215 (2005).

[104] S. Lany and A. Zunger, Phys. Rev. Lett. **98**, 045501 (2007).

[105] S. Lany and A. Zunger, Phys. Rev. B **78**, 235104 (2008).

[106] P. Mooney, J. Appl. Phys. **67**, R1 (1990).

[107] M. Chan and G. Ceder, Phys. Rev. Lett. **105**, 196403 (2010).

[108] L. Sham and M. Schlüter, Phys. Rev. Lett. **51**, 1888 (1983).

[109] J. P. Perdew and M. Levy, Phys. Rev. Lett. **51**, 1884 (1983).

[110] S. Zhang, S.-H. Wei, and A. Zunger, J. Appl. Phys. **83**, 3192 (1998).

[111] A. J. Cohen, P. Mori-Sánchez, and W. Yang, Science **321**, 792 (2008).

[112] Z. H. Levine and D. C. Allan, Phys. Rev. Lett. **63**, 1719 (1989).

[113] V. Fiorentini and A. Baldereschi, J. Phys. Condens. Matter. **4**, 5967 (1992).

[114] S. Zhang, J. Phys. Condens. Matter. **14**, R881 (2002).

[115] P. Bogusl, E. L. Briggs, and J. Bernholc, Phys. Rev. B **51**, 17255 (1995).

[116] S. Lany, H. Raebiger, and A. Zunger, Phys. Rev. B **77**, 241201 (2008).

[117] V. I. Anisimov, F. Aryasetiawan, and A. Lichtenstein, J. Phys. Condens. Matter. **9**, 767 (1997).

[118] S. Dudarev, G. Botton, S. Savrasov, C. Humphreys, and A. Sutton, Phys. Rev. B **57**, 1505 (1998).

[119] A. Janotti and C. G. Van de Walle, Phys. Status Solidi (b) **248**, 799 (2011).

[120] T. R. Paudel and W. R. Lambrecht, Phys. Rev. B **77**, 205202 (2008).

[121] P. Erhart, K. Albe, and A. Klein, Phys. Rev. B **73**, 205203 (2006).

[122] J. P. Perdew and A. Zunger, Phys. Rev. B **23**, 5048 (1981).

[123] W. Körner and C. Elsässer, Thin Solid Films **555**, 81 (2014).

[124] P. Rinke, A. Schleife, E. Kioupakis, A. Janotti, C. Rödl, F. Bechstedt, M. Scheffler, and C. G. Van de Walle, Phys. Rev. Lett. **108**, 126404 (2012).

[125] W. Foulkes, L. Mitas, R. Needs, and G. Rajagopal, Rev. Mod. Phys. **73**, 33 (2001).

[126] W. D. Parker, J. W. Wilkins, and R. G. Hennig, Phys. Status Solidi (b) **248**, 267 (2011).

[127] J. Buckeridge, D. Scanlon, A. Walsh, and C. R. A. Catlow, Comput. Phys. Commun. **185**, 330 (2014).

[128] D. Broberg, B. Medasani, N. E. Zimmermann, G. Yu, A. Canning, M. Haranczyk, M. Asta, and G. Hautier, Comput. Phys. Commun. **226**, 165 (2018).

[129] A. Jain, S. P. Ong, G. Hautier, W. Chen, W. D. Richards, S. Dacek, S. Cholia, D. Gunter, D. Skinner, G. Ceder, *et al.*, APL Mater. **1**, 011002 (2013).

[130] C. Persson, Y.-J. Zhao, S. Lany, and A. Zunger, Phys. Rev. B **72**, 035211 (2005).

[131] S. Chen, J.-H. Yang, X.-G. Gong, A. Walsh, and S.-H. Wei, Phys. Rev. B **81**, 245204 (2010).

[132] A. Togo, F. Oba, I. Tanaka, and K. Tatsumi, Phys. Rev. B **74**, 195128 (2006).

[133] M. Leslie and N. Gillan, J. Phys. C: Solid State Phys. **18**, 973 (1985).

[134] Y. Mishin, M. R. Sø Rensen, and A. F. Voter, Philos. Mag. A **81**, 2591 (2001).

[135] N. H. Hong, J. Sakai, W. Prellier, and A. Hassini, J. Phys. Condens. Matter **17**, 1697 (2005).

[136] C. Fitzgerald, M. Venkatesan, A. Douvalis, S. Huber, J. Coey, and T. Bakas, J. Appl. Phys. **95**, 7390 (2004).

[137] C. Liu, F. Yun, and H. Morkoc, J. Mater. Sci. Mater. Electron. **16**, 555 (2005).

[138] S. Lany and A. Zunger, Model. Simul. Mater. Sci. Eng. **17**, 084002 (2009).

[139] C. Freysoldt, J. Neugebauer, and C. G. Van de Walle, Phys. Status Solidi (b) **248**, 1067 (2011).

[140] Y. Kumagai and F. Oba, Phys. Rev. B **89**, 195205 (2014).

[141] G. Makov and M. Payne, Phys. Rev. B **51**, 4014 (1995).

[142] C. Freysoldt, J. Neugebauer, and C. G. Van de Walle, Phys. Rev. Lett. **102**, 016402 (2009).

[143] H.-P. Komsa, T. T. Rantala, and A. Pasquarello, Phys. Rev. B **86**, 045112 (2012).

[144] G. Makov, R. Shah, and M. Payne, Phys. Rev. B **53**, 15513 (1996).

[145] T. Moss, Proc. Phys. Soc. B **67**, 775 (1954).

[146] E. Burstein, Phys. Rev. **93**, 632 (1954).

[147] P. M. Fahey, P. Griffin, and J. Plummer, Rev. Mod. Phys. **61**, 289 (1989).

[148] H. Peng, A. Bikowski, A. Zakutayev, and S. Lany, APL Mater. **4**, 106103 (2016).

[149] H. Hosono, Y. Ogo, H. Yanagi, and T. Kamiya, Electrochem. Solid-State Lett. **14**, H13 (2011).

[150] J. Varley, A. Schleife, A. Janotti, and C. Van de Walle, Appl. Phys. Lett. **103**, 082118 (2013).

[151] S. Reineke, F. Lindner, G. Schwartz, N. Seidler, K. Walzer, B. Lüssem, and K. Leo, Nature **459**, 234 (2009).

[152] H. Ohta and H. Hosono, Mater. Today **7**, 42 (2004).

[153] R. G. Gordon, MRS Bull. **25**, 52 (2000).

[154] Y.-C. Shih, C. X. Qiu, I. Shih, and C. Qiu, “Indium oxide-based thin film transistors and circuits,” (2007), uS Patent 7,211,825.

[155] S. C. Dixon, D. O. Scanlon, C. J. Carmalt, and I. P. Parkin, J. Mater. Chem. C **4**, 6946 (2016).

[156] M. Morales-Masis, F. Dauzou, Q. Jeangros, A. Dabirian, H. Lifka, R. Gierth, M. Ruske, D. Moet, A. Hessler-Wyser, and C. Ballif, Adv. Funct. Mater. **26**, 384 (2016).

[157] E. Rucavado, Q. Jeangros, D. F. Urban, J. Holovský, Z. Remes, M. Duchamp, F. Landucci, R. E. Dunin-Borkowski, W. Körner, C. Elsässer, A. Hessler-Wyser, M. Morales-Masis, and C. Ballif, Phys. Rev. B **95**, 245204 (2017).

[158] K. G. Godinho, A. Walsh, and G. W. Watson, J. Phys. Chem. C **113**, 439 (2008).

[159] Y. S. Avadhut, J. Weber, E. Hammarberg, C. Feldmann, I. Schellenberg, R. Pöttgen, and J. Schmedt auf der Günne, Chem. Mater. **23**, 1526 (2011).

[160] J. Dominguez, L. Fu, and X. Pan, Appl. Phys. Lett. **81**, 5168 (2002).

[161] S. Lany and A. Zunger, Phys. Rev. Lett. **106**, 069601 (2011).

[162] F. Oba, A. Togo, I. Tanaka, J. Paier, and G. Kresse, Phys. Rev. B **77**, 245202 (2008).

[163] J. Varley, A. Janotti, and C. Van de Walle, Phys. Rev. B **81**, 245216 (2010).

[164] D. Cheng, M. Zhang, J. Chen, C. Yang, X. Zeng, and D. Cao, J. Phys. Chem. C **118**, 2037 (2014).

[165] M. Behtash, P. H. Joo, S. Nazir, and K. Yang, J. Appl. Phys. **117**, 175101 (2015).

[166] D. O. Scanlon and G. W. Watson, J. Mater. Chem. **22**, 25236 (2012).

[167] S. Clark, J. Robertson, S. Lany, and A. Zunger, Phys. Rev. B **81**, 115311 (2010).

[168] J. Vidal, F. Trani, F. Bruneval, M. A. L. Marques, and S. Botti, Phys. Rev. Lett. **104**, 136401 (2010).

[169] M. Nagasawa and S. Shionoya, Phys. Lett. **22**, 409 (1966).

[170] A. Stashans, P. Puchaicela, and R. Rivera, J. Mater. Sci. **49**, 2904 (2014).

[171] P. Deák, A. Gali, B. Aradi, and T. Frauenheim, Phys. Status Solidi B **248**, 790 (2011).

[172] S. Lany and A. Zunger, Phys. Rev. B **81**, 205209 (2010).

[173] S. Lany and A. Zunger, Phys. Rev. B **80**, 085202 (2009).

[174] G. Kresse and D. Joubert, Phys. Rev. B **59**, 1758 (1999).

[175] G. Kresse and J. Furthmüller, Phys. Rev. B **54**, 11169 (1996).

[176] G. Kresse and J. Furthmüller, Comput. Mater. Sci. **6**, 15 (1996).

[177] F. Birch, Phys. Rev. **71**, 809 (1947).

[178] J. Haines and J. Léger, Phys. Rev. B **55**, 11144 (1997).

[179] D. D. Wagman, W. H. Evans, V. B. Parker, R. H. Schumm, and I. Halow, *The NBS tables of chemical thermodynamic properties. Selected values for inorganic and C1 and C2 organic substances in SI units*, Tech. Rep. (DTIC Document, 1982).

[180] A. Rakhshani, Y. Makdisi, and H. Ramazaniyan, J. Appl. Phys. **83**, 1049 (1998).

[181] J. Xu, S. Huang, and Z. Wang, Solid State Commun. **149**, 527 (2009).

[182] H. Peng, J. D. Perkins, and S. Lany, Chem. Mater. **26**, 4876 (2014).

[183] D. Goyal, C. Agashe, B. Marathe, M. Takwale, and V. Bhide, J. Appl. Phys. **73**, 7520 (1993).

[184] X. Huang, M. Feng, and C. Gao, J. Mater. Sci. Mater. Electron. **28**, 7593 (2017).

[185] G. Turgut, E. F. Keskenler, S. Aydın, E. Sönmez, S. Doğan, B. Düzgün, and M. Ertuğrul, Superlattices Microstruct. **56**, 107 (2013).

[186] Y. Huang, Q. Zhang, G. Li, and M. Yang, Mater. Charact. **60**, 415 (2009).

[187] C. Agashe and S. Major, J. Mater. Sci. Lett. **15**, 497 (1996).

[188] C. G. Van de Walle, Physica B Condens. Matter. **376**, 1 (2006).

[189] S. Pan, G. Li, L. Wang, Y. Shen, Y. Wang, T. Mei, and X. Hu, Appl. Phys. Lett. **95**, 222112 (2009).

[190] B. Zhou, S. Dong, H. Zhao, Y. Liu, and P. Wu, J. Magn. Magn. Mater. **362**, 14 (2014).

[191] S. S. Pan, S. Wang, Y. X. Zhang, Y. Y. Luo, F. Y. Kong, S. C. Xu, J. M. Xu, and G. H. Li, Appl. Phys. A **109**, 267 (2012).

[192] M.-M. Bagheri-Mohagheghi and M. Shokooh-Saremi, J. Phys. D: Appl. Phys. **37**, 1248 (2004).

[193] M.-M. Bagheri-Mohagheghi and M. Shokooh-Saremi, Semicond. Sci. Technol. **19**, 764 (2004).

[194] Z. Ji, L. Zhao, Z. He, Q. Zhou, and C. Chen, Mater. Lett. **60**, 1387 (2006).

[195] P.-M. Lee, Y.-S. Liu, L. Villamagua, A. Stashans, M. Carini, and C.-Y. Liu, J. Mater. Chem. C **120**, 4211 (2016).

[196] P. V. Medeiros, S. Stafström, and J. Björk, Phys. Rev. B **89**, 041407 (2014).

[197] P. V. Medeiros, S. S. Tsirkin, S. Stafström, and J. Björk, Phys. Rev. B **91**, 041116 (2015).

[198] H. J. Cho, Y. J. Seo, G. W. Kim, K. Y. Park, S. N. Heo, and B. H. Koo, Korean J. Mater. Res. **23**, 435 (2013).

[199] X. Pan and L. Fu, J. Electroceram. **7**, 35 (2001).

[200] Y. Ogo, H. Hiramatsu, K. Nomura, H. Yanagi, T. Kamiya, M. Hirano, and H. Hosono, Appl. Phys. Lett. **93**, 032113 (2008).

[201] J. P. Allen, D. O. Scanlon, L. F. Piper, and G. W. Watson, J. Mater. Chem. C **1**, 8194 (2013).

[202] E. Fortunato, R. Barros, P. Barquinha, V. Figueiredo, S.-H. K. Park, C.-S. Hwang, and R. Martins, Appl. Phys. Lett. **97**, 052105 (2010).

[203] H. Yabuta, N. Kaji, R. Hayashi, H. Kumomi, K. Nomura, T. Kamiya, M. Hirano, and H. Hosono, Appl. Phys. Lett. **97**, 072111 (2010).

[204] S. A. Miller, P. Gorai, U. Aydemir, T. O. Mason, V. Stevanović, E. S. Toberer, and G. J. Snyder, J. Mater. Chem. C **5**, 8854 (2017).

[205] J. A. Caraveo-Frescas, P. K. Nayak, H. A. Al-Jawhari, D. B. Granato, U. Schwingenschlögl, and H. N. Alshareef, ACS Nano **7**, 5160 (2013).

[206] S. H. Kim, I.-H. Baek, D. H. Kim, J. J. Pyeon, T.-M. Chung, S.-H. Baek, J.-S. Kim, J. H. Han, and S. K. Kim, J. Mater. Chem. C **5**, 3139 (2017).

[207] T. Daeneke, P. Atkin, R. Orrell-Trigg, A. Zavabeti, T. Ahmed, S. Walia, M. Liu, Y. Tachibana, M. Javaid, A. D. Greentree, S. P. Russo, R. B. Kaner, and K. Kalantar-Zadeh, ACS Nano **11**, 10974 (2017).

[208] J. F. Wager, B. Yeh, R. L. Hoffman, and D. A. Keszler, Curr. Opin. Solid State Mater. Sci. **18**, 53 (2014).

[209] Z. Wang, P. K. Nayak, J. A. Caraveo-Frescas, and H. N. Alshareef, Adv. Mater. **28**, 3831 (2016).

[210] E. Fortunato, P. Barquinha, and R. Martins, Adv. Mater. **24**, 2945 (2012).

[211] T. Yang, X. Qin, H.-h. Wang, Q. Jia, R. Yu, B. Wang, J. Wang, K. Ibrahim, X. Jiang, and Q. He, Thin Solid Films **518**, 5542 (2010).

[212] F. Zhuge, L. Zhu, Z. Ye, D. Ma, J. Lu, J. Huang, F. Wang, Z. Ji, and S. Zhang, Appl. Phys. Lett. **87**, 092103 (2005).

[213] N. Quackenbush, J. Allen, D. Scanlon, S. Sallis, J. Hewlett, A. Nandur, B. Chen, K. Smith, C. Weiland, D. Fischer, J. Woicik, B. White, W. GW, and L. Piper, Chem. Mater. **25**, 3114 (2013).

[214] V.-A. Ha, D. Waroquiers, G.-M. Rignanese, and G. Hautier, Appl. Phys. Lett. **108**, 201902 (2016).

[215] W. Guo, L. Fu, Y. Zhang, K. Zhang, L. Liang, Z. Liu, H. Cao, and X. Pan, Appl. Phys. Lett. **96**, 042113 (2010).

[216] S. Grimme, J. Comp. Chem. **27**, 1787 (2006).

[217] J. G. Stark, H. G. Wallace, and M. McGlashan, *Chemistry data book* (Murray London, 1982).

[218] X. Li, L. Liang, H. Cao, R. Qin, H. Zhang, J. Gao, and F. Zhuge, Appl. Phys. Lett. **106**, 132102 (2015).

[219] Y. Ogo, H. Hiramatsu, K. Nomura, H. Yanagi, T. Kamiya, M. Kimura, M. Hirano, and H. Hosono, Phys. Status Solidi (a) **206**, 2187 (2009).

[220] M. S. Moreno, A. Varela, and L. C. Otero-Díaz, Phys. Rev. B **56**, 5186 (1997).

[221] G. Glockler, J. Phys. Chem. **62**, 1049 (1958).

[222] A. Gupta and J. Tossell, Phys. Chem. Miner. **7**, 159 (1981).

[223] M. Moreno, R. Mercader, and A. Bibiloni, J. Phys. Condens. Matter. **4**, 351 (1992).

[224] J. S. Kearney, M. Graužinytė, D. Smith, D. Sneed, C. Childs, J. Hinton, C. Park, J. S. Smith, E. Kim, S. D. Fitch, *et al.*, Angew. Chem. Int. Ed. **57**, 11623 (2018).

[225] S.-K. Song, J.-S. Cho, W.-K. Choi, H.-J. Jung, D. Choi, J.-Y. Lee, H.-K. Baik, and S.-K. Koh, Sens. Actuator B-Chem. **46**, 42 (1998).

[226] C. Agashe, B. R. Marathe, M. G. Takwale, and V. G. Bhide, Sol. Energy Mater. **17**, 99 (1988).

[227] B. Stjerna, E. Olsson, and C. G. Granqvist, J. Appl. Phys. **76**, 3797 (1994).

[228] C. A. Niedermeier, S. Rhode, K. Ide, H. Hiramatsu, H. Hosono, T. Kamiya, and M. A. Moram, Phys. Rev. B **95**, 161202 (2017).

[229] J. W. Hennek, J. Smith, A. Yan, M. G. Kim, W. Zhao, V. P. Dravid, A. Facchetti, and T. J. Marks, J. Am. Chem. Soc. **135**, 10729 (2013).

[230] T. Minami, J. Vac. Sci. Technol. A **17**, 1765 (1999).

[231] H. Frenzel, D. Tobias, P. Schlupp, H. V. Wenckstern, and M. Grundmann, Phys. Status Solidi A **1486**, 1482 (2015).

[232] E. Rucavado, Q. Jeangros, D. F. Urban, J. Holovský, Z. Remes, M. Duchamp, F. Landucci, R. E. Dunin-borkowski, W. Körner, C. Elsässer, A. Hessler-wyser, M. Morales-masis, and C. Ballif, Phys. Rev. B **245204**, 1 (2017).

[233] F. Dauzou, P. C. Bouten, A. Dabirian, Y. Leterrier, C. Ballif, and M. Morales-Masis, Organic Electronics **35**, 136 (2016).

[234] M. Morales-Masis, F. Dauzou, Q. Jeangros, A. Dabirian, H. Lifka, R. Gierth, M. Ruske, D. Moet, A. Hessler-Wyser, and C. Ballif, Adv. Funct. Mater. **26**, 384 (2016).

[235] H. Q. Chiang, J. F. Wager, R. L. Hoffman, J. Jeong, and D. A. Keszler, Appl. Phys. Lett. **86**, 013503 (2005).

[236] S. Han and S. Y. Lee, Phys. Status Solidi A **214**, 1600469 (2017).

[237] J. Werner, A. Walter, E. Rucavado, S.-J. Moon, D. Sacchetto, M. Rienaecker, R. Peibst, R. Brendel, X. Niquille, S. De Wolf, P. Löper, M. Morales-Masis, S. Nicolay, B. Niesen, and C. Ballif, Appl. Phys. Lett. **109**, 233902 (2016).

[238] W. Körner and C. Elsässer, Thin Solid Films **555**, 81 (2014).

[239] W. Körner, P. Gumbsch, and C. Elsässer, Phys. Rev. B **86**, 165210 (2012).

[240] S. D. Wolf, A. Descoeudres, Z. C. Holman, and C. Ballif, Green **0**, 7 (2012).

[241] M. Morales-Masis, S. De Wolf, R. Woods-Robinson, J. W. Ager, and C. Ballif, Adv. Electron. Mater. , 1600529 (2017).

[242] J. Werner, B. Niesen, and C. Ballif, Adv. Mater. Interfaces **1700731**, 1 (2017).

[243] A. Dabirian, S. Martin de Nicolas, B. Niesen, A. Hessler-Wyser, S. De Wolf, M. Morales-Masis, and C. Ballif, Adv. Mater. Interfaces **3**, 1500462 (2016).

[244] T. Kizu, S. Aikawa, T. Nabatame, A. Fujiwara, K. Ito, M. Takahashi, and K. Tsukagoshi, J. Appl. Phys. **120**, 045702 (2016).

[245] N. Mitoma, S. Aikawa, X. Gao, T. Kizu, M. Shimizu, M.-F. Lin, T. Nabatame, and K. Tsukagoshi, Appl. Phys. Lett. **104**, 102103 (2014).

[246] I. Kang, C. H. Park, E. Chong, and S. Y. Lee, Curr. Appl. Phys. **12**, S12 (2012).

[247] T. Minami, H. Sato, H. Nanto, and S. Takata, Jpn. J. Appl. Phys. **25**, L776 (1986).

[248] C. Faure, J. Clatot, L. Teulé-Gay, G. Campet, C. Labrugère, M. Nistor, and A. Rougier, Thin Solid Films **524**, 151 (2012).

[249] N. Rashidi, V. L. Kuznetsov, J. R. Dilworth, M. Pepper, P. J. Dobson, and P. P. Edwards, J. Mater. Chem. C **1**, 6960 (2013).

[250] J. Clatot, G. Campet, A. Zeinert, C. Labrugère, M. Nistor, and A. Rougier, Sol. Energy Mater. Sol. Cells **95**, 2357 (2011).

[251] I. Sorar, D. Saygin-Hinczewski, M. Hinczewski, and F. Tepehan, Appl. Surf. Sci. **257**, 7343 (2011).

[252] J. Y. Choi, K. Heo, K.-s. Cho, S. W. Hwang, S. Kim, and S. Y. Lee, Sci. Rep. **6**, 1 (2016).

[253] R. Summitt, J. A. Marley, and N. F. Borrelli, J. Phys. Chem. Solids **25**, 1465 (1964).

[254] D. Guo and C. Hu, Appl. Surf. Sci. **258**, 6987 (2012).

[255] R. M. Van Ginhoven, H. Jónsson, and L. R. Corrales, Phys. Rev. B **71**, 024208 (2005).

[256] W. Pliskin and H. Lehman, J. Electrochem. Soc. **112**, 1013 (1965).

[257] H. Mizoguchi, H. Kawazoe, and H. Hosono, Chem. Mater. **8**, 2769 (1996).

[258] N. Sato, M. Ichimura, E. Arai, and Y. Yamazaki, Sol. Energy Mater Sol. Cells **85**, 153 (2005).

[259] L.-D. Zhao, S.-H. Lo, Y. Zhang, H. Sun, G. Tan, C. Uher, C. Wolverton, V. P. Dravid, and M. G. Kanatzidis, Nature **508**, 373 (2014).

[260] J. P. Allen, D. O. Scanlon, S. C. Parker, and G. W. Watson, J. Phys. Chem. C **115**, 19916 (2011).

[261] W. Tang, E. Sanville, and G. Henkelman, J. Phys. Condens. Matter **21**, 084204 (2009).

[262] F. Kröger and H. Vink, in *Solid state physics*, Vol. 3 (Elsevier, 1956) pp. 307–435.

[263] M. S. Moreno and R. C. Mercader, Phys. Rev. B **50**, 9875 (1994).

[264] M. Somayazulu, M. Ahart, A. K. Mishra, Z. M. Geballe, M. Baldini, Y. Meng, V. V. Struzhkin, and R. J. Hemley, arXiv:1808.07695 [cond-mat.mtrl-sci] (2018).

[265] D. Duan, Y. Liu, F. Tian, D. Li, X. Huang, Z. Zhao, H. Yu, B. Liu, W. Tian, and T. Cui, Sci. Rep. **4**, 6968 (2014).

[266] A. P. Drozdov, M. I. Eremets, I. A. Troyan, V. Ksenofontov, and S. I. Shylin, Nature **525**, 73 (2015).

[267] P. W. Bridgman, The Nobel Prize in Physics 1946 **-**, (1946).

[268] N. W. Ashcroft, Phys. Rev. Lett. **92**, 187002 (2004).

[269] D. Y. Kim, R. H. Scheicher, S. Lebègue, J. Prasongkit, B. Arnaud, M. Alouani, and R. Ahuja, Proc. Natl. Acad. Sci. U.S.A **105**, 16454 (2008).

[270] S. Wang, H.-k. Mao, X.-J. Chen, and W. L. Mao, Proc. Natl. Acad. Sci. U.S.A **106**, 14763 (2009).

[271] M. Hanfland, J. E. Proctor, C. L. Guillaume, O. Degtyareva, and E. Gregoryanz, Phy. Rev. Lett. **106**, 095503 (2011).

[272] D. Y. Kim, R. H. Scheicher, C. J. Pickard, R. J. Needs, and R. Ahuja, Phys. Rev. Lett. **107**, 117002 (2011).

[273] J. A. Flores-Livas, M. Amsler, T. J. Lenosky, L. Lehtovaara, S. Botti, M. A. L. Marques, and S. Goedecker, Phys. Rev. Lett. **108**, 117004 (2012).

[274] J. Flores Livas, *Computational and experimental studies of sp3-materials at high pressure*, Ph.D. thesis, Lyon 1 (2012).

[275] W. Grochala, R. Hoffmann, J. Feng, and N. W. Ashcroft, Angew. Chem. Int. Edi. **46**, 3620 (2007).

[276] O. Degtyareva, J. E. Proctor, C. L. Guillaume, E. Gregoryanz, and M. Hanfland, Solid State Commun. **149**, 1583 (2009).

[277] Y. Li, G. Gao, Y. Xie, Y. Ma, T. Cui, and G. Zou, Proc. Natl. Acad. Sci. U.S.A **107**, 15708 (2010).

[278] J. A. Flores-Livas, A. Sanna, A. P. Drozdov, L. Boeri, G. Profeta, M. Eremets, and S. Goedecker, Phys. Rev. Mater. **1**, 024802 (2017).

[279] L. Zhang, Y. Wang, J. Lv, and Y. Ma, Nature Rev. Mater. **2**, 17005 (2017).

[280] G. Savini, A. C. Ferrari, and F. Giustino, Phys. Rev. Lett. **105**, 037002 (2010).

[281] B. Militzer and H. F. Wilson, Phys. Rev. Lett. **105**, 195701 (2010).

[282] J. M. McMahon, Phys. Rev. B **84**, 220104 (2011).

[283] S. Zhang, H. F. Wilson, K. P. Driver, and B. Militzer, Phys. Rev. B **87**, 024112 (2013).

[284] C. J. Pickard, M. Martinez-Canales, and R. J. Needs, Phys. Rev. Lett. **110**, 245701 (2013).

[285] T. Bartels-Rausch, V. Bergeron, J. H. Cartwright, R. Escribano, J. L. Finney, H. Grothe, P. J. Gutiérrez, J. Haapala, W. F. Kuhs, J. B. Pettersson, *et al.*, Rev. Mod. Phys. **84**, 885 (2012).

[286] N. Bjerrum, Science **115**, 385 (1952).

[287] B. Kamb, Acta Crystallogr. **17**, 1437 (1964).

[288] E. Whalley, J. Heath, and D. Davidson, J. Chem. Phys. **48**, 2362 (1968).

[289] B. Kamb, A. Prakash, and C. Knobler, Acta Crystallogr. **22**, 706 (1967).

[290] W. Kuhs, J. Finney, C. Vettier, and D. Bliss, J. Chem. Phys. **81**, 3612 (1984).

[291] J. D. Jorgensen and T. G. Worlton, J. Chem. Phys. **83**, 329 (1985).

[292] J. M. Besson, P. Pruzan, S. Klotz, G. Hamel, B. Silvi, R. J. Nelmes, J. S. Loveday, R. M. Wilson, and S. Hull, Phys. Rev. B **49**, 12540 (1994).

[293] R. Hemley, A. Jephcoat, H. Mao, C. Zha, L. Finger, and D. Cox, Nature **330**, 737 (1987).

[294] A. F. Goncharov, N. Goldman, L. E. Fried, J. C. Crowhurst, I. F. Kuo, C. J. Mundy, and J. M. Zaug, Phys. Rev. Lett. **94**, 125508 (2005).

[295] W. L. Vos, L. W. Finger, R. J. Hemley, and H.-k. Mao, Phys. Rev. Lett. **71**, 3150 (1993).

[296] O. Mishima, J. Chem. Phys **100**, 5910 (1994).

[297] T. Loerting, C. Salzmann, I. Kohl, E. Mayer, and A. Hallbrucker, Phys. Chem. Chem. Phys. **3**, 5355 (2001).

[298] R. S. Smith and B. D. Kay, Nature **398**, 788 (1999).

[299] C. A. Angell, Annu. Rev. Phys. Chem. **55**, 559 (2004).

[300] F. Yen, Z. Chi, A. Berlie, X. Liu, and A. F. Goncharov, J. Phys. Chem. C **119**, 20618 (2015).

[301] W. Holzapfel, J. Chem. Phys. **56**, 712 (1972).

[302] P. Pruzan, J. Chervin, and B. Canny, J. Chem. Phys. **99**, 9842 (1993).

[303] P. Pruzan, J. Mol. Struct. **322**, 279 (1994).

[304] A. F. Goncharov, V. V. Struzhkin, H.-k. Mao, and R. J. Hemley, Phys. Rev. Lett. **83**, 1998 (1999).

[305] M. Benoit, D. Marx, and M. Parrinello, Nature **392**, 258 (1998).

[306] M. Benoit, D. Marx, and M. Parrinello, Solid State Ion. **125**, 23 (1999).

[307] A. Goncharov, V. Struzhkin, M. Somayazulu, R. Hemley, and H. Mao, Science **273**, 218 (1996).

[308] J. A. Flores-Livas, A. Sanna, M. Graužinytė, A. Davydov, S. Goedecker, and M. A. Marques, Sci. Rep. **7**, 6825 (2017).

[309] J. M. Sanchez, F. Ducastelle, and D. Gratias, Physica A **128**, 334 (1984).

[310] A. Van der Ven and G. Ceder, Phys. Rev. B **71**, 054102 (2005).

[311] D. B. Laks, L. Ferreira, S. Froyen, and A. Zunger, Phys. Rev. B **46**, 12587 (1992).

[312] H. Glawe, A. Sanna, E. K. U. Gross, and M. A. L. Marques, New J. Phys. **18**, 093011 (2016).

[313] X. Blase, C. R. Phys. **12**, 584 (2011).

[314] A. Hermann, N. W. Ashcroft, and R. Hoffmann, Phys. Rev. B **88**, 214113 (2013).

[315] H. Liu, Y. Yao, and D. D. Klug, Phys. Rev. B **91**, 014102 (2015).

[316] Y. Ma, A. R. Oganov, and C. W. Glass, Phys. Rev. B **76**, 064101 (2007).

[317] A. J. Ochoa-Calle, C. M. Zicovich-Wilson, and A. Ramírez-Solís, Phys. Rev. B **92**, 085148 (2015).

[318] G. Weck, S. Desgreniers, P. Loubeyre, and M. Mezouar, Phys. Rev. Lett. **102**, 255503 (2009).

[319] C. J. Pickard and R. J. Needs, Nat. Phys. **3**, 473 (2007).

[320] M. I. Eremets, A. G. Gavriliuk, I. A. Trojan, D. A. Dzivenko, and R. Boehler, Nature materials **3**, 558 (2004).

[321] F. Bruneval and J.-P. Crocombette, Phys. Rev. B **86**, 140103 (2012).

[322] G. Eliashberg, Teor. Fiz. **38** (1960), [Sov. Phys. FETP **11**, 696 (1960)].

[323] P. B. Allen and B. Mitrović, *Theory of Superconducting Tc*, Solid State Physics, Vol. 37 (Academic Press, 1983) pp. 1 – 92.

[324] W. Kohn, Phys. Rev. Lett. **2**, 393 (1959).

[325] G. S. Smirnov and V. V. Stegailov, J. Phys. Chem. Lett. **4**, 3560 (2013).

[326] G.-R. Qian, A. O. Lyakhov, Q. Zhu, A. R. Oganov, and X. Dong, Sci. Rep. **4** (2014), 10.1038/srep05606.

[327] T. A. Strobel, M. Somayazulu, and R. J. Hemley, J. Phys. Chem. C **115**, 4898 (2011).

[328] S. Ninet, F. Datchi, P. Dumas, M. Mezouar, G. Garbarino, A. Mafety, C. J. Pickard, R. J. Needs, and A. M. Saitta, Phys. Rev. B **89**, 174103 (2014).

[329] X. Jiang, X. Wu, Z. Zheng, Y. Huang, and J. Zhao, Phys. Rev. B **95**, 144104 (2017).

[330] D. Bassett, in *Developments in crystalline polymers—1* (Springer, 1982) pp. 115–150.

[331] D. Chelazzi, M. Ceppatelli, M. Santoro, R. Bini, and V. Schettino, Nature Mater. **3**, 470 (2004).

[332] M. Yasuniwa, R. Enoshita, and T. Takemura, Jpn. J. Appl. Phys. **15**, 1421 (1976).

[333] L. Fontana, D. Q. Vinh, M. Santoro, S. Scandolo, F. Gorelli, R. Bini, and M. Hanfland, Phys. Rev. B **75**, 174112 (2007).

[334] L. Fontana, M. Santoro, R. Bini, D. Q. Vinh, and S. Scandolo, J. Chem. Phys. **133**, 204502 (2010).

[335] M. Thiery and J. Leger, J. Chem. Phys. **89**, 4255 (1988).

[336] L. Ciabini, F. A. Gorelli, M. Santoro, R. Bini, V. Schettino, and M. Mezouar, Phys. Rev. B **72**, 094108 (2005).

[337] L. Ciabini, M. Santoro, F. A. Gorelli, R. Bini, V. Schettino, and S. Raugei, Nature Mater. **6**, 39 (2007).

[338] Y. Wang, L. Wang, H. Zheng, K. Li, M. Andrzejewski, T. Hattori, A. Sano-Furukawa, A. Katrusiak, Y. Meng, F. Liao, *et al.*, J. Phys. Chem. C **120**, 29510 (2016).

[339] S. Goedecker, J. Chem. Phys. **120**, 9911 (2004).

[340] M. Amsler, J. A. Flores-Livas, L. Lehtovaara, F. Balima, S. A. Ghasemi, D. Machon, S. Pailhes, A. Willand, D. Caliste, S. Botti, A. San Miguel, S. Goedecker, and M. A. L. Marques, Phys. Rev. Lett. **108**, 065501 (2012).

[341] M. Amsler, J. A. Flores-Livas, T. D. Huan, S. Botti, M. A. Marques, and S. Goedecker, Phys. Rev. Lett. **108**, 205505 (2012).

[342] M. Sicher, S. Mohr, and S. Goedecker, J. Chem. Phys. **134**, 044106 (2011).

[343] F. Jensen, *Introduction to Computational Chemistry: Second Edition* (JW, 2011).

[344] T. Björkman, Comput. Phys. Commun **182**, 1183 (2011).

[345] A. D. McNaught and A. D. McNaught, *Compendium of chemical terminology*, Vol. 1669 (Blackwell Science Oxford, 1997).

[346] X.-D. Wen, R. Hoffmann, and N. Ashcroft, J. Am. Chem. Soc. **133**, 9023 (2011).

[347] J. A. Flores-Livas, M. Graužinytė, L. Boeri, G. Profeta, and A. Sanna, Eur. Phys. J. B **91**, 176 (2018).

[348] K. Ueno, S. Nakamura, H. Shimotani, H. T. Yuan, N. Kimura, T. Nojima, H. Aoki, Y. Iwasa, and M. Kawasaki, Nat. Nanotechnol. **6**, 408 EP (2011).

[349] D. O. Scanlon, C. W. Dunnill, J. Buckeridge, S. A. Shevlin, A. J. Logsdail, S. M. Woodley, C. R. A. Catlow, M. J. Powell, R. G. Palgrave, I. P. Parkin, G. W. Watson, T. W. Keal, P. Sherwood, A. Walsh, and A. A. Sokol, Nat. Mater. **12**, 798 (2013).

[350] D. Hapiuk, M. A. L. Marques, P. Melinon, J. A. Flores-Livas, S. Botti, and B. Masenelli, Phys. Rev. Lett. **108**, 115903 (2012).

[351] M. Grundmann, F.-L. Schein, M. Lorenz, T. Böntgen, J. Lenzner, and H. von Wenckstern, Phys. Status Solidi (a) **210**, 1671 (2013).

[352] R. U. Chandrasena, W. Yang, Q. Lei, M. U. Delgado-Jaime, K. D. Wijesekara, M. Golalikhani, B. A. Davidson, E. Arenholz, K. Kobayashi, M. Kobata, *et al.*, Nano Lett. **17**, 794 (2017).

[353] U. Aschauer and N. A. Spaldin, Appl. Phys. Lett. **109**, 031901 (2016).

Abbreviations

CBM conduction band minimum. 26, 36, 37, 45–54, 59, 64–66, 78, 79

DFT density functional theory. 11, 13–15, 19, 23, 27–30, 33, 36, 56, 69, 75, 82, 89

DLS defect localized electronic state. 27, 28

DLTS deep-level transient spectroscopy. 2

DOS density of states. 17, 40, 45, 46, 51–53, 97

EDX Energy dispersive X-ray. 76, 77, 79

EPFL École Polytechnique Fédérale de Lausanne. 2, 73, 75, 113

EPR electron paramagnetic resonance. 1

EXAFS extended X-ray absorption fine structure. 1

FOM figure of merit. 75

GGA generalized gradient approximations. 13, 15, 28, 29, 43

HEG homogeneous electron gas. 12, 13

HF Hartree-Fock. 13–15

HP High pressure. 91

LAPW linearized augmented plane wave. 19

LDA local density approximation. 12, 13, 15, 28, 29

MHM minima hopping method. 102

OLED organic light-emitting diode. 2, 42, 74

PAS positron annihilation spectroscopy. 1

PAW projector augmented-wave method. 19, 44, 56, 83

PBE Perdew-Burke-Erzernhof. 13, 41–48, 50–53, 56, 57, 59–62, 64–66, 68, 70, 71, 94, 102, 104

PHS perturbed host state. 27, 28

PV photovoltaic. 2, 3

PV-Lab Photovoltaics and Thin Film Electronics Laboratory. 2

RBS Rutherford backscattering spectrometry. 1, 76

SIC self-interaction correction. 29

SIMS secondary ion mass spectroscopy. 1

TCO transparent conductive oxide. 2–4, 34, 40, 42, 43, 50, 51, 55, 73–75, 78–80, 82, 112, 113

TFT thin film transistors. 54, 55, 74

VBM valence band maximum. 26, 36, 45, 51, 53, 59–63

vdWs van der Waals. 56, 57, 63

XC exchange-correlation. 12, 13

ZPE zero point energy. 98

ZPL zero phonon line. 27

ZTO zinc-tin-oxide. 73–77, 79, 82

Nomenclature

$A_{\textbf{400-800}}$ The average optical absorptance in the 400-800 nm range. 75

C^q The concentration of a defect in a charge state q. 79

E_X^F The formation energy associated with a defect X. 40, 83, 88, 92, 99

E_X^q Energy of a relaxed defective supercell containing a defect X in a charge state q. 92

E_B^v The binding energy of a defect complex evaluated using the charge states of all defects that are the most stable at the valence band maximum. 86–89

E_{cor} The energy arising from different supercell correction terms applied in a defect calculation. 83

H_X^F The formation enthalpy associated with a defect X. 92

P Pressure. 92, 99, 100

Δ The distance between the conduction band minimum and a thermodynamic transition level from a positive to a charge neutral state. 79, 80

$\Delta\epsilon_F$ The Fermi level referenced to the valence band maximum of the bulk crystal. 46, 51, 86

$\Delta\mu_i$ The chemical potential variation (away from the most stable elemental phase) corresponding to an element of species i. 31

Ω Volume of the host supercell. 92

Ω' Volume of the relaxed defective supercell. 92

Ω^{rel} Relaxation volume corresponding to some defect calculated as the difference between Ω' and Ω. 92, 93

$\epsilon(2/0)$ Thermodynamic transition level between a +2 to and a 0 charge state. 78–81

ϵ_F The Fermi level. 40, 78, 79, 83, 84

λ Electron-phonon coupling constant. 101, 108

$\mathrm{T_C}$ The critical temperature of a superconducting transition. 91, 101, 108, 109, 112

μ Mobility of a charge carrier. 39

μ_i The chemical potential corresponding to an element of species i. 30, 83, 93

μ_i^0 The chemical potential corresponding to the most stable elemental phase of an element of species i. 31

$\overline{\tau}$ The average scattering time. 39

σ Electrical conductivity. 39, 75

e The elementary charge. 39

m^* The effective mass of a charge carrier. 39

n_e The number of electrons in the conduction band. 39

n_h The number of holes in the valence band. 39

q Electrical charge. 39, 40, 79, 92

v_F The formation volume typically associated with the introduction of a defect. 92, 93, 99, 100

A Chemical reference

A.1. Tin Dioxide

Table A.1 and Table A.2 list the structural information for the phases used to evaluate the chemical potentials in the tin dioxide, SnO_2, dopant screening study, presented in Section 4.1. Symmetry of the crystal structures together with the formation energies per formula unit are listed. In the case of H_2, O_2 and H_2O the energies of an isolated molecule in a $10 \times 10 \times 10$ Å^3 box were used. For secondary phase formation a handful of lowest energy structures (taken from the Materials Project database) were considered for each element, with only the phases resulting in the strictest chemical potential bounds shown in Table A.2. All structures reported were optimized until the forces were below 0.002 eV/Å. The same VASP settings as those used for defect supercell calculations were used and the k-point meshes were chosen, such that total energies changed by less than 1 meV per atom.

Table A.1. List of the elemental phases used for formation energy calculations.

Defect atom	Spg	MPID	E^{PBE} (eV)	E^{PBE0} (eV)
H	-	-	-1.118	-1.715
O	-	-	-4.937	-7.537
Sn	$Fd\overline{3}m$	**mp-117**	-3.846	-5.012
As	$R\overline{3}m$	**mp-11**	-4.670	-5.595
Au	$Fm\overline{3}m$	**mp-81**	-3.222	-3.423
Be	$P6_3/mmc$	**mp-87**	-3.763	-3.803
Bi	$R\overline{3}m$	**mp-23152**	-3.874	-4.566
Br	$Cmce$	**mp-23154**	-1.635	-2.589
Cl	$Ccme$	**mp-22848**	-1.840	-2.983
I	$Cmce$	**mp-23153**	-1.518	-2.025
Mg	$P6_3/mmc$	**mp-153**	-1.508	-1.529
Nb	$Im\overline{3}m$	**mp-75**	-10.093	-11.715
P	$Cmce$	**mp-157**	-5.375	-6.455
Sb	$R\overline{3}m$	**mp-104**	-4.134	-5.078
Ta	$Im\overline{3}m$	**mp-50**	-11.833	-13.628
Te	$P3_121$	**mp-19**	-3.142	-3.955
W	$Im\overline{3}m$	**mp-91**	-13.032	-15.211

The use of PBE0 for metallic structures may be inappropriate. For O-rich/Sn-poor conditions, however, if a stable oxide phase exists, the metallic reference is eliminated from the formation energy calculation. The Sn-site substitution is also favored under these conditions. The metallic solid results for PBE0 were, therefore, only used to verify the stability of the oxide phases on this level of theory. Cl and Br were the only two elements, with oxide phases found to lie above the convex hull. Elemental (non-metallic) phases were used as a reference for these defect atoms. In all other cases the listed oxide phases were used.

Only relative stability between elements is affected by the inclusion of chemical potentials. Thermodynamic transition levels and, hence, the determination of the stable charge state at the valence band maximum (VBM) or conduction band minimum (CBM) for a given defect is not altered by the choice of chemical potential. Reference phases were, as a consequence, only calculated for those defect atoms that were deemed as interesting dopants in SnO_2.

Table A.2. List of the secondary phases used for formation energy calculations.

Defect atom	Formula	Spg	MPID	E^{PBE} (eV)	E^{PBE0} (eV)
H	H_2O	-	-	-7.053	-7.717
Sn	SnO_2	$P4_2/mnm$	**mp-856**	-4.943	-5.680
As	As_2O_5	$P4_32_12$	**mp-555434**	-7.510	-9.191
Au	Au_2O_3	$F2dd$	**mp-27253**	-0.464	-0.008
Be	BeO	$P6_3mc$	**mp-2542**	-5.538	-5.879
Bi	BiO_2	$C2/c$	**mp-557993**	-3.059	-3.278
I	I_2O_5	$P2_1/c$	**mp-23261**	-1.907	-1.652
Mg	MgO	$Fm\overline{3}m$	**mp-1265**	-5.473	-5.735
Nb	Nb_2O_5	$P1$	**mp-680944**	-17.040	-19.512
P	P_2SnO_7	$P\overline{1}$	**mp-757192**	-20.627	-23.824
Sb	Sb_2O_5	$C2/c$	**mp-1705**	-8.810	-10.379
Ta	Ta_2O_5	$Pmnm$	**mvc-4415**	-19.981	-22.551
Te	TeO_2	$Pbca$	**mp-2125**	-3.133	-3.601
W	WO_3	$Pcnb$	**mp-19342**	-8.525	-9.309

A.2. Tin Monoxide

Table A.3 and Table A.4 provide structural information for the chemical potential reference phases used in the dopant screening study of tin monoxide, SnO, presented in Section 4.2. The space group, materials project ID number of the structure and formation energies per formula unit calculated with the relevant functionals are provided.

A handful of lowest energy structures of Sn_mD_n and D_kO_l compounds (reported in Materials Project database) were considered. For alakali *p*-type dopants ternary compounds were investigated as well, to verify the validity of the low formation energies

Table A.3. List of the secondary phases used for formation energy calculations.

Defect atom	Formula	Spg	MPID	E^{PBE} (eV)	E^{HSE06} (eV)
Au	Sn_2Au	*Pbca*	**mp-1462**	-0.399	-0.239
Cl	$SnCl_2$	*Pnma*	**mp-569152**	-3.007	-2.972
Br	$SnBr_2$	*Pnma*	**mp-29862**	-2.360	-2.438
I	SnI_2	$C2/m$	**mp-27194**	-1.498	-1.550
Li	Li_2SnO_3	$C2/c$	**mp-3540**	-11.338	-11.728
Na	Na_4SnO_4	$P\bar{1}$	**mp-9655**	-14.411	-14.635
K	K_4SnO_4	$P\bar{1}$	**mp-7258**	-13.642	-13.992
Rb	Rb_2SnO_2	$P2_12_12_1$	**mp-27931**	-6.826	-6.986
Cs	Cs_2SnO_3	*Cmcm*	**mp-861243**	-9.257	-9.514
Al	Al_2O_3	$R\bar{3}c$	**mp-1143**	-15.132	-15.993
F	Sn_2OF_2	$C2/m$	**mp-27480**	-9.514	-9.488
Hf	HfO_2	$P2_1/c$	**mp-352**	-10.755	-11.179
Nb	Nb_2SnO_6	$C2/c$	**mp-3324**	-20.707	-21.068
P	$Sn_5(PO_5)_2$	$P\bar{1}$	**mp-560715**	-29.854	-30.633
As	As_2O_5	$P4_32_12$	**mp-555434**	-7.510	-8.136
Ta	Ta_2SnO_6	*Cc*	**mp-556489**	-22.852	-22.408
Ti	Ti_2O_3	$R\bar{3}c$	**mp-458**	-14.250	-14.599
W	WO_3	*Pcnb*	**mp-19342**	-8.525	-8.162
Y	Y_2O_3	$R\bar{3}c$	**mp-754759**	-17.851	-18.770
V	VO_2	$P4_2/mnm$	**mp-19094**	-6.926	-6.733
Sc	Sc_2O_3	$R\bar{3}c$	**mp-755313**	-17.760	-18.655
Zr	ZrO_2	$P2_1/c$	**mp-2852**	-10.397	-10.987

reported. Only the phases found to result in the strictest chemical potential bounds were used in the study and are shown in Table A.3. The narrow (single point) chemical potential bounds for SnO stability resulted in some defect formation energies being completely unaffected by secondary phase formation, these elements were: C, Sb, Tc and Mn.

Crystalline elemental phases were used as reference for all elements except oxygen, where the isolated O_2 molecule in a large box of $10\times10\times10$ Å^3 was used. All calculations were performed with the same PAW files and convergence criteria outlined in Section 4.2. For computational efficiency, non-spin-polarized calculations were chosen. k-point mesh convergence was checked for each individual structure such that changes in energy of no more than 1-3 meV/atom were observed.

The thermodynamic transition levels and, thus, the stable charge state of a given defect at the VBM/CBM is not altered by the choice of chemical potential, as the reference phase contributions cancel. For computational efficiency, reference phases were only evaluated for defect elements that were deemed as interesting dopants, i.e. when the relative stability between these defects and native defects (for example the tin vacancy) becomes of interest.

Table A.4. List of the elemental phases used for formation energy calculations.

Defect atom	Spg	MPID	E^{PBE} (eV)	E^{HSE06} (eV)
Au	$Fm\overline{3}m$	**mp-81**	-3.222	-3.427
Cl	$Cmca$	**mp-22848**	-1.839	-2.662
Br	$Cmca$	**mp-23154**	-1.635	-2.276
Ag	$Fm\overline{3}m$	**mp-124**	-2.716	-2.855
Li	$Im\overline{3}m$	**mp-135**	-1.895	-1.962
Na	$Im\overline{3}m$	**mp-127**	-1.309	-1.399
K	$Im\overline{3}m$	**mp-58**	-1.029	-1.092
Rb	$Im\overline{3}m$	**mp-70**	-0.916	-0.980
Cs	$Im\overline{3}m$	**mp-1**	-0.852	-0.947
I	$Cmca$	**mp-23153**	-1.518	-2.042
O	-	-	-4.937	-7.001
Sn	$Fd\overline{3}m$	**mp-117**	-3.846	-4.543
F	$C2/m$	**mp-561367**	-1.795	-3.248
P	$Cmca$	**mp-157**	-5.375	-6.461
As	$R\overline{3}m$	**mp-11**	-4.670	-5.595
Sb	$R\overline{3}m$	**mp-104**	-4.134	-5.097
V	$Im\overline{3}m$	**mp-146**	-8.939	-10.735
Nb	$Im\overline{3}m$	**mp-75**	-10.093	-11.718
Ta	$Im\overline{3}m$	**mp-50**	-11.833	-13.633
W	$Im\overline{3}m$	**mp-91**	-13.032	-15.225
Y	$P6_3/mmc$	**mp-112**	-6.434	-7.297
Sc	$P6_3/mmc$	**mp-67**	-6.119	-7.325
Os	$P6_3/mmc$	**mp-49**	-11.251	-13.029
Ti	$P6/mmm$	**mp-72**	-7.775	-9.384
Zr	$P6_3/mmc$	**mp-131**	-8.521	-9.845
Hf	$P6_3/mmc$	**mp-103**	-9.957	-11.393
Mn	$Fm\overline{3}m$	**mp-8634**	-8.898	-10.754
Al	$Fm\overline{3}m$	**mp-134**	-3.743	-4.106
C	$Cmma$	**mp-568286**	-9.231	-10.611

A.3. Tin Monoxide – Complexes

Chemical potentials, μ_i, corresponding to a chemical species i used to calculate defect formation energies, reported in the defected complex study of tin monoxide (Section 5.2), were obtained using the elemental reference phases listed in Table A.5. The corresponding Materials Project ID number is reported for each structure, together with the space group of the phase. Each structure was individually relaxed and evaluated using the criteria outlined in Section 5.2. For each structure a Monhhorst-Pack k-point mesh was chosen individually in order to obtain total energies with a convergence of at least 3 meV/atom. As a result, the structures are slightly altered from those provided

by the Materials Project ID number and exact formation energies per formula unit obtained with the HSE06 functional are also reported in Table A.5.

Table A.5. List of the elemental phases used for formation energy calculations.

Defect atom	Spg	MPID	E^F (eV)
Sn	$Fd\bar{3}m$	**mp-117**	-4.543
O	-	-	-7.001
S	$P2/c$	**mp-96**	-5.247
Se	$P3_121$	**mp-14**	-4.444
Te	$P3_121$	**mp-19**	-3.973
Po	$P3_121$	N/A	-3.786
F	$C2/m$	**mp-561367**	-3.248
Cl	$Cmce$	**mp-22848**	-2.662
Br	$Cmce$	**mp-23154**	-2.276
I	$Cmce$	**mp-23153**	-2.042

Elemental crystal phases were used for all species, except oxygen, were an isolated O_2 molecule in a large box of $10 \times 10 \times 10$ Å^3 was used. The lowest energy structure of Sn_mD_n and D_kO_l compounds (extracted from Materials Project database and described in Table A.6) was considered for secondary phase formation. Except for fluorine, where the Sn_2OF_2 phase was used, identified as the one resulting in the strictest chemical potentials in a previous study [15]. For Sn-rich conditions, that prevent SnO oxidation into SnO_2, only Sn_mD_n compositions were found to affect the chemical potential bounds for all other halides and chalcogens.

Table A.6. List of the secondary phases used for formation energy calculations.

Defect atom	Formula	Spg	MPID	E^F (eV)
S	SnS_2	$Pnma$	**mp-2231**	-0.832
Se	$SnSe_2$	$Pnma$	**mp-691**	-0.868
Te	$SnTe_2$	$Fm\bar{3}m$	**mp-1883**	-0.539
Po	$SnPo_2$	$Fm\bar{3}m$	N/A	-0.292
F	Sn_2OF_2	$C2/m$	**mp-27480**	-9.484
Cl	$SnCl_2$	$Pnma$	**mp-569152**	-2.972
Br	$SnBr_2$	$Pnma$	**mp-29862**	-2.438
I	SnI_2	$C2/m$	**mp-27194**	-1.550

In the case of polonium, no phase information could be found in the Materials Project database. Thus, hypothetical phases were constructed using the stable structures of tellurium as a basis and optimizing both lattice parameters and atomic positions. Naturally, more appropriate phases may result in stricter chemical potential bounds.

B Electronic Density of States

This appendix provides the electronic density of states (DOS) plots for all n-type dopants that were not eliminated in the PBE pre-screening of the dopant search in tin dioxide, SnO_2, presented in Section 4.1. The DOS plots compare the PBE and PBE0 electronic structure predictions.

Fig. B.1 shows the DOS of the n-type dopants, i.e. elements that were found to be stable in a positive charge state when the Fermi level is at the CBM, using both GGA and the hybrid functional level of theory. These are all elements of category (a) discussed in Section 4.1 - elements resulting in no defect states inside the band gap. As these elements preserve the electronic structure of the SnO_2 host, we can easily evaluate their effect on the fundamental band gap. The difference between the conduction band minimum (CBM) and the valence band maximum (VBM) energies in eV is, therefore, also included in the plot for these elements, revealing a closing of the band gap effect of group VA elements (left panel) and opening of the band gap caused by group VB elements (right panel).

Fig. B.2 shows the DOS for Te and Fr. Both of these elements were predicted to be n-type dopants with PBE (left panels), but were found to be stable in the charge neutral state using PBE0 (right panels). While both of these elements show defect states inside the band gap, the intriguing nature of these states lead us to investigate them using PBE0 level of theory. These elements were placed in category (b) in Section 4.1, as Te-doped SnO_2 case resulted in a defect state (comprised of Sn-s states only) separated into the mid-gap – a rather peculiar finding. Fr-doped SnO_2 resulted in an occupied state near the VBM (which should not strongly affect the optical properties of SnO_2) as well as unoccupied defect states above the CBM.

Fig. B.3 shows the DOS of Cl, Au and Bi. These elements were predicted to be n-type dopants with PBE (left panels), but were found to be stable in the acceptor state using PBE0 (right panels). All three of these elements, like Fr show strong deviations from the SnO_2 electronic structure at the CBM, but no states inside the band gap and could, thus, still act as electron donors without affecting the transparency. We observe, however, that with PBE0 level of theory this behaviour is not preserved and the defect states are localized inside the gap.

Fig. B.4 shows the DOS for Br - the only element in category (a) (see Section 4.1 for more details) found to be non-donating using hybrid functional level of theory - and W - the only element in category (b) found to still be donating using hybrid functional level of theory. We show both the DOS for PBE and PBE0 stable charge states. When the Fermi level is at the CBM bromine is stable in a $q = 1$ state and tungsten is stable in a $q = 2$ charge state, using PBE level of theory. PBE0, on the other hand, predicts $q = -1$ (Br) and $q = 1$ (W) states to be stable.

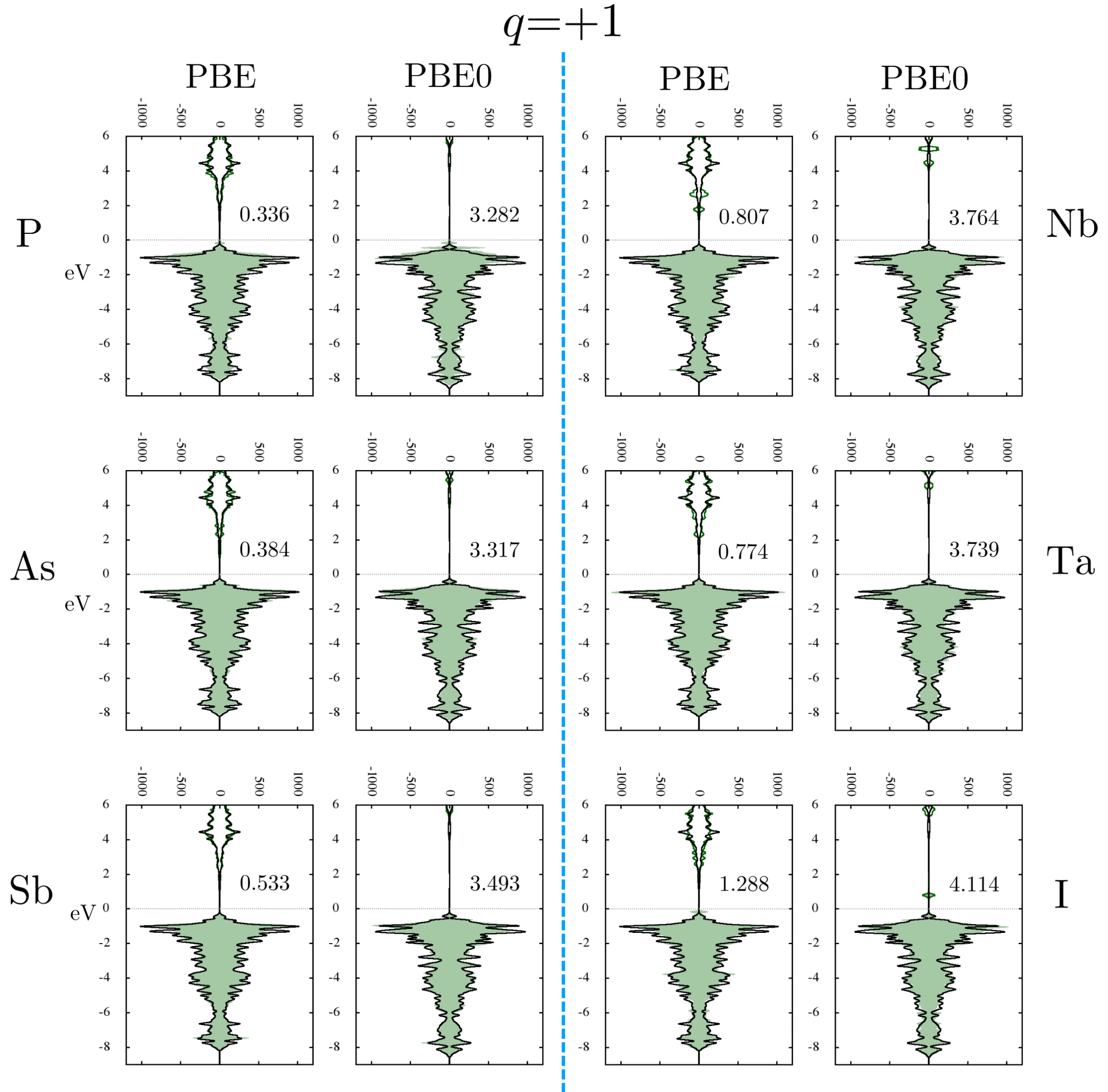

Figure B.1. Electronic density of states for selected dopant atoms at charge $q = 1$ state. Black solid line shows the DOS of pure SnO_2 as a reference, with the Fermi level of the pure SnO_2 crystal aligned to zero. Green solid line shows the DOS of the doped system, with shaded areas indicating the occupied states only.

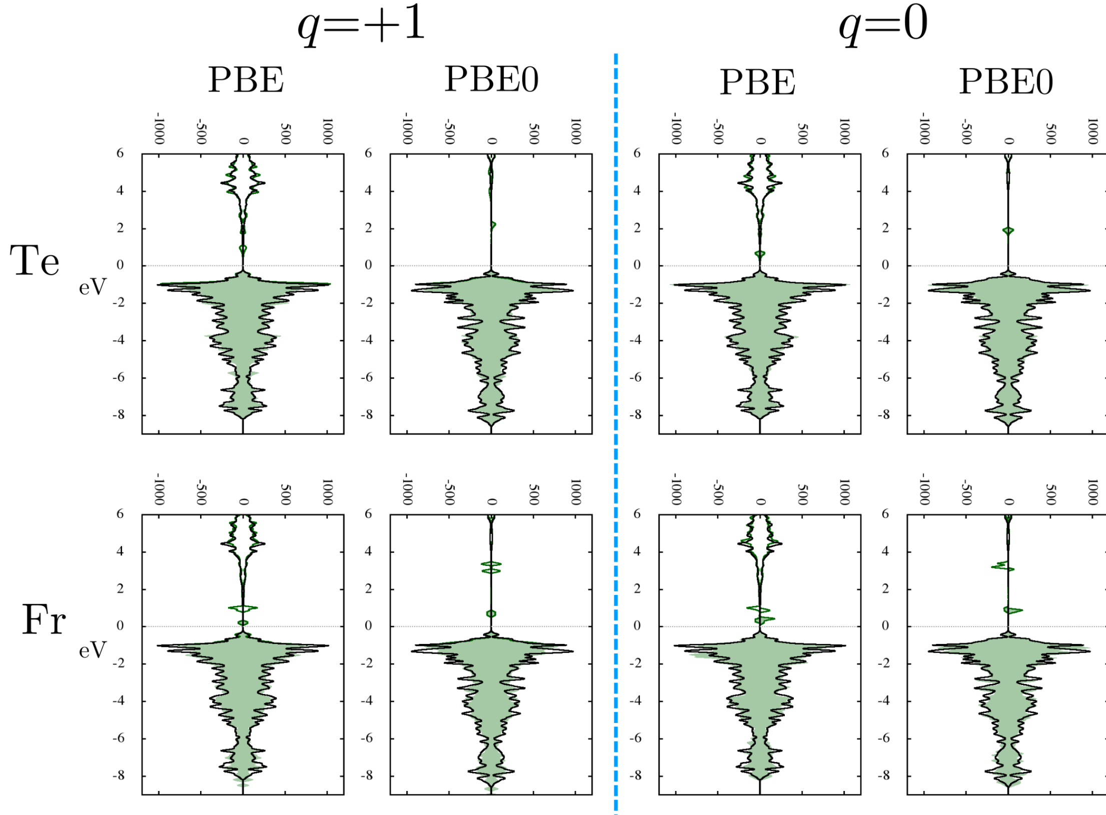

Figure B.2. Electronic density of states for selected dopant atoms. The PBE stable $q = 1$ charge state (two left side panels) and the PBE0 stable $q = 0$ charge state (two right side panels) when the Fermi level is at the CBM is shown. Black solid line shows the DOS of pure SnO_2, with the Fermi level of the pure SnO_2 crystal aligned to zero. Green solid line shows the DOS of the doped system, with shaded area indicating the occupied states only.

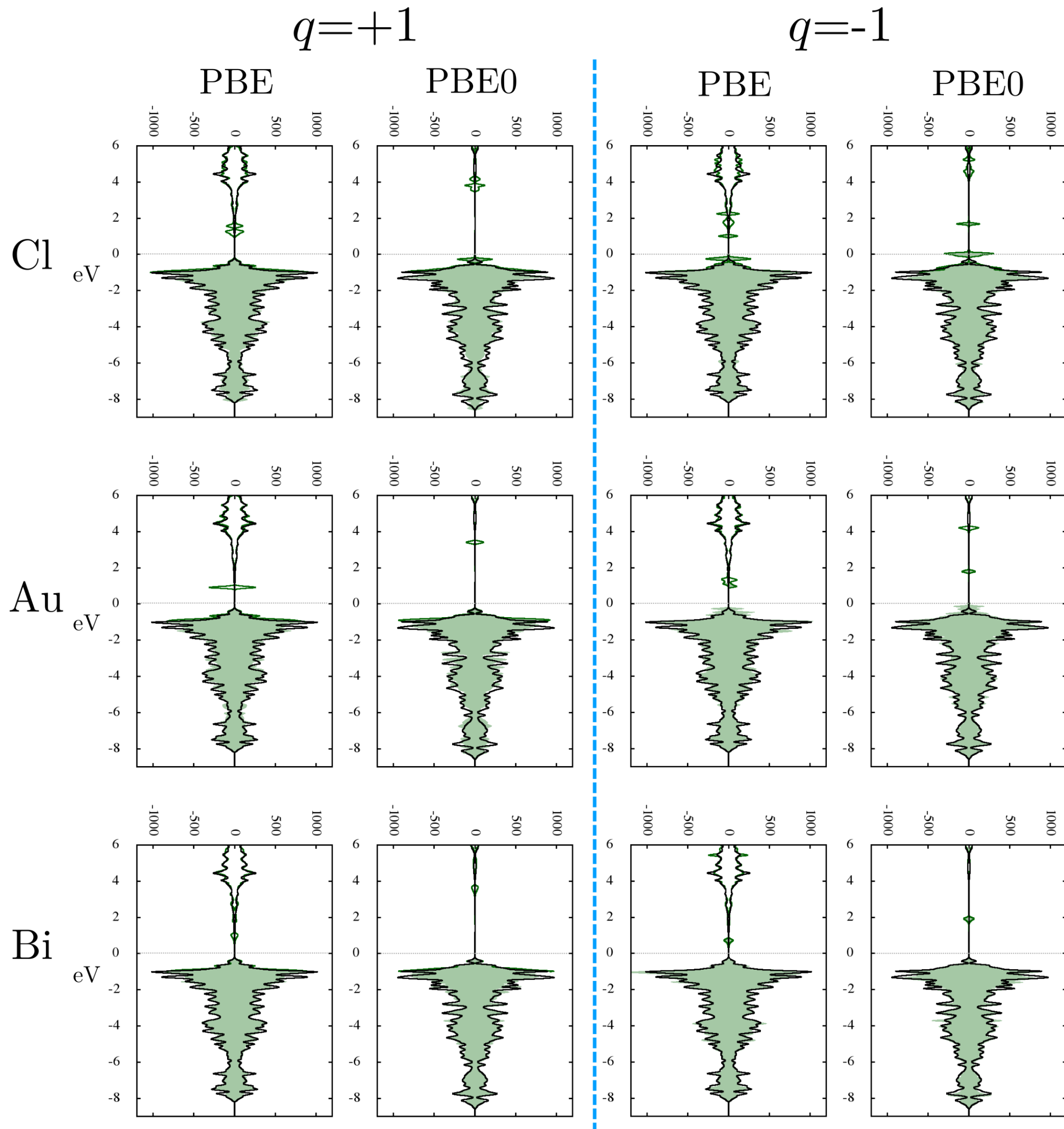

Figure B.3. Electronic density for selected dopant atoms. The PBE stable $q = +1$ charge state (two left side panels) and the PBE0 stable $q = -1$ charge state (two right side panels) when the Fermi level is at the CBM is shown. Black solid line shows the DOS of pure SnO_2, with the Fermi level of the pure SnO_2 crystal aligned to zero. Green solid line shows the DOS of the doped system, with shaded area indicating the occupied states only.

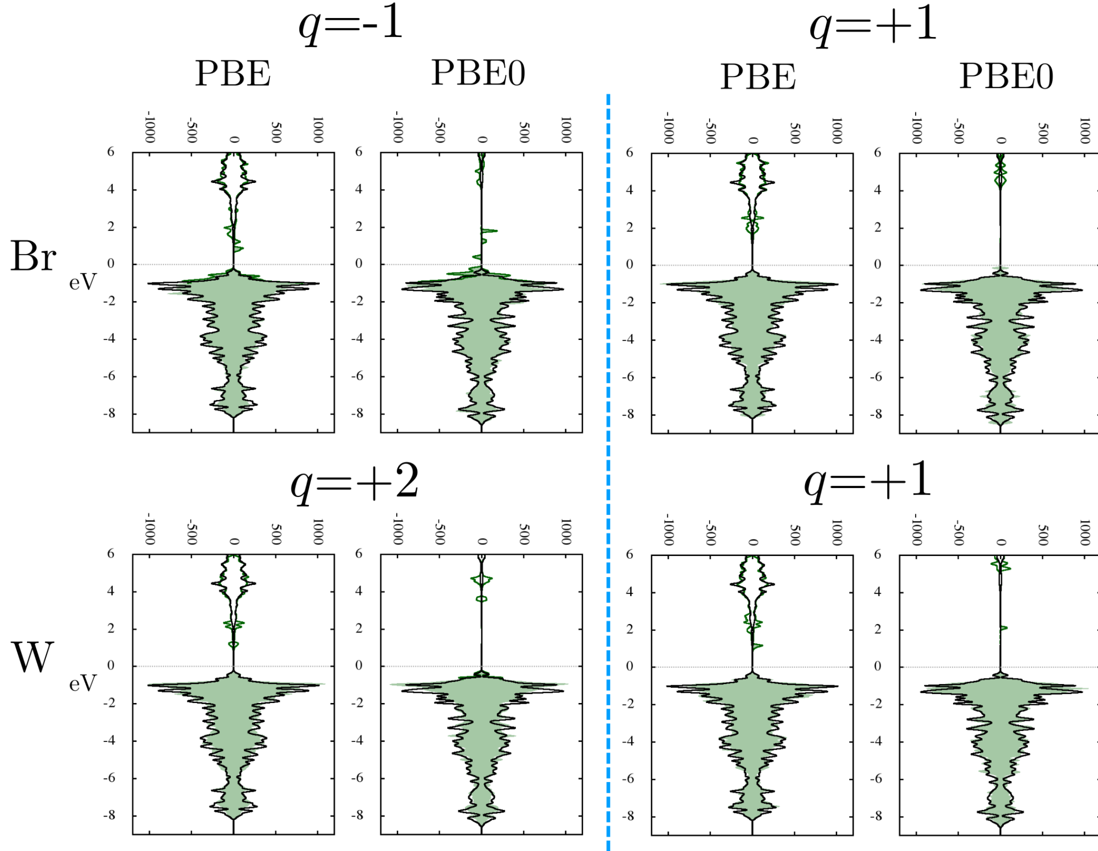

Figure B.4. Electronic density of states for selected dopant atoms. The PBE (two left side panels) and the PBE0 (two right side panels) stable charge states when the Fermi level is at the CBM are shown. Black solid line shows the DOS of pure SnO_2, with the Fermi level of the pure SnO_2 crystal aligned to zero. Green solid line shows the DOS of the doped system, with shaded area indicating the occupied states only.

C HSE06 Relaxations

The approach of simply compressing relaxed PBE defect structures to match the HSE06 lattice, used in the dopant screening study of SnO presented in Section 4.2, was tested by considering full atomic relaxations using the hybrid exchange correlation functional for a small subset of elements. In Table C.1 the effects of such relaxations are summarized by using two values: (i) the total change in the supercell energy upon relaxation given by $\Delta E = E_{\text{relax}} - E_{\text{fixed}}$ and (ii) the change in the bond lengths between the defect atom, D, and the nearest neighbor oxygens, $\Delta \mathrm{d}^{\mathrm{D-O}} = \mathrm{d}^{\mathrm{D-O}}_{\text{relax}} - \mathrm{d}^{\mathrm{D-O}}_{\text{fixed}}$. In the case of a tin vacancy, the latter could not be evaluated, however, Table C.1 reveals that the formation energies are virtually unchanged by HSE06 relaxations, despite the lighter (and, hence, more mobile) oxygen atoms that make up the local defect environment.

Table C.1. Summary of local atomic relaxation effects using the HSE06 functional for a selection of atoms. ΔE is the energy change due to atomic relaxations. $\Delta \mathrm{d}^{\mathrm{D-O}}$ is the change in the bond distances between the defect D and the surrounding O atoms. All bond distances were seen to increase with relaxation.

Defect type	charge (q)	ΔE (meV)	$\Delta d^{\mathrm{D-O}}$ (Å)
V_{Sn}	0	-1.71	–
V_{Sn}	-2	-1.03	–
Ag_{Sn}	-1	-13.03	0.049
Ag_{Sn}	+1	-13.02	0.040
Y_{Sn}	-1	-16.74	0.025
Y_{Sn}	+1	-16.99	0.025
Ta_{Sn}	-1	-53.75	0.027
Ta_{Sn}	+1	-41.89	0.026

Similarly, local relaxations of the Ag_{Sn} (representing p-type dopants) and the Y_{Sn} (representing n-type dopants) defects resulted in total energy changes below 20 meV. The transition state energies, determined as energy difference between charged states, were even less affected (< 1 meV). The small impact of atomic relaxations could have been anticipated given the focus of our investigation – a search for shallow donors/acceptors. The shallow nature of the defects identified as useful indicates bulk-derived occupied bands. The defect atom and, hence, atomic relaxations around it provide only a fractional contribution to such bands.

Only six (Hf, Ti, Zr, Nb, Ta and Os) elements out of the twenty dopants suggested, result in occupied defect-atom-derived states (see Fig. 4.16 in Chapter 4). Here, the

strongest atomic relaxation effects are expected. Among these elements, tantalum requires the least energy to form at 3.6 eV. We find that ~50 meV in energy can be gained by structural relaxations for this defect. At such high formation energies, this small change would be negligible for room temperature SnO. Furthermore, the transition between the $q = +1$ and $q = -1$ charge states is shifted by a much smaller energy of just 12 meV. Such values are well below the errors anticipated from the electrostatic charge correction terms, such as potential alignment, and as a consequence can be safely neglected when searching for useful dopants.

D Defect Concentrations in Thermal Equilibrium

Defect concentrations, C_{D_x}, in thermodynamic equilibrium were determined for nominally undoped SnO films, using the approach presented in Section 3.5.2. The electron concentration in the conduction band, n, and the hole concentration in the valence band, p of the material were obtained by replacing the Fermi-Dirac integral with a sum over one-electron energies obtained from a unit cell calculation. Here HSE06 functional was used with a Γ-centered k-point mesh of 12×12×12, following the approach of Togo *et al.* [132]. The k-point mesh size used in determining the free carrier concentrations was limited by the expensive HSE06 calculations. Tests performed with PBE level of theory showed that using a 30×30×30 mesh instead of a 12×12×12 changed defect and free-carrier concentrations by less than an order of magnitude. Chemical potentials of the defects were fixed to the intersection between SnO_2 and metallic α-Sn, in analogy to the work presented in Section 4.2.

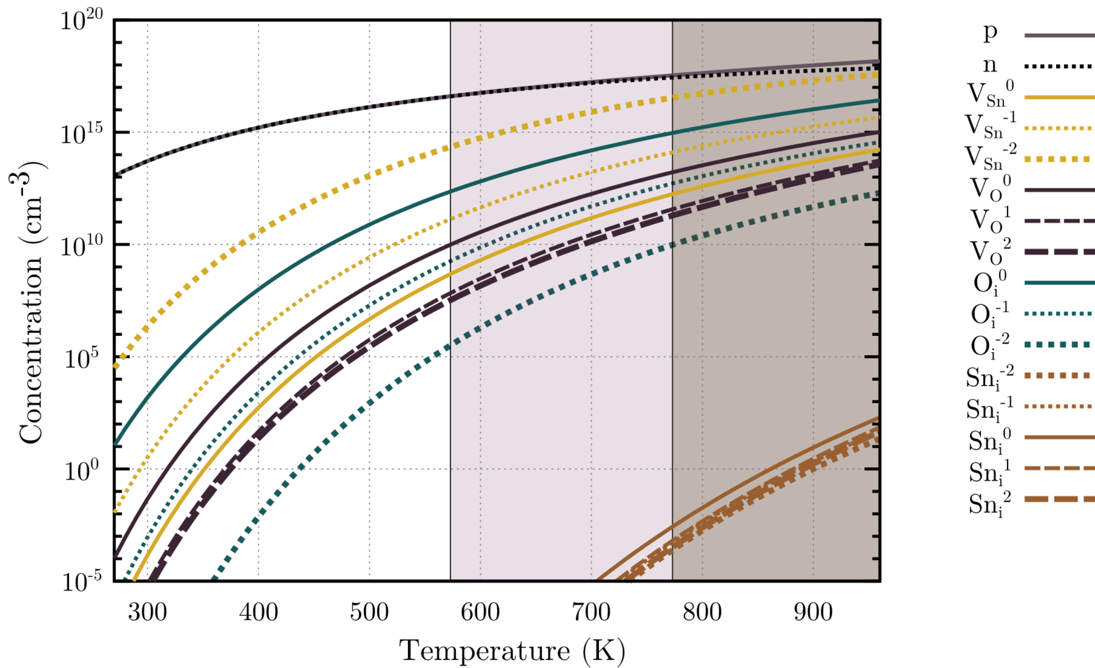

Figure D.1. Native defect concentrations in SnO as a function of temperature. Hole (p) and electron (n) concentrations are shown, indicating that undoped SnO is intrinsic carrier dominated. SnO is unstable in temperature regions shaded in pink, while in the brown areas SnO and SnO_2 are reported to coexist [223].

Native defect concentrations in thermal equilibrium as a function of temperature for undoped SnO are shown in Figure D.1. Only four native defects were considered: V_{Sn}, V_O, Sn^i and O^i. The region of stability of SnO is also indicated in the figure, as reported in Ref. [223]. In the light pink shaded temperature region, additional phases, such as SnO_2 and metallic Sn, are reported to start appearing in the film. In the brown shaded zone the SnO film is replaced completely by the dioxide phase. It can be seen from Figure D.1 that the dominant intrinsic defect among those considered is the V_{Sn}^{-2}. However, in the temperature range in which the SnO film is expected to be stable intrinsic carriers would dominate those produced by the tin vacancies – a consequence of the small fundamental band gap of SnO and the rather large formation energies of V_{Sn}^{-2}. As a result dopant-free SnO would be expected to act as an intrinsic semiconductor.

E Shallow Acceptor Correction

In Section 5.2 formation energies of defect complexes in tin monoxide were calculated. In the case of shallow acceptor behavior (all complexes shown in Figure 5.5) a charge correction corresponding to the ionized defect state was applied to every charge state. For high charges ($Q = -4$ or $Q = -3$), the corresponding electrostatic corrections are sizable, therefore, the basis for and the consequences of this choice are illuminated here.

First, we demonstrate in Figure E.1 the difference in the electronic charge density between the stable charge state ($Q = -4$) of the (V_{Sn^T} + S_i) complex and a selection of lower charge states. The results are qualitatively similar for all charge states. Here, the sulfur defect complex is used as an example, but analogous behavior is observed for all chalcogen and halogen complexes. It is clear that any additional charge in the system is completely delocalized throughout the monolayers surrounding the impurity site (indicated by a yellow sphere in Fig. E.1). Thus, in the lower charge states ($Q = -2$ and $Q = 0$) the holes are not observed to localize on the sulfur site, but instead a picture analogous to a compensating jellium background (see Section 3.6) emerges.

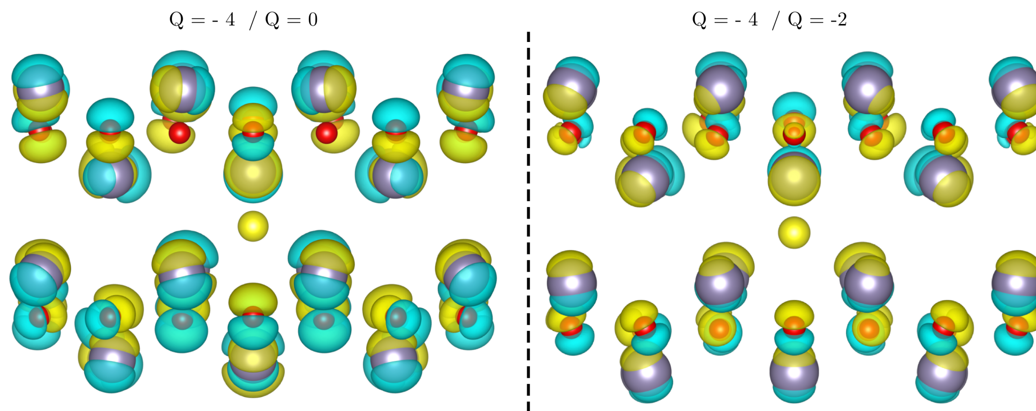

Figure E.1. Differences in the charge density calculated between $Q = -4$ and $Q = 0$ charge states (left) and $Q = -4$ and $Q = -2$ charge states (right) for supercells containing an interstitial sulfur neighbouring a tin vacancy. Oxygen atoms are shown in red, tin is represented by purple, sulfur interstitial is indicated in yellow. Positive differences are shown in yellow, negative differences are shown in blue. The isosurface value is set to 0.01.

This demonstrates the validity of using an identical charge correction term between different nominally charged supercells: the V_{Sn^T} site retains its $q = -4$ charge irrespective of the overall charge (Q) of the supercell. Nevertheless, to highlight the effect this

choice has on the calculated formation energies and charge state stability of the defect complexes, we reproduce in Figure E.2 the results of Figure 5.5, with using charge corrections that correspond to the nominal charge state of the supercell.

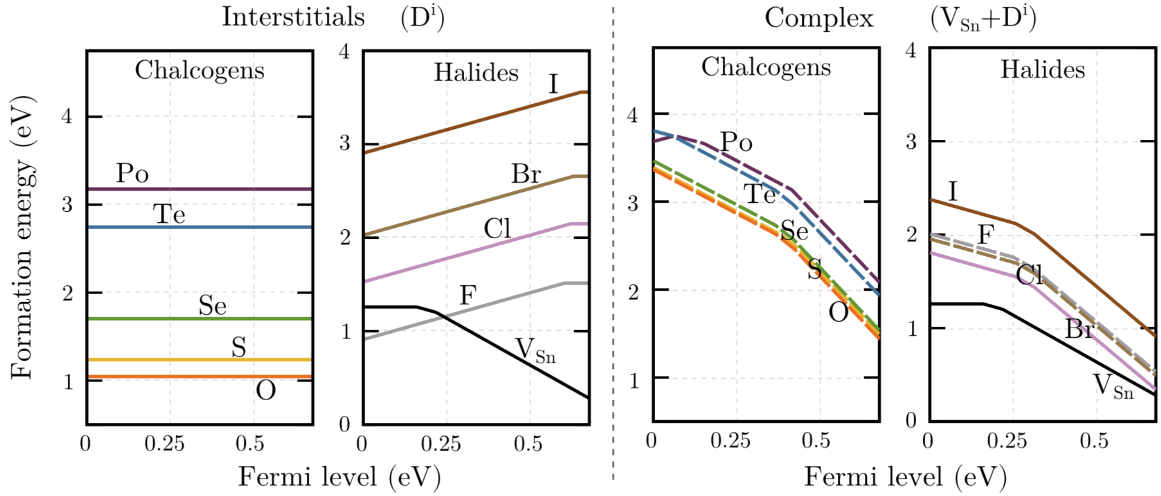

Figure E.2. Defect formation energies calculated with charge corrections applied to the supercell based on its nominal charge state. These are shown for comparison with Figure 5.5 in Chapter 4.

It is clear that the interstitial energies are largely unaffected by the shallow charge correction. At the same time, lower charge states of the defect complex become favored energetically at Fermi levels in the mid-gap region. Regardless, all impurity complexes (except that of polonium), still maintain the acceptor charge state to much lower Fermi levels than the isolated V_{Sn}. Thus, the behavior reported in Section 5.2 for *p*-type SnO is preserved. Furthermore, the lower formation energy of the $Q = -2$ and $Q = -1$ charge states stable at the VBM would make these complexes much easier to form, than those predicted in Section 5.2. We conclude that the choice of charge correction does not change the qualitative nature of our predictions and only changes the quantitative nature towards making the proposed defect-complex mechanism more favorable.

Publications

- **A divalent path to enhance p-type conductivity in a SnO transparent semiconductor** Graužinytė, M., Tomerini, D., Goedecker, S., Flores-Livas, J. A. *J. Phys. Chem.*,123(24), 14909, 2019.
- **Towards bipolar tin monoxide: revealing unexplored dopants** Graužinytė, M., Goedecker, S., Flores-Livas, J. A. *Phys. Rev. Mater.*, 2, 104604, 2018.
- **Pressure tuneable visible-range band gap in the ionic spinel tin nitride** Kearney, J., Graužinytė, M., Smith, D., Gulans, A., Sneed, D., Childs, C., Hinton, J., Park, C., Smith, J. S., Kim, E., Fitch, S. D. S., Hector, A. L., Pickard, C. J., Flores-Livas, J. A., Salamat, A. *Angew. Chem. Int. Ed.*, 2018.
- **A New Route for "Cold-Passivation" of Defects in Tin-Based Oxides** Rucavado, E., Graužinytė, M., Flores-Livas, J. A., Jeangros, Q., Landucci, F., Lee, Y., Koida, T., Goedecker, S., Hessler-Wyser, A., Ballif, C., Morales-Masis, M. *J. Phys. Chem.*, 122 (31), 17612, 2018.
- **Superconductivity in doped polyethylene at high pressure** Flores-Livas, J. A., Graužinytė, M., Boeri, L., Profeta, G., Sanna, A. *Euro. Phys. J. B*, 91(8), 176, 2018.
- **Computational Screening of Useful Hole–Electron Dopants in SnO_2** Graužinytė, M., Goedecker, S., Flores-Livas, J. A. *Chem. Mater.*, 29(23), 10095-10103, 2017.
- **Emergence of superconductivity in doped H_2O ice at high pressure** Flores-Livas, J. A., Sanna, A., Graužinytė, M., Davydov, A., Goedecker, S., Marques, M. A. *Sci. Rep.*, 7(1), 6825, 2017.
- **A fingerprint based metric for measuring similarities of crystalline structures** Zhu, L., Amsler, M., Fuhrer, T., Schaefer, B., Faraji, S., Rostami, S., Ghasemi, S. A., Sadeghi, A., Graužinytė, M., Wolverton, C., Goedecker S. *J. Chem. Phys.*, 144(3), 03420, 2015.
- **Particle-Stabilized Water Droplets that Sprout Millimeter-Scale Tubes** Graužinytė, M., Forth, J., Rumble, K. A., Clegg, P. S. *Angew. Chem.*, 127(5), 1476-1480, 2015.